PACIFIC EARTHQUAKE ENGINEERING RESEARCH CENTER

Boore-Atkinson NGA Ground Motion Relations for the Geometric Mean Horizontal Component of Peak and Spectral Ground Motion Parameters

David M. Boore

U.S. Geological Survey, Menlo Park, California

and

Gail M. Atkinson

University of Western Ontario, Canada

Technical Report Documentation Page

1. Report No. PEER 2007/01	2. Government Accession No.	3. Recipient's Catalog No.	
4. Title and Subtitle Boore-Atkinson NGA Ground Motion Relations for the Geometric Mean Horizontal Component of Peak and Spectral Ground Motion Parameters.		5. Report Date May 2007	
		6. Performing Organization Code	
7. Author(s) David M. Boore and Gail M. Atkinson		8. Performing Organization Report No.	
9. Performing Organization Name and Address Pacific Earthquake Engineering Research Center 325 Davis Hall MC 1792 University of California Berkeley, CA 94720		10. Work Unit No. (TRAIS)	
		11. Contract or Grant No. 65A0058	
12. Sponsoring Agency Name and Address California Department of Transportation Engineering Service Center 1801 30th St., West Building MS-9 Sacramento, CA 95807		13. Type of Report and Period Covered Technical report through June 2006	
		14. Sponsoring Agency Code 06681	

15. Supplementary Notes

16. Abstract

This report contains ground motion prediction equations (GMPEs) for a particular measure of horizontal-component ground motions as a function of earthquake mechanism, distance from source to site, local average shear-wave velocity, and fault type. Our equations are for peak ground acceleration (PGA), peak ground velocity (PGV), and 5%-damped pseudo-absolute-acceleration spectra (PSA) at periods between 0.01 s and 10 s. The equations were derived by empirical regression of the PEER NGA strong-motion database. For periods of less than 1 s, the analysis used 1574 records from 58 mainshocks in the distance range from 0 km to 400 km (the number of available data decreased as period increased).

17. Key Words Ground motion prediction equations, site amplification, record processing, response spectra, NEHRP site class	18. Distribution Statement Unlimited		
19. Security Classif. (of this report) Unclassified	20. Security Classif. (of this page) Unclassified	21. No. of Pages 242	22. Price

Form DOT F 1700.7 (8-72) **Reproduction of completed page authorized**

Boore-Atkinson NGA Ground Motion Relations for the Geometric Mean Horizontal Component of Peak and Spectral Ground Motion Parameters

David M. Boore
U.S. Geological Survey, Menlo Park, California

and

Gail M. Atkinson
Department of Earth Sciences
University of Western Ontario, Canada

ABSTRACT

This report contains ground motion prediction equations (GMPEs) for a particular measure of horizontal-component ground motions as a function of earthquake mechanism, distance from source to site, local average shear-wave velocity, and fault type. Our equations are for peak ground acceleration (PGA), peak ground velocity (PGV), and 5%-damped pseudo-absolute-acceleration spectra (PSA) at periods between 0.01 s and 10 s. The equations were derived by empirical regression of the PEER NGA strong-motion database. For periods of less than 1 s, the analysis used 1574 records from 58 mainshocks in the distance range from 0 km to 400 km (the number of available data decreased as period increased).

ACKNOWLEDGMENTS

CONTENTS

LIST OF FIGURES

xi

LIST OF TABLES

1 Introduction

Ground motion prediction equations (GMPEs), giving ground motion intensity measures such as peak ground motions or response spectra as a function of earthquake magnitude and distance, are important tools in the analysis of seismic hazard. These equations are typically developed empirically by a regression of recorded strong-motion amplitude data versus magnitude, distance, and possibly other predictive variables. (Some terminology surrounding these equations is discussed in Appendix A.) The equations in this report were derived as part of the Pacific Earthquake Engineering Research Center's Next Generation Attenuation project (PEER NGA) (Power et al. 2006), using an extensive database of thousands of records compiled from active shallow crustal tectonic environments worldwide. These equations represent a substantive update to GMPEs that were published by Boore and his colleagues in 1997 (Boore et al. 1997— hereafter "BJF97"; note that BJF97 summarized work previously published by Boore et al. in 1993 and 1994). The 1997 GMPEs of Boore et al. were based on a fairly limited set of data in comparison to the results of this study. The increase in data quantity, by a factor of approximately 14, is particularly important for PSA; in addition, PGV equations are provided in this study (but were not given in BJF97). The amount of data used in regression analysis is an important issue, as it bears heavily on the reliability of the results, especially in magnitude and distance ranges that are important for seismic hazard analysis.

2 Data

2.1 DATA SOURCES

The source of the strong ground motion data for the development of the GMPEs of this study is the database compiled in the PEER–NGA project (Power et al. 2006); the aim of this project was to develop empirical GMPEs using several investigative teams to allow a range of interpretations (this paper is the report of one team). The use of this database, referred to as the "NGA flatfile," was one of the "ground rules" of the GMPE development exercise. However, investigators were free to decide whether to use the entire NGA flatfile database or to restrict their analyses to selected subsets. We used what we call v.7.27 of the flatfile. This is the version given in the file *NGA Flatfile V7.2 (07-11-05).xls*, with corrections provided by the file *727Brian.xls* sent by Brian Chiou, in an email dated February 17, 2006. The values of the response variable are different in the two versions. In v.7.2, the rotation angle used to combine the two horizontal components (see next section) for each recording was based on all periods for which PSA was computed, regardless of the low-cut filter frequency applied to each record. In v.7.27, the rotation angle was determined using periods only up to the maximum useable period (T_{MAX}). As apparently a number of the NGA developers have used v7.2, we include a comparison of the response variables for the two versions in Appendix B. Although the bulk of the data are not changed between the two versions, there are some differences. The comparisons in Appendix B suggest that it should make little or no difference to the GMPEs whether version 7.2 or 7.27 of the flatfile is used; the best test of this, of course, is to develop GMPEs using both versions. We used the corrected version of the flatfile; testing the sensitivity of the GMPEs to the version of the flatfile is beyond the scope of our study.

In addition to the data in the NGA flatfile, we also used data compiled by J. Boatwright and L. Seekins for three small events and data from the 2004 Parkfield mainshock from the

Berkeley Digital Seismic Network station near Parkfield, as well as data from the Strong-Motion Instrumentation Program of the California Geological Survey and the National Strong-Motion Program of the U.S. Geological Survey. These additional data were used in a study of the distance attenuation function that constrained certain regression coefficients, as discussed later, but were not included as part of the final regression (to be consistent with the NGA ground rules regarding the database for regression).

2.2   RESPONSE VARIABLES

The ground motion parameters that are the dependent variables of the GMPEs (also called response variables or ground motion intensity measures) include peak ground acceleration (PGA), peak ground velocity (PGV), and response spectra (PSA, the 5%-damped pseudo-acceleration), all for the horizontal component. In this study, the response variables are not the geometric mean of the two horizontal component (as was used in BJF97), but rather the values not dependent on the particular orientation of the instruments used to record the horizontal motion. The measure used was introduced by Boore et al. (2006). In that paper a number of orientation-independent measures of ground motion were defined. In this report we use GMRotI50 (which we abbreviate "GMRotI"); this is the geometric mean determined from the 50th percentile values of the geometric means computed for all nonredundant rotation angles and all periods of less than the maximum useable period. The advantage of using an orientation-independent measure of the horizontal-component amplitude can be appreciated by considering the case in which the motion is perfectly polarized along one component direction; in this case the geometric mean would be 0.

This report includes GMPEs for PGA, PGV, and 5%-damped PSA for periods between 0.01 s and 10 s. Equations for peak ground displacement (PGD) are not included. In our view, PGD is too sensitive to the low-cut filters used in the data processing to be a stable measure of ground shaking. In addition there is some bias in the PGD values obtained in the NGA dataset from records for which the low-cut filtering was not performed as part of the NGA project. Appendix C contains a short discussion of these points. We recommend using response spectra at long periods instead of PGD.

Data were excluded from our analysis based on a number of criteria, the most important of which (in terms of number of records excluded from the analysis) is that no aftershock

recordings were used. Aftershock records were not used because of some concern that the spectral scaling of aftershocks differs from mainshocks (see Boore and Atkinson 1989, and Atkinson 1993). This restriction cut the dataset almost in half because about half the records in the NGA flatfile are aftershocks of the 1999 Chi-Chi earthquake. The other exclusion criteria that were applied are listed in Table 2.1, taken from the accompanying spreadsheet *flag_definitions.xls*. Another spreadsheet, *recnum_flag.xls*, contains a flag entry for each record in the NGA flatfile; only data with flag = 0 were used in our analysis. Response variables were excluded for oscillator periods greater than T_{MAX} (the inverse of the lowest useable frequency entry in the NGA flatfile).

Table 2.1 Exclusion criteria.

Flag	Meaning
1	one h component
2	Jensen Admin Bldg?
3	V_{S30} missing
4	spikes, baseline problems (see, e.g., Appendix H)
5	dam abutments
6	dam toe
7	base of column
8	base of pier
9	basement, 12.7 m below ground, 1.8 m above bedrock
10	basement, 6.4 m below ground
11	greater than or equal to 3 stories
12	S triggers
13	older events not included in Boore et al. (1997), probably because distances are too uncertain
14	proprietary records with restrictions on use
15	earthquake in oceanic crust
16	stable continental region (SCR) events
17	basement recordings
18	Geomatrix C, D, E, F, G, H, J (but not including Lexington Dam for LP89 and LA Dam for NR94, and Martis Creek Dam for 2001 Mohawk)
19	duplicate record?
20	aftershocks
21	Chi-Chi_quality D (Lee et al. 2001)
22	chi_chi_colocated (remove record from older instrument), Many such records were removed earlier because they are quality class D
23	second trigger
24	dam crest
25	only SMART1 data for this quake, should be considered a one observation earthquake (recall Boore et al. (1997) criteria).

A potential bias in regression results can result from not including low-amplitude data for distance ranges for which larger amplitude data for the same earthquake are included in the dataset. Low-amplitude data can be below trigger thresholds of instruments, can cause the recording to begin sometime during the S-wave arrival, can be too small to digitize, or can be below the noise threshold used in determining low-cut filter frequencies. Any collection of data in a small distance range will have a range of amplitudes because of the natural variability in the ground motion (due to such things as source, path, and site variability). At distances far enough from the source (depending on magnitude), some of the values in the collection will be below the amplitude cutoff and would therefore be excluded. If only the larger motions (above the cutoff) were included, this would lead to a bias in the predicted distance decay of the ground motion— there would be a tendency for the predicted ground motions to decay less rapidly with distance than the real data. BJF97 attempted to avoid this bias by excluding data for each earthquake beyond the closest distance to an operational, nontriggered station (most of the data used by BJF97 were obtained on triggered analog stations). Unfortunately, information is not available in the NGA flatfile that would allow us to apply a similar distance cutoff, at least for the case of triggered analog recordings. Furthermore, a similar bias can also exist in nontriggered digital recordings because of the presence of long-period noise. It would be possible to devise a strategy to avoid potential bias by using information available in the NGA flatfile. For example, one could exclude all data beyond the closest station to a given event for which the maximum useable period of the processed recording is less than the oscillator period of interest. We did not attempt to define such a criterion, however, and as a result, we think that our distance dependence for small earthquakes and long periods is biased toward a decay that is less rapid than the true decay (discussed later).

2.3   PREDICTOR VARIABLES

The predictor variables (independent variables in the regression analysis) are moment magnitude **M**, R_{JB} distance (closest distance to the surface projection of the fault plane), and continuous V_{S30} (time-averaged shear-wave velocity over the top 30 m) for site characterization. We also considered the effect of fault type (i.e., normal, strike-slip, and reverse). Each of these predictor variables was taken from the NGA database. The values of V_{S30} were taken from column IE of the NGA flatfile; the values in this column are based on measured values when available and

estimates otherwise (only about 30% of the stations that provided data in the NGA flatfile had a value of V_{S30} based on a local measurement). Column IE includes W. Silva's interpretation of NCREE measurements for Taiwan as well as Brian Chiou's correlation method for Taiwan, for sites in Taiwan for which measurements are not available. The values in column IE were updated from the file *Update 1 (02-17-06) to NGA Flatfile V7.2 (07-11-05).xls*, which uses some of Rob Kayen's V_{S30} estimates based on SASW measurements. The fault type was specified by the plunge of the *P*- and *T*-axes, as described in Appendix D. The R_{JB} distances estimated by Youngs (2005) were used for earthquakes with unknown fault geometry.

2.4   DISTRIBUTION OF DATA BY M, R_{JB}, FAULT TYPE, AND SITE CLASS

The distribution of data used to develop our GMPEs are shown in Figures 2.1–2.2 by **M** and R_{JB}, with the symbols representing different fault types. The distribution by V_{S30} (as given by binning the data by NEHRP site class) is given in Figures 2.3(a)–(b). The total number of recordings for the analysis (after all exclusions) is shown as a function of oscillator period in Figure 2.4 (which also breaks down the total number of recordings into digital and analog recordings). Figure 2.4 shows that the full dataset is available for periods out to 1 s, with a slight decrease at 2 s, and a rapid fall off in the number of available data at periods longer than 2 s; note the dearth of analog recordings for periods of 9 and 10 s.
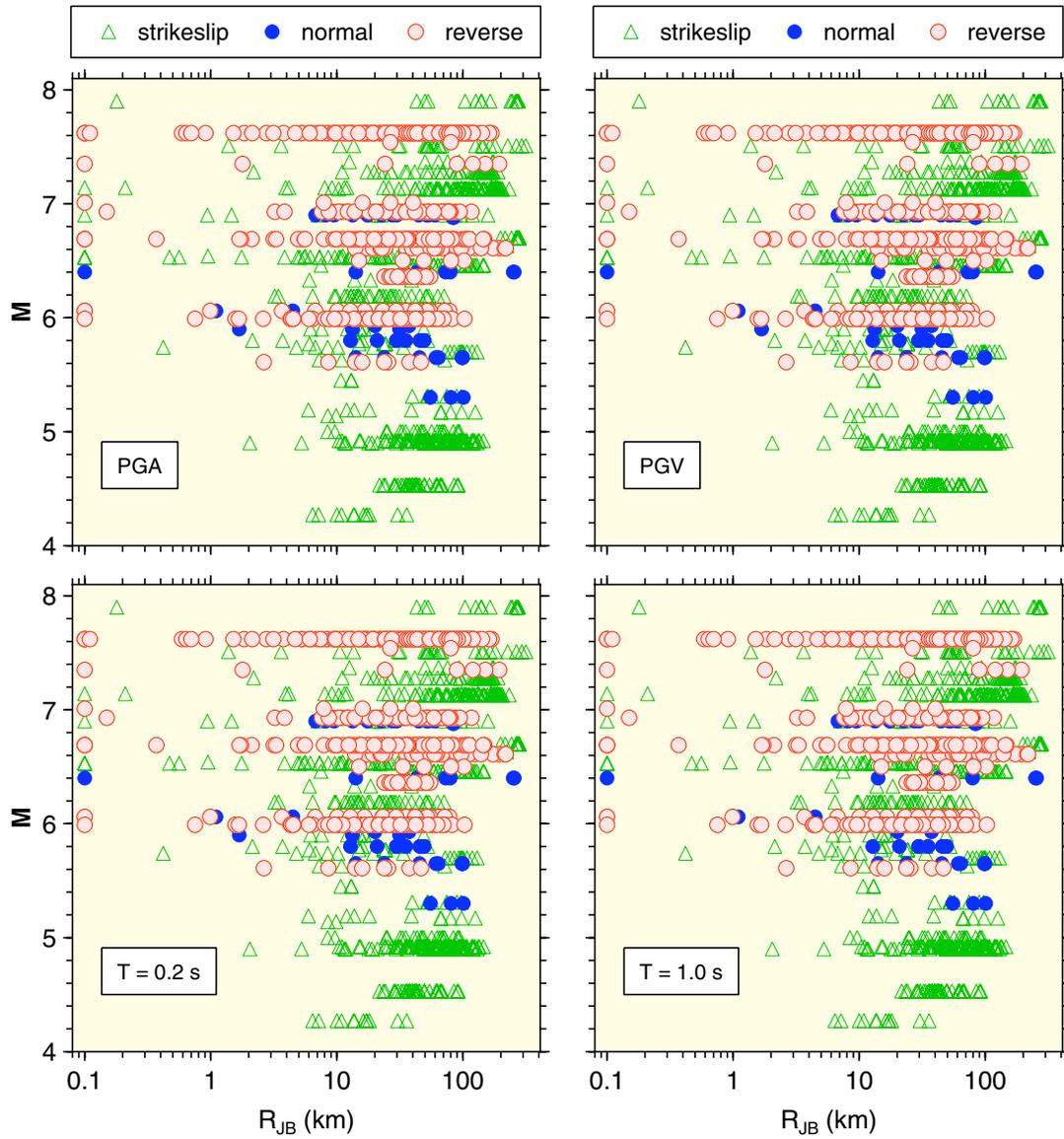
Fig. 2.1 Distribution of data used in BA07 regression equations for PGA, PGA, and PSA at 0.2 s and 1.0 s, differentiated by fault type (points with R_{JB} less than 0.1 km plotted at 0.1 km).
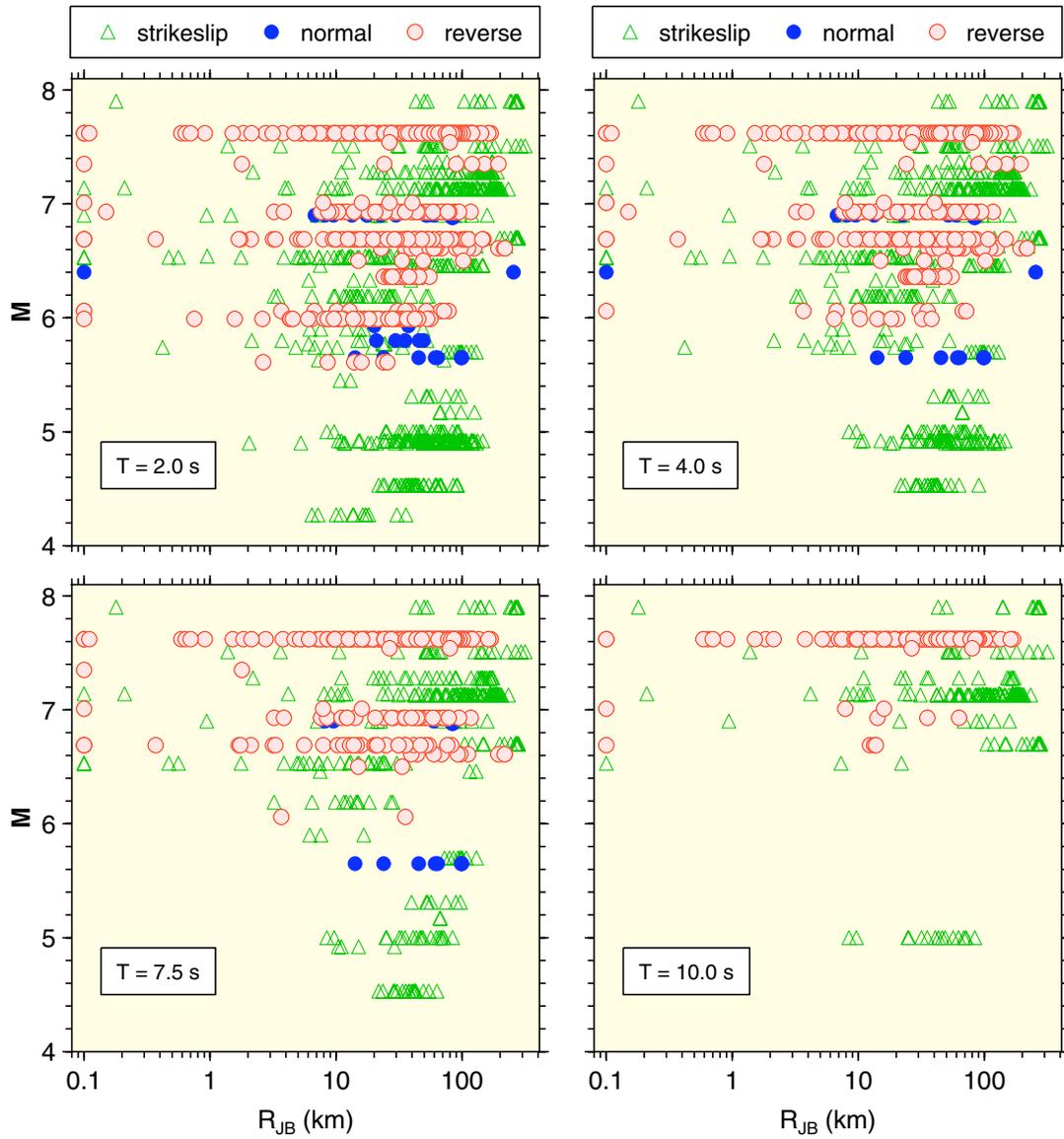
Fig. 2.2 **Distribution of data used in BA07 regression equations for PSA at periods of 2.0, 4.0, 7.5, and 10.0 s, differentiated by fault type (points with R_{JB} less than 0.1 km plotted at 0.1 km).**

9
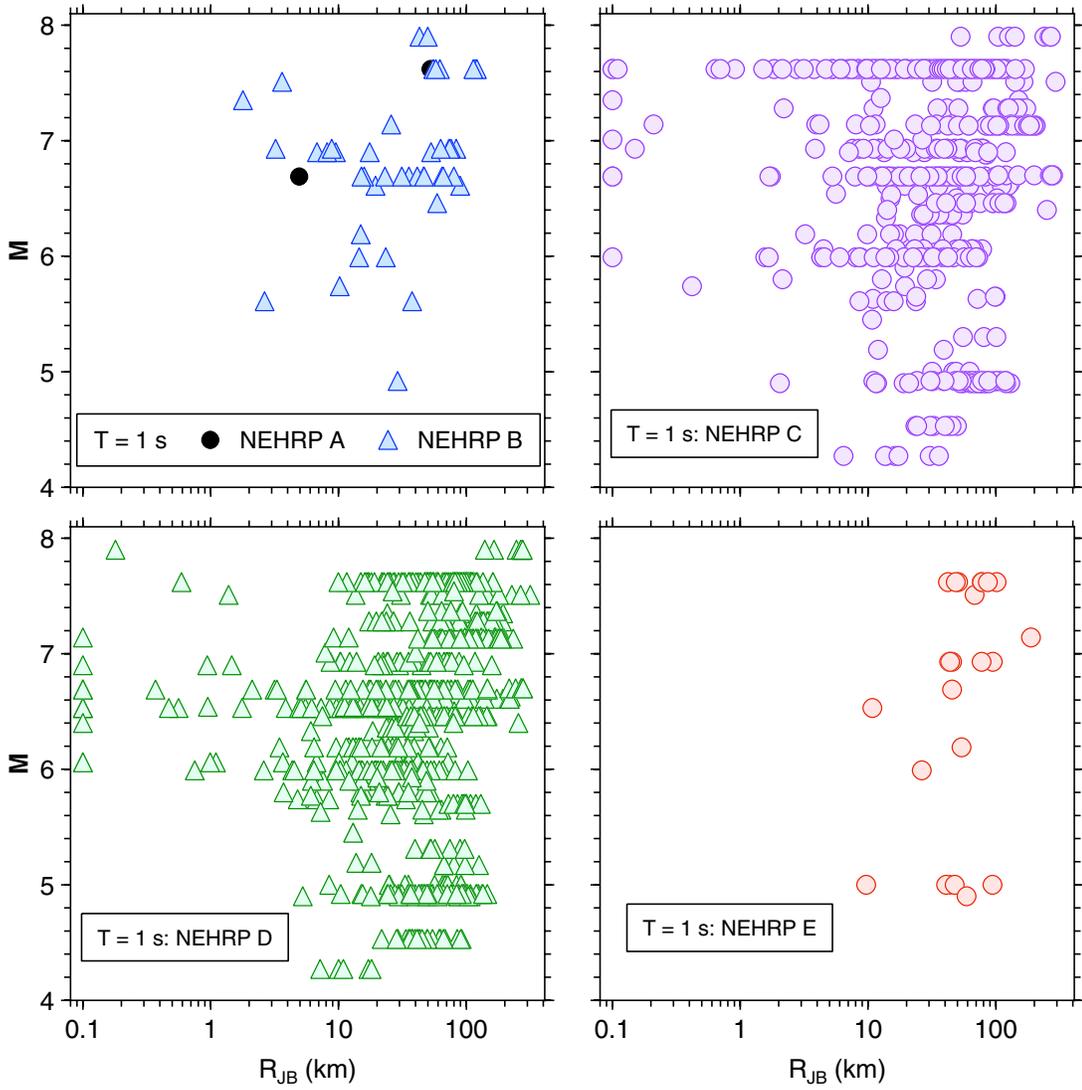
(a)

Fig. 2.3 Distribution of data used in BA07 regression equations for PSA at 1.0 s for various NEHRP site classes (points with R_{JB} less than 0.1 km plotted at 0.1 km).

(b)

Fig. 2.3—*Continued*

Records satisfying the Boore-Atkinson selection criteria
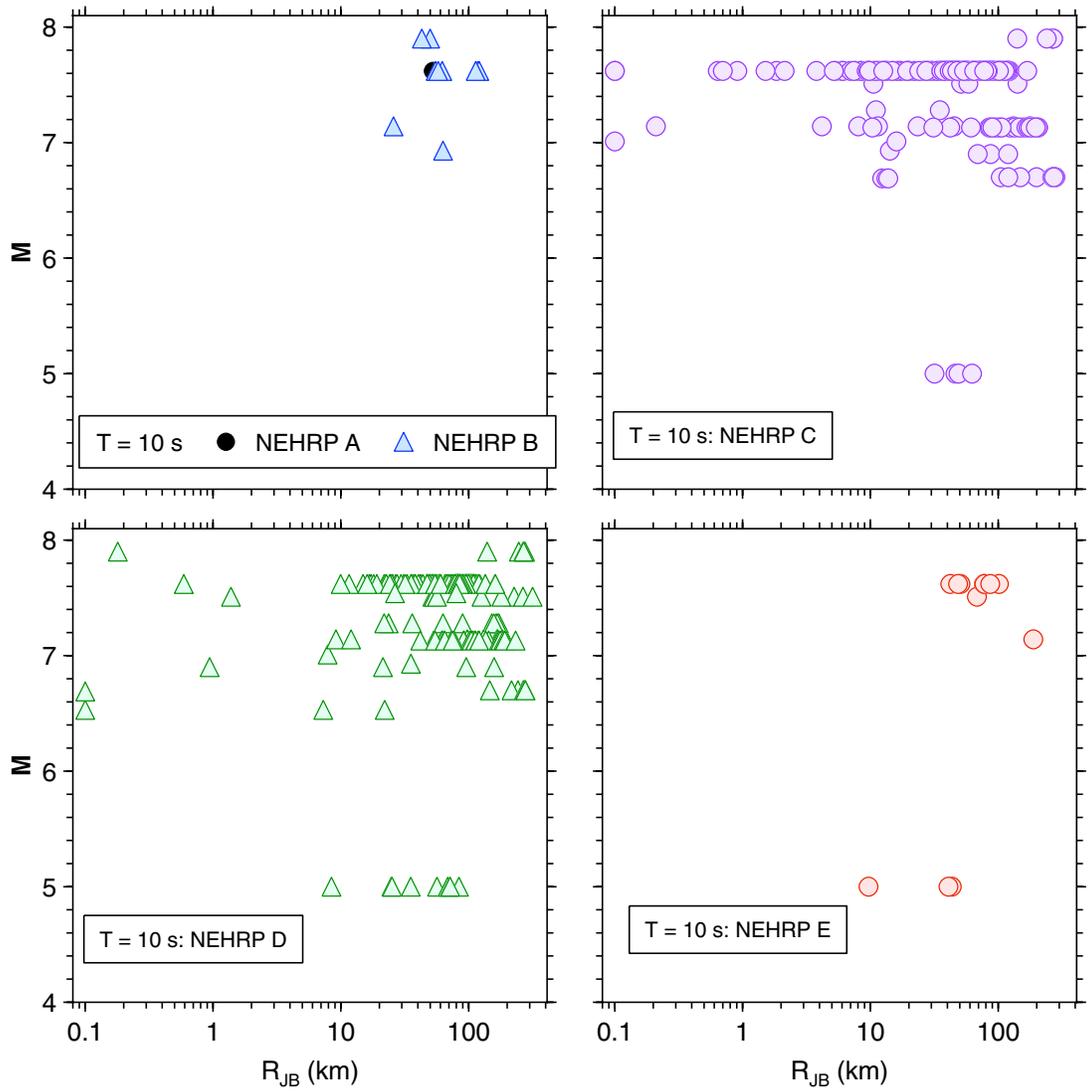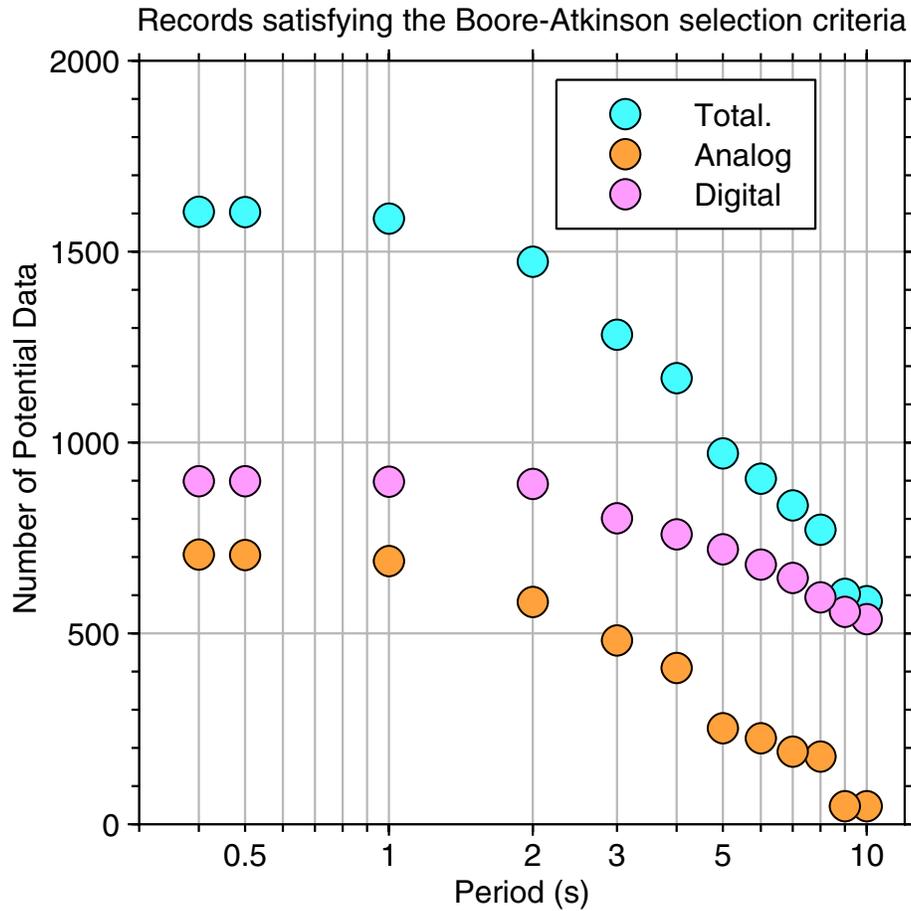
Fig. 2.4 Number of data in NGA flatfile satisfying our selection criteria, including limitation based on highest useable period, as function of oscillator period. Count includes a few recordings from singly recorded earthquakes that did not contribute to our GMPEs.

The distribution of the data by fault type, rake angle, and dip angle is shown in Figure 2.5. This figure also shows that the classification scheme used by BJF97 (shown by horizontal gray lines) produces essentially the distributions of fault type as the method used here, based on the plunge of the *P*- and *T*-axes.
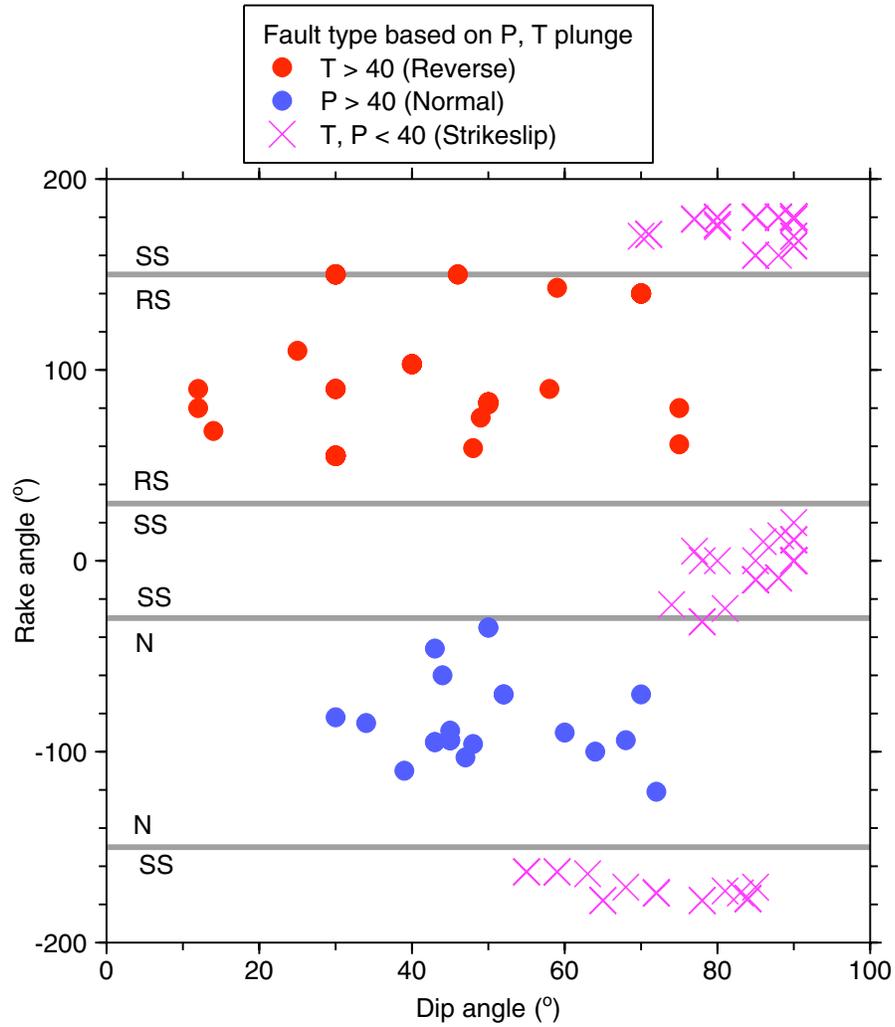
Fig. 2.5 Distribution of data we used in rake-angle and dip-angle space. Horizontal gray lines indicate boundaries between fault types used by BJF97, and symbols and colors indicate our classification based on plunges of P- and T-axes (our classification scheme indicated in legend).

The distributions of the data over the predictor variable space, as shown in Figures 2.1–2.5, necessarily influence the GMPEs. Note in particular the lack of data at close distances for small earthquakes. This means that the near-source ground motions for small events will not be constrained by observations. For long oscillator periods, there are very few data for small earthquakes at any distance (the points in Fig. 2.2 for $T = 10\,\mathrm{s}$ are all from a single event—the 2000 Yountville, California, earthquake), so the magnitude scaling at long periods will be poorly determined for small magnitudes.

The widest range of magnitudes is for strike-slip earthquakes, while the narrowest range is for normal-slip earthquakes. This suggests that the magnitude scaling is better determined for strike-slip than for normal-slip earthquakes—a problem that we circumvented by using a common magnitude scaling for all types of events, as discussed later.

The distribution by site class shows that very few data were from class A sites (hard rock). The bulk of the data are from class C and D sites, which range from soft rock to firm soil. More detail can be found in Appendix E, which includes two possible sets of V_{S30} values to use in evaluating our equations for a particular NEHRP site class.

3   The Equations

Following the philosophy of Boore et al. (1993, 1994, 1997), we seek simple functional forms for our GMPEs, with the minimum required number of predictor variables. We started with the simplest reasonable form for the equations (that used in BJF97), and then added complexity as demanded by comparisons of the predictions of ground motions from the simplest equations with the observed ground motions. The selection of functional form was heavily guided by subjective inspection of nonparametric plots of data; many such plots were produced and studied before commencing the regression analysis. For example, the BJF97 equations modeled the far-source attenuation of amplitudes with distance by a single magnitude-independent effective geometric spreading factor—a straight line amplitude decay of log amplitude versus log distance. This form appeared sufficient for the distance range of <80 km that BJF97 used. The data, however, clearly show that curvature of the line is required to accommodate the effects of anelastic attenuation when modeling data beyond 80 km; furthermore, the data show that the effective geometric spreading factor is dependent on magnitude. To accommodate these trends, we (1) added an "anelastic" coefficient to the form of the equations, in which $\ln Y$ is proportional to R (where Y is the response variable) and (2) introduced a magnitude-dependent "geometrical spreading" term, in which $\ln Y$ is proportional to $\ln R$ and the proportionality factor is a function of **M**. These features allow the equations to predict amplitudes to 400 km; the larger size of the NGA database at greater distances and for larger magnitudes, in comparison to that available to BJF97, enabled robust determination of the additional coefficients. Our functional form does not include such factors as depth-to-top of rupture, hanging wall/footwall terms, or basin depth, because residual analysis does not clearly show that the introduction of such factors would improve their predictive capabilities on average. The equations are data driven and make little use of simulations. They include only those terms that are truly required to adequately fit the observational database, according to our analysis. Our equations may provide a useful alternative

to the more complicated equations provided by other NGA models, as they will be easier to implement in many applications.

Our equation for predicting ground motions is:

$$\ln Y = F_M(\mathbf{M}) + F_D(R_{JB}, \mathbf{M}) + F_S(V_{S30}, R_{JB}, \mathbf{M}) + \varepsilon\sigma_T, \qquad (3.1)$$

In this equation, F_M, F_D, and F_S represent the magnitude scaling, distance function, and site amplification, respectively. $\mathbf{M}$ is moment magnitude, R_{JB} is the Joyner-Boore distance (defined as the closest distance to the surface projection of the fault, which is approximately equal to the epicentral distance for events of $\mathbf{M}$<6), and V_{S30} is the time-averaged shear-wave velocity over the top 30 m of the site. The predictive variables are $\mathbf{M}$, R_{JB}, and V_{S30}; the fault type is an optional predictive variable that enters into the magnitude scaling term as shown in Equation (3.5) below. ε is the fractional number of standard deviations of a single predicted value of $\ln Y$ away from the mean value of $\ln Y$ (e.g., $\varepsilon = -1.5$ would be 1.5 standard deviations smaller than the mean value). All terms, including the coefficient σ_T, are period dependent. σ_T is computed using the equation:

$$\sigma_T = \sqrt{\sigma^2 + \tau^2}, \qquad (3.2)$$

where σ is the intra-event aleatory uncertainty and τ is the inter-event aleatory uncertainty (this uncertainty is slightly different for cases where fault type is specified and where it is not specified; we distinguish these cases by including a subscript on τ).

3.1 DISTANCE AND MAGNITUDE FUNCTIONS

The distance function is given by:

$$F_D(R_{JB}, \mathbf{M}) = [c_1 + c_2(\mathbf{M} - \mathbf{M}_{ref})]\ln(R/R_{ref}) + c_3(R - R_{ref}), \qquad (3.3)$$

where

$$R = \sqrt{R_{JB}^2 + h^2} \qquad (3.4)$$

and c_1, c_2, c_3, $\mathbf{M}_{ref}$, R_{ref}, and h are the coefficients to be determined in the analysis.

The magnitude scaling is given by:

(a) $\mathbf{M} \leq \mathbf{M}_h$

$$F_M(\mathbf{M}) = e_1 U + e_2 SS + e_3 NS + e_4 RS + e_5(\mathbf{M} - \mathbf{M}_h) + e_6(\mathbf{M} - \mathbf{M}_h)^2, \qquad (3.5a)$$

(b) $\mathbf{M} > \mathbf{M}_h$

$$F_M(\mathbf{M}) = e_1 U + e_2 SS + e_3 NS + e_4 RS + e_7 (\mathbf{M} - \mathbf{M}_h),$$ (3.5b)

where *U*, *SS*, *NS*, and *RS* are dummy variables used to specify unspecified, strike-slip, normal-slip, and reverse-slip fault type, respectively, as given by the values in Table 3.1, and $\mathbf{M}_h$, the "hinge magnitude" for the shape of the magnitude scaling, is a coefficient to be set during the analysis.

The determination of the coefficients in the distance and magnitude functions is discussed in the section of the report following the next section on site amplification.

Table 3.1 Values of dummy variables for different fault types.

Fault Type	U	SS	NS	RS
unspecified	1	0	0	0
strike-slip	0	1	0	0
normal	0	0	1	0
thrust/reverse	0	0	0	1

3.2   SITE AMPLIFICATION

We did not solve for the site amplification terms in our analysis, but rather used a slight modification of the site amplification given by Choi and Stewart (2005). The equation and the coefficients of the equation are provided in this section. The site amplification equation is given by:

$$F_S = F_{LIN} + F_{NL},$$ (3.6)

where F_{LIN} and F_{NL} are the linear and nonlinear terms, respectively.

The linear term is given by:

$$F_{LIN} = b_{lin} \ln(V_{S30} / V_{ref}),$$ (3.7)

where b_{lin} is a period-dependent coefficient, and V_{ref} is the specified reference velocity (=760 m/s), corresponding to NEHRP B/C boundary site conditions; these coefficients were prescribed based on the work of Choi and Stewart (2005); they are empirically based, but were not determined by the regression analysis in our study.

The nonlinear term is given by:

(a) $pga4nl \leq a_1$:

$$F_{NL} = b_{nl} \ln(pga\_low / 0.1)$$ (3.8a)

(b) $a_1 < pga4nl \leq a_2$:

$$F_{NL} = b_{nl} \ln(pga\_low / 0.1) + c[\ln(pga4nl / a_1)]^2 + d[\ln(pga4nl / a_1)]^3$$ (3.8b)

(c) $a_2 < pga4nl$:

$$F_{NL} = b_{nl} \ln(pga4nl / 0.1)$$ (3.8c)

where a_1 (=0.03g) and a_2 (=0.09g) are assigned to threshold levels for linear and nonlinear amplification, respectively, pga_low (=0.06 g) is a variable assigned to transition between linear and nonlinear behaviors, and $pga4nl$ is an initial estimate of the predicted PGA in g for $V_{ref} = 760$ m/s, as given by Equation (3.1) with $F_S = 0$ and $\varepsilon = 0$. The period-dependent and V_{S30}-dependent coefficients b_{nl}, c, and d are prescribed based on a slight modification of the empirical analysis results presented by Choi and Stewart (2005), where the modification was designed to smooth the predicted soil amplifications more effectively over amplitude and V_{S30}. As discussed below, the three equations for the nonlinear portion of the soil response (Eq. 3.8) are required for two reasons: (1) to prevent the nonlinear amplification from increasing indefinitely as $pga4nl$ decreases and (2) to smooth the transition from amplification to no amplification.

The nonlinear slope b_{nl} is a function of both period and V_{S30} as given by:

(a) $V_{S30} \leq V_1$:

$$b_{nl} = b_1.$$ (3.9a)

(b) $V_1 < V_{S30} \leq V_2$:

$$b_{nl} = (b_1 - b_2) \ln(V_{S30} / V_2) / \ln(V_1 / V_2) + b_2.$$ (3.9b)

(c) $V_2 < V_{S30} < V_{ref}$:

$$b_{nl} = b_2 \ln(V_{S30} / V_{ref}) / \ln(V_2 / V_{ref}) \, . \tag{3.9c}$$

(d) $\quad V_{ref} \leq V_{S30}$:

$$b_{nl} = 0.0 \, . \tag{3.9d}$$

where $V_1 = 180\,\text{m/s}$, $V_2 = 300\,\text{m/s}$, and b_1 and b_2 are period-dependent coefficients (and consequently, b_{nl} is a function of period as well as V_{S30}).

The coefficients c and d in Equation (3.8b) are given by:

$$c = (3\Delta y - b_{nl}\Delta x) / \Delta x^2 \tag{3.10}$$

and

$$d = -(2\Delta y - b_{nl}\Delta x) / \Delta x^3 \, , \tag{3.11}$$

where

$$\Delta x = \ln(a_2 / a_1) \tag{3.12}$$

and

$$\Delta y = b_{nl} \ln(a_2 / pga\_low) \, . \tag{3.13}$$

The coefficients needed to evaluate the site-response equations are listed in Tables 3.2 and 3.3. Note that for the reference velocity of 760 m/s, $F_{LIN} = F_{NL} = F_S = 0$. Thus the soil amplifications are specified relative to motions that would be recorded on a B/C boundary site condition. It is important to emphasize that the site-response equations were prescribed, based on the work of Choi and Stewart (CS05), rather than determined by our regression. The reason for this is that we were concerned that the NGA database would be insufficient to simultaneously determine all coefficients for the nonlinear soil equations and the magnitude-distance scaling, due to trade-offs that occur between parameters, particularly when soil nonlinearity is introduced. It was therefore deemed preferable to "hard-wire" the soil response based on the best-available empirical analysis in the literature, and allow the regression to determine the remaining magnitude and distance scaling factors. It is recognized that there are implicit trade-offs involved, and that a change in the prescribed soil response equations would lead to a change in the derived magnitude and distance scaling. However, note that our prescribed soil response terms are similar to those adopted by other NGA developers who used different approaches; thus there appears to be consensus as to the appropriate level for the soil response factors.

Table 3.2 Period-dependent site-amplification coefficients.

period	b_{lin}	b_1	b_2
PGV	-0.600	-0.500	-0.06
PGA	-0.360	-0.640	-0.14
0.010	-0.360	-0.640	-0.14
0.020	-0.340	-0.630	-0.12
0.030	-0.330	-0.620	-0.11
0.050	-0.290	-0.640	-0.11
0.075	-0.230	-0.640	-0.11
0.100	-0.250	-0.600	-0.13
0.150	-0.280	-0.530	-0.18
0.200	-0.310	-0.520	-0.19
0.250	-0.390	-0.520	-0.16
0.300	-0.440	-0.520	-0.14
0.400	-0.500	-0.510	-0.10
0.500	-0.600	-0.500	-0.06
0.750	-0.690	-0.470	0.00
1.000	-0.700	-0.440	0.00
1.500	-0.720	-0.400	0.00
2.000	-0.730	-0.380	0.00
3.000	-0.740	-0.340	0.00
4.000	-0.750	-0.310	0.00
5.000	-0.750	-0.291	0.00
7.500	-0.692	-0.247	0.00
10.000	-0.650	-0.215	0.00

Table 3.3 Period-independent site-amplification coefficients.

Coefficient	Value
a_1	0.03 g
pga_low	0.06 g
a_2	0.09 g
V_1	180 m/s
V_2	300 m/s
V_{ref}	760 m/s

The details of setting the coefficients for the soil response equations are as follows. The linear amplification coefficients b_{lin} were adopted from CS05. As shown in Figure 3.1, they are similar to the linear soil coefficients derived by BJF97. For periods not provided by CS05, we

20

interpolated the b_{lin} values as shown in Figure 3.1. As periods get very large (>5 s), we would expect the relative linear site amplification to decrease (and a trend in this direction has been found by some of the other NGA developers). For this reason, we subjectively decided on the linear trend in terms of the log period shown in Figure 3.1 as the basis for choosing the values for the longer periods.
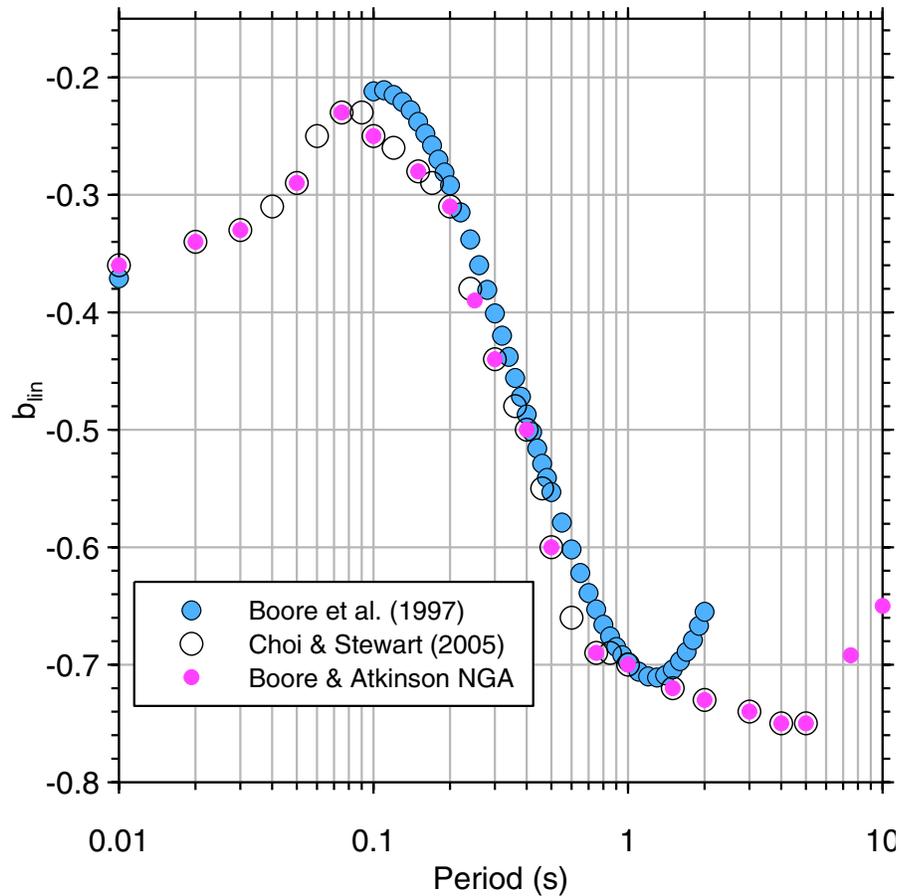
Fig. 3.1 Coefficient controlling linear amplification, as function of period. Values used in equations in this report indicated by magenta circles.
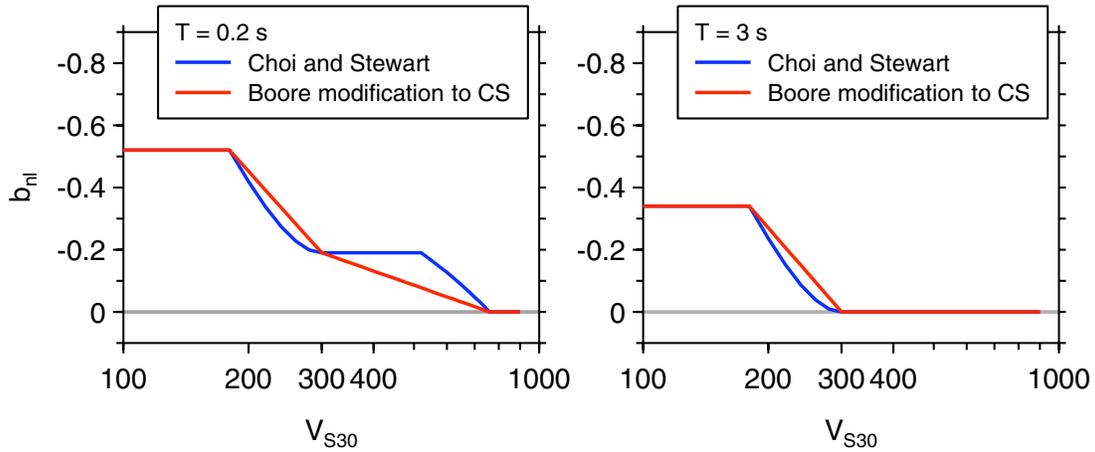
Fig. 3.2 Comparison of slope that controls nonlinear amplification function.

The nonlinear slope factor b_{nl} depends on V_{S30} through the equations given above. Our equations define a somewhat simpler relation than that used by CS05. We compare the two definitions of the coefficient b_{nl} for periods of 0.2 and 3.0 s in Figure 3.2. The values of b_{nl} at the hinge points $V_{S30} = V_1$ and $V_{S30} = V_2$ are given by the coefficients b_1 and b_2, respectively, and these are functions of period. We use CS05's values for most periods, as shown in Figures 3.3 and 3.4. To extend the value of b_1 to periods longer than 5 s, we fit two quadratic curves to their values: one for all of the values and another for values corresponding to periods greater than 0.2 s. As shown in Figure 3.3, the results were similar. We based our value of b_1 at periods of 7.5 s and 10 s on the quadratic fit to all of the CS05 values. This curve was also used for the value at 5 s, but the results of using the CS05 value at 5 s versus our value makes almost no difference in the predicted ground motions for 5 s periods.
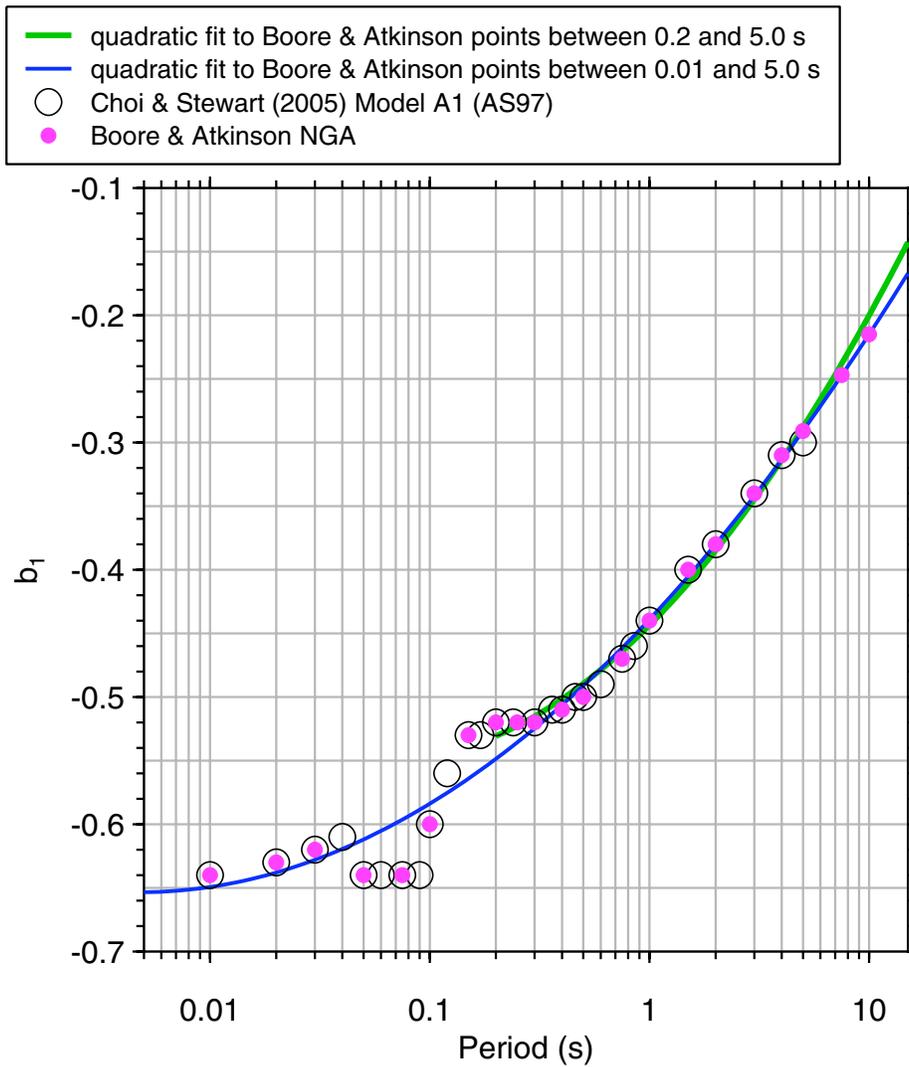
Fig. 3.3 Basis for choice of nonlinear amplification coefficient b_1. We used Choi and Stewart (2005) (CS05) when available, except for periods of 5, 7.5, and 10 s, for which we used values from quadratic fit to all of CS05's values.
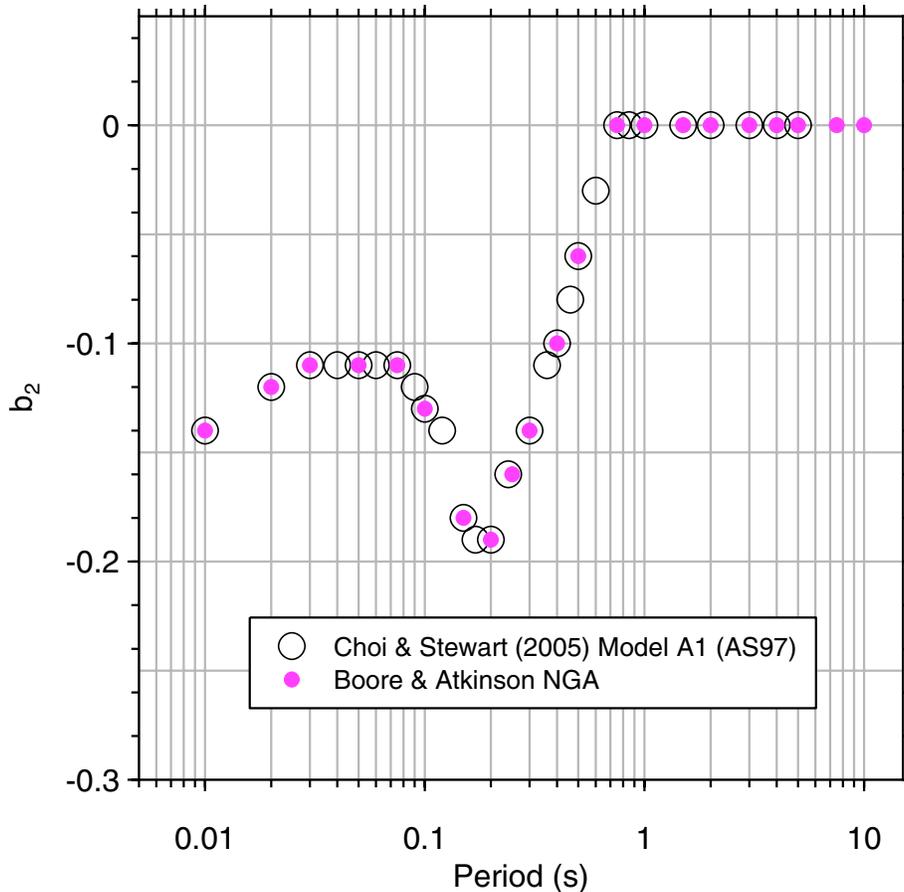
Fig. 3.4 Basis for choice of nonlinear amplification coefficient b_2. We used Choi and Stewart (2005) (CS05) when available, except for periods of 7.5 and 10 s, for which we used CS05's value for period of 5 s.

We point out a potential confusion in terminology: according to Equation (3.8c), $F_{NL} = 0.0$ when $pga4nl = 0.1\,\mathrm{g}$. Does this mean that there is no nonlinear amplification for this level of rock motion? No. The amplification for this value of *pga4nl* is given entirely by the F_{LIN} term because CS05 derived the "linear" amplifications (F_{LIN}) for motions with a mean PGA on rock close to 0.1 g. F_{NL} is not necessarily zero, however, for values of *pga4nl* less than and greater than 0.1 g. So although the amplification at $pga4nl = 0.1\,\mathrm{g}$ is completely determined by F_{LIN}, the amplification can be nonlinear for values of *pga4nl near* 0.1 g.

CS05 use only Equation (3.8c) to describe the nonlinear amplification, and they do not limit the nonlinear response to $pga4nl > 0.1\,\mathrm{g}$. It is clear from Figure 3 of CS05 and their comment (Choi and Stewart 2005, p. 24) that they consider Equation (3.8c) to be valid for

24

pga4nl from 0.02 to 0.8 g. This means that the total amplification (F_S) can be greater than the "linear" amplification (F_{LIN}) for small values of *pga4nl*; their nonlinear amplification continues to increase without bound as *pga4nl* decreases. We made an important modification to the CS05 procedure to prevent nonlinear amplification from extending to small values of *pga4nl*, by capping the amplifications at a low value of *pga4nl*. Simply terminating the nonlinear amplification at *pga*4*nl* = *pga_low* results in kinks in plots of ground motion vs. distance. For that reason we included a transition curve, as given in Equation (3.8b). A plot of the nonlinear amplification that shows the effect of this transition region is given in Figure 3.5, where the "smoothed" curve represents our formulation through Equations (3.8a, b, c).
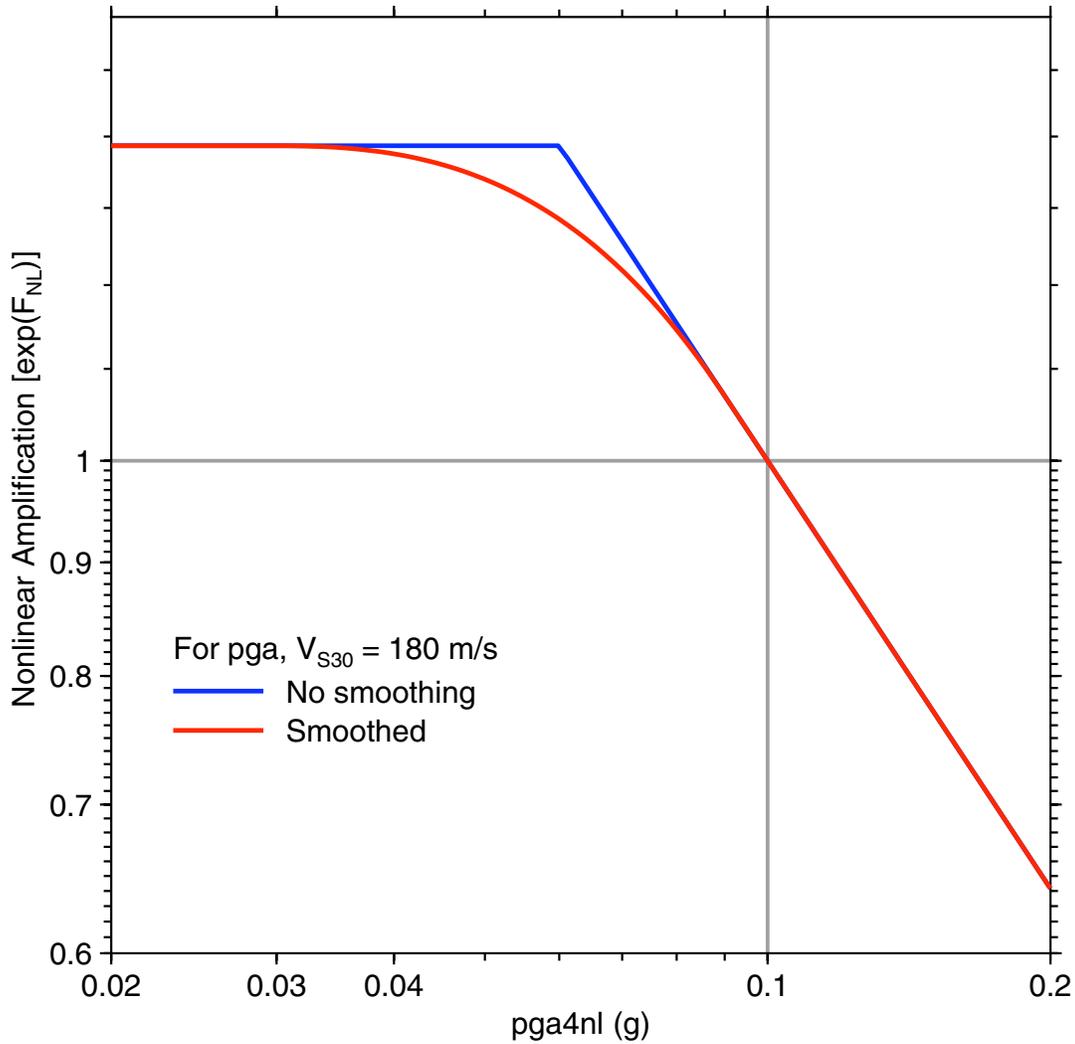
Fig. 3.5 Nonlinear contribution to site amplification showing how cubic polynomial gives smoothed version of amplification. Amplification is for $V_{S30} = 180$ m/s.

The total amplification for a short (0.2 s) and a long (3.0 s) period oscillator is shown in Figure 3.6 as a function of *pga4nl* for a range of V_{S30}. At short periods the nonlinear term can result in a significant reduction of motions on sites underlain by relatively low velocities. At long periods soil nonlinearity can still affect ground motions, but the large "linear" amplification is not outweighed by the nonlinear effect for large values of *pga4nl*. For periods longer than 0.75 s (see Table 3.2) there is no nonlinear contribution to the amplification for $V_{S30} > 300$ m/s.
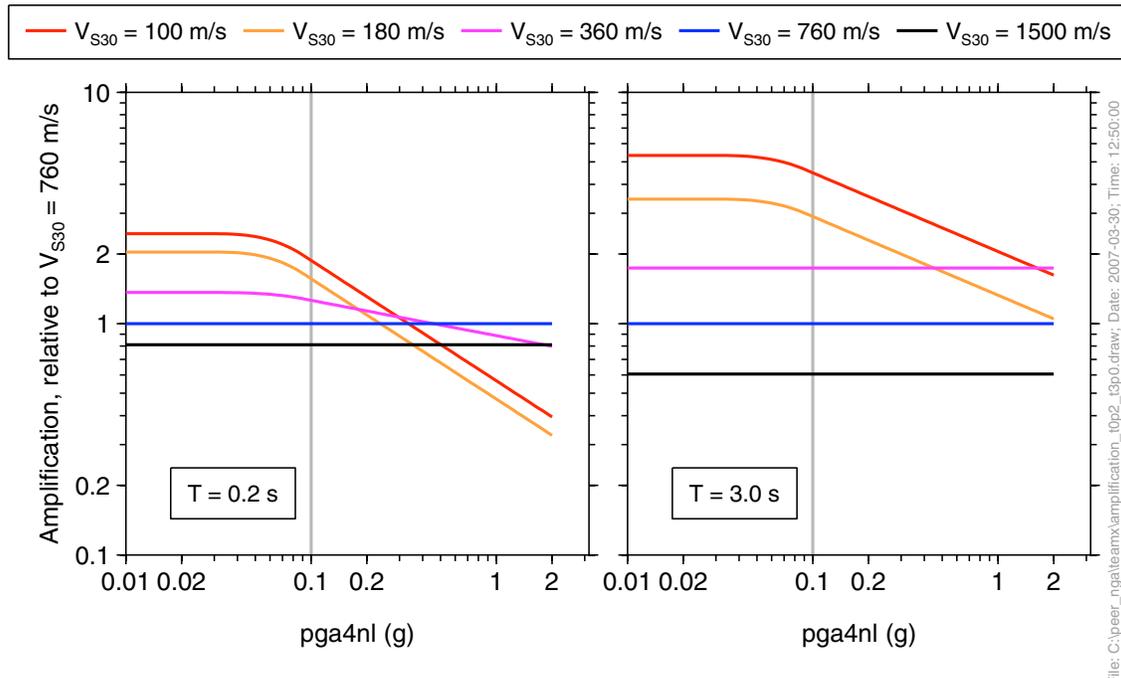
Fig. 3.6 Combined amplification for $T = 0.2s$ and $T = 3.0s$ as function of *pga4nl*, for suite of V_{S30}. Note at short periods (left graph), purely linear amplification does not occur on soft soils until $pga4nl < 0.03$ g.

It should be noted that the empirical studies on which the soil amplification functions were based contained very few data for hard sites, with $V_{S30} > 1000$ m/s. The amplification functions are probably reasonable for values of V_{S30} up to about 1300 m/s, but should not be applied for very hard rock sites ($V_{S30} \geq 1500$ m/s).

4 Determination of Coefficients

4.1 METHODOLOGY

The selected response variables in the NGA database were regressed to Equation (3.1) to determine F_D and F_M, after first correcting all observations to the reference velocity of 760 m/s, using Equations (3.6)–(3.13). This allows us to perform the regression analyses for the case where $F_S = 0$. The analyses were performed using the two-stage regression discussed by Joyner and Boore (1993, 1994); the first stage determines the distance dependence (as well as event terms used in the second stage and the inter-event aleatory variability, σ), and the second stage determines the magnitude dependence (and the intra-event variability, τ). All regressions were done period by period; there was no smoothing of the coefficients that were determined by the regression analyses (although some of the constrained coefficients were smoothed).

4.1.1 Stage 1: Distance Dependence

The distance dependence is determined in the first stage regression, where the dependent response variable is PGA, PGV, or PSA at a selected period, in each case corrected to the reference velocity of 760 m/s by subtracting F_S as defined in Equations (3.6)–(3.13) from $\ln Y_{observed}$. The corrected response variables for our selected subset of the NGA dataset (using the exclusion criteria of Table 2.1, with distances out to 400 km) are regressed against distance using Equation (4.1), which is the same as Equation (3.2) but with dummy variables ($c_0(event)$) added to represent the event term for each earthquake (the event term is thus the average motion of the observations for each earthquake corrected to $R = R_{ref}$).

$$F_D(R_{JB}, \mathbf{M}) = c_0(event) + [c_1 + c_2(\mathbf{M} - \mathbf{M}_{ref})]\ln(R/R_{ref}) + c_3(R - R_{ref}) \qquad (4.1)$$

In this equation, "$c_0(event)$" is shorthand for the sum:

$$(c_0)_1 \delta_1 + (c_0)_2 \delta_2 + \cdots + (c_0)_{NE} \delta_{NE}, \qquad\qquad (4.2)$$

where $(c_0)_j$ is the event term for event j, δ_j equals 1 for event j and zero otherwise, and NE is the number of earthquakes.

There are several significant issues in performing this regression. One is that regional differences in attenuation are known to exist (e.g., Boore 1989; Benz et al. 1997), even within relatively small regions such as California (e.g., Bakun and Joyner 1984, Boatwright et al. 2003; Hutton and Boore 1987; Mori and Helmberger, 1996). We ignore this potential pitfall and assume that the distance part of the GMPEs apply for crustal earthquakes in all active tectonic regimes represented by the NGA database. This is a reasonable initial approach, as the significance of regional effects can be tested later by examining residual trends (model errors) for subsets of data organized by region. The second difficulty is more problematic: the data in the NGA flatfile become increasingly sparse for distances beyond about 80–100 km, especially for moderate events. This makes it difficult, if not impossible, to obtain a robust simultaneous determination of c_1 and c_3 (slope and curvature). To overcome this database limitation, we have used additional ground motion data from California that are not in the NGA flatfile to first define the "anelastic" term, c_3, as a function of period. We then used these fixed values of c_3 in the regression of the NGA dataset in order to determine the remaining coefficients.

Determination of c3 (anelastic term): The data used to determine c_3 include the data compiled in the NGA database for three small California events, plus many more data for these same events recorded by accelerometers at "broadband" stations in California; these additional data, compiled by J. Boatwright and L. Seekins, were not available from the traditional strong-motion data agencies used in compiling the NGA flatfile . We also used response variables computed from 74 two-component recordings of the 2004 Parkfield mainshock (**M** 6.0) in the determination of c_3; these data were recorded after the compilation of the NGA database had concluded. The numbers of stations providing data for our analysis and the corresponding numbers of stations in the NGA flatfile are given in Table 4.1 (see also Appendices M and N).

Table 4.1   Comparisons of numbers of stations in NGA flatfile and in extended dataset used to determine anelastic coefficient.

Earthquake	# of Stations in NGA	# of Stations used by BA
2001 Anza (**M** 4.92)	73	197
2002 Yorba Linda (**M** 4.27)	12	207
2003 Big Bear City (**M** 4.92)	37	262
2004 Parkfield (**M** 6.0)	0	74

For the additional data for the three small California earthquakes, we used site classes assigned by Boatwright and Seekins to correct the response spectra to $V_{S30} = 760$ m/s . For the Parkfield recordings we did not correct to a common value of V_{S30}, as we had no site class information. For all of the data from the four events, we used spectra from the two horizontal components as if they were separate recordings (we did not combine the horizontal components). We did the regressions on this data subset with c_1 fixed at -0.5, -0.8, and -1.0. We set c_2 to zero and solved for c_3 and h. In other words, we are fixing a single straight-line slope (c_1) and then determining the curvature, c_3, required to match the more rapid decay of the data at greater distances (c_3 must be less than 0) and the near-source effective depth coefficient, h, required to match the less rapid increase of the data as distance decreases at close distances. An event term that gives the relative amplitude level, (c_0), is also determined for each of the four earthquakes (these are the coefficients of the dummy variables for each event). Figure 4.1 compares the regression fits to the observations, where the observations have been normalized to a common amplitude level by subtracting the event terms (c_0). We also found the best values of c_3 and h to fit the distance functions determined in southern California by Raoof et al. (1999). The equivalent values from the Raoof et al. (1999) analysis were similar to those from our analysis of the four-event California subset described above. We chose the c_3 values determined for the case $c_1 = -0.8$ as the fixed c_3 values to apply in the regression of the NGA dataset because $c_1 = -0.8$ is a typical value determined in empirical regressions for the effective geometric slope parameter at intermediate periods (BJF97; this study). To assign values of c_3 for all periods for which the NGA equations were to be determined, we fit a quadratic to the c_3 values from the analysis of our four-event data subset. This is shown in Figure 4.2. We did not allow the value of c_3 at short

29

periods to be less than that for PGA, thus placing an upper limit on $|c_3|$ at $|c_3| = 0.01151$. Similarly, we fixed the values for long periods to be that determined for $T = 3\,\text{s}$, thus placing a lower limit on $|c_3|$ of $|c_3| = 0.00191$ (we did not think it physically plausible for the anelastic attenuation to increase with period at T>5 s).
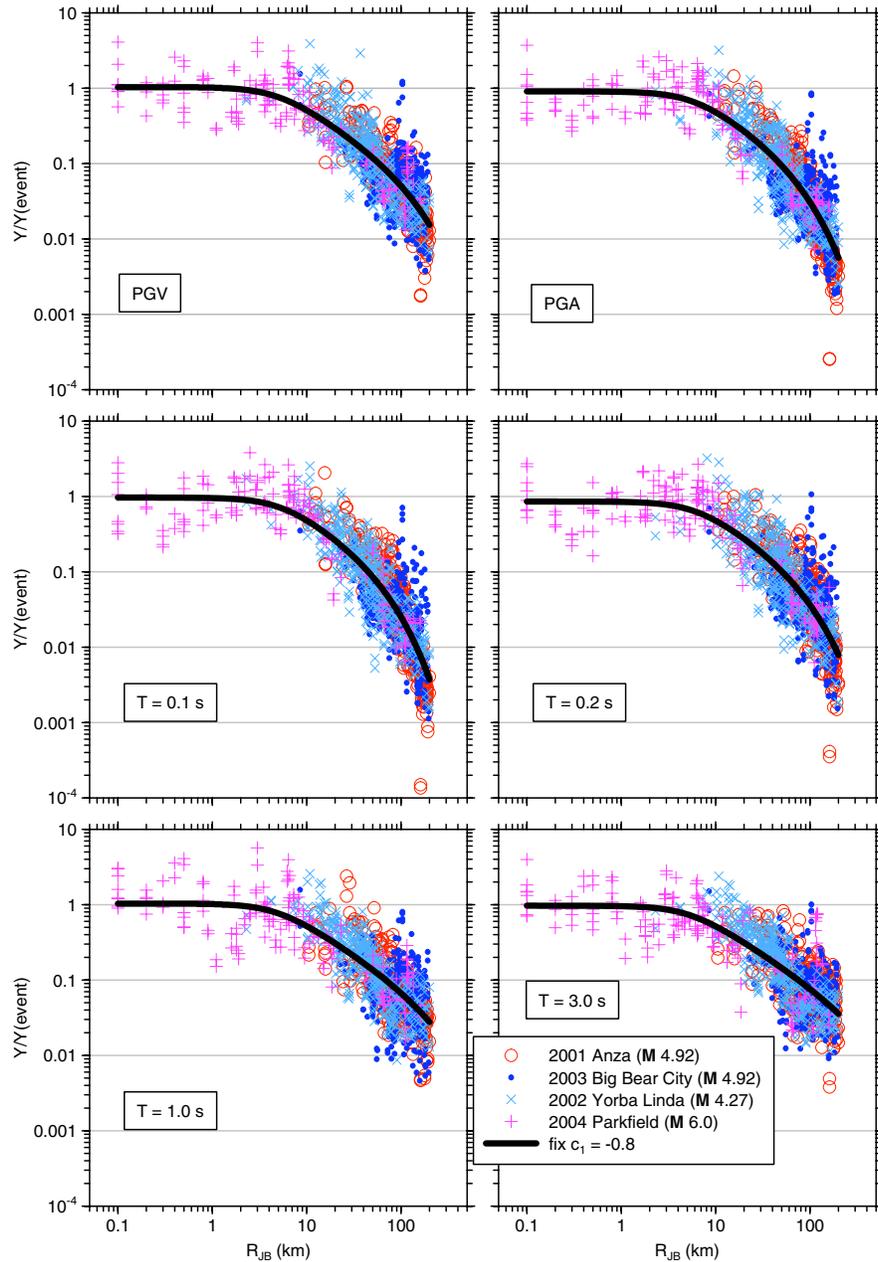
Fig. 4.1 Normalized ground motions for four events, using extended dataset (more data than in NGA flatfile). Black curve is regression fit obtained with constraints $c_1 = -0.8$ and $c_2 = 0.0$.
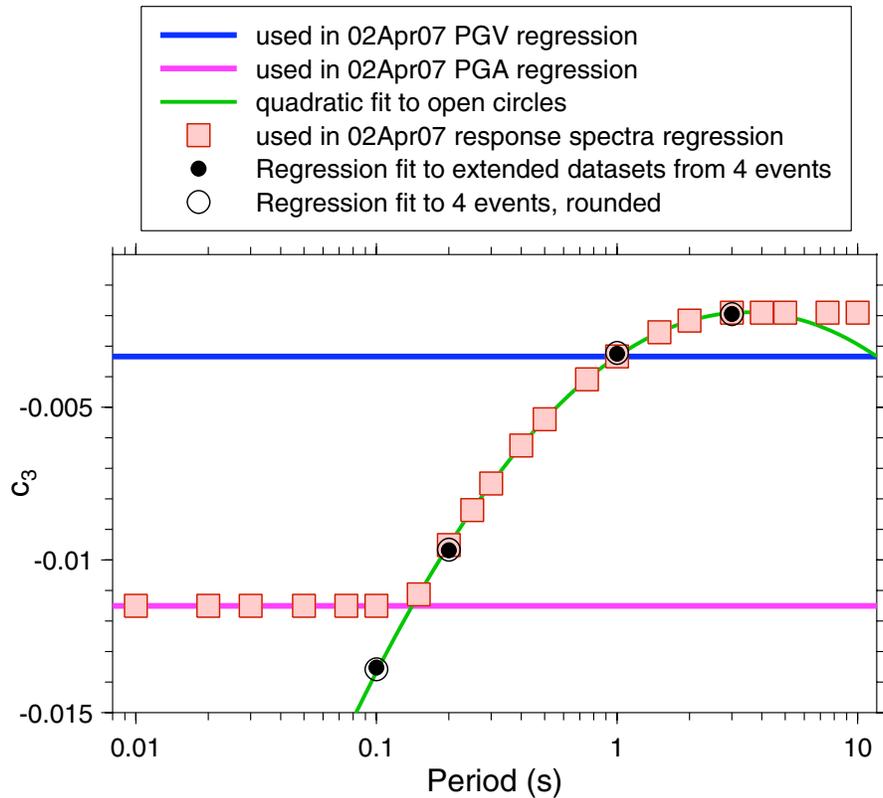
Fig. 4.2 **Basis for choice of** c_3 **at periods other than analyzed in regression in extended dataset from four earthquakes (see text).**

We also constrained the c_3 values for the PGV regressions to be that for the $T = 1.0$ s regression. This choice is a compromise between the similarity in magnitude scaling that we observed between PGV and PSA at 3 s and the recommendation of Bommer and Alarcón (2006) that PGV is related to PSA at 0.5 s.

Determination of h: It is desirable to constrain the pseudo-depth h in the regression in order to avoid overlap in the curves for large earthquakes at very close distances. We did this by performing initial regressions with h as a free parameter, then modifying the obtained values of h as required to avoid overlap in the spectra at close distances (for the reference site condition of 760 m/s). In this regression, c_1 was a free variable and c_3 was constrained to the values in use at the time. Our procedure is shown in Figure 4.3, along with the final values of h (squares). The black dots were determined when h was a free parameter. We fit the values with a quadratic (dashed green line), but observed that the h value at 0.05 s was very small, much below that determined for PGA. We increased the h value at 0.05 s to match the value for a regression of

31

PGA with h unconstrained, and refit the quadratic (solid green line) with this change in the data points. We used the modified quadratic as the basis for assigning h for all periods. The value of h at short periods was guided by the unequivocal statement that PSA is equal to PGA at periods much less than 0.1 s. For PGA, we adopted the value implied by the modified quadratic for the $T = 0.05$ s oscillator. We then assigned values of h for periods between 0.01 s and 0.05 s to be the same as that for 0.05 s. Consistent with the convention adopted for the c_3 coefficient, we used the value of h at 1 s for PGV.
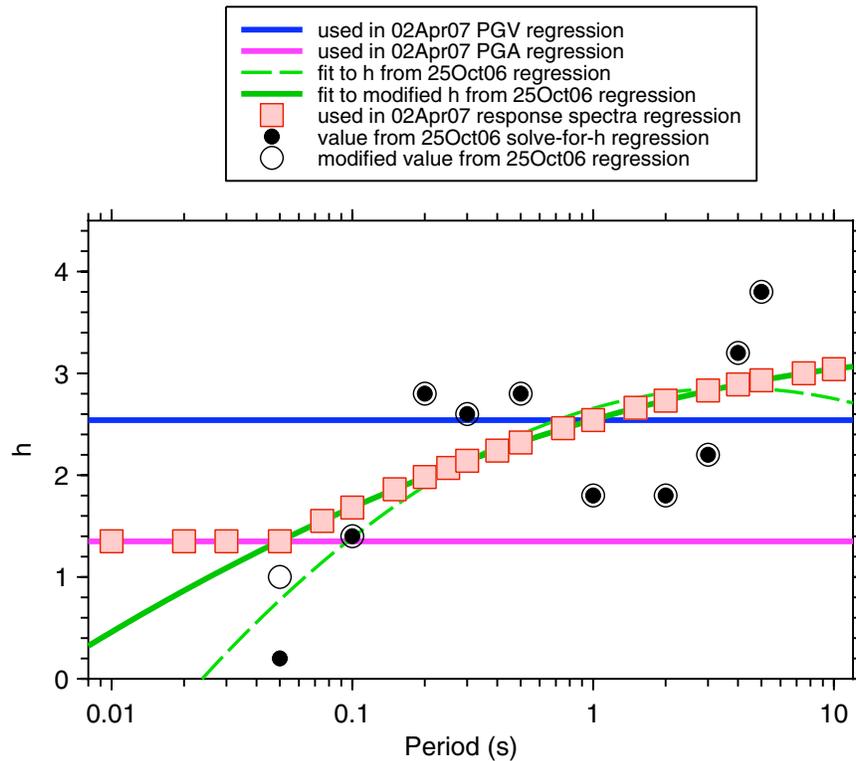
Fig. 4.3 Basis for choice of h at all periods (see text).

These pre-analyses establish smooth, constrained values for c_3 and h that facilitated robust and well-behaved determinations of the remaining parameters by regression of the NGA database.

Determination of c1, c2, and σ: With h and c_3 constrained, we regressed the response variables of the NGA database to solve for c_1 and c_2 (Eq. 3.3), along with the event terms (c_0) for each earthquake, using all data (subject to the exclusions of Table 2.1) for distances less than 400 km (we originally included a magnitude dependence to the anelastic term but found that the

resulting ground motion predictions tended to increase with increasing distance). The c_1 coefficient is the effective geometric spreading rate (slope) for an event of $\mathbf{M} = \mathbf{M}_{ref}$, while the c_2 coefficient provides a means to describe magnitude-dependent distance decay (it changes the slope for events that are greater or smaller than $\mathbf{M}_{ref}$). The intra-event aleatory uncertainty σ is given by the standard deviation of the residuals from the Stage 1 regression.

The regression used assigned values for the reference distance, R_{ref}, at which near-source predictions are pegged, and for the reference magnitude, $\mathbf{M}_{ref}$, to which the magnitude dependence of the geometric spreading is referenced. The assigned values for these reference values are arbitrary, and are largely a matter of convenience. For $\mathbf{M}_{ref}$, we chose a value of 4.5, since this is the approximate magnitude of much of the data used to determine the fixed c_3 coefficients; this choice means that the magnitude dependence of the slope will be referenced to that observed for small events. For R_{ref}, we use the value of 1 km. This is convenient because the curves describing the distance dependence pivot around $R = R_{ref}$. The curves for larger magnitudes are flatter than for smaller magnitudes, which can lead to overlap of curves at distances less than the pivot distance. This was avoided this by choosing $R_{ref} = 1\,\text{km}$, although any value such that $R_{ref} < \min(h)$, where the minimum is taken over all periods, would prevent undesirable overlapping of prediction curves near the source (i.e., we want to ensure that R will always be greater than the pivot distance of R_{ref}, even when $R_{JB} = 0$ km).

4.1.2 Stage 2: Magnitude Dependence

The event terms (coefficients $(c_0)_j$ in Eq. (4.1)) from the Stage 1 regression were used in a weighted Stage 2 regression to determine the magnitude scaling of the response variables. As discussed in Joyner and Boore (1993), the Stage 2 weighted regression was iterative in order to solve for the inter-event variability τ. Only events with more than one observation were used in the regression. The basic form we selected for the magnitude scaling is a quadratic, similar to the form used by BJF93. However, we imposed a constraint that the quadratic not reach its maximum at $\mathbf{M} < 8.5$, in order to prevent "oversaturation" (the prediction of decreasing amplitudes with increasing magnitude). The following algorithm was used to implement the constrained quadratic magnitude dependence:

1. Fit the event terms $(c_0)_j$ for a given period to a second-order polynomial. If the **M** for which the quadratic starts to decrease ($\mathbf{M}_{max}$) is greater than 8.5, we adopt this regression for the magnitude dependence for this period.

2. If $\mathbf{M}_{max}$ for a given period is less than 8.5, we perform a two-segment regression, hinged at $\mathbf{M}_h$ (described below), with a quadratic for $\mathbf{M} \leq \mathbf{M}_h$ and a linear function for $\mathbf{M}_h < \mathbf{M}$. If the slope of the linear function is positive, we adopt this two-segment regression for the magnitude dependence for this period.

3. If the slope of the linear segment is negative, we redo the two-segment regression for that period, constraining the slope of the line above $\mathbf{M}_h$ to be 0.0. Note that the equations for almost all periods of less than or equal to 1.0 s required the constraint of zero slope; this is saying that for short periods the data actually indicated oversaturation. We felt that because of limited data and knowledge, oversaturation was too extreme at this stage of equation development, and we chose to impose saturation rather than allow the data to dictate an oversaturated form. More observations from ground motions near large earthquakes, as well as theoretical simulations using dynamic rupture models (e.g., Schmedes and Archuleta 2007) may give us confidence in allowing oversaturation in future versions of GMPEs.

Choice of M_h: The parameter $\mathbf{M}_h$ is the hinge magnitude at which the constrained magnitude scaling in the two-segment regression changes from the quadratic form to the linear form. Subjective inspection of nonparametric plots of data clearly indicated that near-source ground motions at short periods do not get significantly larger with increasing magnitude, beyond a magnitude in the range of 6.5 to 7. On this basis, we initially set $\mathbf{M}_h = 7.0$, but there are a few periods for which $\mathbf{M}_{max}$ was less than 7.0. Consequently the use of $\mathbf{M}_{max} = 7$ would lead to a slight decrease of magnitude scaling between $\mathbf{M}_{max}$ and $\mathbf{M}_h$, which is contrary to our requirement that our equations give no oversaturation of ground motion for sites with purely linear amplification. The adoption of $\mathbf{M}_h$ slightly lower than the minimum value of $\mathbf{M}_{max}$ over all periods prevented this problem.

Fault-Type Dependence: Plots of event terms against magnitude (presented later) showed that normal-fault earthquakes have amplitudes that are consistently below those for

strike-slip and reverse earthquakes for most periods. We used this observation to guide our determination of the dependence on fault type. We first grouped the data from all fault types together and solved for the coefficients e_1, e_5, e_6, e_7, and e_8 in Equation (3.5), setting e_2, e_3, and e_4 to 0.0. The regression was then repeated, fixing the coefficients e_5, e_6, e_7, and e_8 to the values obtained when lumping all fault types together, and solving for the coefficients e_2, e_3, and e_4 of the fault type dummy variables SS, NS, and RS. Thus we have constrained the relative scaling of amplitudes with magnitude to be the same for all event types, but we allow an offset in the average predicted amplitude level according to the fault mechanism. The inter-event aleatory uncertainty (τ) was slightly different for these two cases, so subscript "U" and "M" distinguish between unspecified and specified fault type, respectively, in the table of aleatory uncertainties.

All analyses were done using Fortran programs developed by the first author, in some cases incorporating legacy code from programs and subroutines written by W. B. Joyner.

4.2   RESULTS

4.2.1   Coefficients of Equations

The coefficients for the GMPEs are given in Tables 3.2–3.3 and 4.2–4.5. The coefficients are for $\ln Y$, where Y has units of g for PSA and PGA, and cm/s for PGV. The units of distance and velocity are km and m/s, respectively. The coefficients of the equation for $pga4nl$ are given in the first row in Tables 4.2 and 4.4 (with $\mathbf{M}_{ref}$ and R_{ref} as given in Table 4.3); there is no site amplification for $pga4nl$ (it applies to sites with the reference velocity of 760 m/s). The coefficients for $pga4nl$ were developed as an initial estimate early in the project, using only data for which $R_{JB} \leq 80$ km and $V_{S30} > 360$ m/s , and therefore the predictions of PGA from this equation will differ somewhat from the predictions of PGA for $V_{S30} = 760$ m/s using the coefficients in the third row of the tables. The equation for $pga4nl$ need only give approximately-correct values for the peak acceleration on rock-like sites. The equation provided for $pga4nl$ maintains internal consistency; the site amplifications were used to reduce the observations to a reference velocity before doing the regressions, and thus the same site amplifications should be used when predicting ground motions using the results of the regressions.

Table 4.2 Period-dependent distance-scaling coefficients.

period	c_1	c_2	c_3	h
pga4nl	-0.55000	0.00000	-0.01151	3.00
PGV	-0.87370	0.10060	-0.00334	2.54
PGA	-0.66050	0.11970	-0.01151	1.35
0.010	-0.66220	0.12000	-0.01151	1.35
0.020	-0.66600	0.12280	-0.01151	1.35
0.030	-0.69010	0.12830	-0.01151	1.35
0.050	-0.71700	0.13170	-0.01151	1.35
0.075	-0.72050	0.12370	-0.01151	1.55
0.100	-0.70810	0.11170	-0.01151	1.68
0.150	-0.69610	0.09884	-0.01113	1.86
0.200	-0.58300	0.04273	-0.00952	1.98
0.250	-0.57260	0.02977	-0.00837	2.07
0.300	-0.55430	0.01955	-0.00750	2.14
0.400	-0.64430	0.04394	-0.00626	2.24
0.500	-0.69140	0.06080	-0.00540	2.32
0.750	-0.74080	0.07518	-0.00409	2.46
1.000	-0.81830	0.10270	-0.00334	2.54
1.500	-0.83030	0.09793	-0.00255	2.66
2.000	-0.82850	0.09432	-0.00217	2.73
3.000	-0.78440	0.07282	-0.00191	2.83
4.000	-0.68540	0.03758	-0.00191	2.89
5.000	-0.50960	-0.02391	-0.00191	2.93
7.500	-0.37240	-0.06568	-0.00191	3.00
10.000	-0.09824	-0.13800	-0.00191	3.04

Table 4.3 Period-independent distance scaling coefficients.

Coefficient	Value
$\mathbf{M}_{ref}$	4.5
R_{ref}	1.0

Table 4.4 Magnitude-scaling coefficients.

Period	e_1	e_2	e_3	e_4	e_5	e_6	e_7	$\mathbf{M}_h$
pga4nl	-0.03279	-0.03279	-0.03279	-0.03279	0.29795	-0.20341	0.00000	7.00
PGV	5.00121	5.04727	4.63188	5.08210	0.18322	-0.12736	0.00000	8.50
PGA	-0.53804	-0.50350	-0.75472	-0.50970	0.28805	-0.10164	0.00000	6.75
0.010	-0.52883	-0.49429	-0.74551	-0.49966	0.28897	-0.10019	0.00000	6.75
0.020	-0.52192	-0.48508	-0.73906	-0.48895	0.25144	-0.11006	0.00000	6.75
0.030	-0.45285	-0.41831	-0.66722	-0.42229	0.17976	-0.12858	0.00000	6.75
0.050	-0.28476	-0.25022	-0.48462	-0.26092	0.06369	-0.15752	0.00000	6.75
0.075	0.00767	0.04912	-0.20578	0.02706	0.01170	-0.17051	0.00000	6.75
0.100	0.20109	0.23102	0.03058	0.22193	0.04697	-0.15948	0.00000	6.75
0.150	0.46128	0.48661	0.30185	0.49328	0.17990	-0.14539	0.00000	6.75
0.200	0.57180	0.59253	0.40860	0.61472	0.52729	-0.12964	0.00102	6.75
0.250	0.51884	0.53496	0.33880	0.57747	0.60880	-0.13843	0.08607	6.75
0.300	0.43825	0.44516	0.25356	0.51990	0.64472	-0.15694	0.10601	6.75
0.400	0.39220	0.40602	0.21398	0.46080	0.78610	-0.07843	0.02262	6.75
0.500	0.18957	0.19878	0.00967	0.26337	0.76837	-0.09054	0.00000	6.75
0.750	-0.21338	-0.19496	-0.49176	-0.10813	0.75179	-0.14053	0.10302	6.75
1.000	-0.46896	-0.43443	-0.78465	-0.39330	0.67880	-0.18257	0.05393	6.75
1.500	-0.86271	-0.79593	-1.20902	-0.88085	0.70689	-0.25950	0.19082	6.75
2.000	-1.22652	-1.15514	-1.57697	-1.27669	0.77989	-0.29657	0.29888	6.75
3.000	-1.82979	-1.74690	-2.22584	-1.91814	0.77966	-0.45384	0.67466	6.75
4.000	-2.24656	-2.15906	-2.58228	-2.38168	1.24961	-0.35874	0.79508	6.75
5.000	-1.28408	-1.21270	-1.50904	-1.41093	0.14271	-0.39006	0.00000	8.50
7.500	-1.43145	-1.31632	-1.81022	-1.59217	0.52407	-0.37578	0.00000	8.50
10.000	-2.15446	-2.16137	0.00000	-2.14635	0.40387	-0.48492	0.00000	8.50

Table 4.5 Aleatory uncertainties.

Period	σ	τ_U	σ_{TU}	τ_M	σ_{TM}
PGV	0.500	0.286	0.576	0.256	0.560
PGA	0.502	0.265	0.566	0.260	0.564
0.010	0.502	0.267	0.569	0.262	0.566
0.020	0.502	0.267	0.569	0.262	0.566
0.030	0.507	0.276	0.578	0.274	0.576
0.050	0.516	0.286	0.589	0.286	0.589
0.075	0.513	0.322	0.606	0.320	0.606
0.100	0.520	0.313	0.608	0.318	0.608
0.150	0.518	0.288	0.592	0.290	0.594
0.200	0.523	0.283	0.596	0.288	0.596
0.250	0.527	0.267	0.592	0.267	0.592
0.300	0.546	0.272	0.608	0.269	0.608
0.400	0.541	0.267	0.603	0.267	0.603
0.500	0.555	0.265	0.615	0.265	0.615
0.750	0.571	0.311	0.649	0.299	0.645
1.000	0.573	0.318	0.654	0.302	0.647
1.500	0.566	0.382	0.684	0.373	0.679
2.000	0.580	0.398	0.702	0.389	0.700
3.000	0.566	0.410	0.700	0.401	0.695
4.000	0.583	0.394	0.702	0.385	0.698
5.000	0.601	0.414	0.730	0.437	0.744
7.500	0.626	0.465	0.781	0.477	0.787
10.000	0.645	0.355	0.735	0.477	0.801

4.2.2 Discussion of "Geometrical Spreading" Coefficients

Figure 4.4 plots the "geometrical spreading terms" c_1 and c_2; Figure 4.5 shows the effective "geometrical spreading" factor obtained by the combination $c_1 + c_2 (\mathbf{M} - \mathbf{M}_{ref})$. The coefficients have more variation with period than seems reasonable, but to some extent this may be a result of forcing very smooth period dependence for the other distance-related coefficients. Note that the signs of the c_1 and c_2 coefficients differ for periods of less than 4 s. As a result, the effective geometrical spreading factor decreases with magnitude for periods of less than about 4 s, as shown in Figure 4.5. This is expected from simulation studies. On the other hand, the magnitude coefficient c_2 becomes negative for periods greater than 4 s, leading to a decrease of the geometrical spreading factor for smaller earthquakes. This is not expected. The reason for this

apparently anomalous behavior might be the relative sparseness of data for small magnitudes at long periods, in combination with the bias discussed earlier due to data censoring. For these reasons, the predictions of PSA at period above about 4 or 5 s and magnitudes less than about 5.6 should be treated with some skepticism. Judging from the plot in Figure 4.4, the coefficient controlling the magnitude dependence of the geometrical spreading (c_2) would be 0.0 at about T= 4.6 s, thus explaining the convergence of the curves at that period.
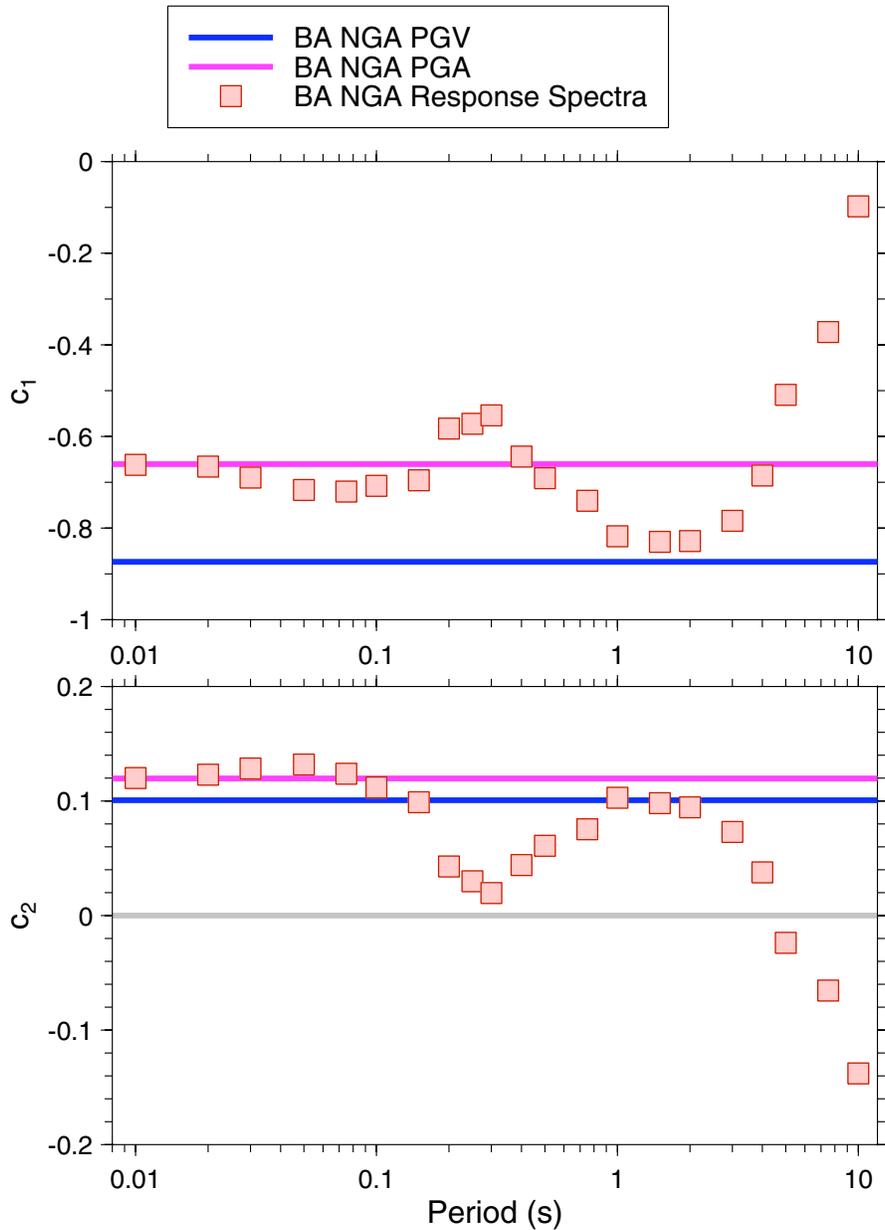
Fig. 4.4 Coefficients c_1 and c_2 from regression analysis. Horizontal lines show values for PGA and PGV (see legend).
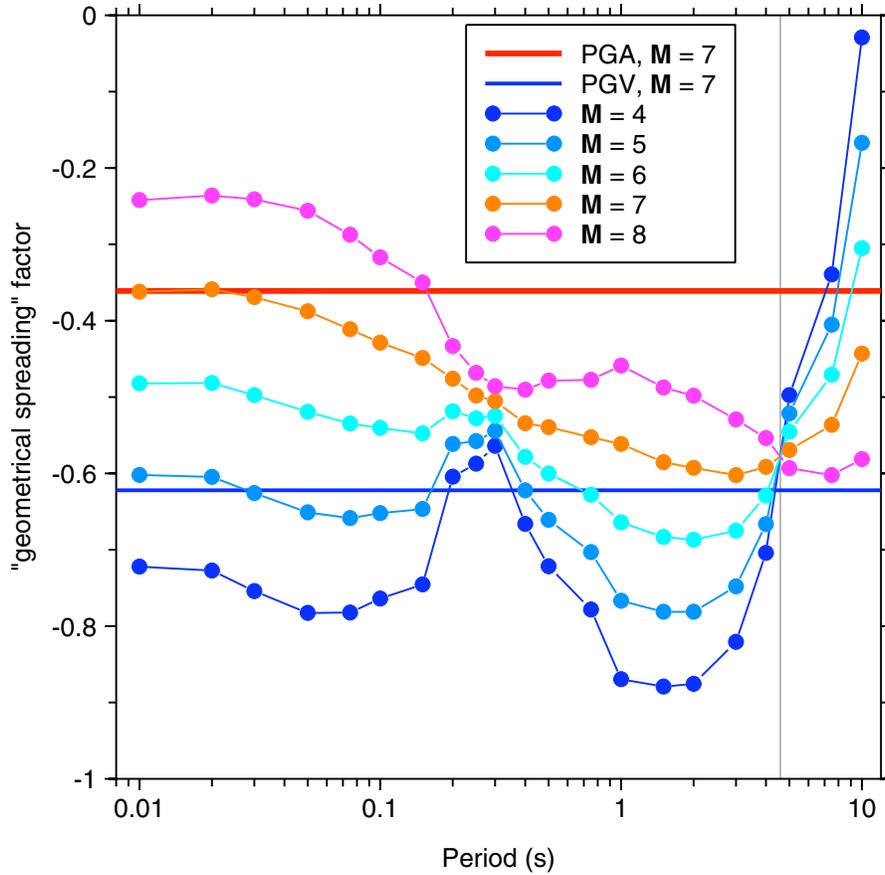
Fig. 4.5 Effective geometrical spreading coefficient, given by $c_1 + c_2 (\mathbf{M} - \mathbf{M}_{ref})$ **.**

4.2.3   Fit of Stage 1 Regressions

Figures 4.6–4.11 are a series of graphs showing the observations in comparison to the Stage 1 regression predictions. These figures provide a visual test of the ability of our functional form to represent the distance dependence of the response variables. The Yorba Linda data points are from the smallest earthquake in the NGA flatfile and are included on each figure to provide a basis for judging the magnitude scaling (note that data for that earthquake is missing for $T = 3$ s because the maximum useable period is 2.6 s). In all plots, records with R_{JB} less than 0.1 km have been plotted at 0.1 km. The curves are from the regression fits and include the event terms found for the specific regression—they are intended to help assess the Stage 1 regression and do not include event-to-event variability (see the plots of event terms for the Stage 2 regressions, shown later, for this variability). The figures contain data from all but one (St. Elias) of the **M** 7

earthquakes, in addition to the 1994 Northridge, 1995 Kobe, and 1989 Loma Prieta earthquakes. Overall, the agreement between our simple functional form and the observations appears to be quite good.

(a)
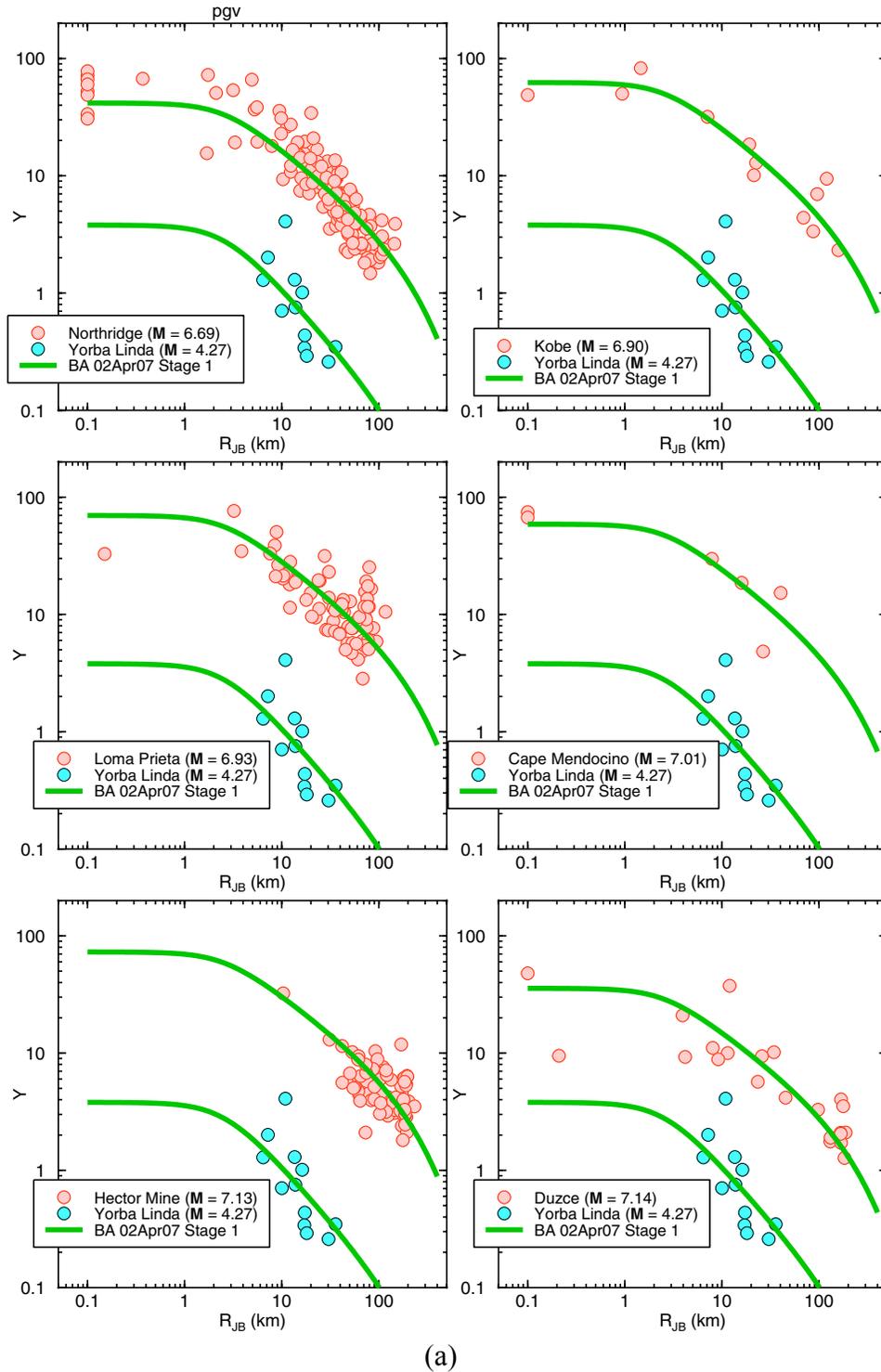
Fig. 4.6 Symbols: PGV observations, corrected to $V_{S30} = 760$ m/s, as function of distance for indicated events; Curves: Stage 1 regression fits.

(b)
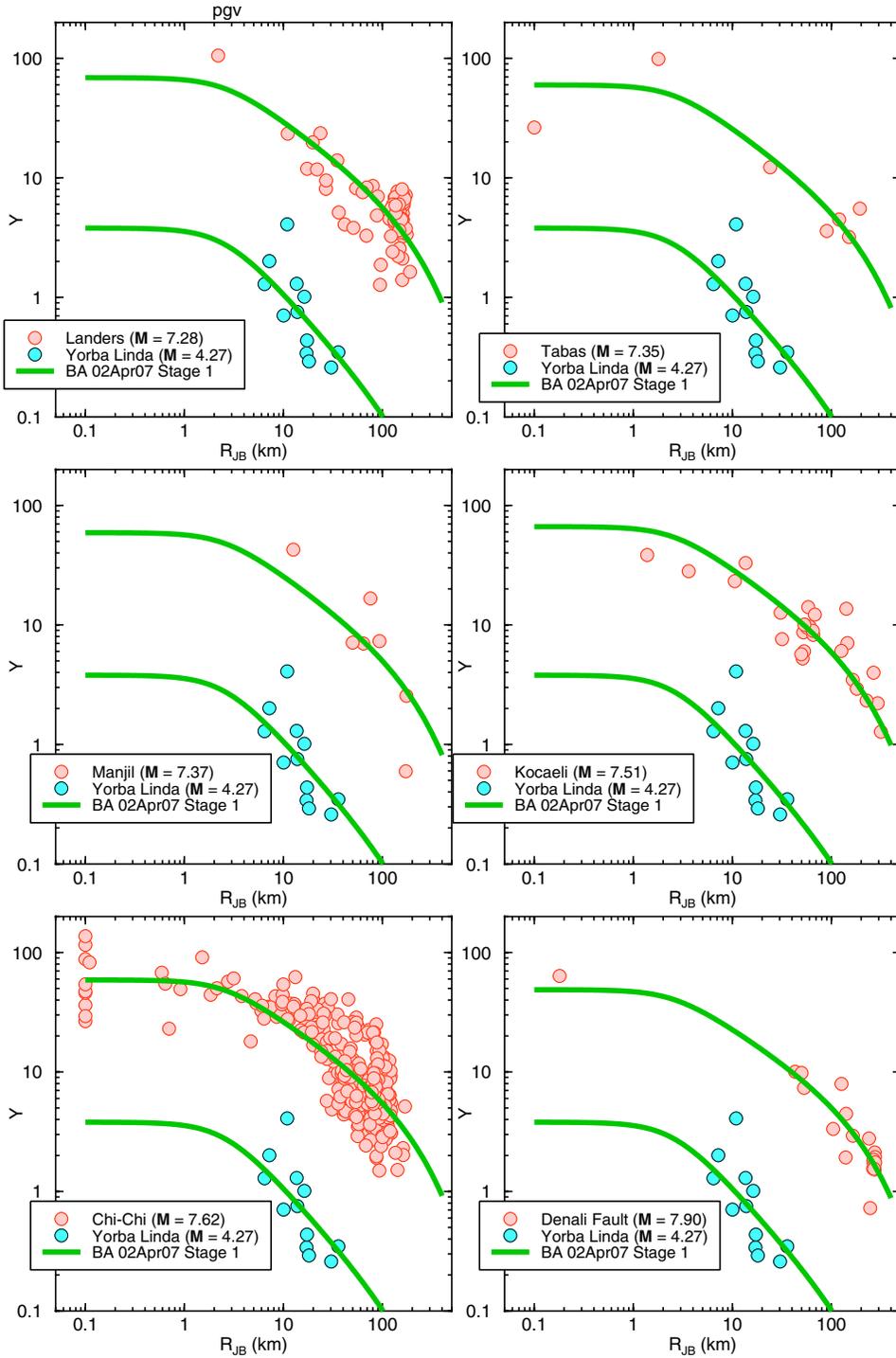
Fig. 4.6 —*Continued*
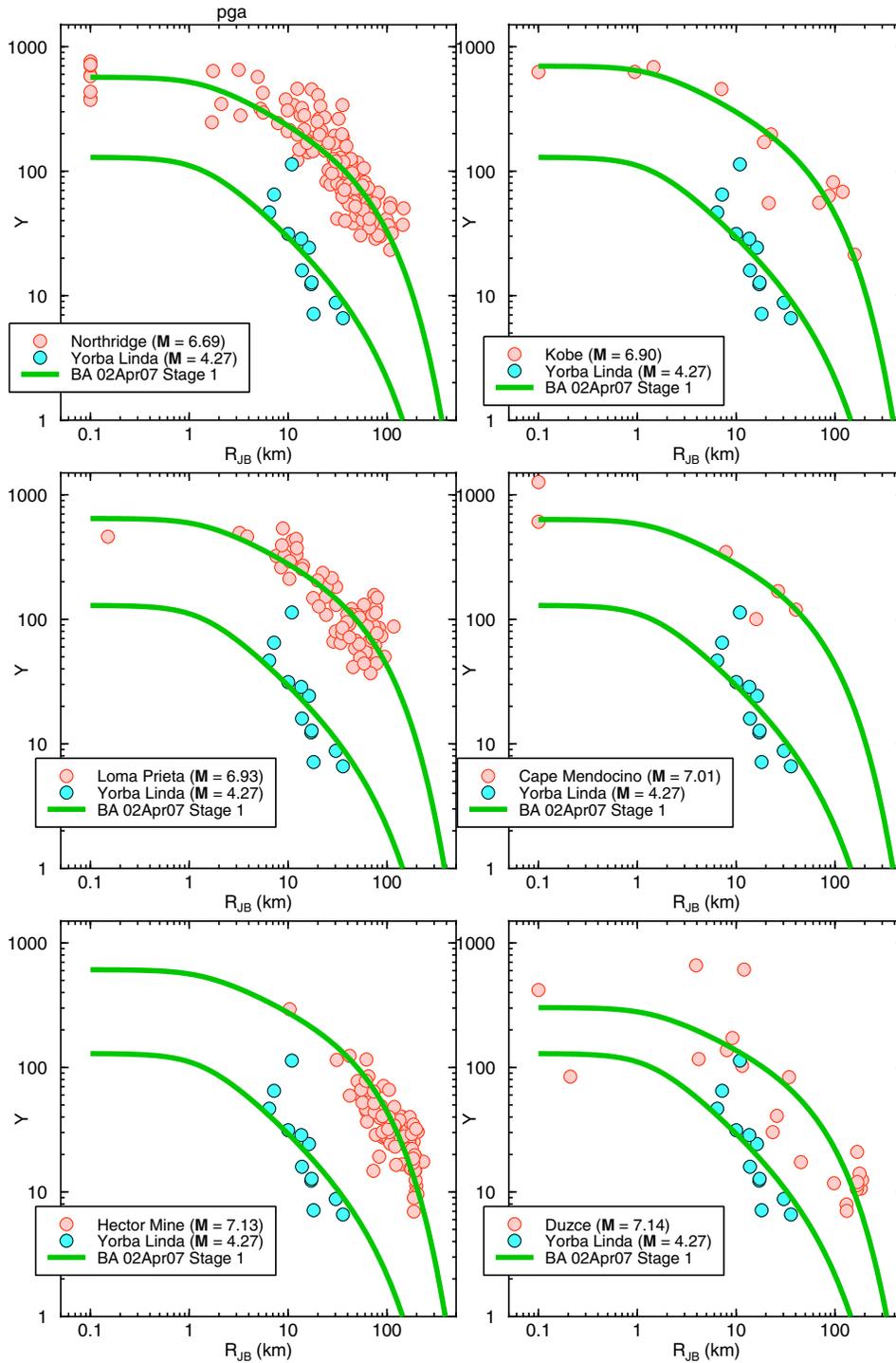
Fig. 4.7 **Symbols: PGA observations, corrected to** $V_{S30} = 760\,\text{m/s}$**, as function of distance for indicated events; Curves: Stage 1 regression fits.**

43

(b)

Fig. 4.7—*Continued*

44
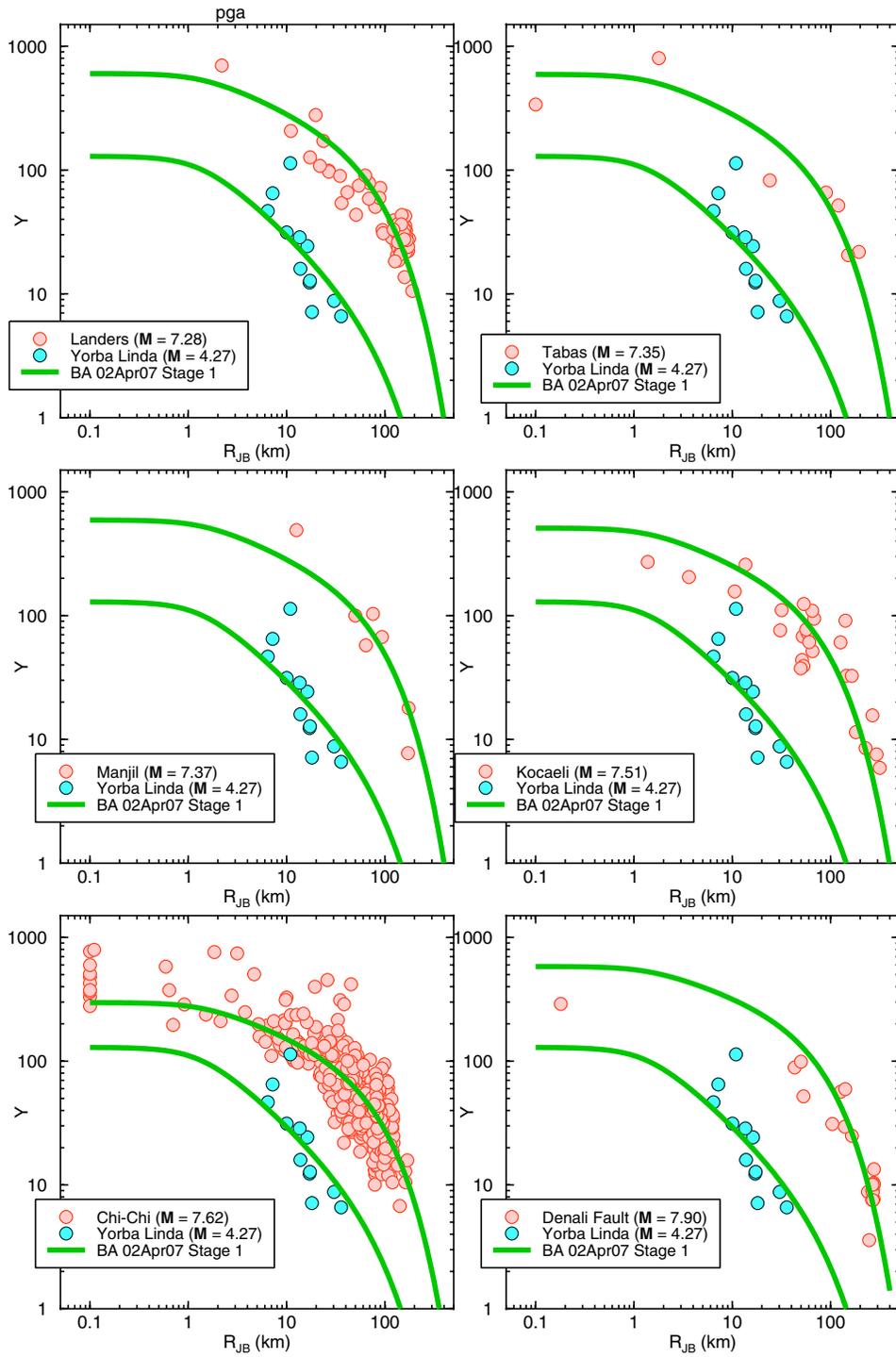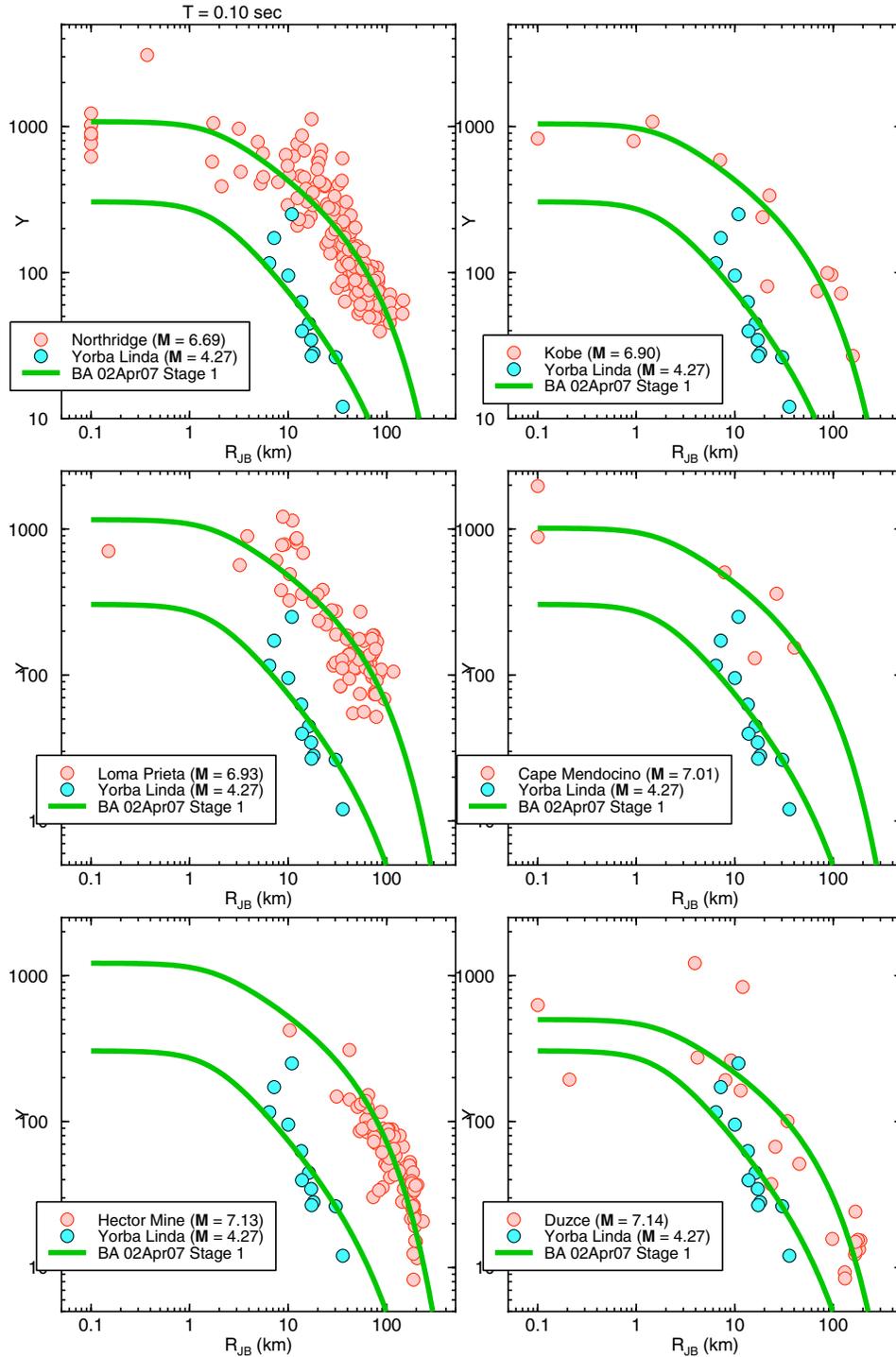
(a)

Fig. 4.8 Symbols: 0.1 s PSA observations, corrected to $V_{S30} = 760$ m/s, **as function of distance for indicated events; Curves: Stage 1 regression fits**.

(b)

Fig. 4.8—*Continued*

46
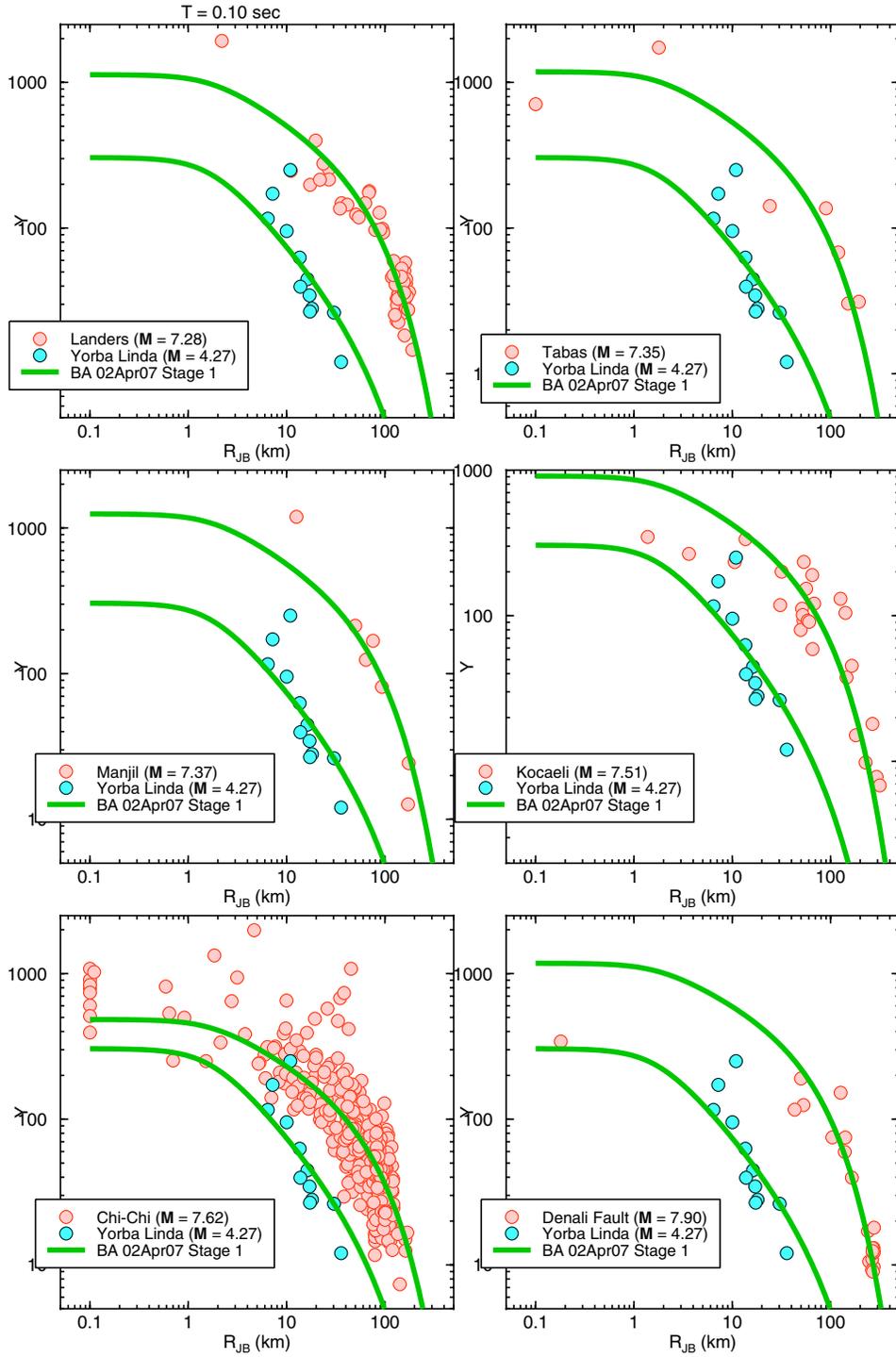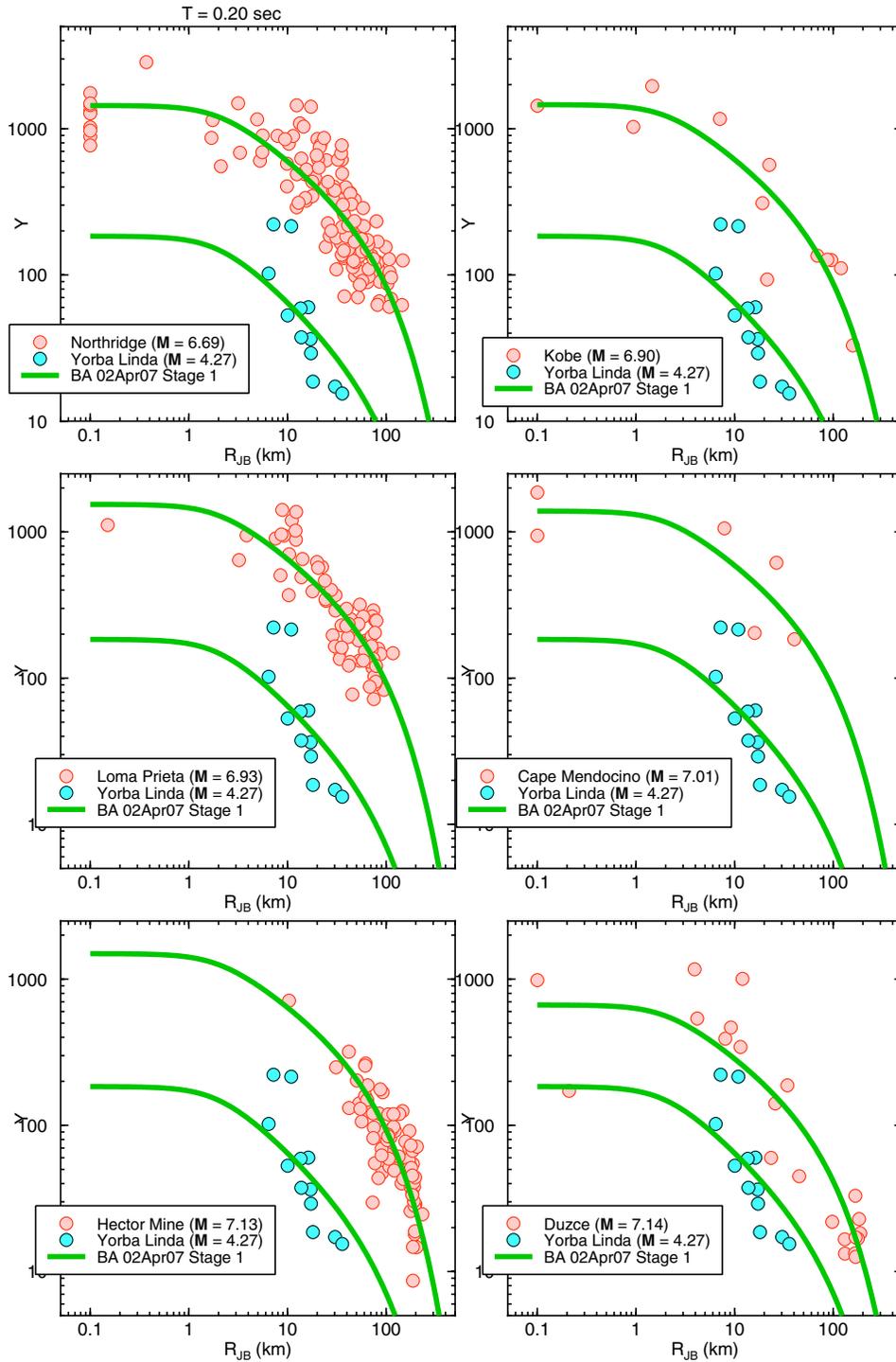
(a)

Fig. 4.9 Symbols: 0.2 s PSA observations, corrected to $V_{S30} = 760$ m/s, as function of distance for indicated events; Curves: Stage 1 regression fits.
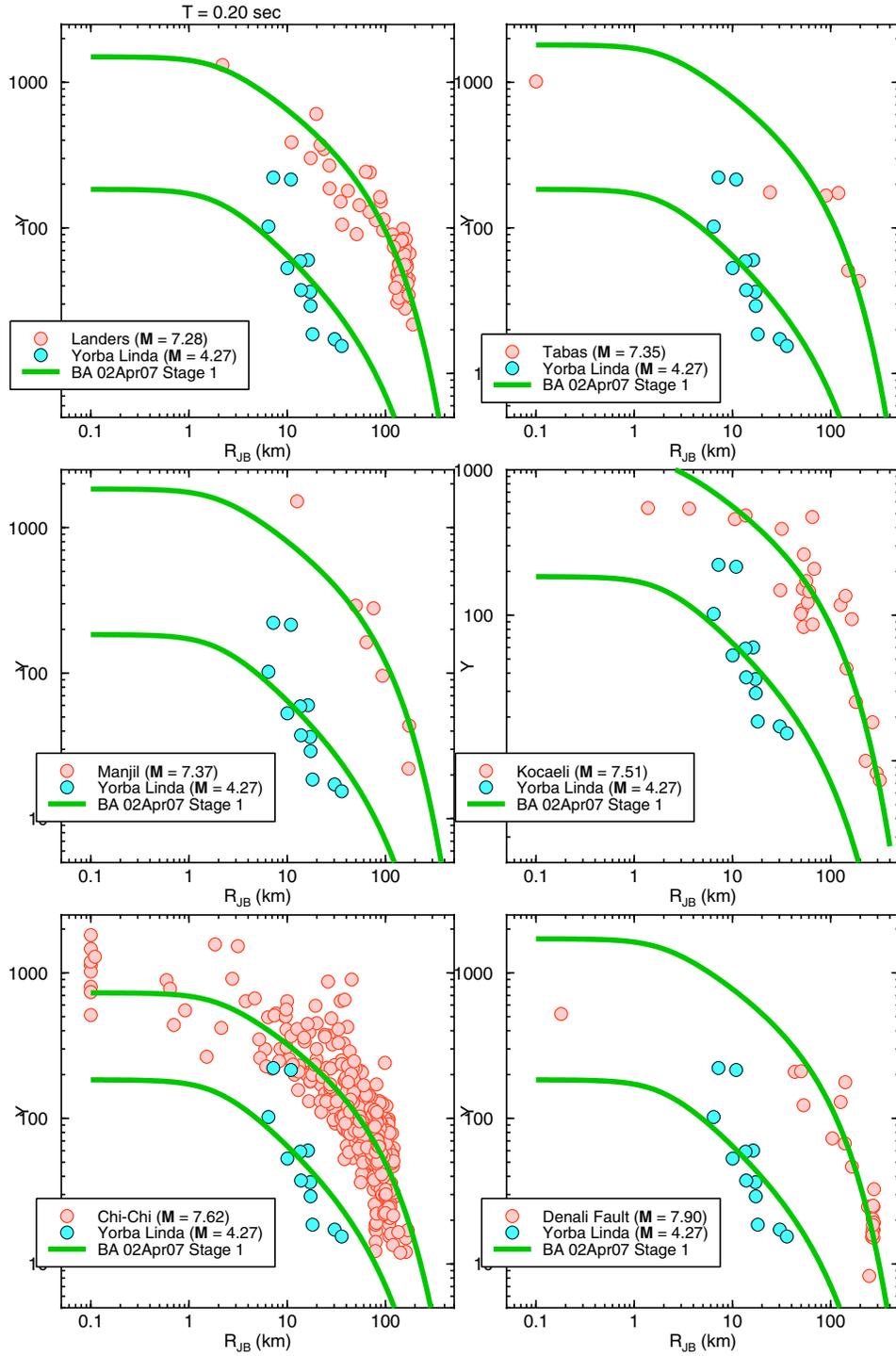
(b)

Fig. 4.9—_Continued_
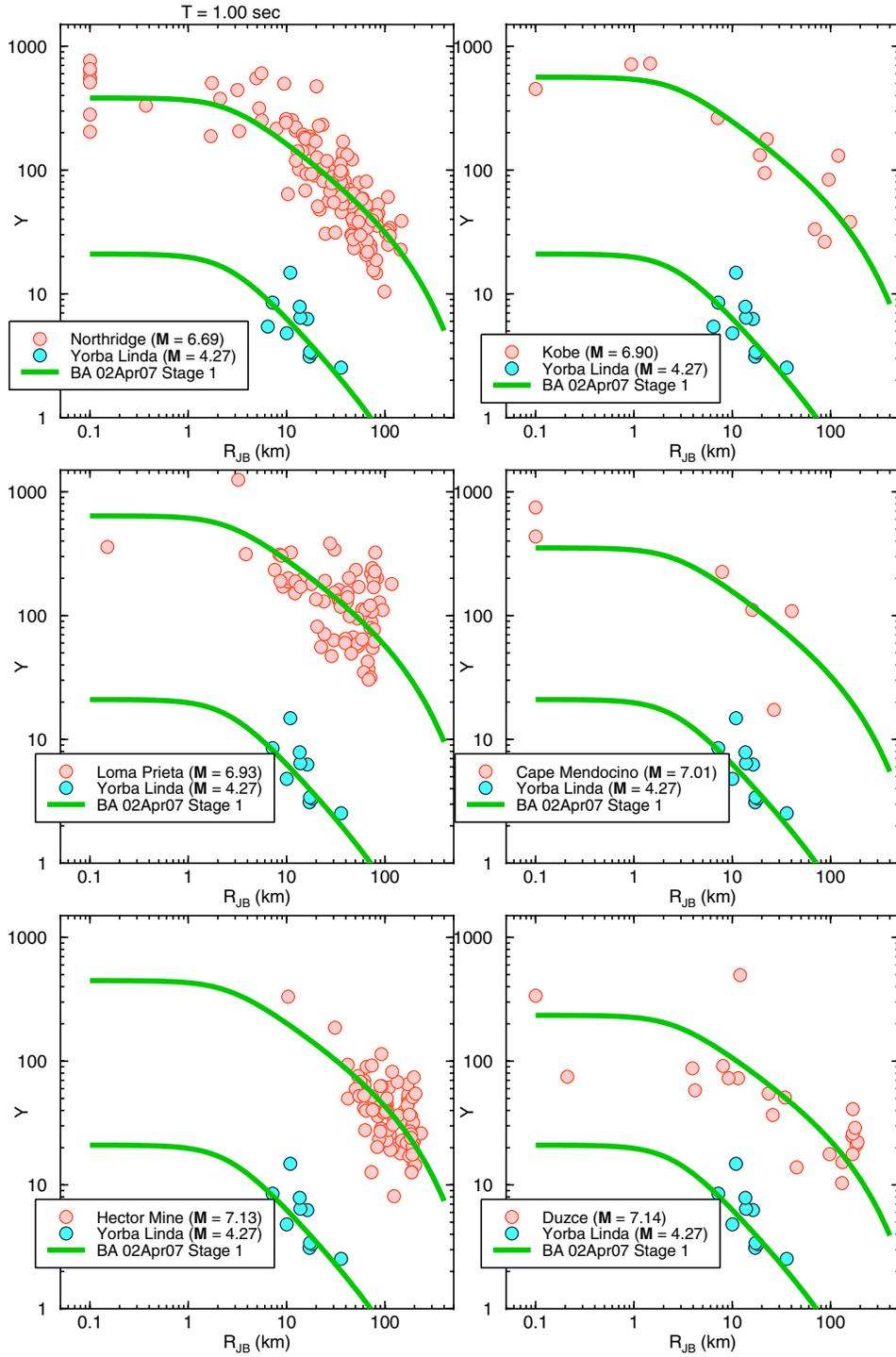
(a)

Fig. 4.10 Symbols: 1.0 s PSA observations, corrected to $V_{S30} = 760$ m/s, as function of distance for indicated events; Curves: Stage 1 regression fits.
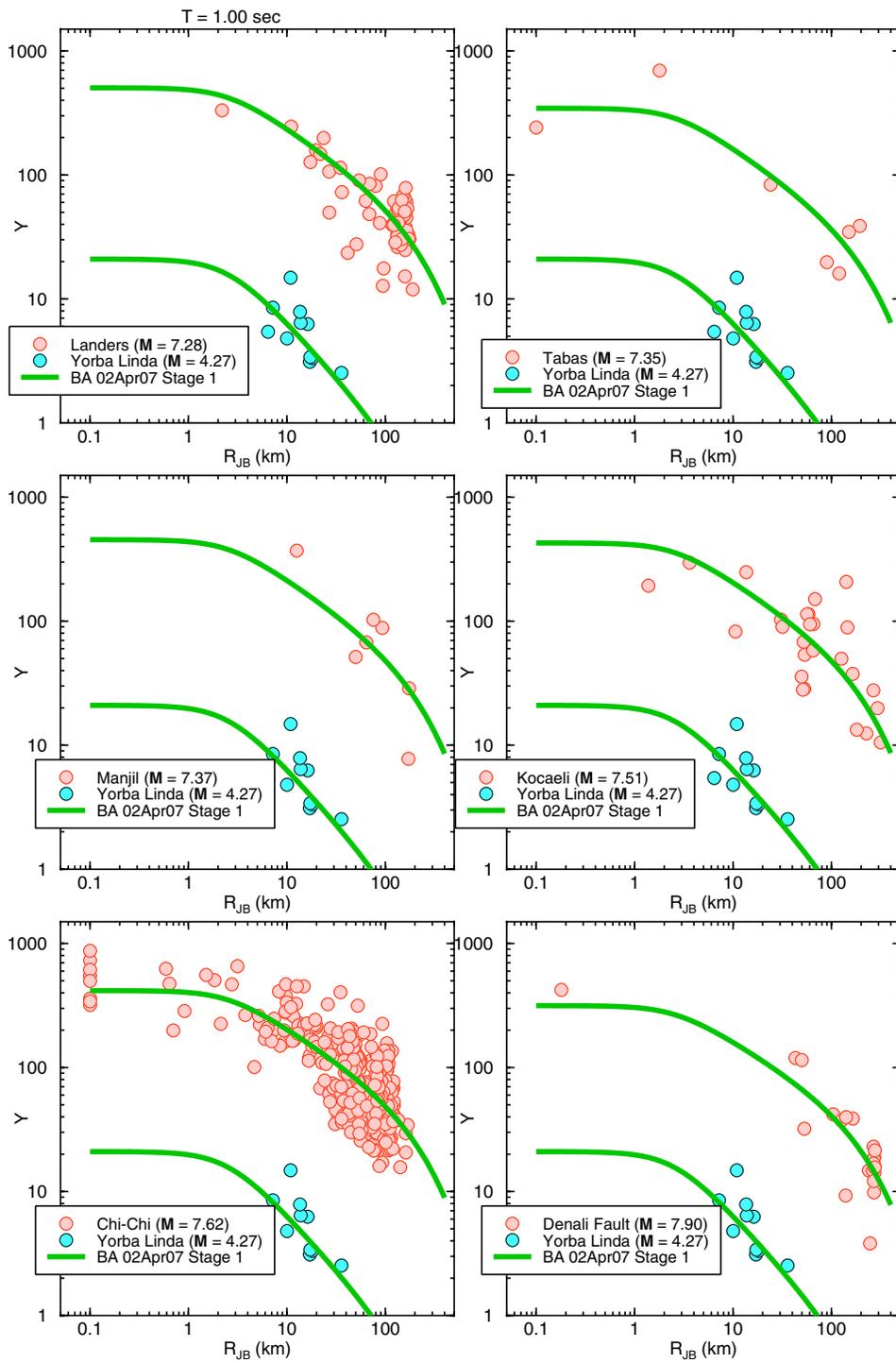
(b)

Fig. 4.10—*Continued*
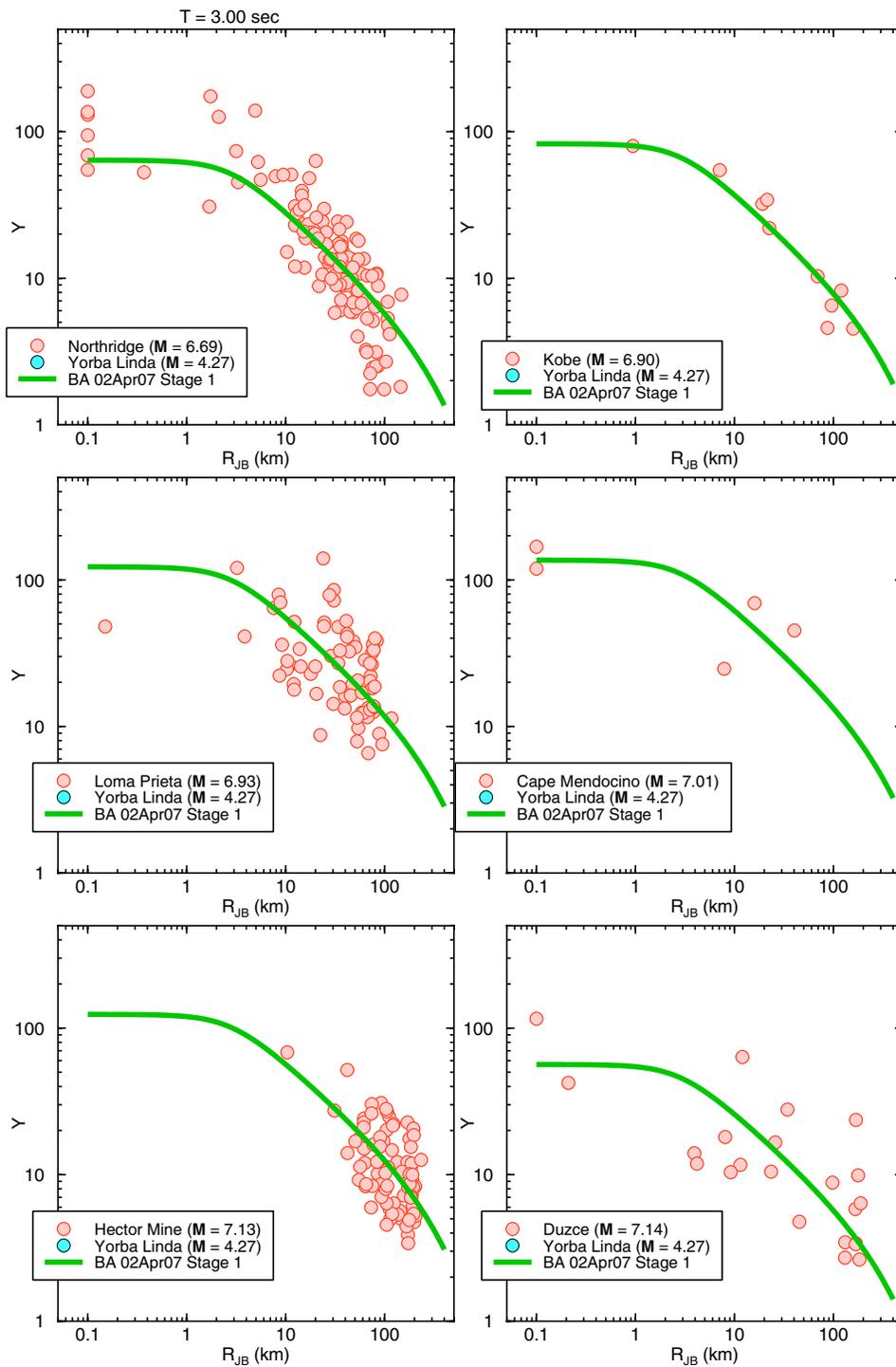
Fig. 4.11 Symbols: 3.0 s PSA observations, corrected to $V_{S30} = 760\ \mathrm{m/s}$, as function of distance for indicated events; Curves: Stage 1 regression fits.
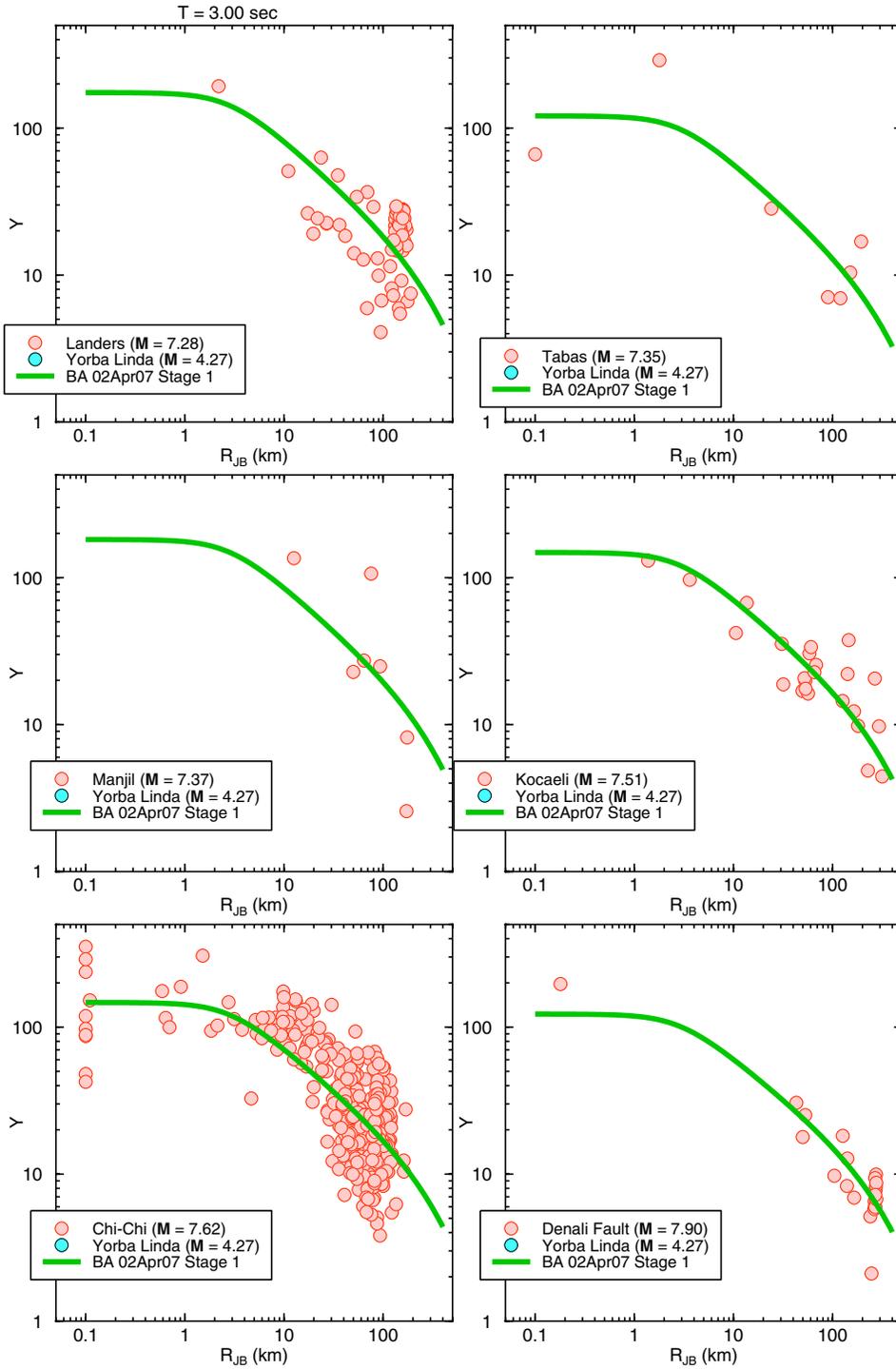
(b)

Fig. 4.11—*Continued*

52

A more precise way of looking for systematic mismatches between predictions and observations is to plot the residuals, defined as the ratio of observed to predicted ground motions. Figures 4.12(a)–(c) show residuals as a function of distance for earthquakes less than or equal to magnitude 7; Figures 4.13(a)–(c) show residuals from larger earthquakes, excluding the 1999 Chi-Chi earthquake, and Figures 4.14(a)–(c) show residuals just for the Chi-Chi earthquake. While there are some systematic departures for various periods and distances, the fit between observations and our predictions was judged to be adequate.
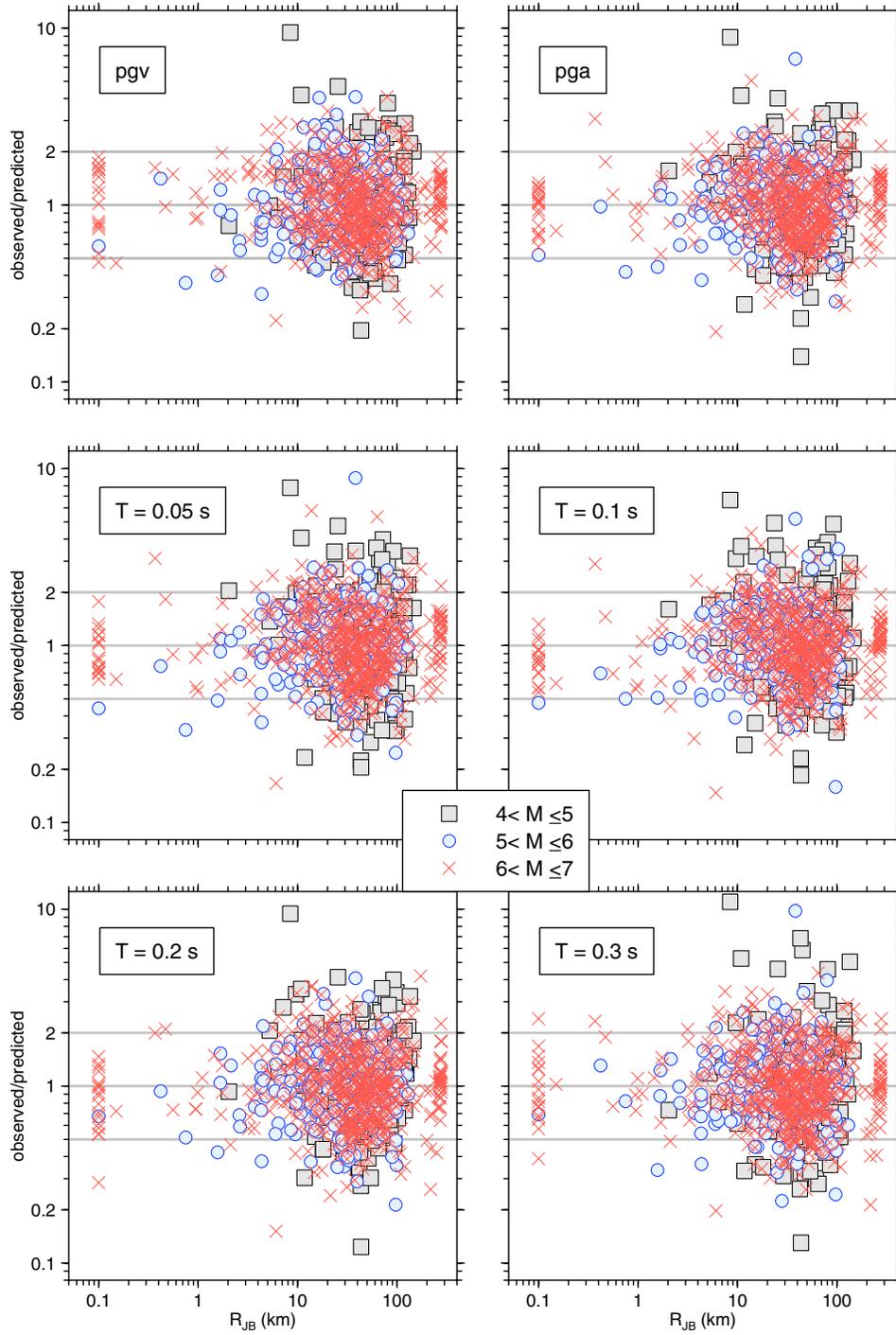
(a)

Fig. 4.12 Stage 1 residuals for earthquakes less than or equal to 7.0.
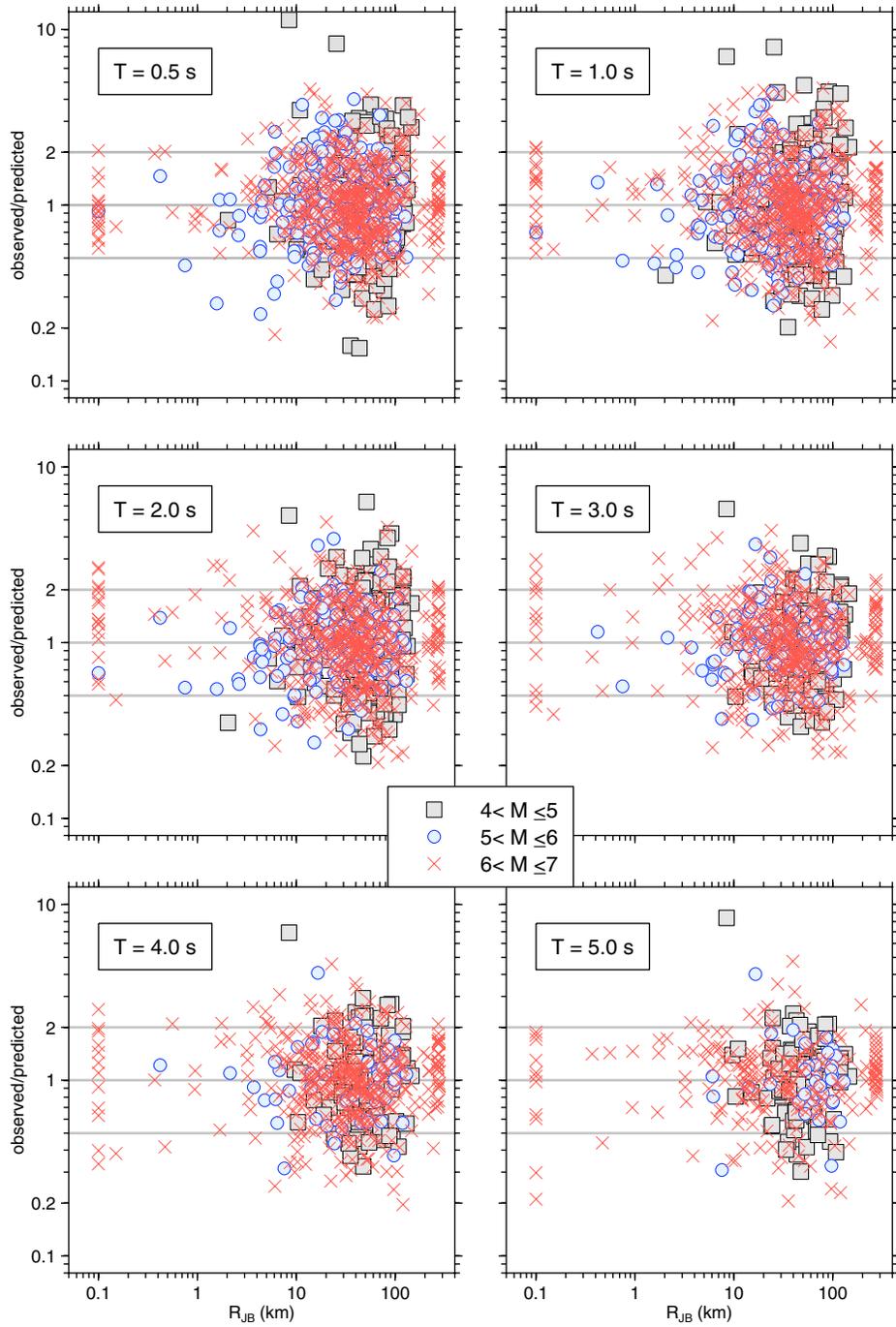
(b)

Fig. 4.12—*Continued*
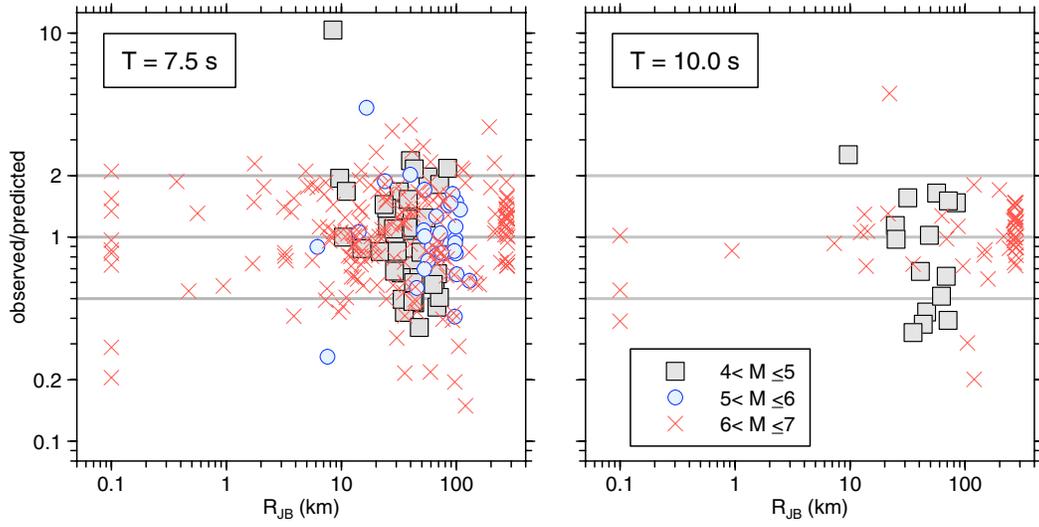
(c)

Fig. 4.12—*Continued*
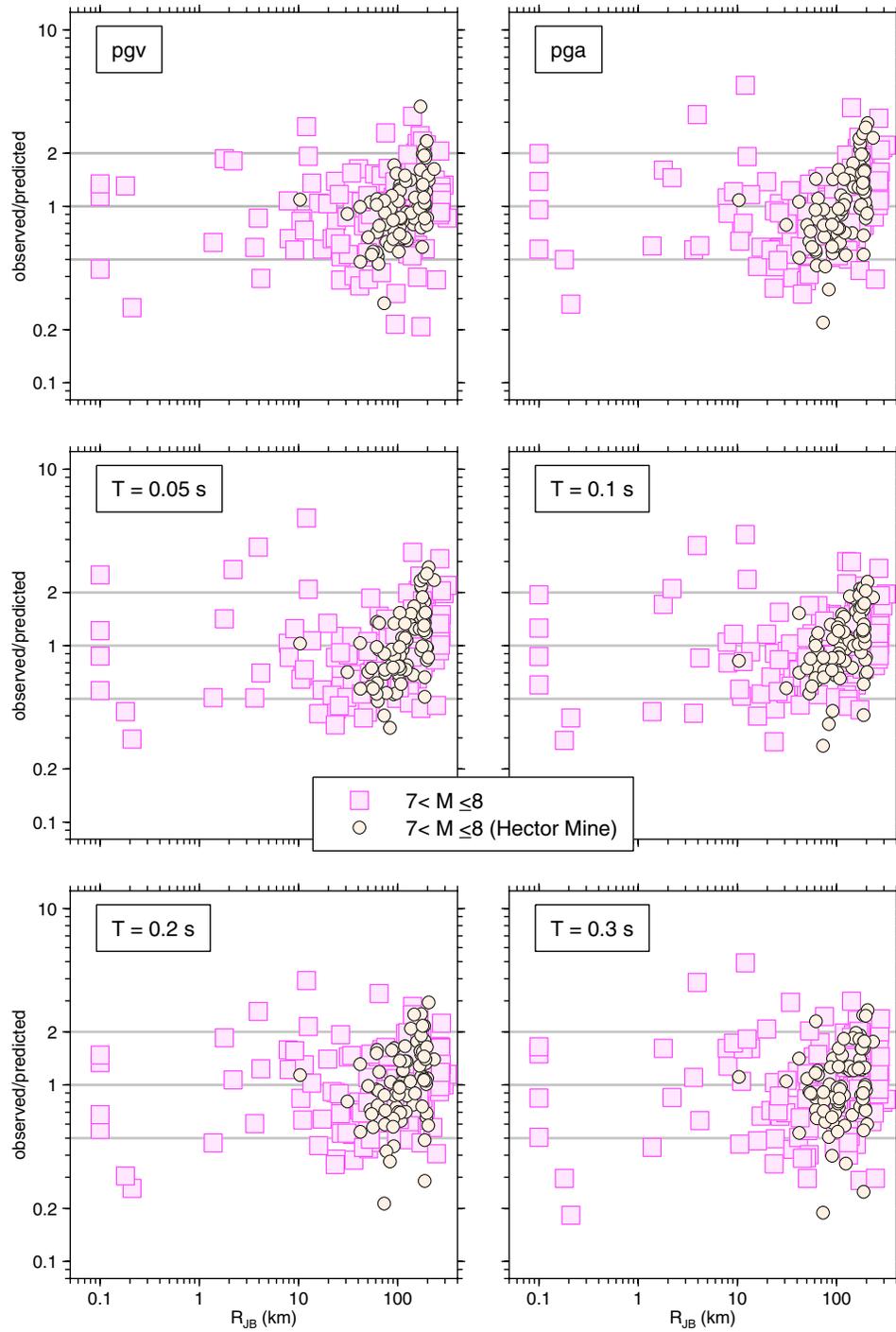
(a)

Fig. 4.13 Stage 1 residuals for earthquakes greater than 7.0, excluding 1999 Chi-Chi.

57
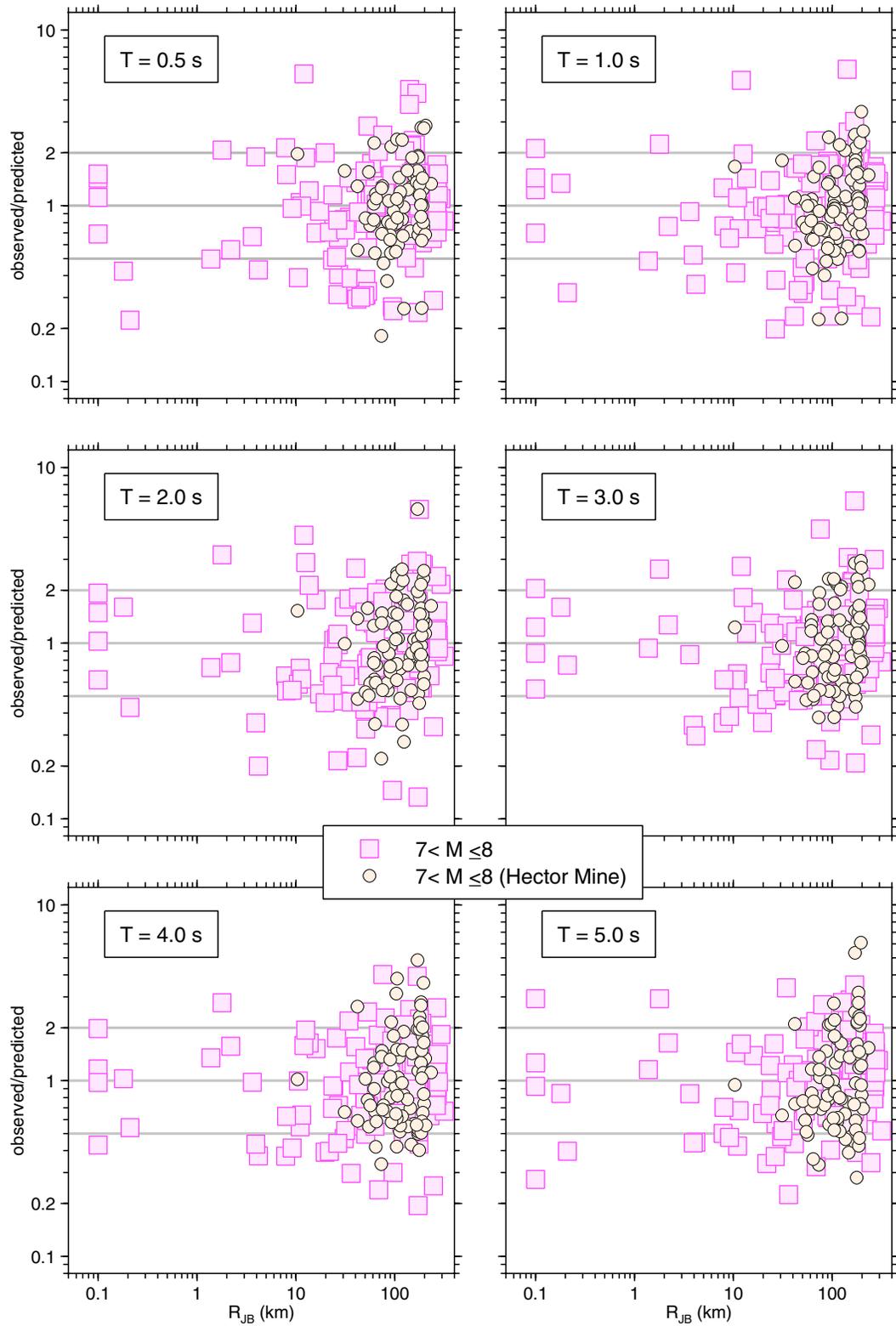
(b)

Fig. 4.13—*Continued*

58
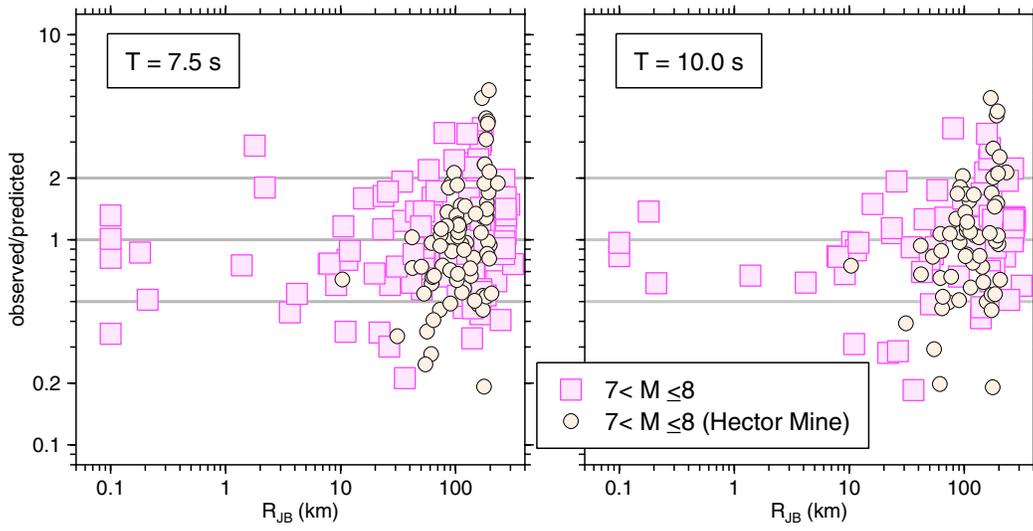
(c)

Fig. 4.13—*Continued*
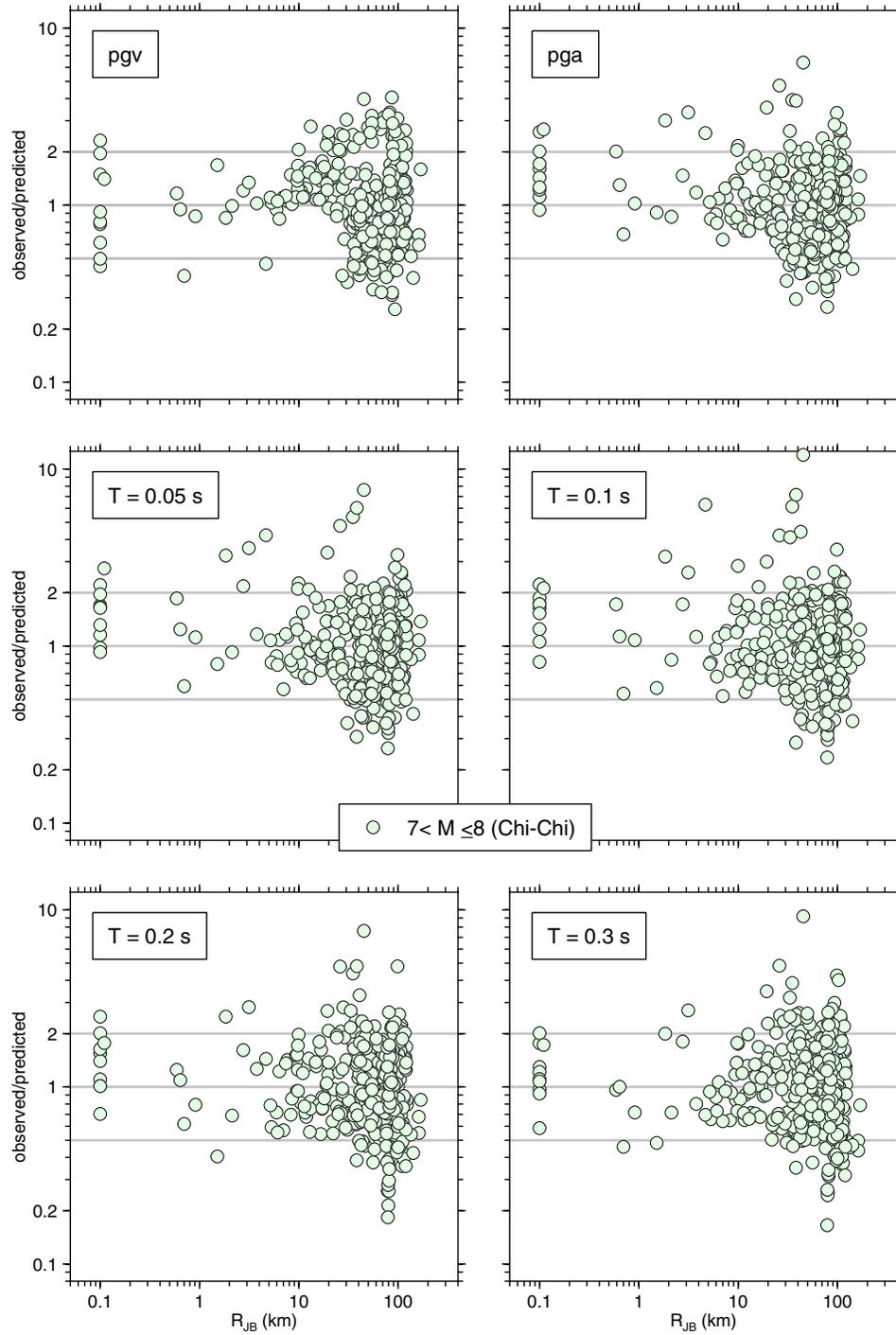
(a)

Fig. 4.14 Stage 1 residuals for 1999 Chi-Chi mainshock.
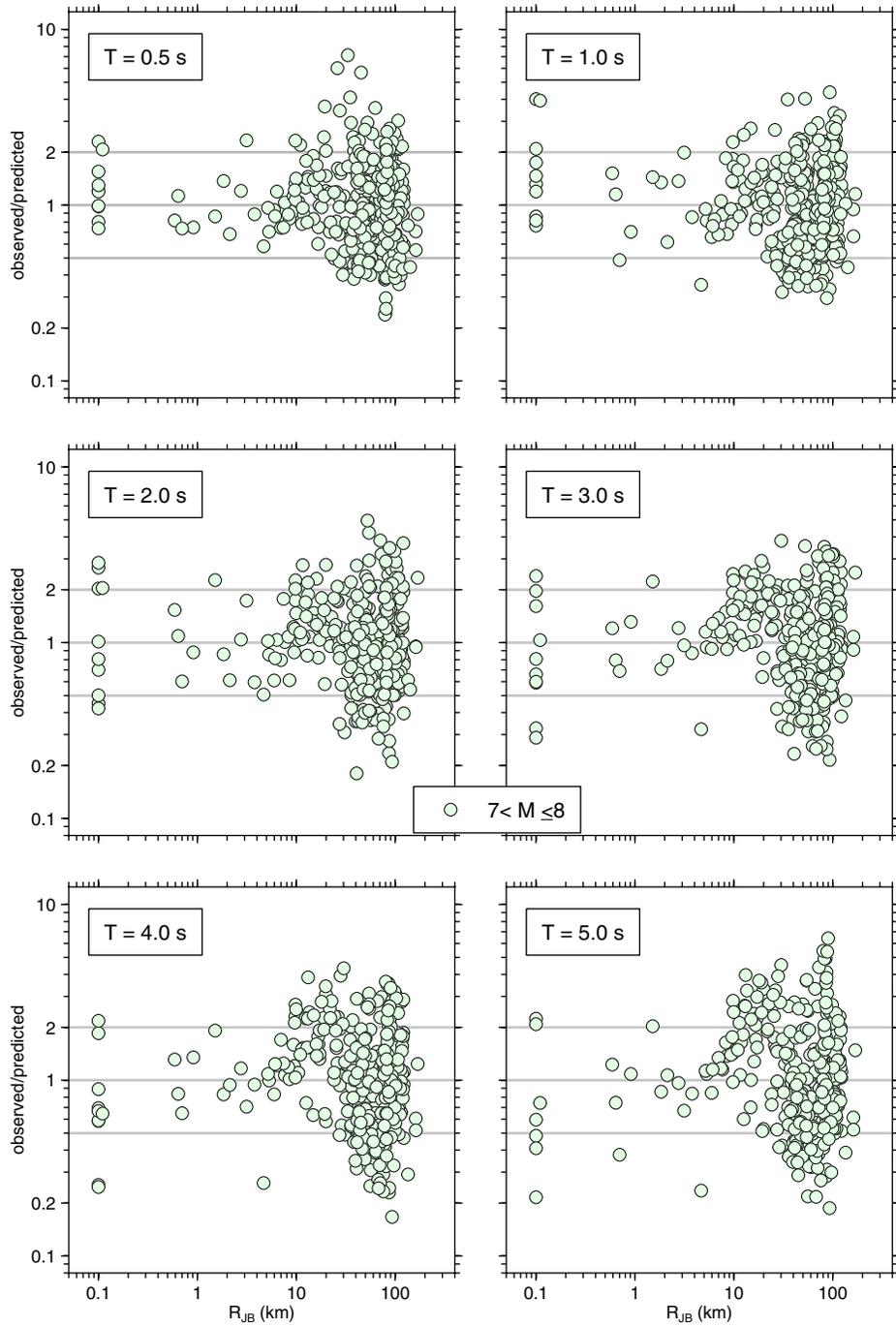
(b)

Fig. 4.14—*Continued*
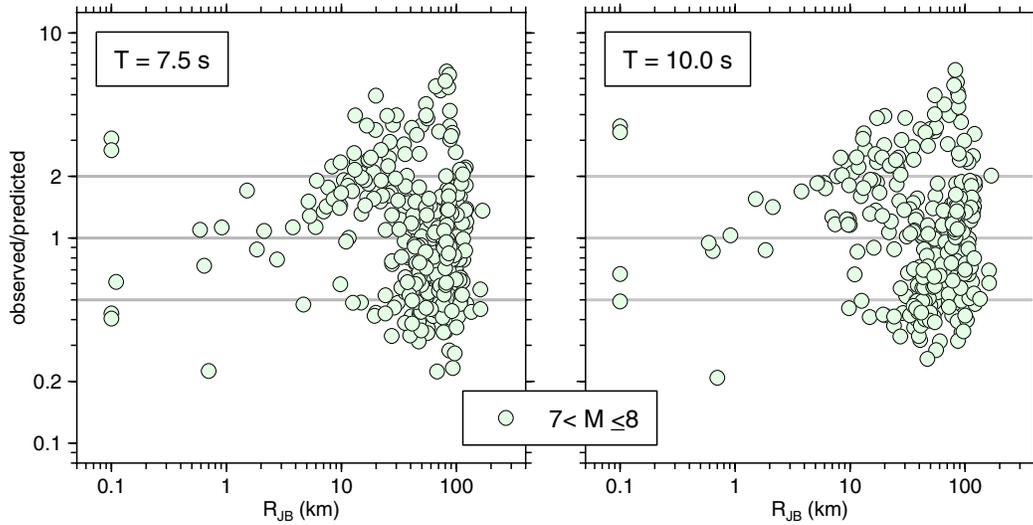
(c)

Fig. 4.14—Continued

4.2.4   Fit of Stage 2 Regressions

Figures 4.15(a)–(c) are plots of the event terms $(c_0)_j$ from the Stage 1 regression as a function of magnitude, with the Stage 2 regression fit to these terms superimposed. The fault type for each earthquake is indicated, as are curves for fault type unspecified and for strike-slip, normal, and thrust/reverse faults (the fault type is indicated by the color of the symbols). The functional form provides a reasonable fit to the near-source amplitude data. Note that the magnitude scaling for T=10 s at **M**<6.5 is strongly controlled by the data from only one small earthquake (2000 Yountville, **M** 5.0), and may therefore be unreliable for **M**<6.5.

62
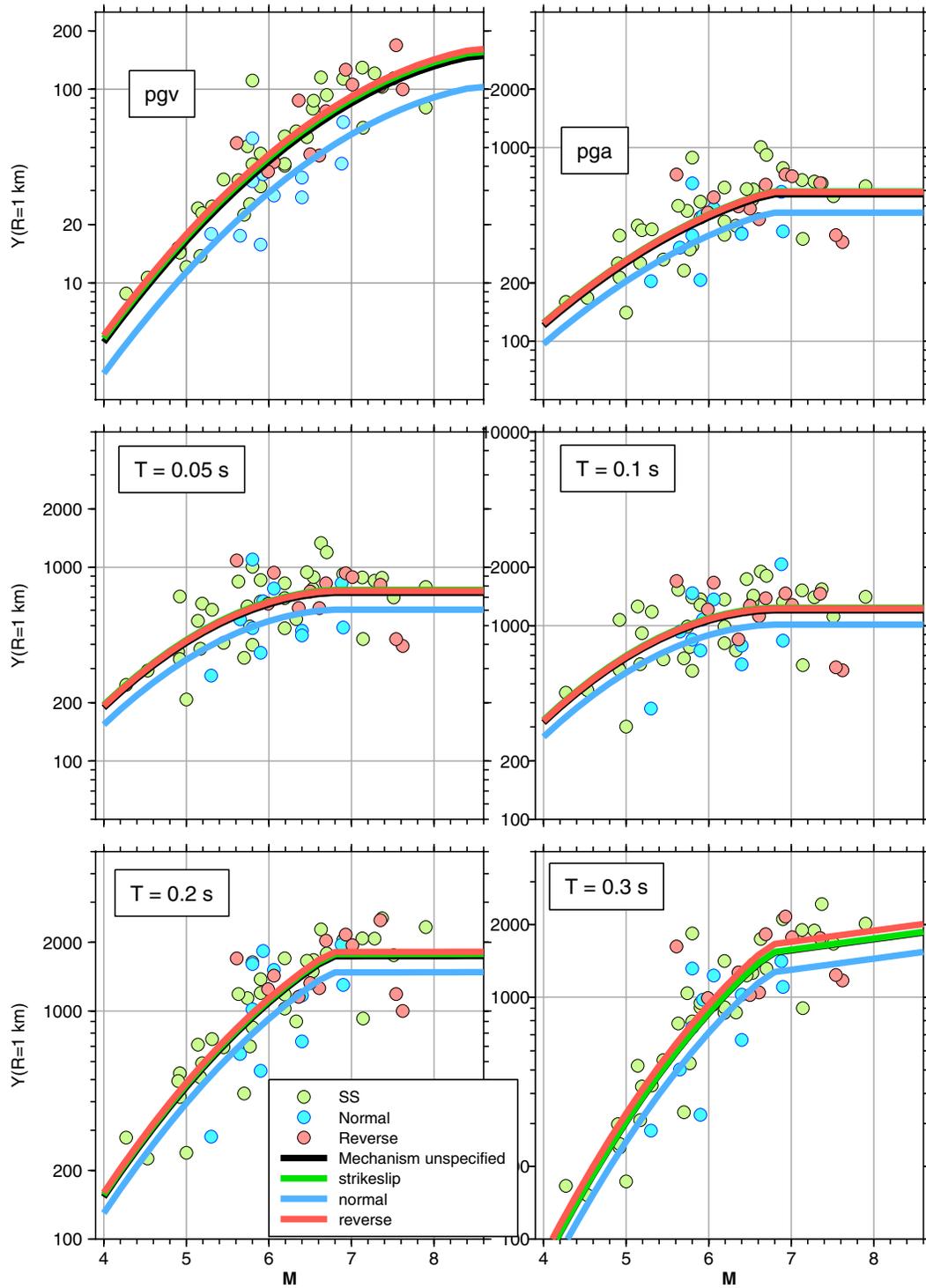
Fig. 4.15 Event terms and Stage 2 regression fits.

63
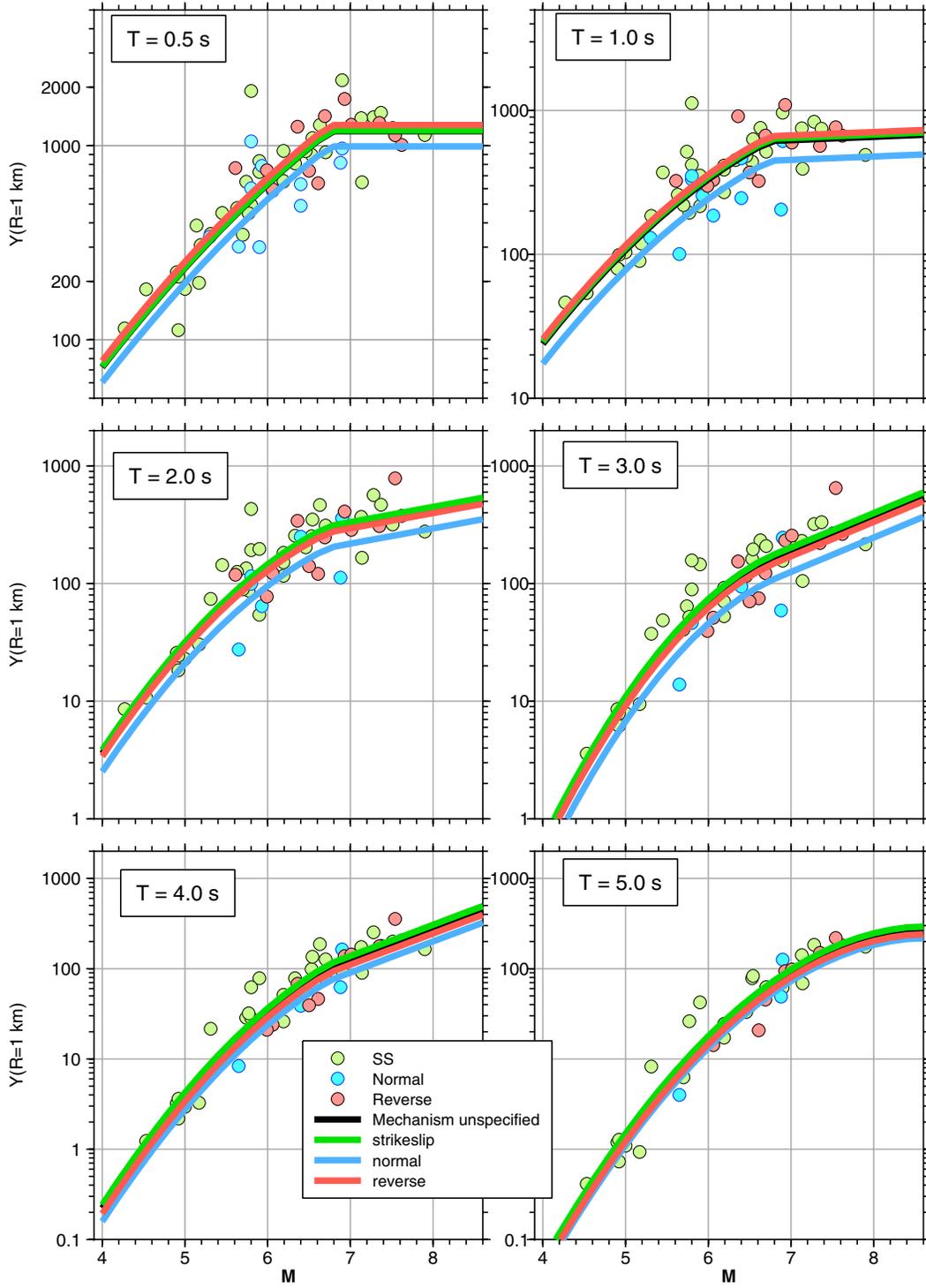
(b)

Fig. 4.15—*Continued*
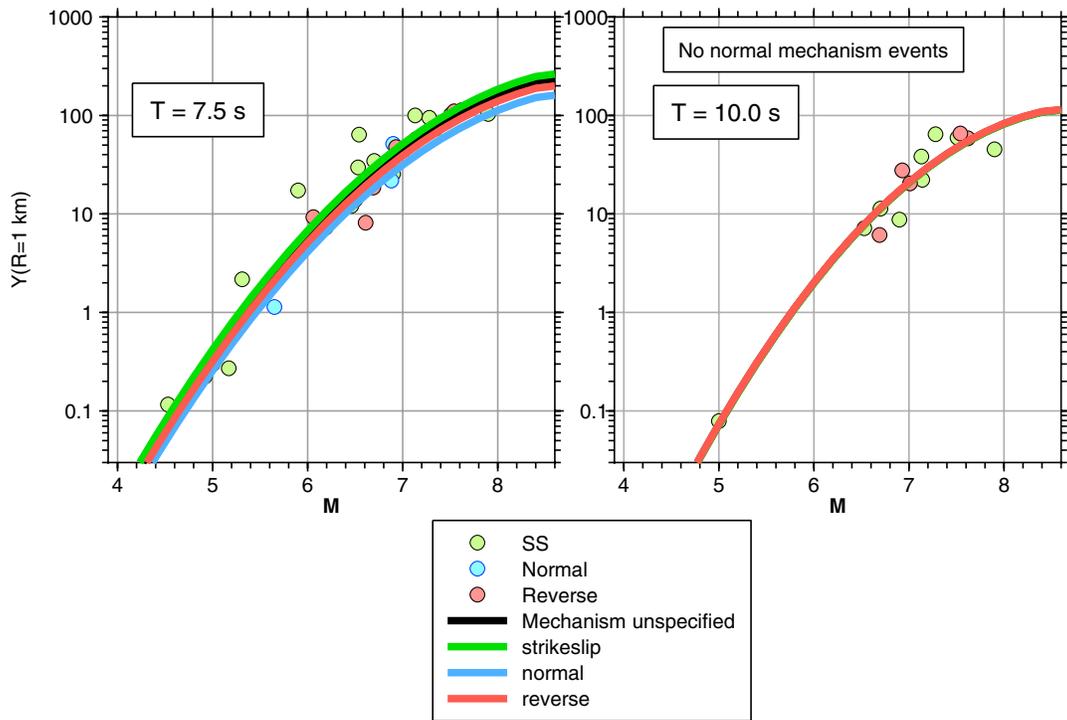
(c)

Fig. 4.15—*Continued*

4.2.5 Predictions of PSA from Combined Stage 1 and Stage 2 Regressions

Graphs of PSA and PGA predicted from our equations for three values of R_{JB} and four magnitudes are shown in Figure 4.16. The curves for the larger earthquakes tend to pinch together for periods near 0.2–0.3 s, probably a reflection of the pinching together of the effective geometric spreading factor for these periods (Fig. 4.5). But otherwise the PSA are quite smooth, especially considering that many of the coefficients were determined independently for each period.
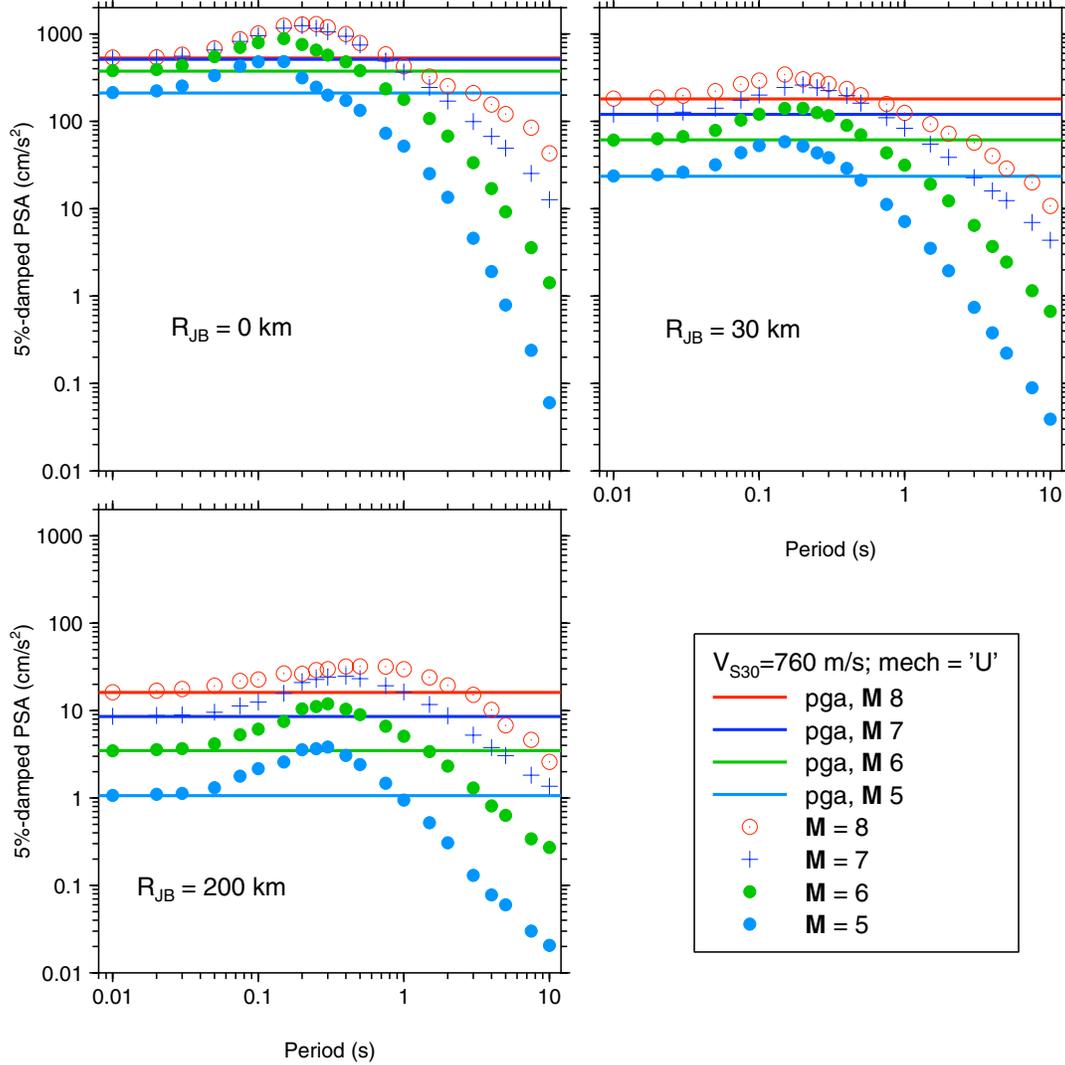
Fig. 4.16 PSA from our equations, as function of period; see legend for details.

Plots of PSA as a function of distance are shown in Figures 4.17(a)–(f) for the whole range of periods. The figures are in pairs, one for $V_{S30} = 760$ m/s (NEHRP B/C boundary), followed by one for $V_{S30} = 250$ m/s (NEHRP D; see Appendix E).
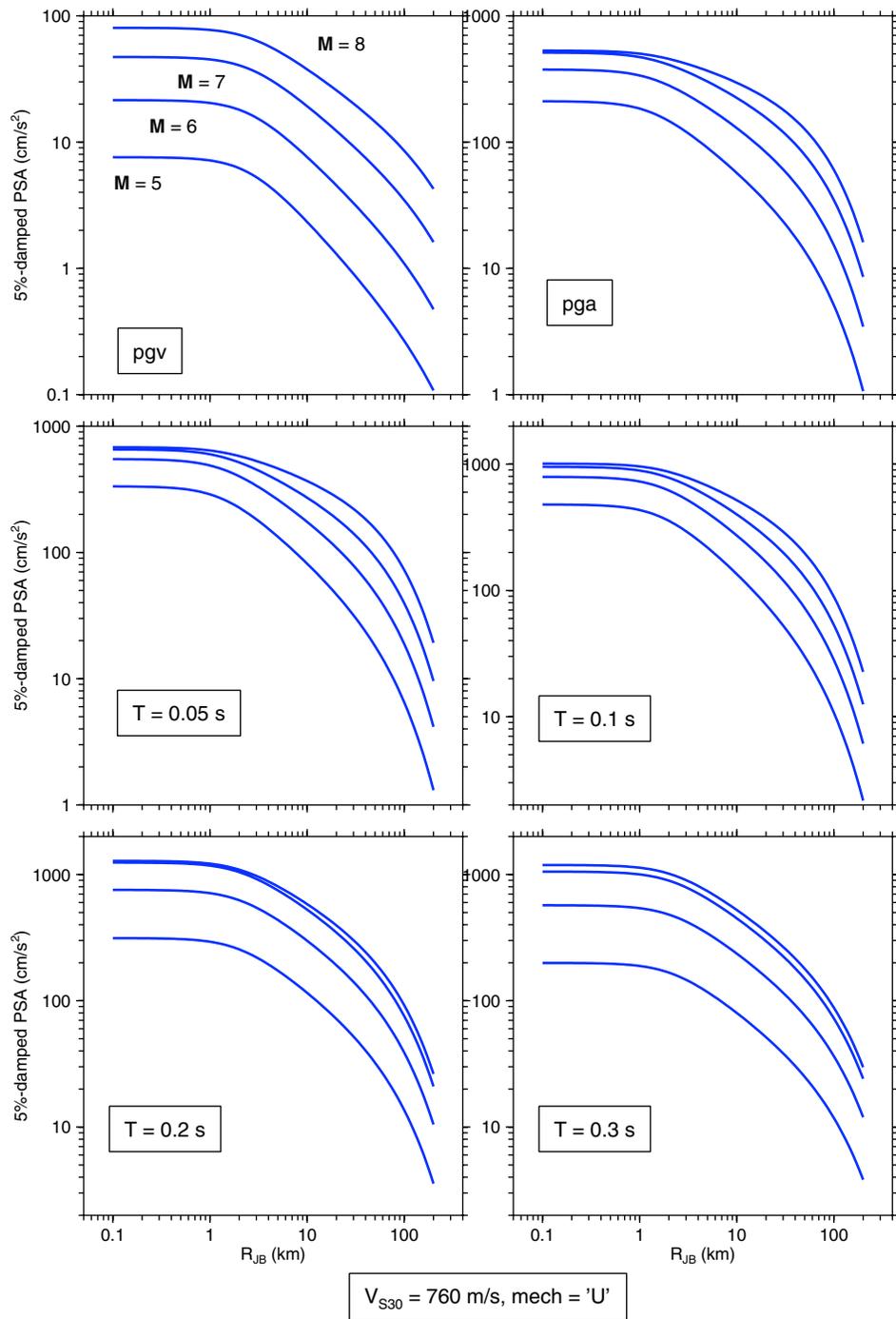
(a)

Fig. 4.17 PSA from our equations, as function of distance; see legend for details.
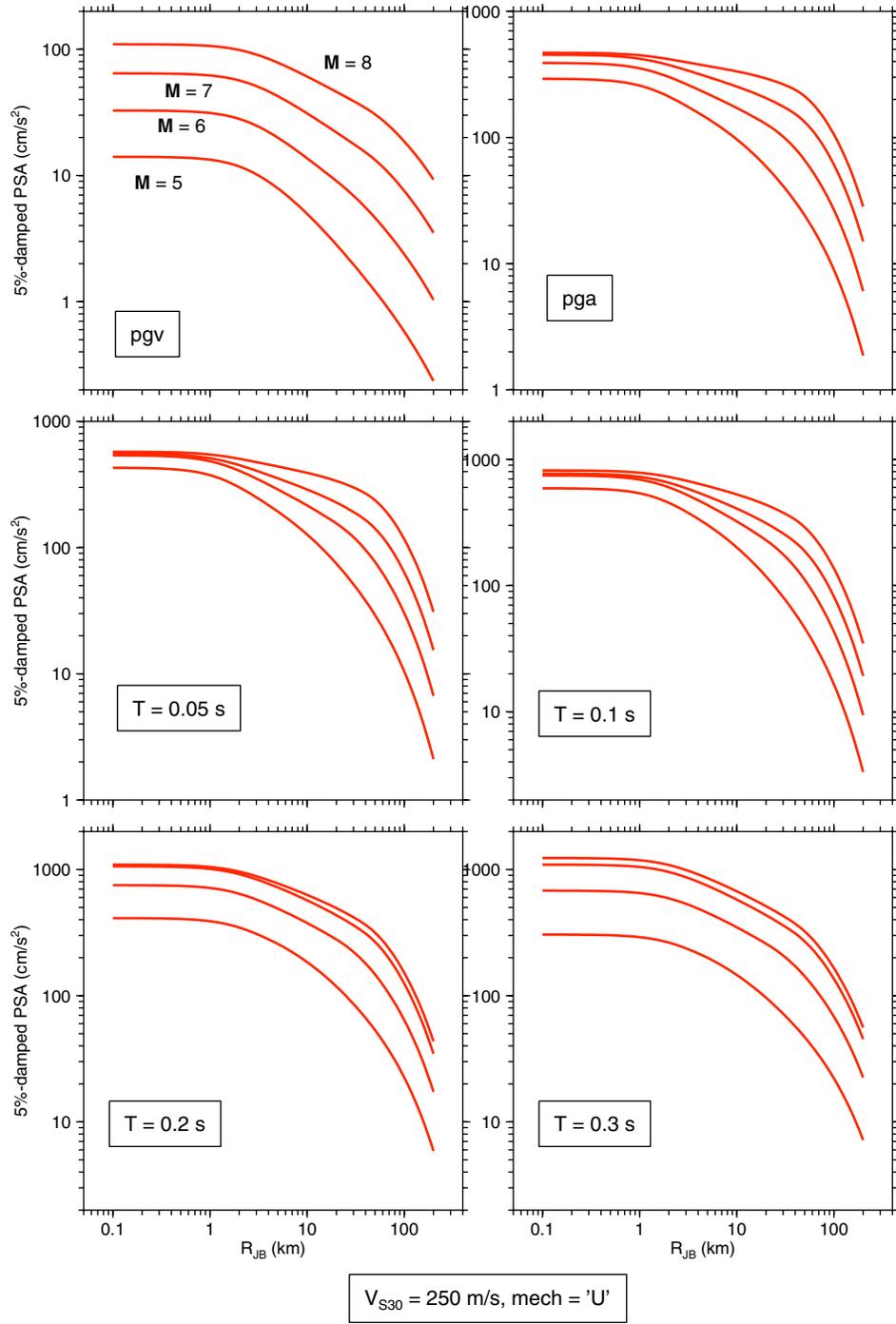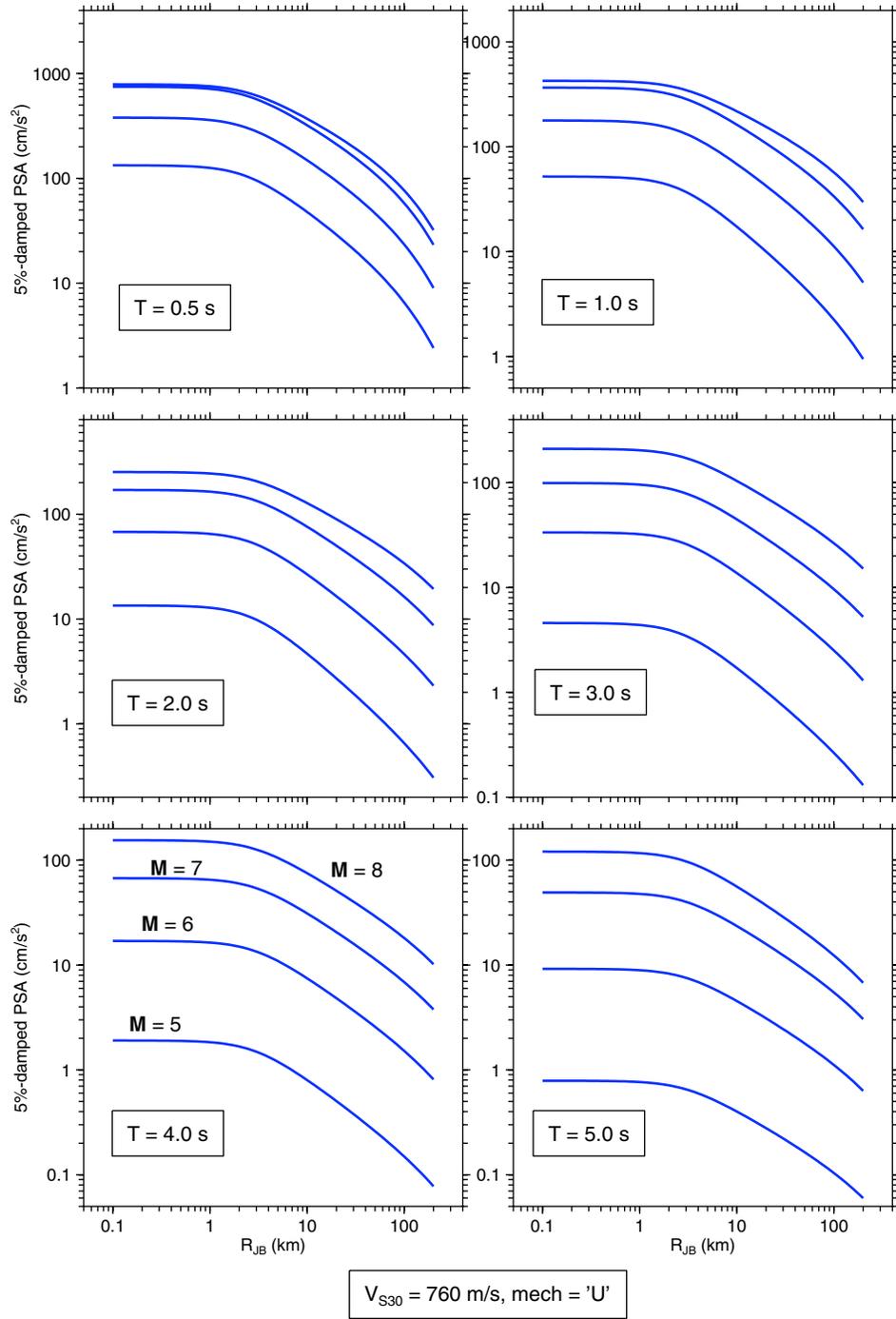
Fig. 4.17—*Continued*
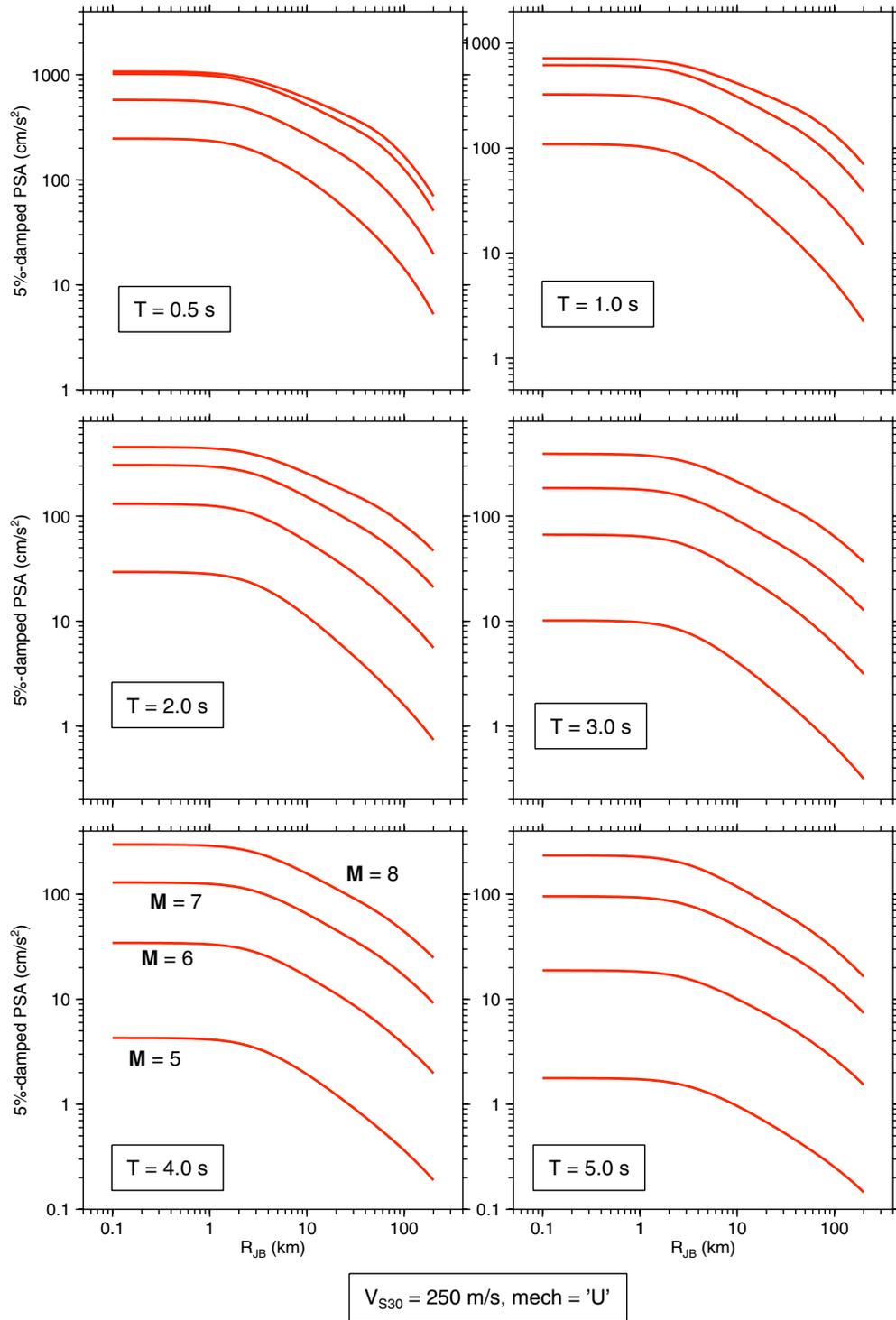
Fig. 4.17—*Continued*
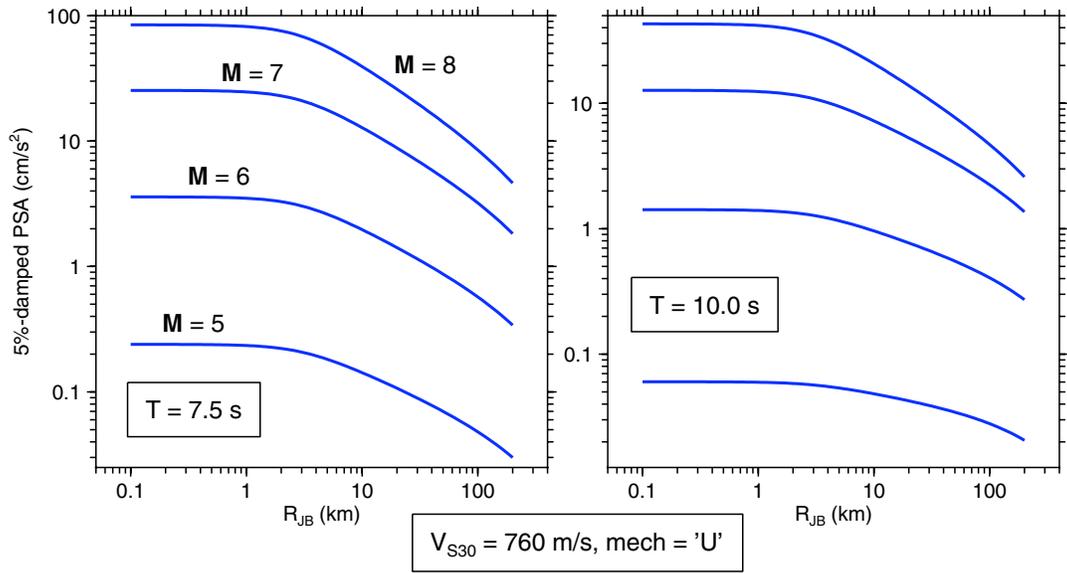
Fig. 4.17—*Continued*

(e)

Fig. 4.17—*Continued*
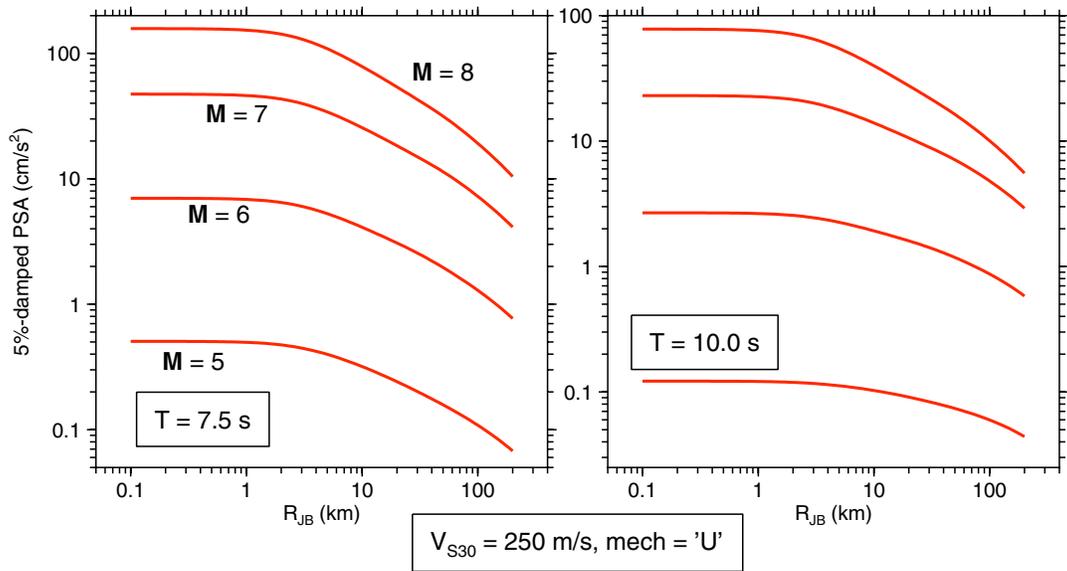
(f)

Fig. 4.17—*Continued*

The effect of V_{S30} on predicted ground motion amplitude is shown more directly in Figure 4.18. Nonlinear soil amplification causes the curves to cross, such that at close distances lower values of V_{S30} (softer sites) will have lower predicted amplitudes than stiffer sites, due to nonlinear deamplification. The effect is more pronounced at short periods than at long periods.
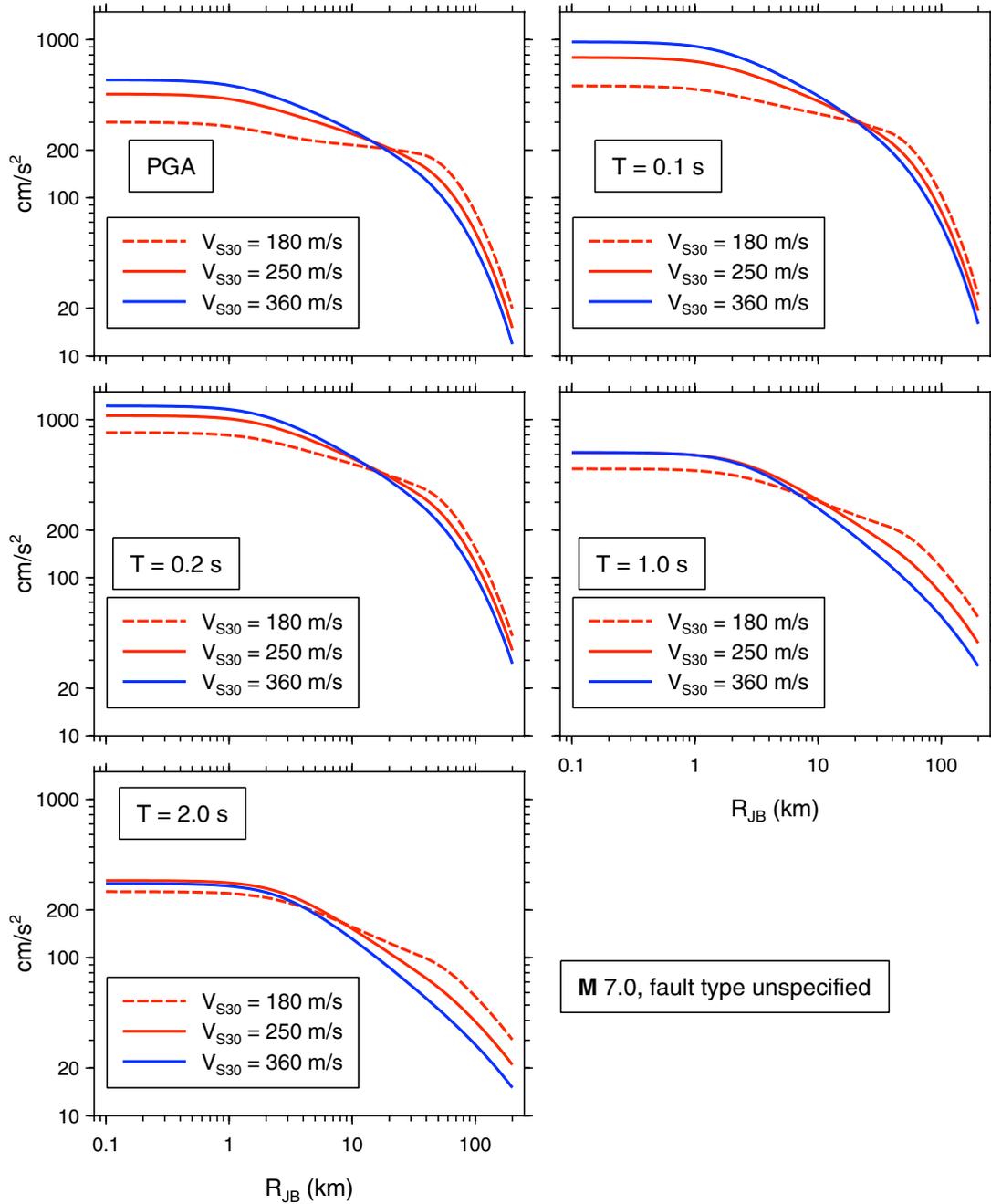
Fig. 4.18 PSA from our equations, as a function of distance; see legend for details.

4.2.6 Surface-Slip vs. No-Surface-Slip Earthquakes

Several authors (e.g., Somerville and Pitarka (2006)) have proposed that the high-frequency ground motions from earthquakes with faults that break to the surface are smaller than from those with faults that remain buried. We search for evidence of this effect in Figures 4.19(a)–(c), which show the event terms from the Stage 1 regression plotted against **M** for the two classes of earthquakes. The first thing to notice is that most surface-slip earthquakes correspond to larger magnitudes, with almost no buried ruptures for magnitude greater than **M** 7. For this reason any reduction in motions for surface-slip earthquakes will be mapped into reduced magnitude scaling in the Stage 2 magnitude regression. In order to differentiate magnitude scaling from the effects of surface versus buried rupture, data from both class of rupture are needed for the same range of magnitudes. As seen in Figures 4.19(a)–(c), it is only for strike-slip earthquakes that there are more than one of each class of earthquake in a common magnitude range (there are several strike-slip events of 5.7–6.7 in both classes). There is no indication for these earthquakes that the event terms are systematically different for the two classes of data. Therefore, there was no need to include dummy variables for surface slip/buried earthquakes in our functional forms. As confidence in simulations from dynamic models of rupture propagation increases, it might be that in the future we will add a buried/surface faulting term to the equations, even though the data do not demand it. By doing so, the apparent saturation of the magnitude scaling would not be as dramatic (i.e., the larger earthquakes are entirely surface slip events, and if these produce smaller ground motions than buried events, as has been suggested by Somerville and colleagues (e.g., Somerville and Pitarka (2006)), then there will be an apparent tendency for saturation if the events are not separated into two classes according to whether they break to the surface or not).
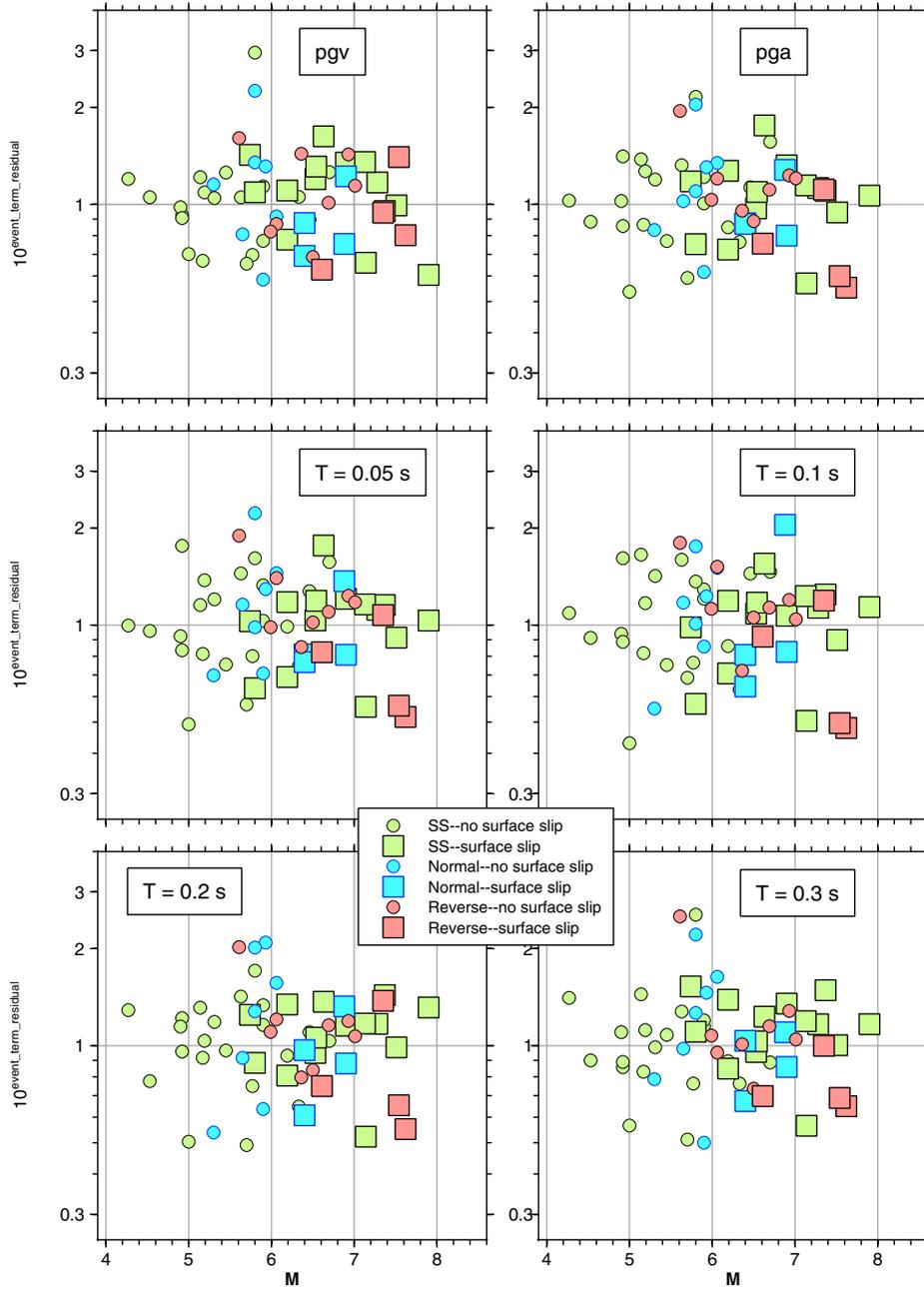
Fig. 4.19 Antilogarithms of event terms, plotted against magnitude and differentiated by events of different fault types, for which faults did or did not break to surface.

74
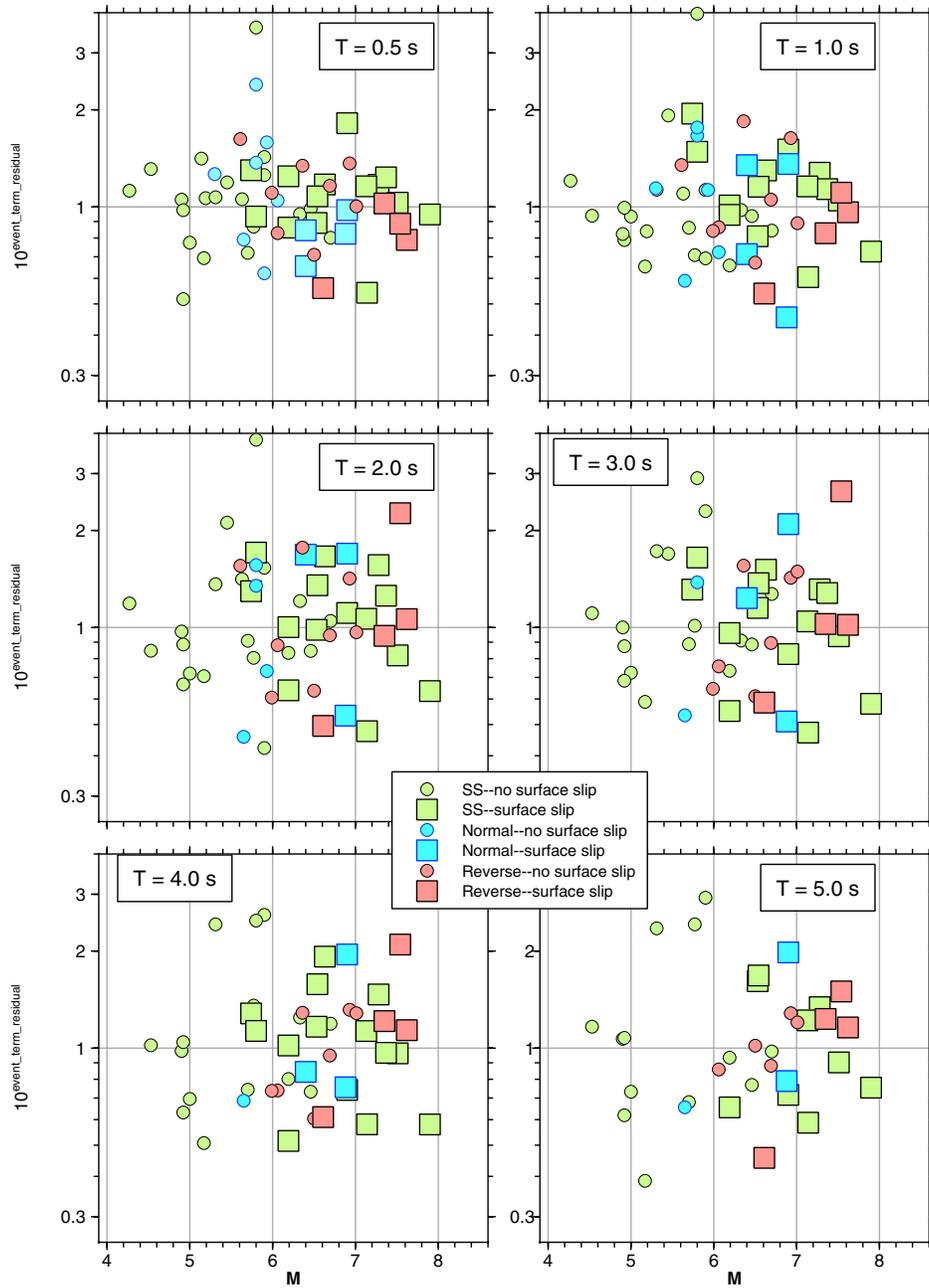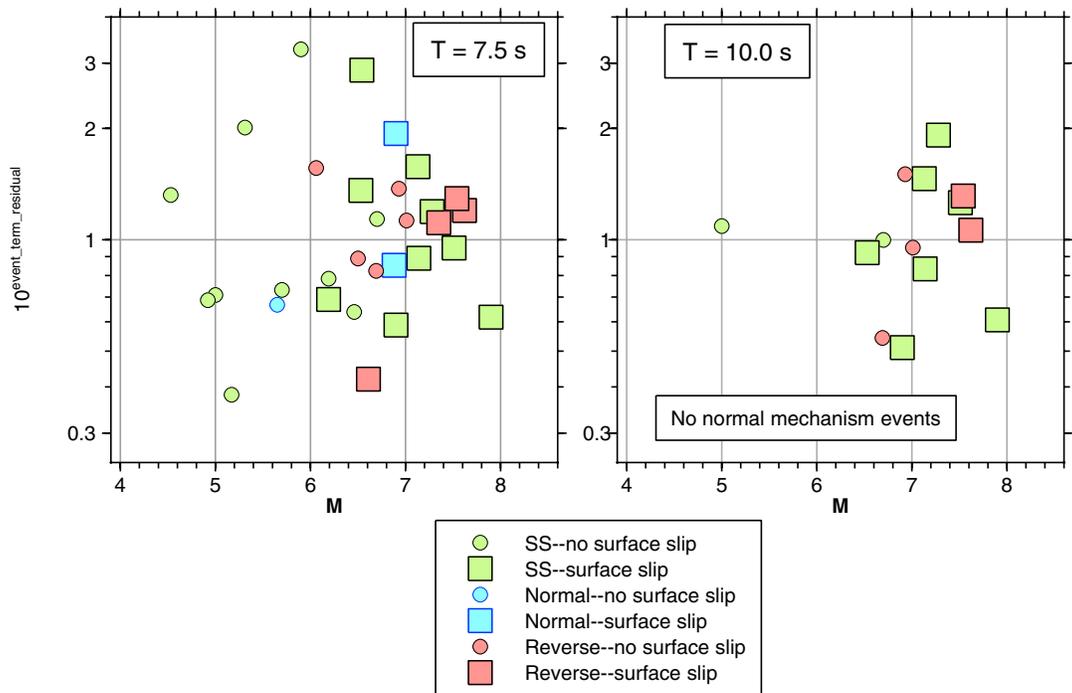
Fig. 4.19—*Continued*

(c)

Fig. 4.19—*Continued*

4.2.7 Dependence of Event Terms on Dip Angle

Figures 4.20(a)–(c) plot the event terms against dip angle. There are no obvious systematic effects of dip angle on the ground motion amplitudes.
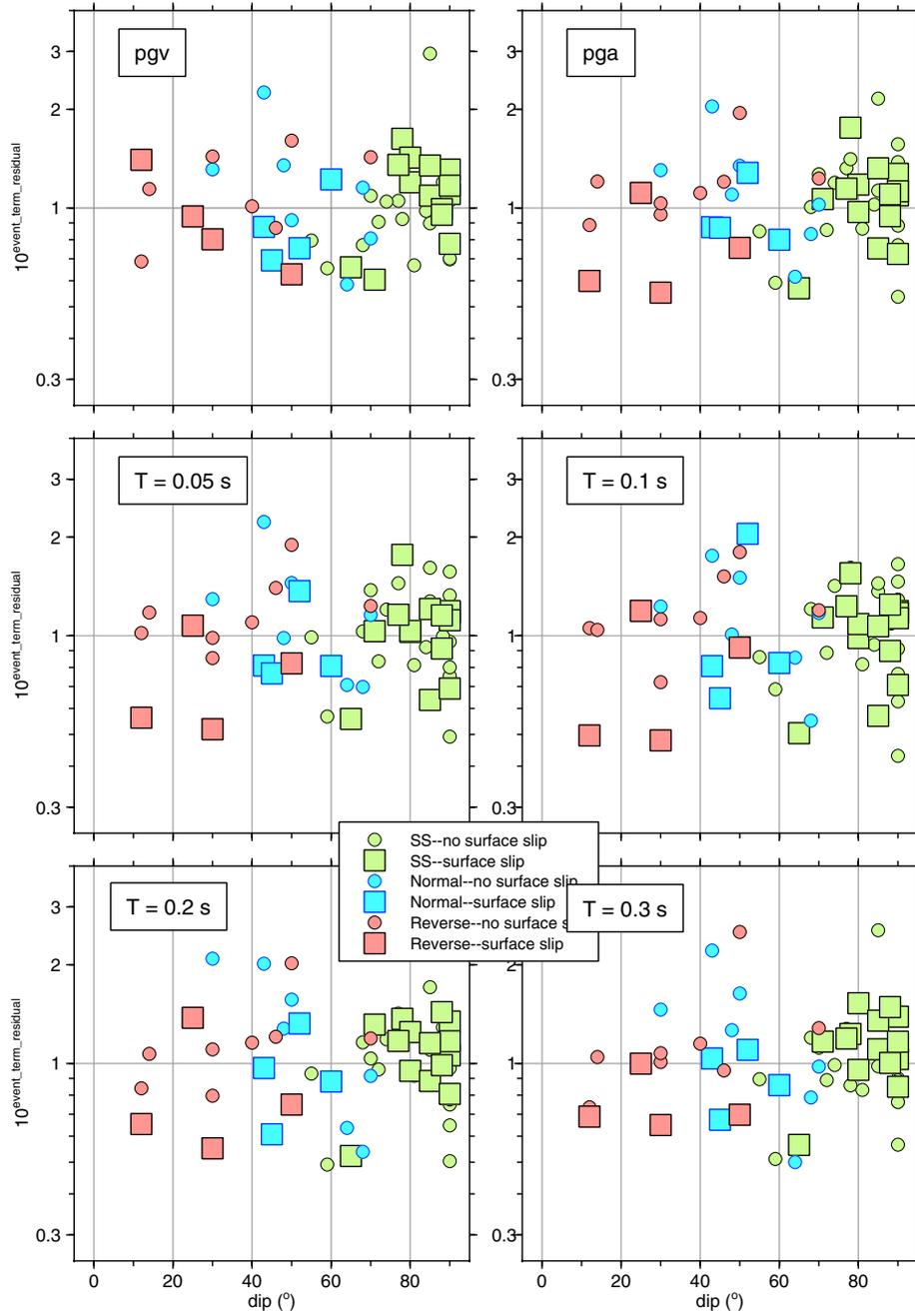
Fig. 4.20 Antilogarithms of event terms, plotted against dip and differentiated by events of different fault types, for which faults did or did not break to surface.

77
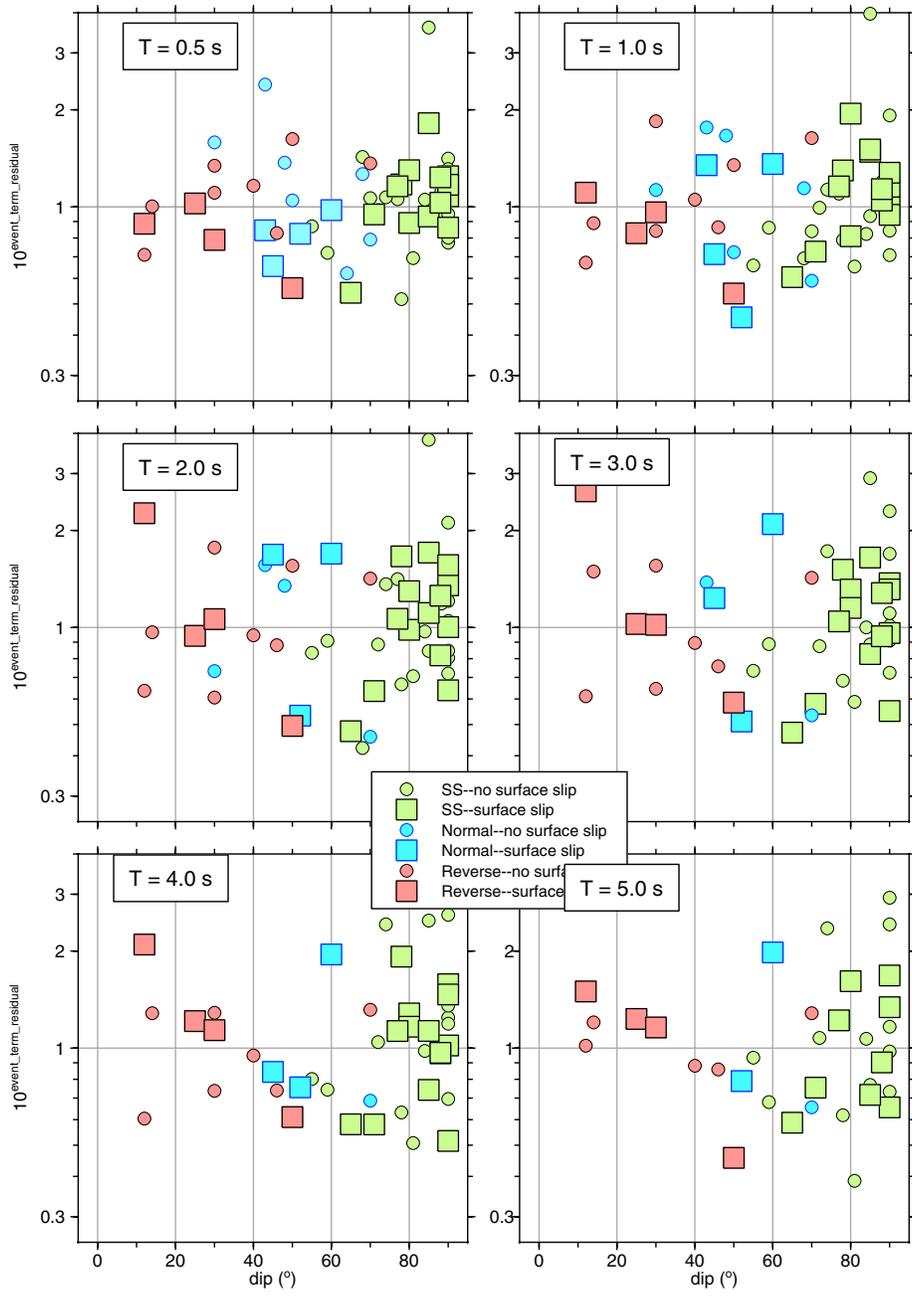
(b)

Fig. 4.20—*Continued*
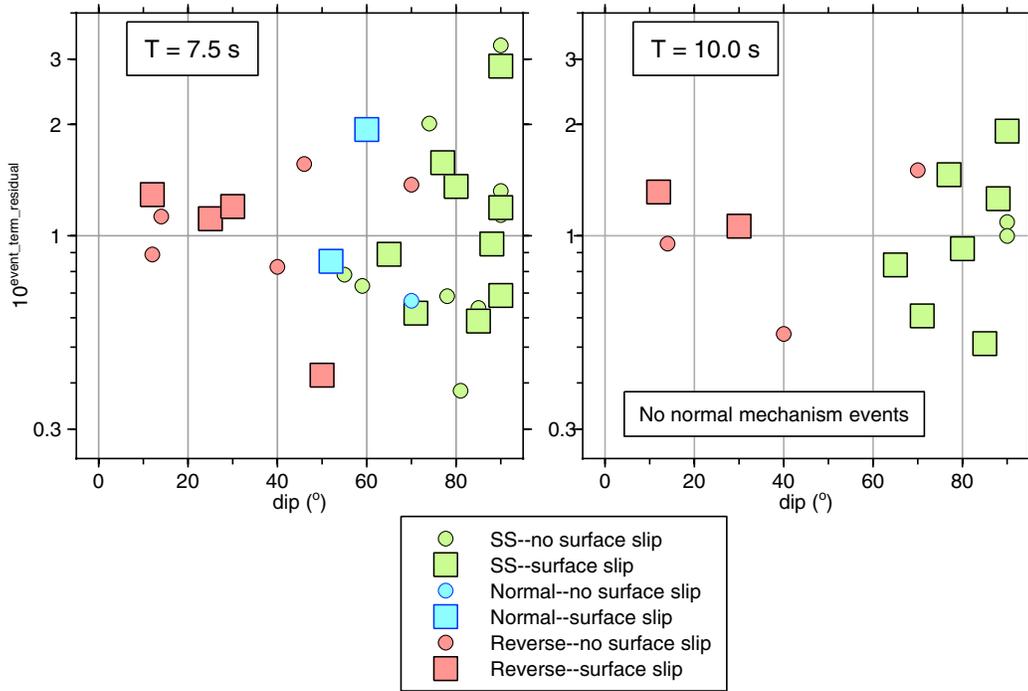
(c)

Fig. 4.20—*Continued*

4.2.8 Dependence of Stage 1 Residuals on *pga4nl*

Our amplification factors were taken from an empirical analysis by Choi and Stewart (2005). There is a large overlap in the dataset they used and in the NGA flatfile, but there are also many small differences, including added data in the NGA flatfile and redeterminations of both ground motion intensity measures and V_{S30}. For these reasons it is important to search for systematic trends in the Stage 1 residuals for different ranges of V_{S30} and for different *pga4nl* (it is best to examine Stage 1 residuals for this analysis to exclude event-to-event variation that may obscure actual trends). This serves as a test of the effectiveness of the applied site-amplification factors in removing site effects. Figures 4.21(a)–(c) show the Stage 1 residuals plotted against *pga4nl*, with the residuals grouped into different bins of V_{S30} (NEHRP site classes). We split the NEHRP class D into two parts in order to see better any systematic trends in this class (about half the data come from this NEHRP class). In addition, we consider only data for $R_{JB} \leq 80$ km to avoid

79

mapping inadequacies in the distance function into systematic trends that might manifest themselves in the site-response functions. Figures 4.21(a)–(c) address the adequacy of the site-response functions by site class (which speaks mainly to the linear component of the correction) and by the strength of shaking (addressing the nonlinear component). Overall, the residuals do not depend on site class or the strength of ground shaking, with some significant apparent exceptions. In particular, the class E ($V_{S30} \leq 180$ m/s) residuals appear to be low (average residual <1) for most periods, indicating an overcorrection of the data to the reference velocity of 760 m/s. In addition, the data with 180 m/s $< V_{S30} \leq 250$ m/s appear to be systematically high for *pga4nl* > 0.1 g, but low for smaller values of *pga4nl*. This suggests that the nonlinear component of the site response may have been overestimated for soft sites (<250 m/s). Future work may be able to improve upon the soil-amplification factors.
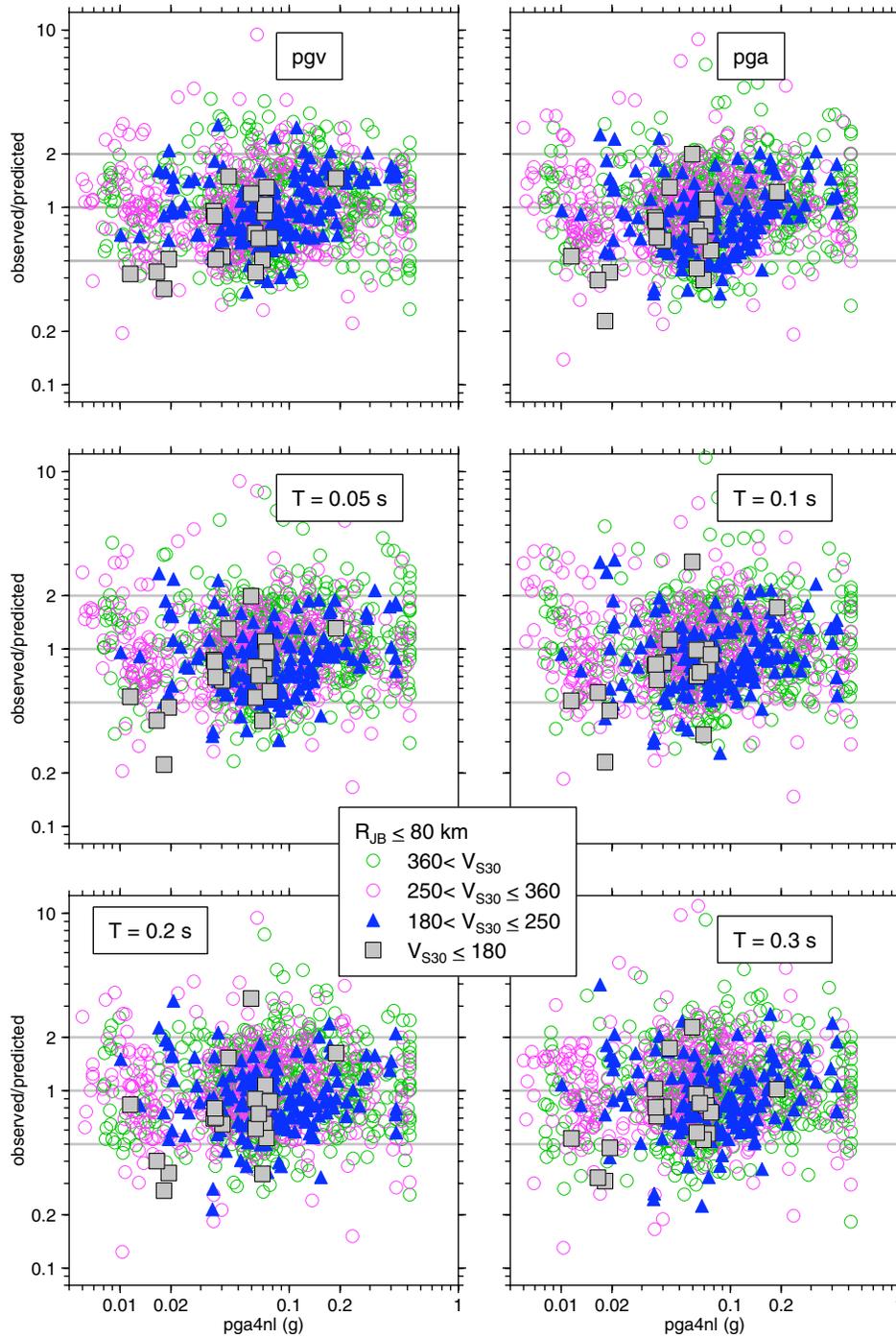
(a)

Fig. 4.21 Stage 1 residuals plotted against pga4nl, differentiated by V_{S30} **, for** $R_{JB} \leq 80$ km **.**
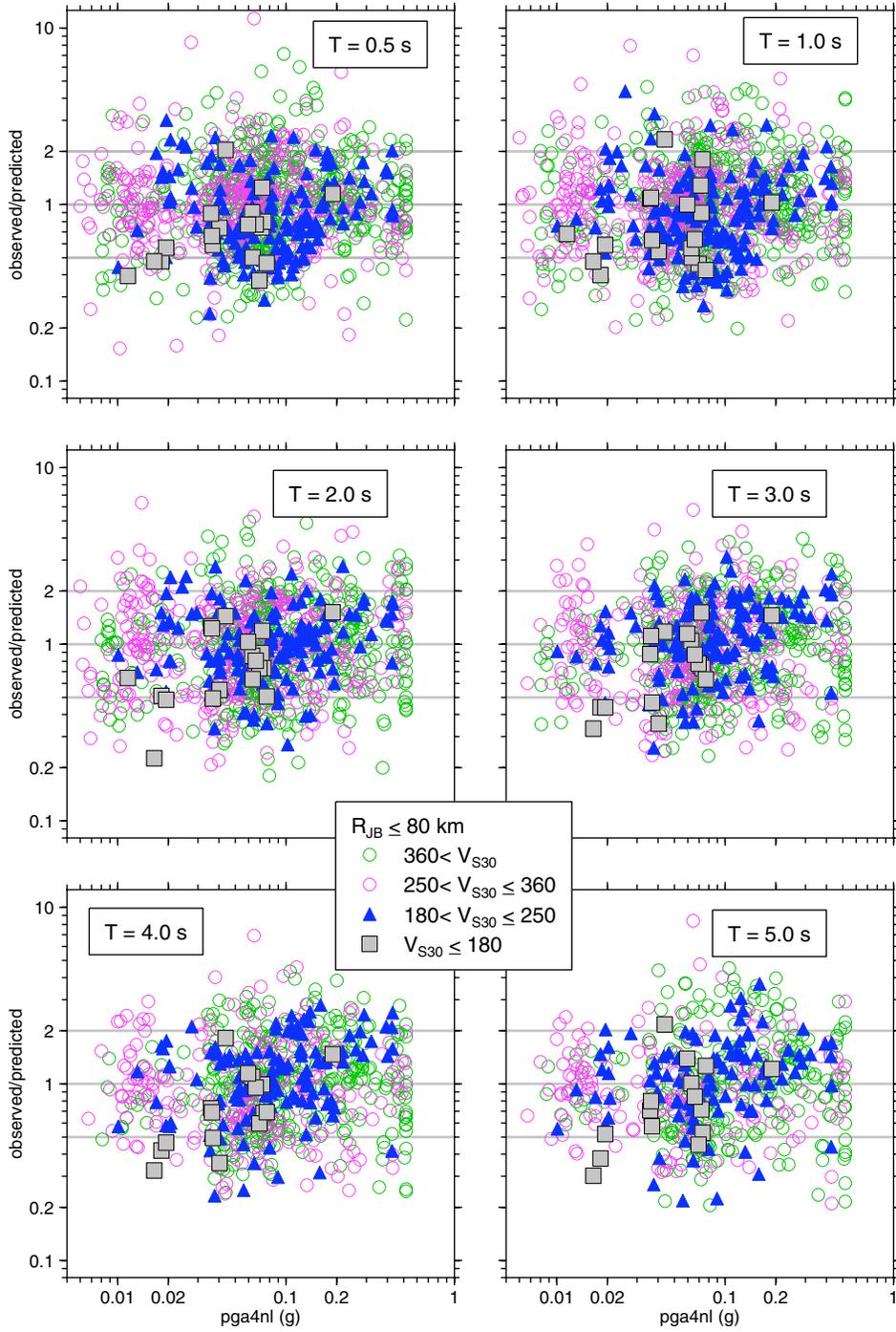
(b)

Fig. 4.21—*Continued*
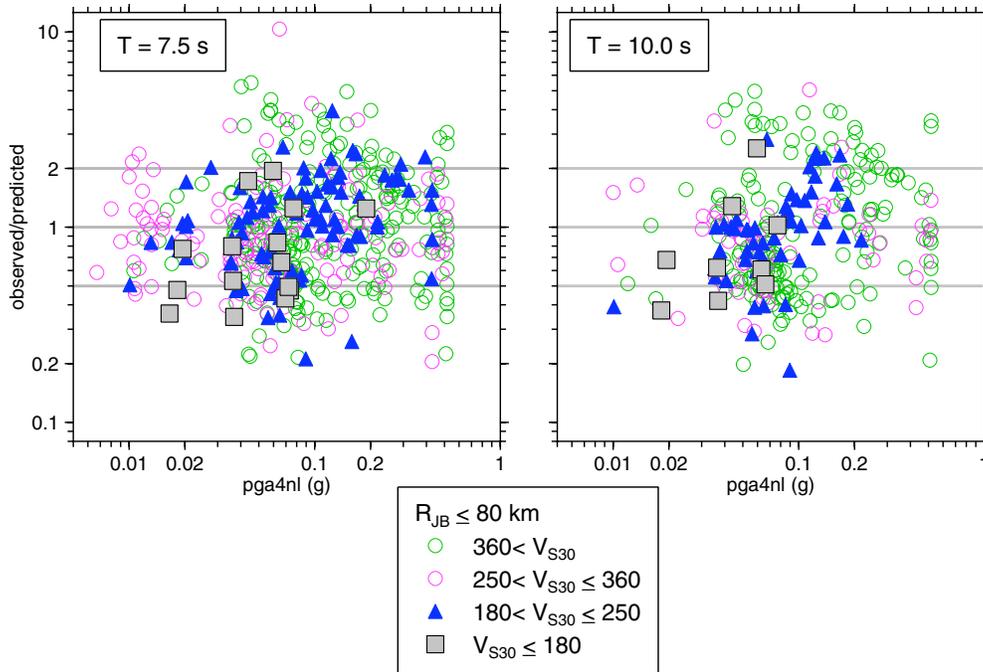
(c)

Fig. 4.21—*Continued*

4.2.9 Dependence of Stage 1 Residuals on Basin Depth

Another ground motion effect that we searched for in the residuals of the Stage 1 regression was that of basin depth. Basin-depth effects on ground motion amplitudes have been reported in empirical studies (Field, 2000), and from simulations (Day et al. 2005; Day et al. 2006). One of the reasons that we did not include a basin-depth term in our equations is indicated in Figure 4.22, which shows the distribution of V_{S30} and two measures of basin depth. The plot shows all data in the NGA flatfile for which both V_{S30} has been measured and basin depth has been estimated. It is clear that the softer sites are in basins, and hence basin depth and V_{S30} are strongly correlated. Therefore any basin depth effect will tend to have been captured by the empirically-determined site amplification. To try to separate the amplification and the basin-depth effects in the data would require use of additional information or assumptions. For example, one could use simulations to estimate the basin-depth effects and incorporate them into the GMPE model. Since we are opting for the simplest equations required by the data, no attempt was made to break down the site-response function into basin depth and the amplification terms.

83

Instead, our equations implicitly capture the basin-depth effect (attributing it to site amplification), provided that applications of our equations are in similar situations for which the data were recorded.
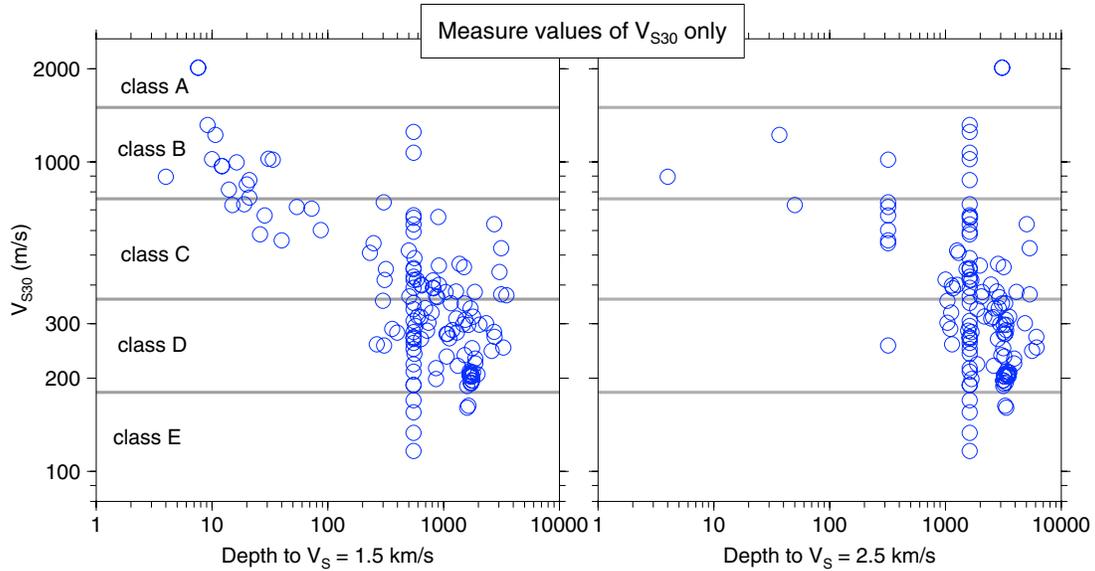
Fig. 4.22 V_{S30} **plotted against two measures of basin depth. All values in NGA flatfile with basin depths and measured values of** V_{S30} **shown.**

To show that there is no significant basin-depth effect that is not already captured implicitly via the site-amplification function, Figures 4.23–4.28 plot the Stage 1 residuals against the depth to $V_{S30} = 1.5 \, \text{km/s}$ (plots are shown in pairs, for all distances and for $R_{JB} \leq 80 \, \text{km}$). There is no obvious dependence of the residuals on basin depth. This is not surprising in light of the observations made above regarding the correlation between basin parameters and V_{S30}. (Note: similar results were obtained if the depth to 2.5 m/s was used as the measure of basin depth.)
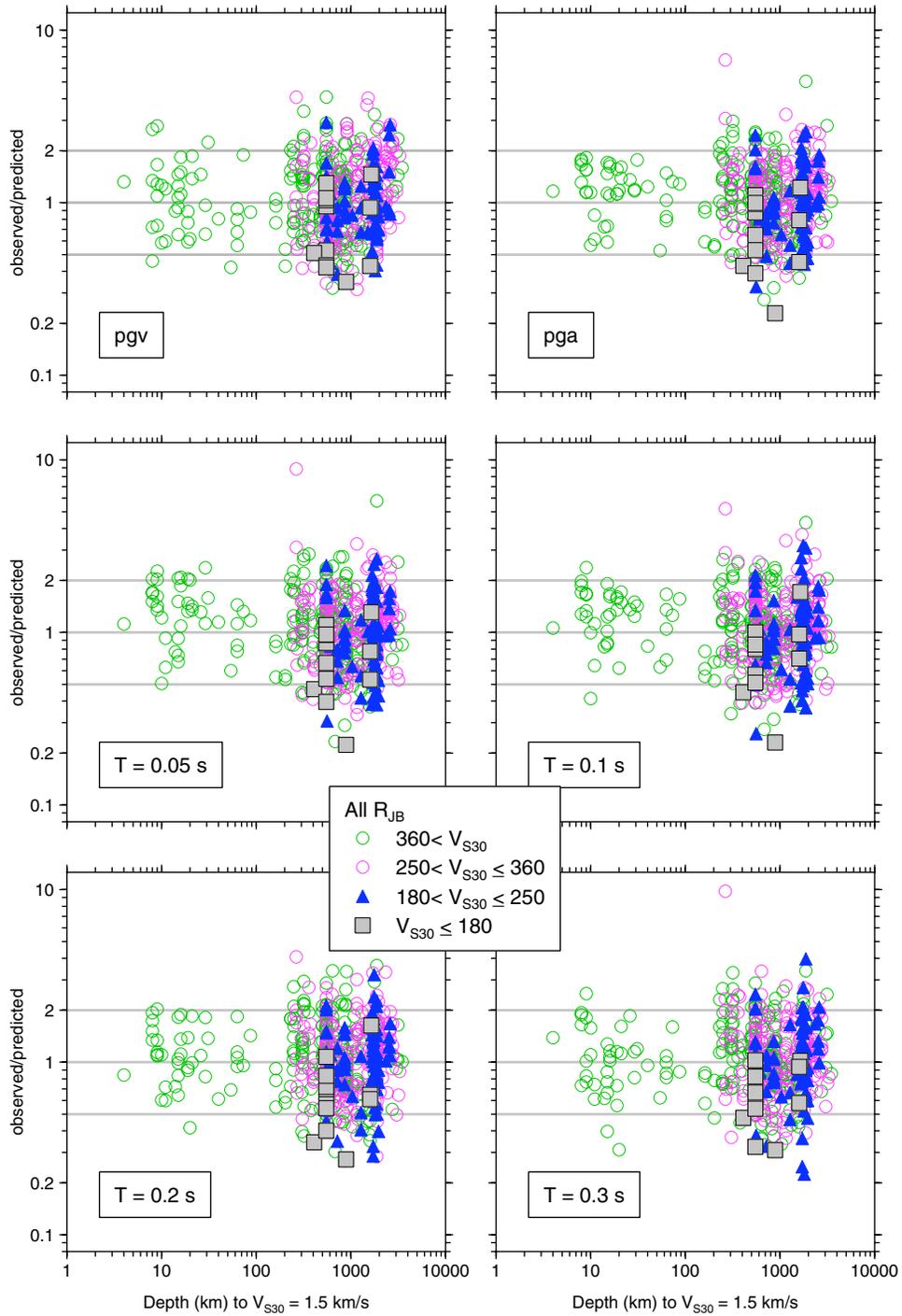
Fig. 4.23 **Stage 1 residuals plotted against depth to** $V_S = 1.5\ \text{km/s}$ **, differentiated by** V_{S30} **, for all distances.**
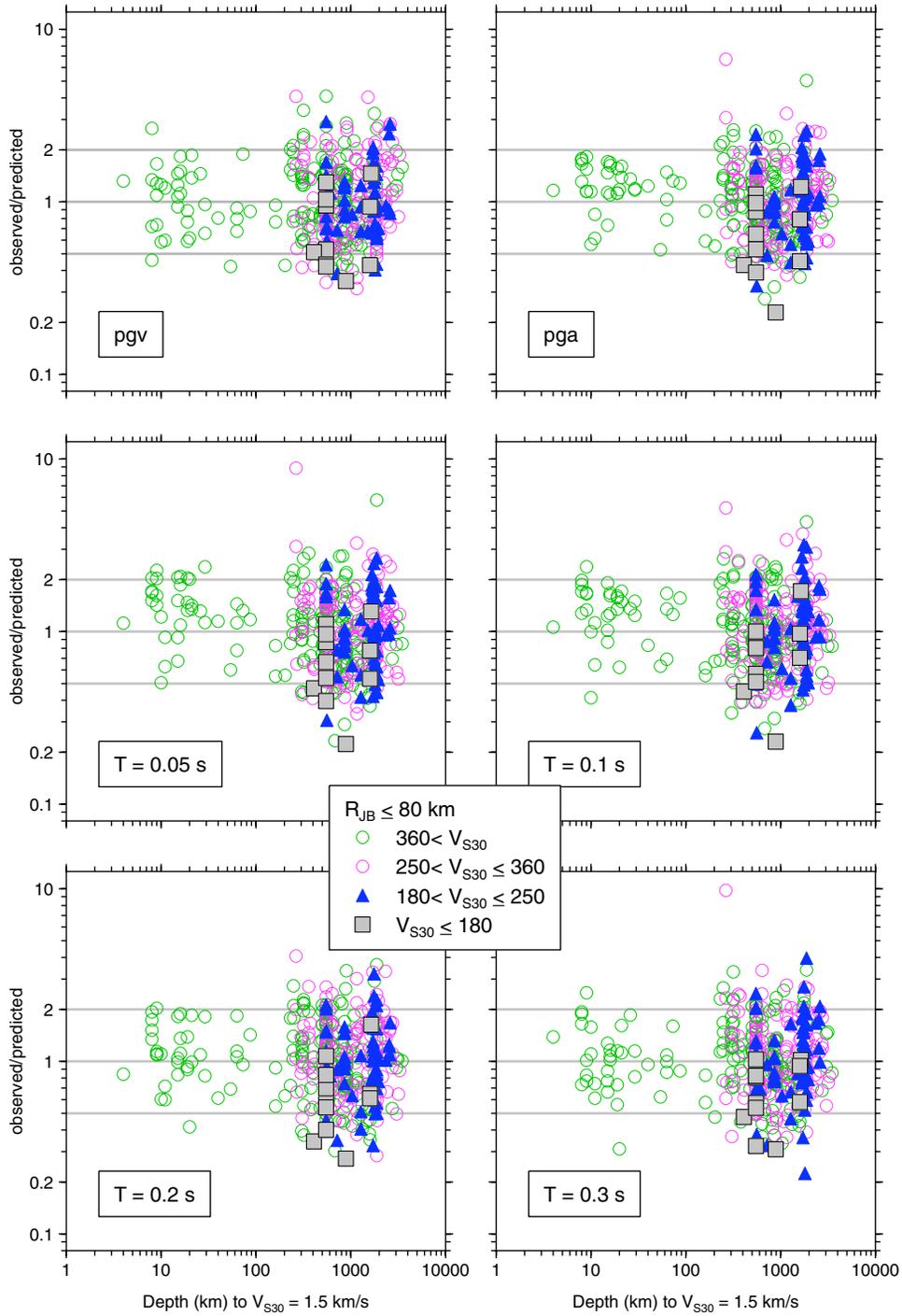
Fig. 4.24 **Stage 1 residuals plotted against depth to** $V_s = 1.5$ km/s **, differentiated by** V_{S30} **, for** $R_{JB} \leq 80$ km **.**
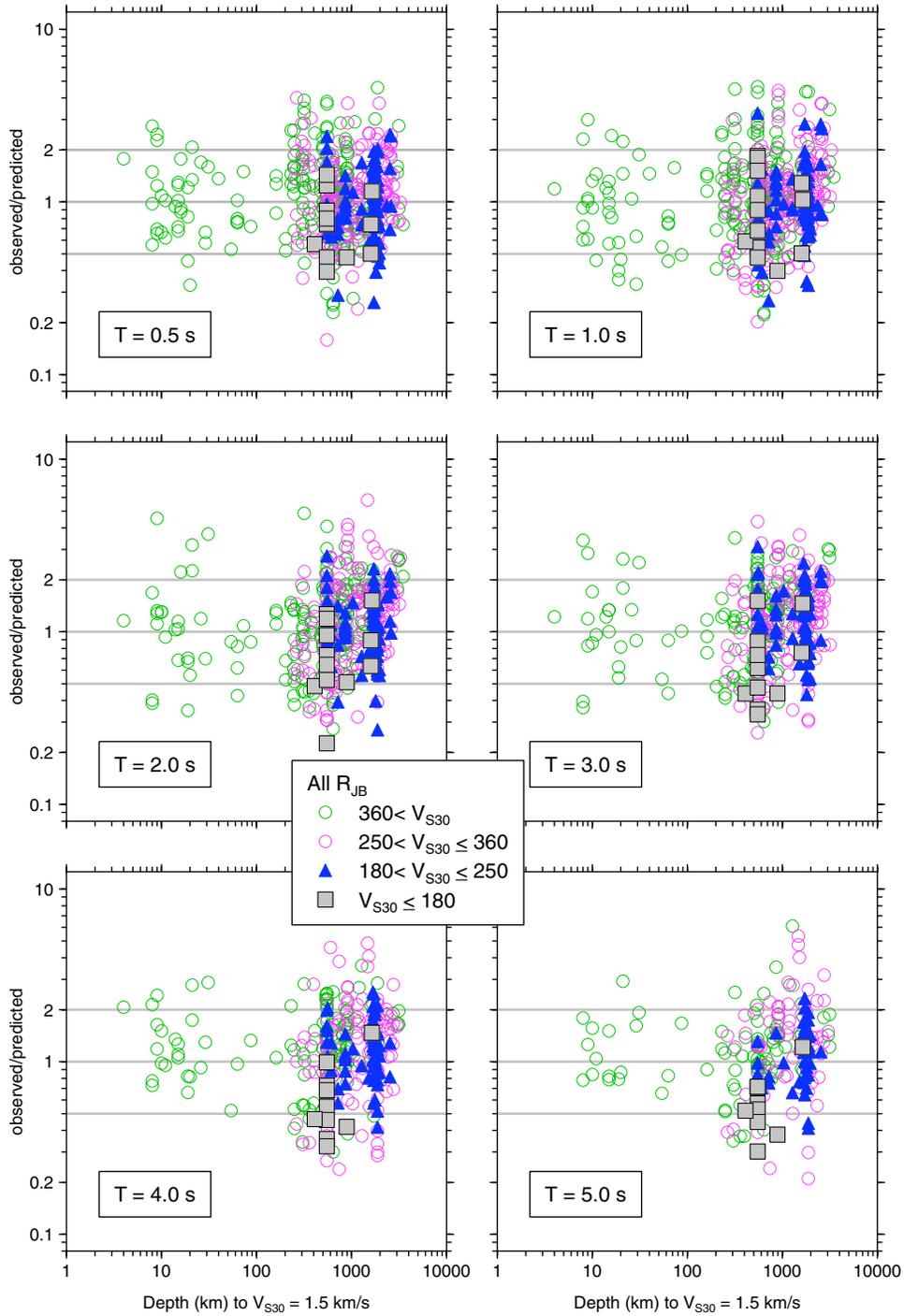
Fig. 4.25   Stage 1 residuals plotted against depth to $V_S = 1.5$ km/s , differentiated by V_{S30}, for all distances.
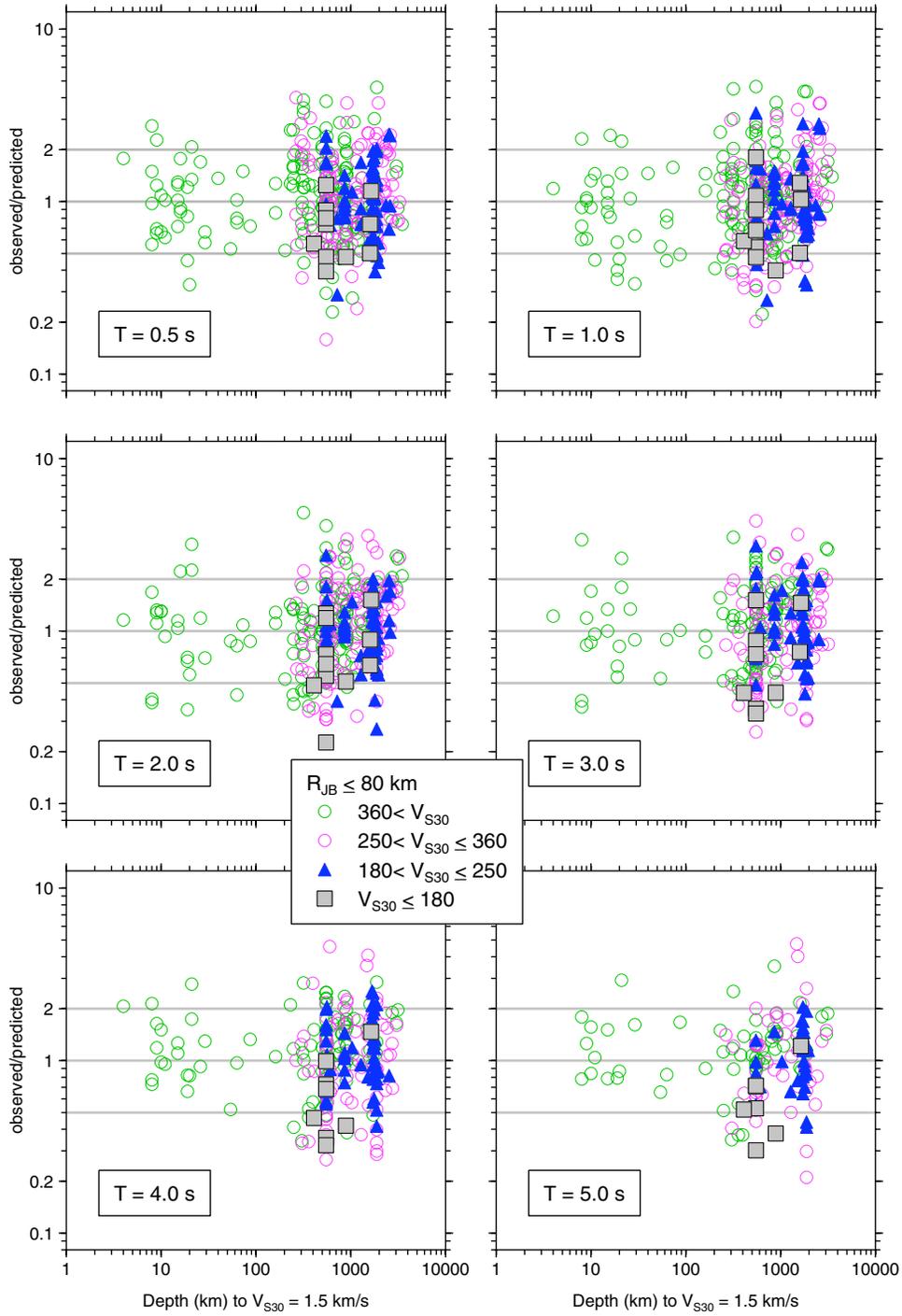
Fig. 4.26 **Stage 1 residuals plotted against depth to** $V_S = 1.5 \, \text{km/s}$ **, differentiated by** V_{S30} **, for** $R_{JB} \leq 80 \, \text{km}$ **.**
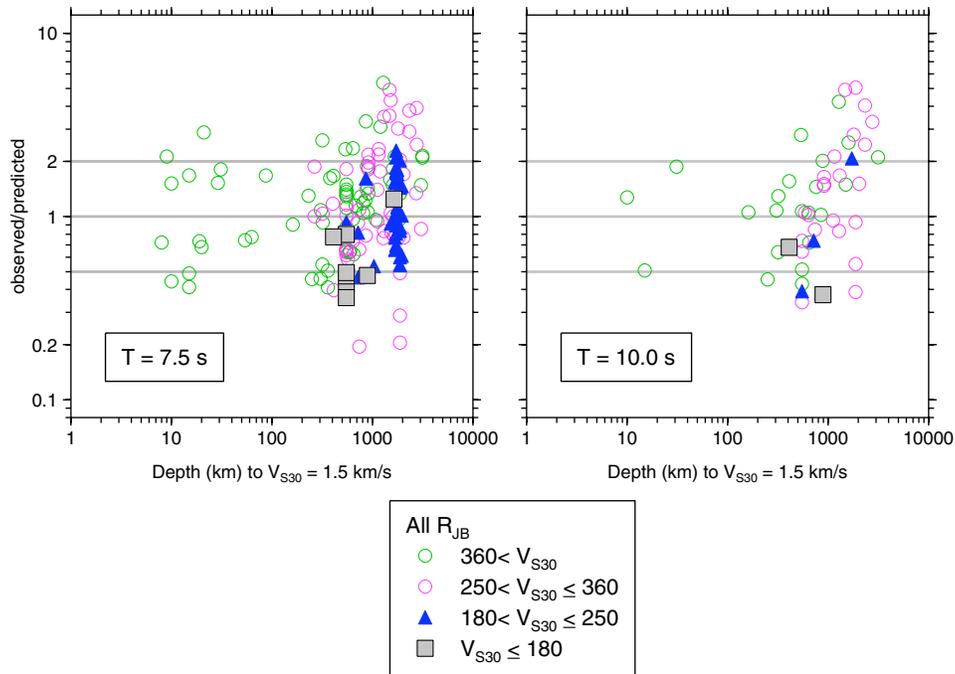
Fig. 4.27 Stage 1 residuals plotted against depth to $V_S = 1.5\,\text{km/s}$, differentiated by V_{S30}, for all distances.
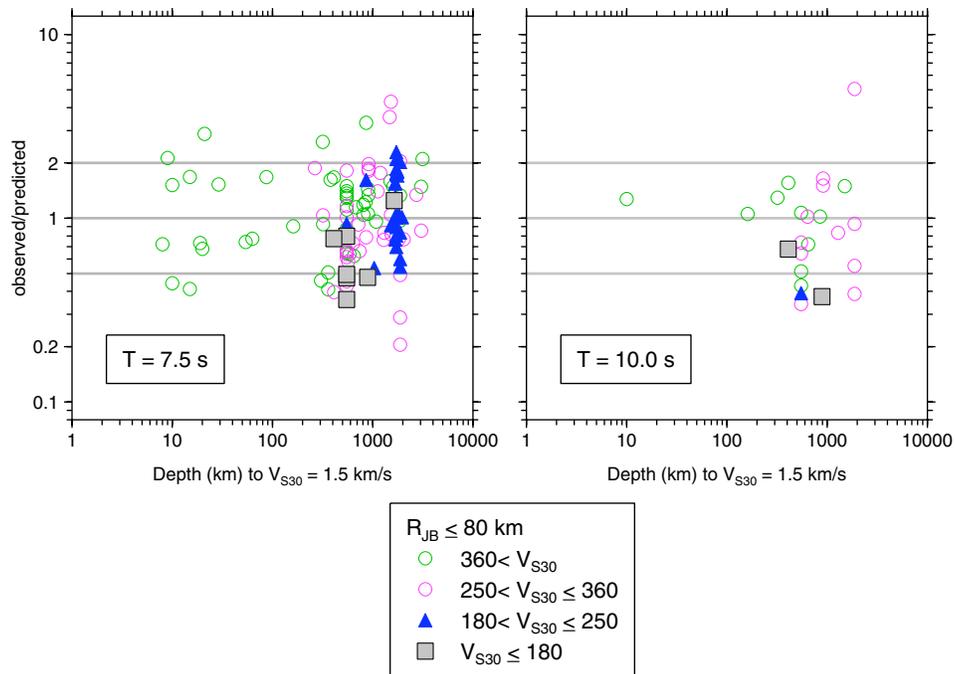
Fig. 4.28 Stage 1 residuals plotted against depth to $V_S = 1.5\,\text{km/s}$, differentiated by V_{S30}, for $R_{JB} \le 80\,\text{km}$.

4.2.10 Comparison of GMPEs from One- and Two-Stage Regressions

We used the two-stage regression method discussed in Joyner and Boore (1993, 1994) as it was most computationally convenient; it has been previously shown that one-stage and two-stage regression methods (when properly implemented) are equivalent (Joyner and Boore 1993, 1994). Dr. John Douglas has implemented the Joyner and Boore one-stage regression scheme in Matlab. Prof. Sinan Akkar revised the program to accommodate our functional form and used it to compute regression coefficients. The ground motions predicted from our equations at a sample period (T= 5 s), based on the two-stage method, are compared with those from the equations developed from the one-stage regression (as implemented by Douglas and Akkar) in Figure 4.29. The comparison is excellent, which serves as a useful check on the regression results.
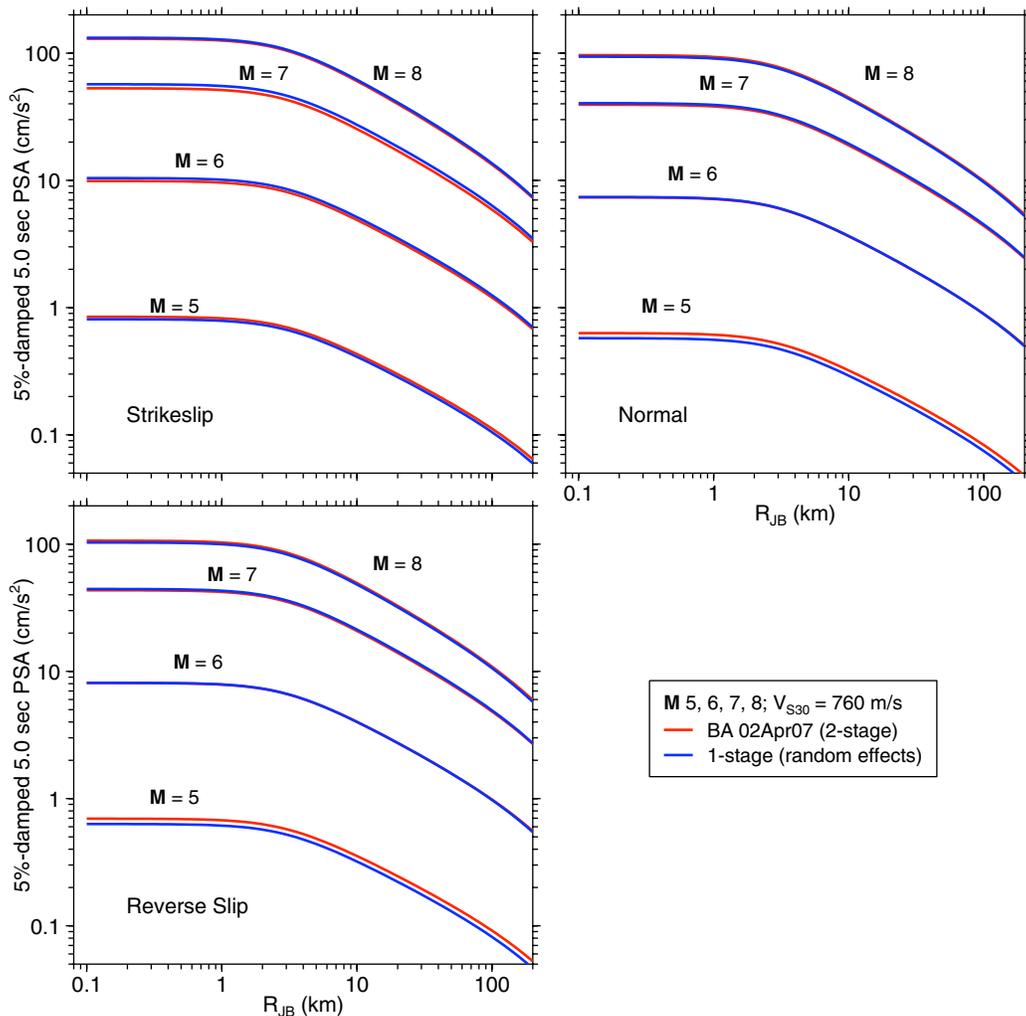
Fig. 4.29 Comparison of PSA from equations developed using one-stage weighted regression and two-stage regression (using algorithms of Joyner and Boore 1993, 1994).

4.2.11 Comparison of GMPEs Developed with and without 1999 Chi-Chi Earthquake

Because the Chi-Chi earthquake forms a significant fraction of the dataset we used in developing our equations, it is important to see how the equations would change if the data from the Chi-Chi earthquake were eliminated from both the Stage 1 and the Stage 2 regressions. We therefore repeated the analysis without the Chi-Chi data. Figure 4.30 compares selected ground motion intensity measures given by the two sets of equations. The figures also show the percent of data used in the regression analysis from the Chi-Chi earthquake (the number of Chi-Chi recordings is the numerator of the ratio). It is clear that the fraction of the dataset contributed by the Chi-Chi earthquake increases with period, reaching 64% of the dataset for a period of 10 s. For this reason it is not surprising that the predictions of 10 s PSA are quite different for the equations developed with and without the Chi-Chi data (the ordinate scales of all graphs in Figure 4.30 are the same, to facilitate comparisons of the relations between the two predictions between periods). At intermediate to short periods, the differences are not dramatic, but are significant even at small magnitudes (despite the fact that we include only the Chi-Chi mainshock, not its aftershocks). We think this is because the Chi-Chi earthquake is very well recorded, and thus dominates the Stage 1 regression, for which each recording of an earthquake has equal weight in determining the distance terms in the equations. These distance terms then affect the event terms, and this in turn controls the magnitude scaling. We conclude that although the Chi-Chi earthquake affects the GMPEs, it is only a major controlling factor in the predictions of PSA at periods of greater than 5 s.
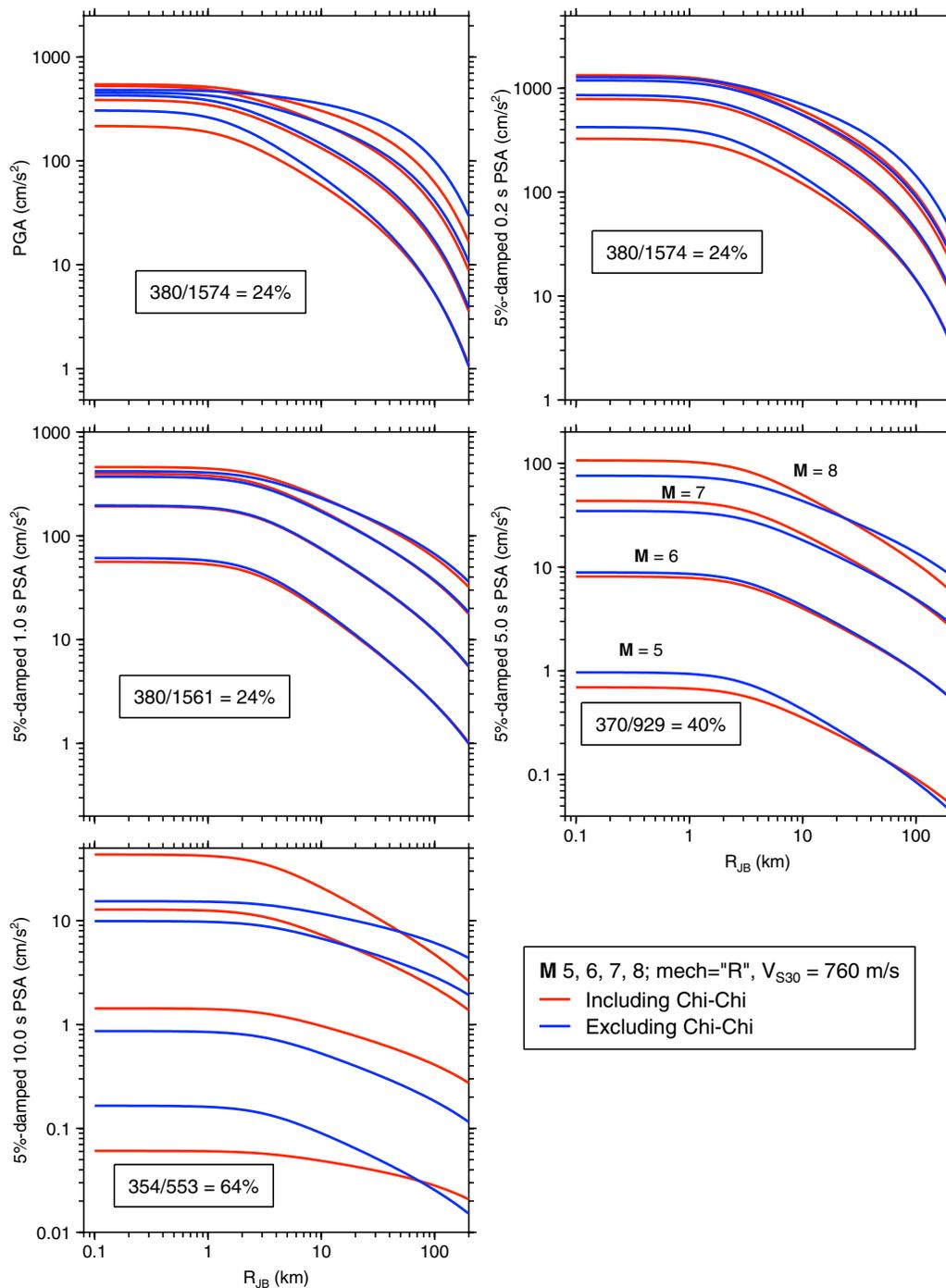
Fig. 4.30 Comparisons of PSA from equations developed with and without 1999 Chi-Chi mainshock. Seismic intensity measure is given by ordinate title. Ratios are number of Chi-Chi recordings used to develop final equations divided by total number of recordings.

92

4.2.12 Comparison of BA07 and BJF97 GMPEs

It is interesting to compare our new predicted ground motions with those from the Boore et al. (1997) (BJF97) equations. Figure 4.31 compares the magnitude-distance distribution of the data used in each study. It is apparent that many more data are used in the new equations; the NGA data fill gaps at close distances for all magnitudes, add more data at small magnitudes at all distances, add data for large magnitudes, and fill out the distribution so that no longer is there a strong correlation between distance and magnitude in the dataset. For this reason, the new equations provide a more robust prediction of ground motion amplitudes over a wide range of magnitudes and distances.
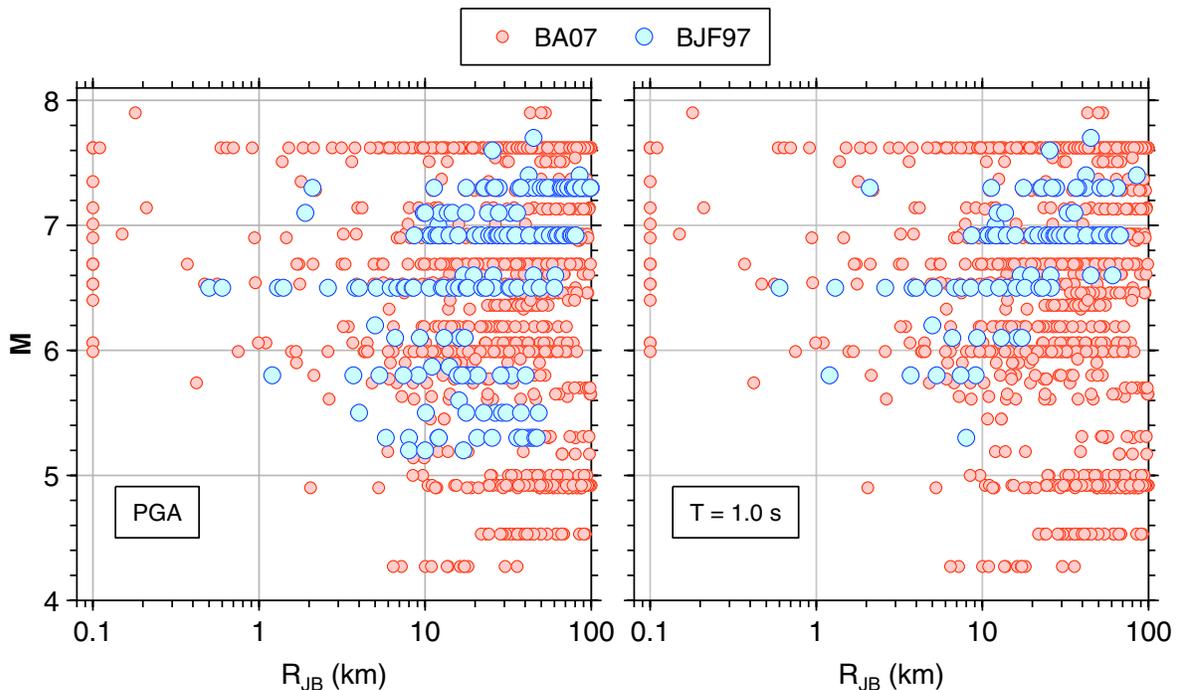
Fig. 4.31 Comparison of magnitude-distance distribution of data used by BJF97 and by us in developing GMPEs, for PGA and 1.0 s PSA.

We compare predicted ground motions from the BJF97 equations and from our current equations in Figure 4.32, for $V_{S30} = 420$ m/s, which is near the weighted geometric mean of the velocities for the sites used in the BJF97 regression analysis. We use the same scale for the ordinates in all graphs. The new and old equations predict similar amplitudes for $\mathbf{M}$ and R_{JB} ranges for which data were available for the BJF97 equation development. Large differences

93

occur in regions of the magnitude-distance space for which data were not available in BJF97; the differences in the predicted values of seismic ground motion intensity are largely attributable to the overly simplified distance-independent magnitude scaling used in the BJF97 equations.
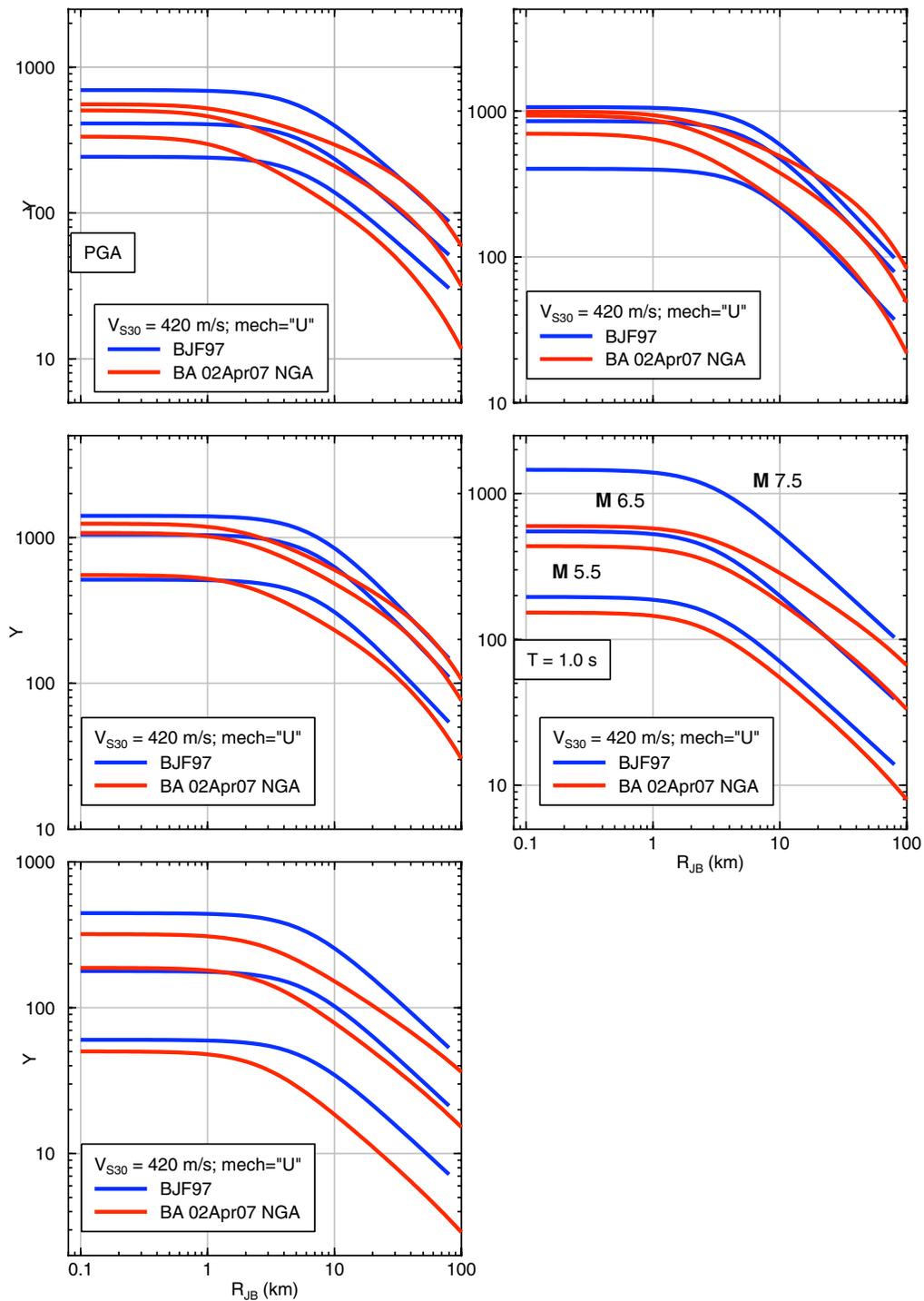
Fig. 4.32 Comparisons of PSA from BJF97 equations and our new equations.

At all periods, the new equations predict significantly smaller motions than do the BJF97 equations for large magnitudes. This is probably the most important change in the new equations compared to the old equations. The difference in the predicted motions is particularly large for $T = 1\,\text{s}$ and $\mathbf{M} = 7.5$. Almost no data were available in BJF97 for $\mathbf{M}\sim7.5$ and $R_{JB} < 10\,\text{km}$ (see Fig. 4.31), so discrepancies are not surprising. The BJF97 data were for R_{JB} centered about 30 km. The discrepancy between the predictions from the BJF97 and the new equations is not nearly as strong for R_{JB} near 30 km as it is for $R_{JB} < 10\,\text{km}$. Observed differences at $R_{JB} \approx 30\,\text{km}$ are likely due to including more data for large earthquakes in our current equations. The values of the BJF97 motions at close distances are strongly controlled by the assumption of distance-independent $\mathbf{M}$ scaling (and therefore the scaling at close distances is driven by the $R_{JB} \approx 30\,\text{km}$ data). The current equations allow for the $\mathbf{M}$-dependent distance scaling.

A comparison of aleatory uncertainties for the new equations and for the BJF97 equations is given in Table 4.6. Note that the total aleatory uncertainties, as well as the intra- and inter-event uncertainties are significantly larger for the new equations. The larger uncertainties will offset to some extent the smaller ground motions for large magnitudes in the construction of seismic hazard maps.

Table 4.6 Comparison of intra-event (σ), inter-event (τ), and total (σ$_T$) standard errors for BA 02Apr07 (mechanism specified) and Boore et al. (1997) equations. For latter, intra-event error is S1, which does not include component-to-component variation. This is appropriate in view of measure of ground motion intensity being used in this report.

per	σ: ba_02apr07	σ: bjf97	τ: ba_02apr07	τ: bjf97	σ$_T$: ba_02apr07	σ$_T$: bjf97
pga	0.502	0.431	0.260	0.184	0.564	0.469
0.10	0.520	0.440	0.318	0.000	0.608	0.440
0.20	0.523	0.435	0.288	0.009	0.596	0.435
0.30	0.546	0.440	0.269	0.048	0.608	0.443
0.50	0.555	0.454	0.265	0.115	0.615	0.468
1.00	0.573	0.474	0.302	0.214	0.647	0.520
2.00	0.580	0.495	0.389	0.276	0.700	0.567

4.2.13 Some Comments on Pseudo-Depth Variable *h*

There are correlations between many of the variables in the prediction equations; these correlations can affect the reliability of the GMPEs, especially when applied in magnitude-distance ranges with few data. A significant correlation issue involves the pseudo-depth variable *h*. Figure 4.33 shows *h* determined from the extended four-event dataset that we used to explore the anelastic attenuation coefficient, as determined under different assumptions about the geometrical spreading and anelastic distance-scaling coefficients. The largest values of *h* are for regressions assuming no anelastic attenuation, in which case the geometrical spreading term c_1 is large and negative (approximately -1.5 for the periods shown). On the other hand, when c_1 is constrained to be -1.0, -0.8, and -0.5, the values of *h* decrease systematically. Thus the value of *h* is linked to the geometric spreading term.
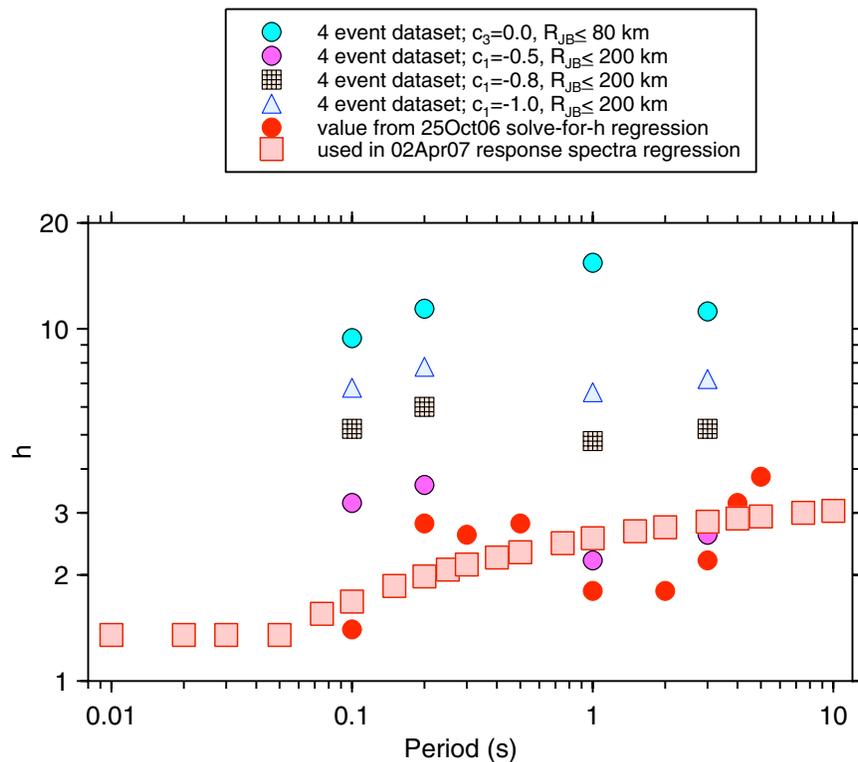
Fig. 4.33   Pseudo-depth variable from regressions on extended four-event dataset, compared with values from NGA dataset

In addition to the correlations between h, c_1, and c_3 just demonstrated, we notice an inconsistency between values of h that we determined from the four-event regressions and those subsequently determined from the regression on our subset of the entire NGA dataset. Recall that in order to constrain h to be a smooth and well-behaved function, we performed a regression of the NGA dataset in which h was a free parameter, but in which we constrained c_3; the constrained c_3 values were associated with $c_1 = -0.8$ in the four-event database that we used to study attenuation. We then defined a smooth function for h based on these results. From Figure 4.5, the effective geometrical spreading factor for our equations is somewhere between -0.5 and -0.8 for the magnitudes in the extended four-event dataset. The values of h for the four-event dataset, however, are larger than those obtained from regression of the NGA dataset (Fig. 4.8). At one NGA Developer's workshop, N. Abrahamson suggested that the relatively small value of h in our equations might be a consequence of not including a hanging wall/footwall term in our equations. It is possible that high values of ground motion on the hanging wall close to the fault outcrop might force small values of h. In future work we will investigate this possibility by determining h using only strike-slip earthquakes.

4.2.14 Comparison of BA07 and Data from Four Earthquakes Wholly or Largely Missing from NGA Flatfile

In this section the ground motion predictions from our equations (BA07) are checked with data wholly or largely missing from the NGA flatfile. These earthquakes, discussed before, are the 2001 Anza, 2002 Yorba Linda, 2003 Big Bear City, and 2004 Parkfield earthquakes. Figures 4.34–4.35 show the comparisons for the first three earthquakes and with the Parkfield earthquake, respectively. The comparisons are relatively good, but recall that the data in the figures were used in deriving the c_3 coefficient. It is worth remembering that the NGA dataset flatfile contains many fewer points for the three events than shown in Figure 4.34 (see Table 4.1) and no data from the Parkfield earthquake. For this reason, Figures 4.34–4.35 constitute a check of the predictions against data not used in the derivation of the equations (other than the coefficient c_3).
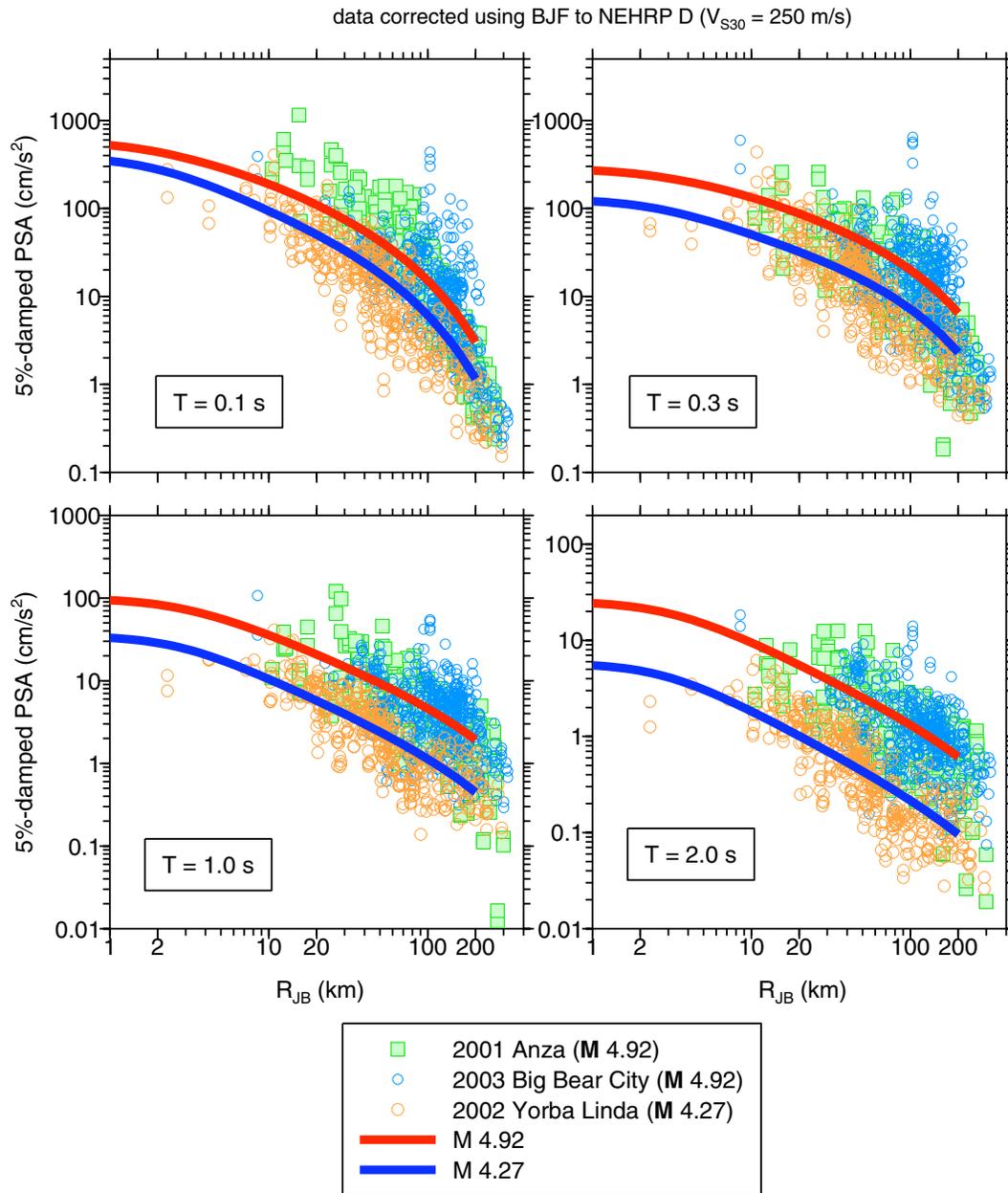
Fig. 4.34 **Comparison of data from three small earthquakes with predictions from BA07 GMPEs.**
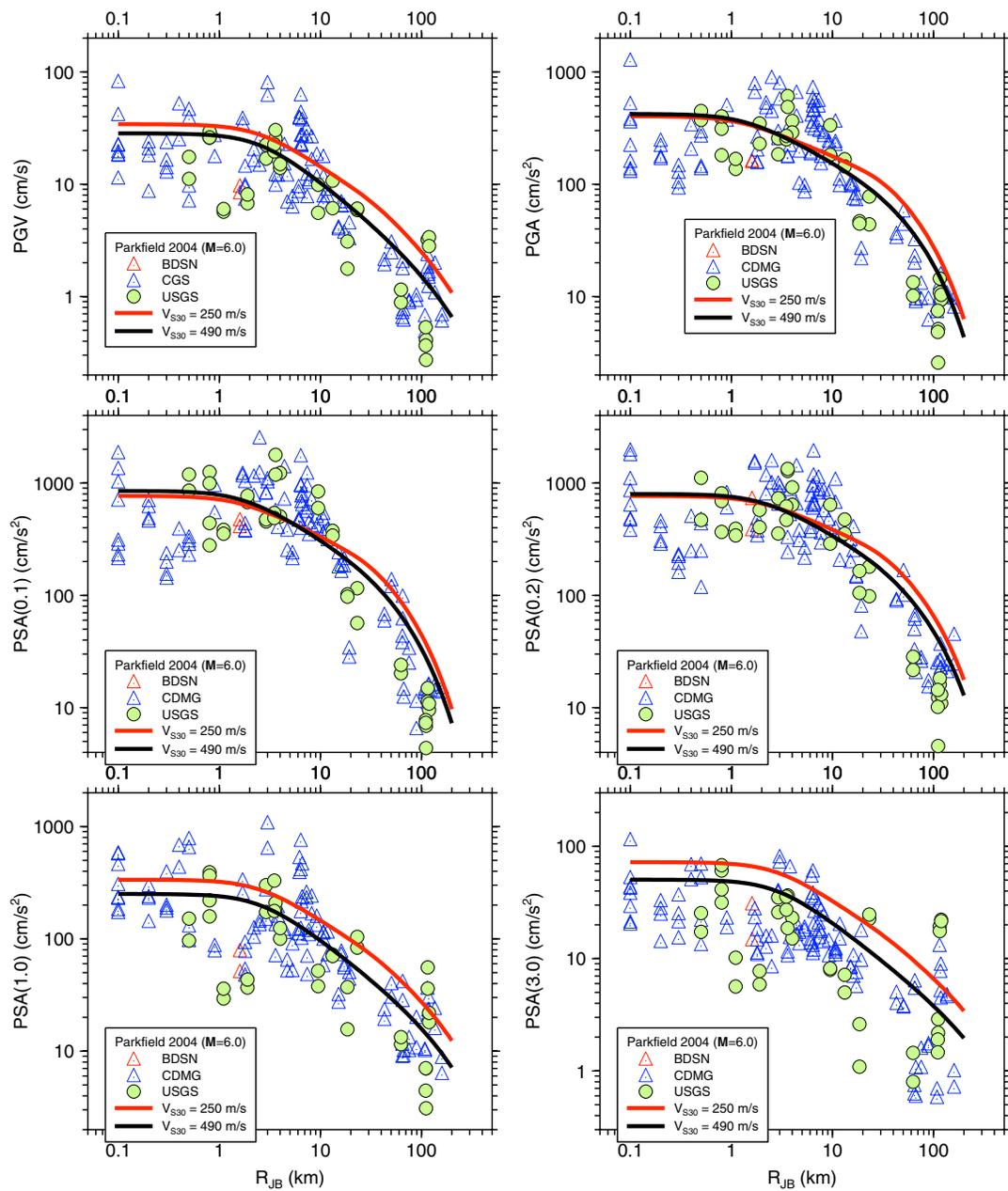
Fig. 4.35   Comparison of data from 2004 Parkfield earthquake with predictions from BA07 GMPEs.

4.2.15 Comparisons of PSA M-Scaling with Simulations

The most striking difference between previous GMPEs and the NGA GMPEs (not just those of BJF97 and BA07, but of all NGA developers) is the prediction of near- or complete saturation of PSA at short periods in the NGA equations (e.g., Figs. 4.16 and 4.17(a)). As a first step in understanding the reason for this saturation, Figure 4.36 shows the magnitude scaling at $R = 30$ km predicted by two point-source scaling models that were defined to mimic finite-fault effects: the Atkinson and Silva (2000) and the Joyner (1984) models. The simulations were made using the SMSIM program *tmr_rv_drvr* (Boore, 2000). For both source models we used the Raoof et al. (1999) distance attenuation parameters. Given that the motions predicted from SMSIM are simple point-source predictions of absolute motion from the source to the site (as opposed to motion relative to some particular distance, magnitude, period, or site condition), with no effort made to adjust parameters to match the motions predicted by the BA07 equations, the agreement is quite good. Adjustments of the geometrical spreading and Q functions, as well as the site amplifications (which used the generic rock amplifications of Boore and Joyner, 1997), could be made to provide better agreement between the BA07 and the simulated ground motions. Finite-fault stochastic-simulation models (Motazedian and Atkinson 2005), or more detailed broadband-simulation methods (Hartzell et al. 1999) could also be applied to better understand the observed scaling. It is interesting, though, that the scaling of motions for large magnitudes seems to fall between that predicted by two simple point-source models.
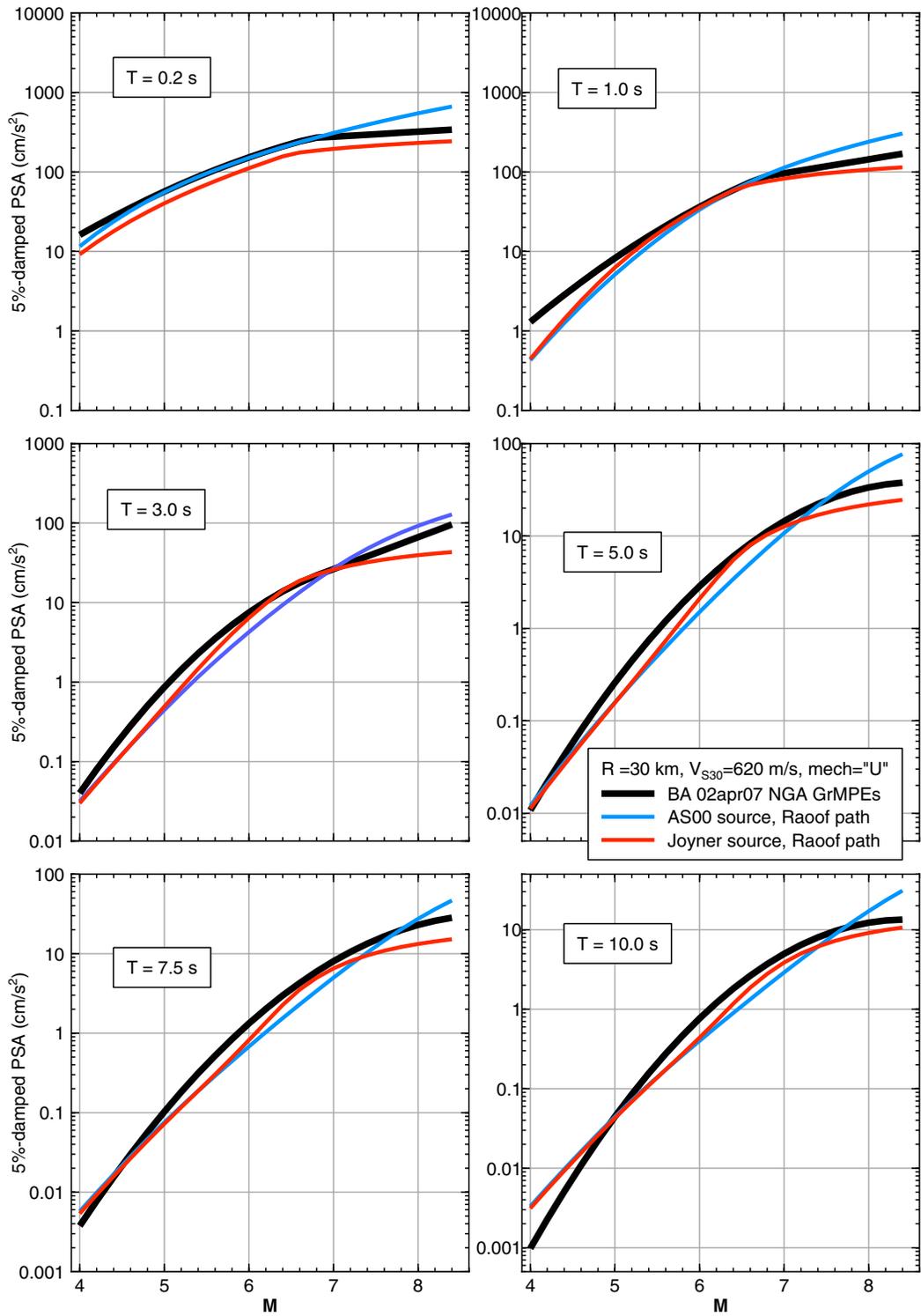
Fig. 4.36 Observed and predicted scaling with magnitude at $R = 30$ km .

5 Guidelines for Usage

5.1 LIMITS ON PREDICTOR VARIABLES

Although we know perfectly well that people will ignore the following limits for the predictor variables, for the record we state that our equations should be used only for predictor variables in these ranges:

- $\mathbf{M} = 5\text{--}8$
- $R_{JB} < 200$ km
- $V_{S30} = 180 - 1300$ m/s

These limits are subjective estimates based on the distributions of the recordings used to develop the equations.

5.2 PREDICTIONS FOR OTHER MEASURES OF SEISMIC INTENSITY

The NGA GMPEs are for the GMRotI measure of seismic intensity. Simple conversion factors between GMRotI and other measures of seismic intensity are given by Beyer and Bommer (2006) and Watson-Lamprey and Boore (2007), as well as by Campbell and Bozorgnia (this volume).

6 Discussion and Summary

We have presented a set of ground motion prediction equations that we believe are the simplest formulation demanded by the NGA database used for the regressions. Future versions of the equations might include additional terms if these can be unambiguously supported by data. Many ground motion observations that have not been included in the NGA flatfile, or should be reprocessed in an attempt to provide more data at long periods; additional data could potentially support the inclusion of more predictive variables. In spite of this, we note that the aleatory uncertainties in our equations are similar to those of other NGA developers who included more predictive variables. Therefore we do not think that our simplified analysis limits the usefulness of our equations, at least for those situations for which predictor variables not included in our equations are not crucial in site-specific hazard analysis.

One modification we would like to address in future versions of our equations is potential regional variations in distance attenuation, particularly at distances beyond about 80 km. The near-source data could be used to constrain magnitude scaling for all regions, which could be patched onto regionally dependent distance functions. The approach taken in this study, in which the anelastic coefficient was constrained using data from a few earthquakes in central and southern California, is not optimal. Furthermore, there are inconsistencies in the pseudo-depths that might be attributed to forcing the values of the anelastic coefficient into the regression of the worldwide dataset. Notwithstanding these limitations, the new relations developed here provide a demonstrably reliable description of recorded ground motion amplitudes for shallow crustal earthquakes in active tectonic regions over a wide range of magnitudes and distances.

REFERENCES

Ambraseys, N. N., J. Douglas, S. K. Sarma, and P. M. Smit (2005). Equations for the estimation of strong ground motions from shallow crustal earthquakes using data from Europe and the Middle East: Horizontal peak ground acceleration and spectral acceleration. *Bull. Earthquake Engineering* **3:** 1–53.

Atkinson, G. M. (1993). Earthquake source spectra in eastern North America. *Bull. Seism. Soc. Am.* **83:** 1778–98.

Bakun, W. H., and W. B. Joyner (1984). The M_L scale in central California. *Bull. Seism. Soc. Am.* **74:** 1827–43.

Atkinson, G. M., and D. M. Boore (2003). Empirical ground-motion relations for subduction zone earthquakes and their application to Cascadia and other regions. *Bull. Seism. Soc. Am.* **93:** 1703–29.

Bakun, W. H., and W. B. Joyner (1984). The M_L scale in central California. *Bull. Seism. Soc. Am.* **74:** 1827–43.

Benz, H. M., A. Frankel, and D. M. Boore (1997). Regional *Lg* attenuation for the continental United States. *Bull. Seism. Soc. Am.* **87:** 606–19.

Beyer, K., and J. J. Bommer (2006). Relationships between median values and between aleatory variabilities for different definitions of the horizontal component of motion. *Bull. Seism. Soc. Am.* **96**: 1512–22.

Boatwright, J., H., Bundock, J. Luetgert, L. Seekins, L. Gee, and P. Lombard (2003). The dependence of PGA and PGV on distance and magnitude inferred from northern California ShakeMap data. *Bull. Seism. Soc. Am.* **93:** 2043–55.

Bommer, J. J., and J. E. Alarcón (2006). The prediction and use of peak ground velocity. *J. of Earthquake Engineering* **10:** 1–31.

Bommer, J. J., J. Douglas and F. O. Strasser (2003). Style-of-faulting in ground-motion prediction equations. *Bull. Seism. Soc. Am.* **93:** 171–203.

Boore, D. M. (1989). The Richter scale: its development and use for determining earthquake source parameters. *Tectonophysics* **166:** 1–14.

Boore, D. M. (2000). SMSIM–Fortran programs for simulating ground motions from earthquakes: version 2.0 — A revision of OFR 96-80-A. *U. S. Geological Survey Open-File Report* **00-509**, 55 pp.

Boore, D. M. (2003). A compendium of *P*- and *S*-wave velocities from surface-to-borehole logging: Summary and reanalysis of previously published data and analysis of unpublished data. *U. S. Geological Survey Open-File Report* **03-191**, 13 pp.

Boore, D. M. (2005). On pads and filters: Processing strong-motion data. *Bull. Seism. Soc. Am.* **95:** 745–50.

Boore, D. M., and S. Akkar (2003). Effect of causal and acausal filters on elastic and inelastic response spectra. *Earthquake Engineering and Structural Dynamics* **32:** 1729–48.

Boore, D. M., and G. M. Atkinson (1989). Spectral scaling of the 1985 to 1988 Nahanni, Northwest Territories, earthquakes. *Bull. Seism. Soc. Am.* **79:** 1736–61.

Boore, D. M., and W. B. Joyner (1997). Site amplifications for generic rock sites. *Bull. Seism. Soc. Am.* **87**: 327–41.

Boore, D. M., W. B. Joyner, and T. E. Fumal (1993). Estimation of response spectra and peak accelerations from western North American earthquakes: An interim report. *U. S. Geological Survey Open-File Report* **93-509**, 72 pp.

Boore, D. M., W. B. Joyner, and T. E. Fumal (1994). Estimation of response spectra and peak accelerations from western North American earthquakes: An interim report, Part 2. *U. S. Geological Survey Open-File Report* **94-127**, 40 pp.

Boore, D. M., W. B. Joyner, and T. E. Fumal (1997). Equations for estimating horizontal response spectra and peak acceleration from western North American earthquakes: A summary of recent work. *Seism. Research Letters* **68:** 128–53.

Boore, D. M., J. Watson-Lamprey, and N. A. Abrahamson (2006). GMRotD and GMRotI: Orientation-independent measures of ground motion. *Bull. Seism. Soc. Am.* **96:** 1502–11.

Choi, Y., and J. P. Stewart (2005). Nonlinear site amplification as function of 30 m shear wave velocity. *Earthquake Spectra* **21:** 1–30.

Day, S. M., J. Bielak, D. Dreger, R. Graves, S. Larsen, K. Olsen, A. Pitarka (2005). *3D ground motion simulation in basins.* Final report prepared for the Pacific Earthquake Engineering Research Center, Project 1A03, by San Diego State University, Carnegie-Mellon University, University of California at Berkeley, Lawrence Livermore National Laboratory, and URS Corporation.

Day, S. M., J. Bielak, D. Dreger, R. Graves, S. Larsen, K. Olsen, A. Pitarka, and L. Ramirez-Guzman (2006). Numerical simulation of basin effects on long-period ground motion. In *Proceedings, Eighth National Conference on Earthquake Engineering,* Paper No. 1857.

Ellsworth, W. L., M. Celebi, M., J. R. Evans, E. G. Jensen, R. Kayen, M. C. Metz, D. J. Nyman, J. W. Roddick, P. Spudich, and C. D. Stephens (2004). Near-field ground motions of the 2002, Denali Fault, Alaska, earthquake recorded at Pump Station 10. *Earthquake Spectra* **20:** 597–615.

Field, E. H. (2000). A modified ground-motion attenuation relationship for southern California that accounts for detailed site classification and a basin-depth effect. *Bull. Seism. Soc. Am.* **90:** S209–21.

Frohlich, C., and K. D. Apperson (1992). Earthquake focal mechanisms, moment tensors, and the consistency of seismic activity near plate boundaries. *Tectonics* **11:** 279–96.

Hartzell, S., S. Harmsen, A. Frankel, and S. Larsen (1999). Calculation of broadband time histories of ground motion: Comparison of methods and validation using strong-ground motion from the 1994 Northridge earthquake. *Bull. Seism. Soc. Am.* **89:** 1484–1504.

Hutton, L. K., and D. M. Boore (1987). The M_L scale in southern California. *Bull. Seism. Soc. Am.* **77:** 2074–94.

Joyner, W. B. (1984). A scaling law for the spectra of large earthquakes. *Bull. Seism. Soc. Am.* **74:** 1167–88.

Joyner, W. B. and D. M. Boore (1993). Methods for regression analysis of strong-motion data, *Bull. Seism. Soc. Am.* **83:** 469–87.

Joyner, W. B., and D. M. Boore (1994). Errata, *Bull. Seism. Soc. Am.* **84:** 955–56.

Komatitsch, D., Q. Liu, J. Tromp, P. Süss, C. Stidham, and J. H. Shaw (2004). Simulations of ground motion in the Los Angeles Basin based upon the Spectral-Element Method. *Bull. Seism. Soc. Am.* **94**: 187–206.

Lee, W. H. K., T. C. Shin, K. W. Kuo, K. C. Chen, and C. F. Wu (2001). CWB free-field strong-motion data from the 21 September Chi-Chi, Taiwan, earthquake. *Bull. Seism. Soc. Am.* 91: 1370–76.

Liu, Q., J. Polet, D. Komatitsch, and J. Tromp (2004). Spectral-element moment tensor inversions for earthquakes. *Bull. Seism. Soc. Am.* **94:** 1748–61.

Mori, J., and D. Helmberger (1996). Large-amplitude Moho reflections (SmS) from Landers aftershocks, southern California. *Bull. Seism. Soc. Am.* **86**: 1845–52.

Motazedian, D., and G. Atkinson (2005). Stochastic finite fault modeling based on a dynamic corner frequency. *Bull. Seism. Soc. Am.* **95:** 995–1010.

Oglesby, D. D., and S. M. Day (2001). The effect of fault geometry on the 1999 Chi-Chi (Taiwan) earthquake. *Geophysical Research Letters* **28:** 1831–34.

Power, M., B. Chiou, N. Abrahamson, and C. Roblee (2006). The "Next Generation of Ground Motion Attenuation Models" (NGA) project: An overview. In *Proceedings, Eighth National Conference on Earthquake Engineering,* Paper No. 2022.

Raoof, M., R. Herrmann and L. Malagnini (1999). Attenuation and excitation of three-component ground motion in southern California. *Bull. Seism. Soc. Am.* **89:** 888–902.

Rathje, E. M., K. H. Stokoe II, and B. Rosenblad (2003). Strong motion station characterization and site effects during the 1999 earthquakes in Turkey. *Earthquake Spectra* **19:** 653–75 (for more details, see http://www.ce.utexas.edu/prof/rathje/research/turkey_velocity.html).

Rathje, E. M., K. H. Stokoe II, and B. Rosenblad (2004). Erratum: ''Strong motion station characterization and site effects during the 1999 earthquakes in Turkey''[Earthquake Spectra 19: 653–75 (2003)], *Earthquake Spectra* **20:** 283.

Schmedes, J., and R. J. Archuleta (2007). Oversaturation of peak ground velocity near strike slip faults (abs). *Seismological Research Letters* **78:** 272.

Somerville, P., and A. Pitarka (2006). Differences in earthquake source and ground motion characteristics between surface and buried earthquakes. In *Proceedings, Eighth National Conference on Earthquake Engineering,* Paper No. 977.

Trifunac, M. D., M. I. Todorovska, and V. W. Lee (1998). The Rinaldi strong motion accelerogram of the Northridge, California earthquake of 17 January 1994. *Earthquake Spectra* **14:** 225–39.

Watson-Lamprey, J. A., and D. M. Boore (2007). Beyond *SaGMRotI*: Conversion to Sa_{Arb}, Sa_{SN}, and Sa_{MaxRot}. *Bull. Seism. Soc. Am.* **97:** (in press).

Youngs, R. (2005). Estimation of distance and geometry measures for earthquakes without finite rupture models, unpublished notes, dated December 8, 2005, distributed to PEER NGA developers.

Zoback, M. L. (1992). First- and second-order patterns of stress in the lithosphere: The World Stress Map Project. *J. Geophysical Research* **97:** 11,703–28.

Appendices

INTRODUCTION

A number of appendices are contained in this report. Some of them are new, and some are based on notes created by the first author during the progress of the NGA project (many of these notes are available from *http://quake.wr.usgs.gov/~boore/daves_notes.php*). We have included a number of the earlier "notes" because they represent work the first author did on the project, and we felt that this work should be documented in the final report.

Several appendices document problems that the first author found with data in the NGA flatfile; some of these problems have been fixed, but we have not had time to check the current version of the flatfile to see if all of them have been corrected.

Because it is inaccurate to refer to "we" when the first author was solely responsible for the notes, the more accurate pronoun "I" is used in some of the appendices to refer to David M. Boore.

Appendix A: Terminology

A.1 "GMPES" VS. "ATTENUATION RELATIONS"

I propose that we do away with the term "attenuation relations" to describe the equations predicting ground motion. I realize that this term is deeply ingrained in our profession, but like jargon in other fields, does not promote a clear understanding of the subject. The problem in earthquake engineering is that the equations do more than predict attenuation (the change of amplitude with distance); they also predict absolute levels of ground motion and therefore also the change in amplitude as a function of earthquake magnitude at a given distance (as controlled largely by source scaling). In addition, ground motions along a given profile might actually increase with distance (think "Moho bounce"), and in the future more sophisticated path- and/or regionally dependent predictions of ground motion might include an increase of motion at some distance ranges. Finally, there is the potential for confusion because some people really do mean Q and geometrical spreading when using the term "attenuation relations." What do I suggest as a replacement? I doubt that any term is without potential misunderstanding or would receive universal approval, but here are several possibilities: "ground-motion prediction equations," although some people do not like the word "prediction"; "ground-motion estimation equations"; or "ground-motion models" (a term preferred by Ken Campbell, recognizing that some models are in the form of look-up tables rather than equations). All of the phrases can be preceded by one of these qualifiers, as appropriate: empirical, hybrid, or theoretical. In this report we use "GMPEs." This is to be pronounced "gumpys."

For your entertainment, here is Tom Hanks's view of the matter, (Hanks, T.C., and C.A. Cornell, "Probabilistic Seismic Hazard Analysis: A Beginner's Guide," to be published in *Earthquake Spectra)*: "… we need what's known in the trade as a ground-motion attenuation relation. (What is really meant here is the excitation/attenuation relationship, admittedly a

polysyllabic mouthful for our language-challenged colleagues who nevertheless know perfectly well that earthquake strong ground motion is a function of magnitude (excitation) and distance (attenuation)).”

A.2   MODIFIERS OF “FREQUENCY” AND “PERIOD”

Just as frequencies are usually described as being “low” or “high,” and periods are described as being “short” or “long,” we should use “longest useable period” rather than “highest useable period.” But to be perverse, we use “maximum useable period” and “T_{MAX}” instead.

A.3   “LOW-CUT FILTER” OR “HIGH-PASS FILTER”?

We prefer “low-cut filter” to “high-pass filter,” although both refer to the same thing; “high-pass filter” probably derived from analog circuits that only “passed” certain frequencies, whereas the active process of a digital filter is to remove or cutout frequencies—thus “low-cut” rather than “high-pass.” Unfortunately, many engineers have not caught up with the newer terminology.

Appendix B: Comparing NGA Flatfiles v. 7.2 and 7.27

In the NGA flatfile, values of PSA are provided for periods up to 10 s no matter what low-cut filtering was needed to remove long-period noise. The lowest useable frequency, based on the low-cut filter frequency and the order and type of the filter, is provided for each record in the flatfile, and this variable is used to guide the choice of the portion of the PSA for each record to be used in the regression. (We find it more convenient to work with the longest useable period, which we denote T_{MAX}, rather than the lowest useable frequency; T_{MAX} is the reciprocal of the lowest useable frequency.) In developing the NGA database, the first version of the flatfile to provide GMRotI (version 7.2) based on the choice of the rotation angle used to compute GMRotI on all periods to 10 s, regardless of the filter cutoff used in processing each record. Formally, it is not valid to include portions of the response spectrum above T_{MAX} in choosing the rotation angle used to compute GMRotI because the spectrum at periods greater than T_{MAX} might not correspond to the actual ground-motion spectrum that would exist in the absence of the noise that required the low-cut filter in the first place. This error was corrected in what we call version 7.27 of the NGA flatfile (this is not a new flatfile distributed to the developers by Brian Chiou, but one that the first author made by inserting the information in *727brian.xls* into the v. 7.2 flatfile; the file *727brian.xls* was distributed to the developers, but it was up to each developer to replace the incorrect values in the flatfile with the correct values). Two things are included in this Appendix: (1) a comparison of GMRotI from the version 7.2 and version 7.27 flatfiles and (2) some plots relevant to whether GMRotD should be used instead of GMRotI (only a brief discussion of this is given, with no conclusions).

The ratios are shown in Figures B.1–B.8, for PGV, PGA, and PSA for oscillator periods $T_{OSC} = 0.1$, 0.2, 1.0, 3.0, 5.0, and 10.0 s (the y-axis title can be used to identify the period). The ratios are values from version 7.27 divided by values from version 7.2. A few outliers have been flagged with the NGA flatfile record number, event, and recording station. The comparison between the version 7.27 and 7.2 ground-motion values is worse for longer period measures of ground-motion intensity. Note the color coding indicating whether T_{OSC} is less than or greater than T_{MAX}. Our expectation was that most of the scatter of the ratio away from unity for the longer oscillator periods would correspond to recordings for which $T_{MAX} < T_{OSC}$, but that does not seem to be the case. This is easiest to see in Figures B.4–B.8, which show the ratios of ground motions plotted against T_{OSC} / T_{MAX}. The red symbols indicate ratios for which $T_{MAX} < T_{OSC}$, but the ratios for these recordings are no farther removed from unity than are the ratios for recordings for which T_{MAX} is much greater than T_{OSC}. Although there appears to be considerable scatter, particularly at longer periods, the graphs are misleading---they do not show that many observations have ratios close to unity. Statistical tests of the kurtosis show that the distributions are not normal. In the worst case ($T_{OSC} = 10.0\,\text{s}$), 50% of the ratios are between 0.992 and 1.005, and 90% of the values are between 0.880 and 1.072. Our conclusion is that it should make little or no difference in the GMPEs if version 7.2 of the flatfile is used rather than version 7.27.
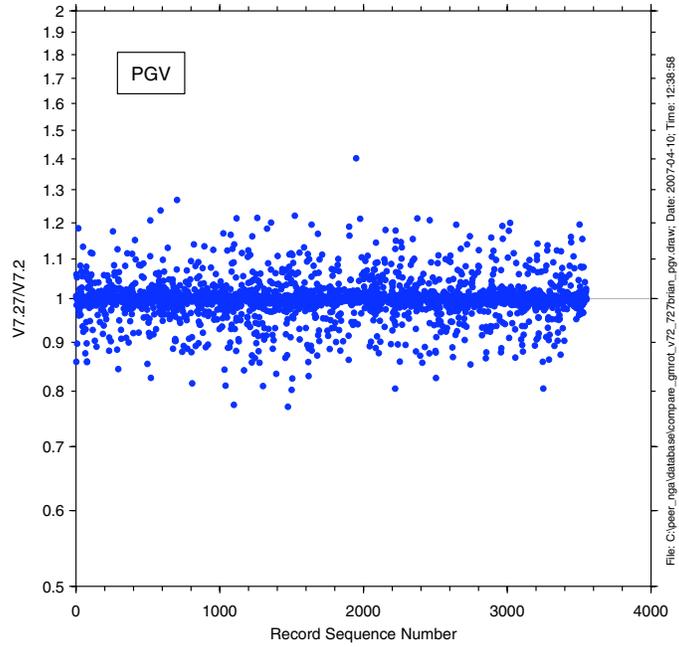
Fig. B.1 Ratio of PGV values from NGA flatfile, versions 7.27 and 7.2.
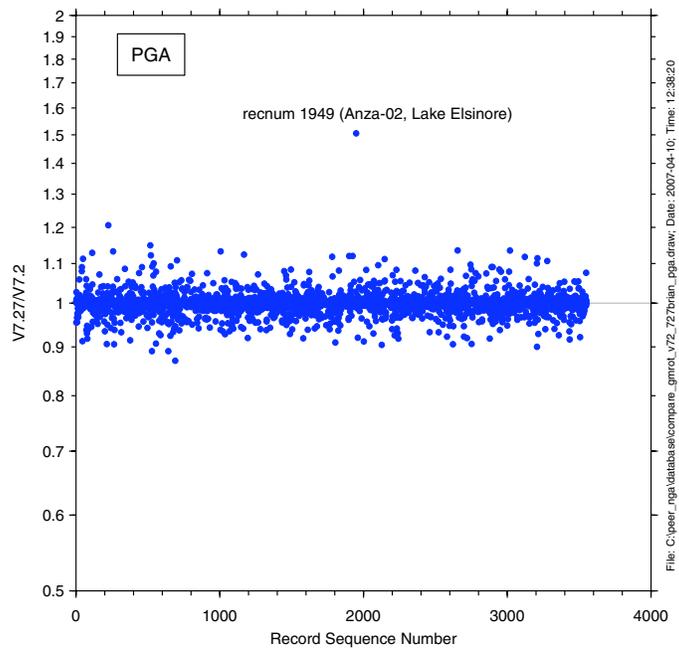
Fig. B.2 Ratio of PGA values from NGA flatfile, versions 7.27 and 7.2.
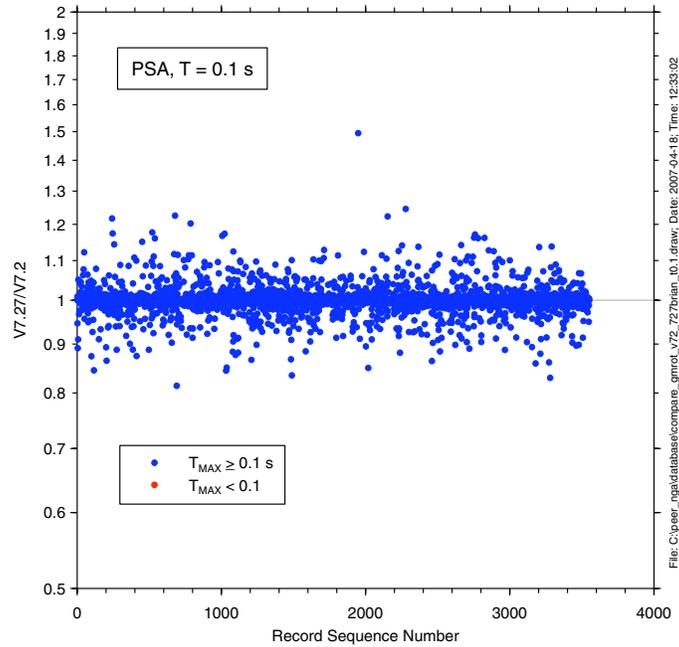
Fig. B.3 Ratio of 5%-damped 0.1 s PSA values from NGA flatfile, versions 7.27 and 7.2. As indicated in legend, symbol colors indicate values for which highest useable period (T_{MAX}) is greater than or less than oscillator period. In this case, period is so short that T_{MAX} s for all records are greater than oscillator period.
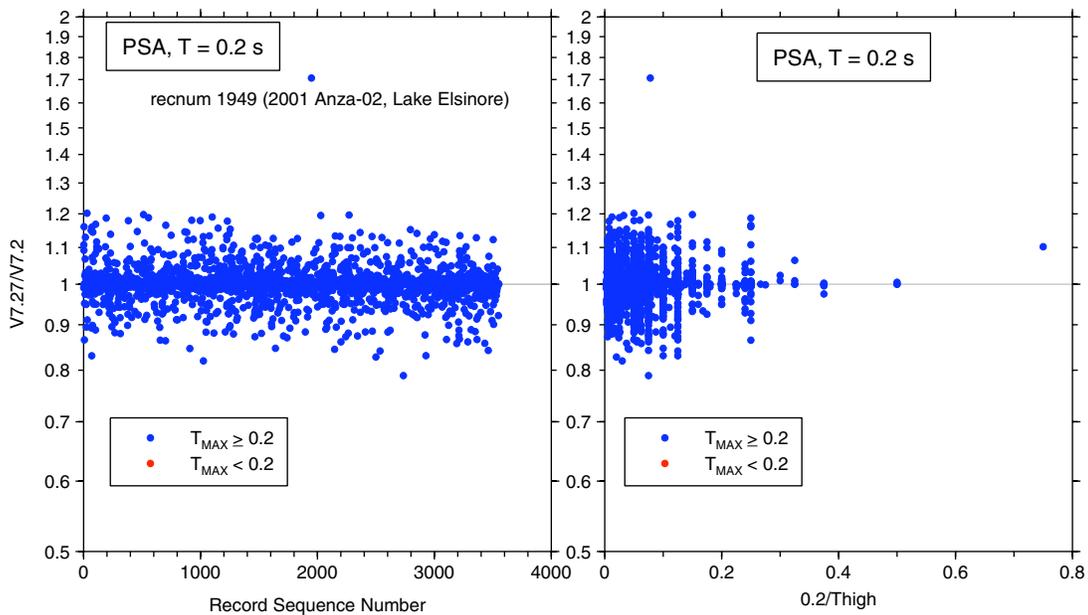
Fig. B.4 Ratio of 5%-damped 0.2 s PSA values from NGA flatfile, versions 7.27 and 7.2. As indicated in legend, symbol colors indicate values for which highest useable period (T_{MAX}) is greater than or less than oscillator period. In this case, period is so short that T_{MAX} s for all records are greater than oscillator period.
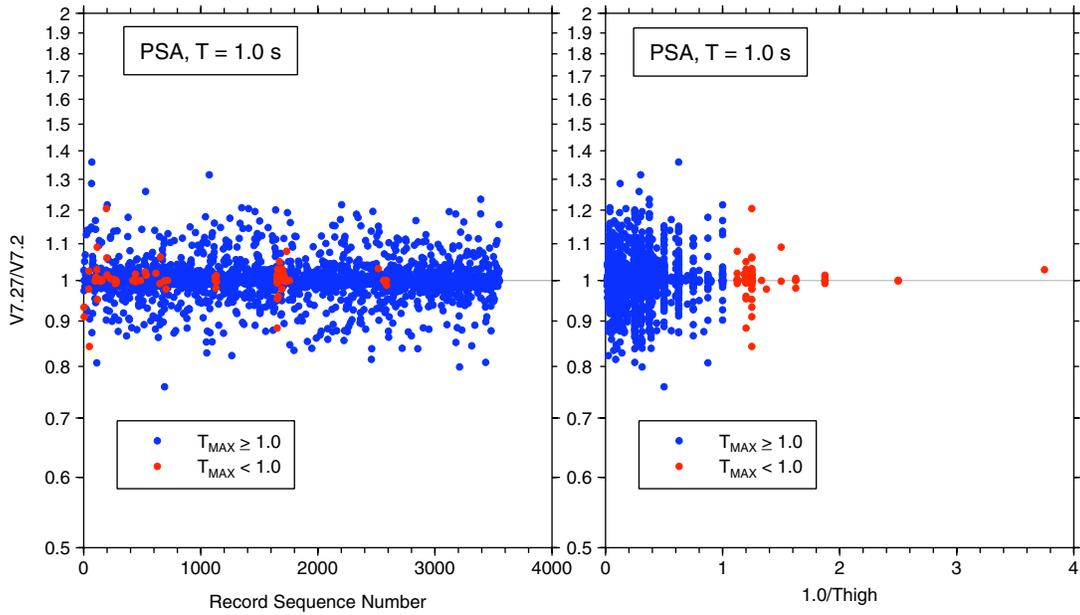
Fig. B.5 Ratio of 5%-damped 1.0 s PSA values from NGA flatfile, versions 7.27 and 7.2. As indicated in legend, symbol colors indicate values for which highest useable period (T_{MAX}) is greater than or less than oscillator period.
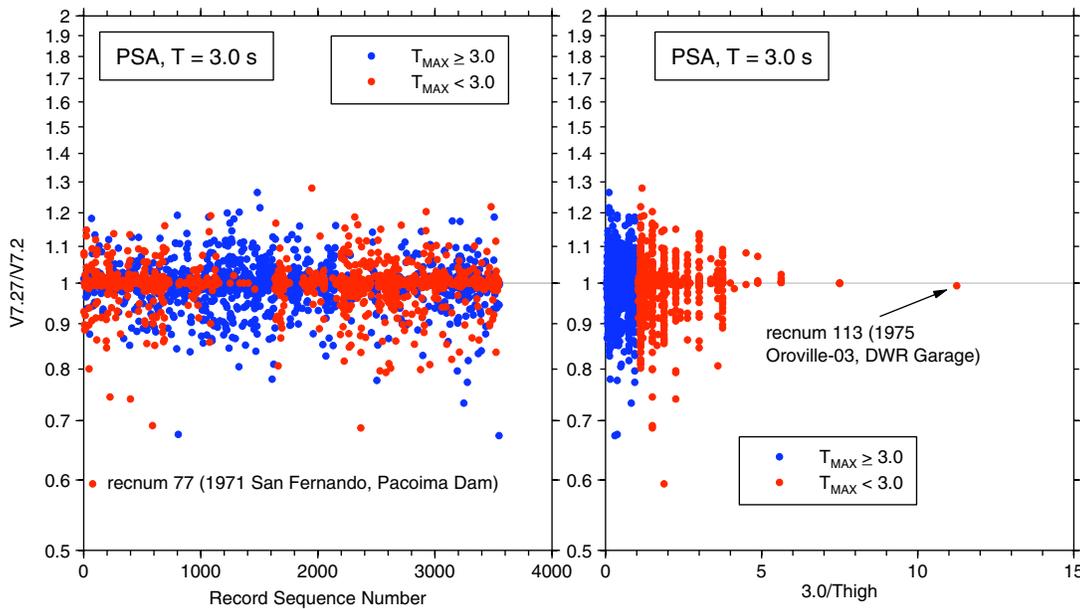
Fig. B.6 Ratio of 5%-damped 3.0 s PSA values from NGA flatfile, versions 7.27 and 7.2. As indicated in legend, symbol colors indicate values for which highest useable period (T_{MAX}) is greater than or less than oscillator period.

A - 11
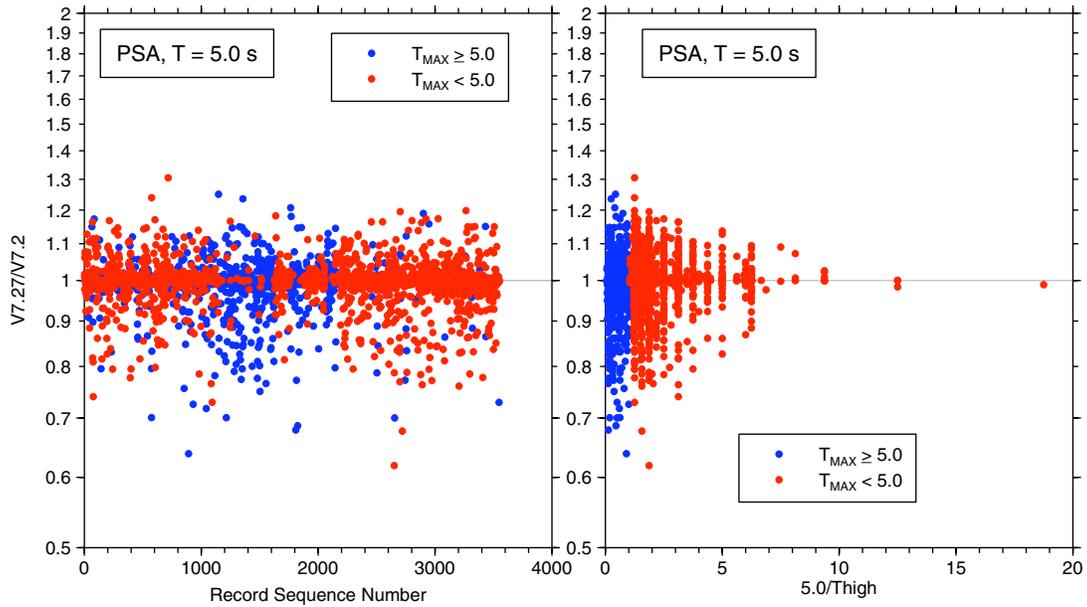
Fig. B.7 Ratio of 5%-damped 5.0 s PSA values from NGA flatfile, versions 7.27 and 7.2. As indicated in legend, symbol colors indicate values for which highest useable period (T_{MAX}) is greater than or less than oscillator period.
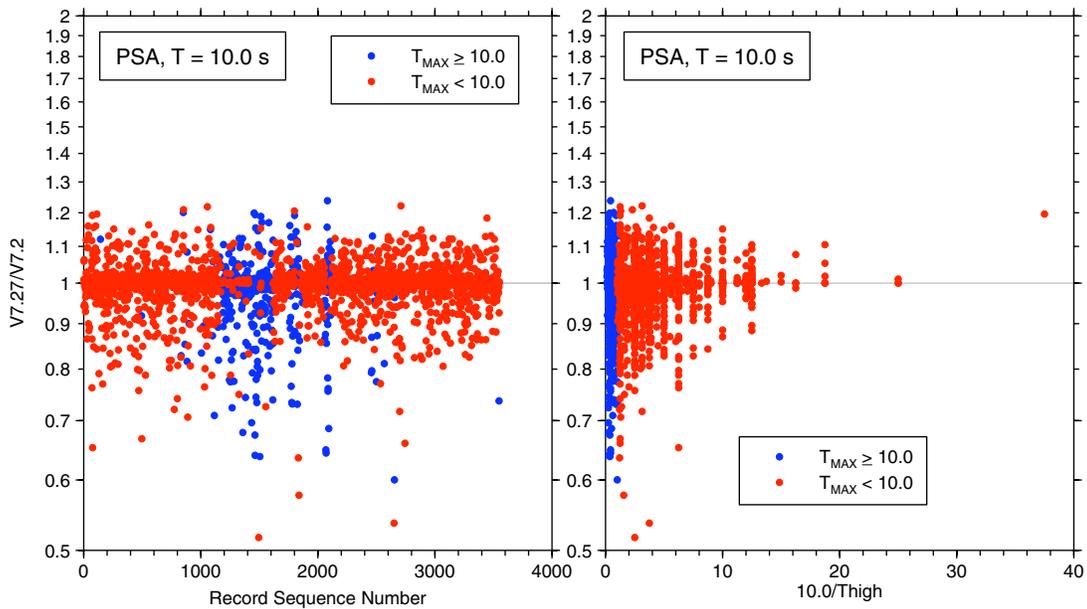
Fig. B.8 Ratio of 5%-damped 10.0 s PSA values from NGA flatfile, versions 7.27 and 7.2. As indicated in legend, symbol colors indicate values for which highest useable period (T_{MAX}) is greater than or less than oscillator period.

As noted in Boore et al. (2006), GMRotI can be sensitive to the range of periods used in computing the penalty function, which is not the case for GMRotD. (Note: Boore et al., 2006, used the terminology "GMRotI50" and "GMRotD50" to stand for what we are calling "GMRotI" and "GMRotD"). This raises a question of whether it would be better to use GMRotD instead of GMRotI. We include here a few figures adapted from Boore et al. (2006), the first (Fig. B.9) showing the ratio of GMRotI to GM as recorded (and the standard deviation of the logarithm of the ratio, expressed as a factor), and the second (Fig. B.10) showing the ratio of GMRotI to GMRotD (and the standard deviation of the logarithm of the ratio, expressed as a factor). Clearly there are significant trends for longer periods. It is not possible to say whether the numerator or the denominator contributes most to the standard deviation, but in either case, the factor is small compared to the inter- and intra-event uncertainties. These plots show that the ratio of GMRotI to GMRotD varies little from unity (the maximum being a 1% reduction at 10 s period); we conclude that it makes no difference if GMRotI instead of GMRotD is used in developing the GMPEs.
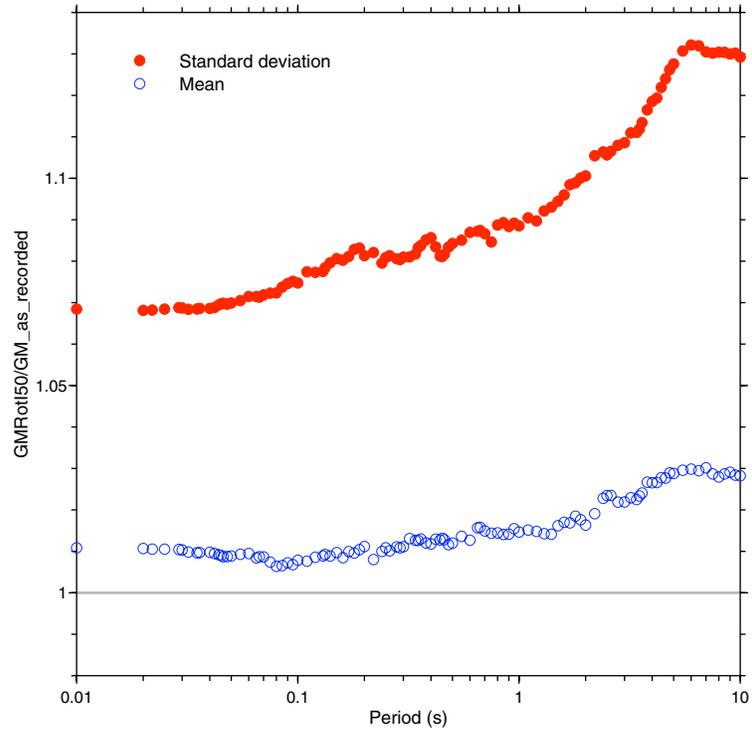
Fig. B.9 Average of ratio of GMRotI to as-recorded geometric mean and standard deviation of ratio, as function of oscillator period.
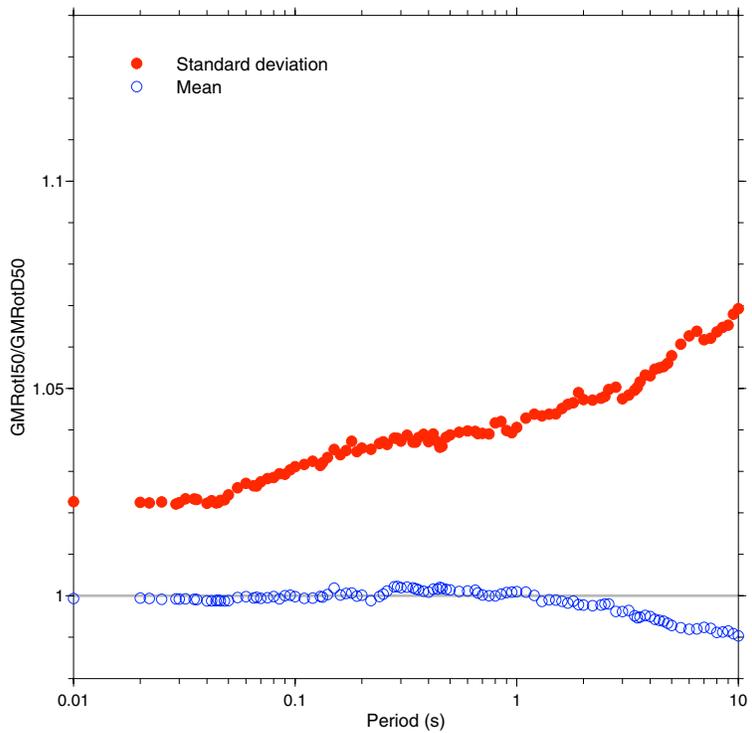
Fig. B.10   Average of ratio of GMRotI to GMRotD and standard deviation of ratio, as function of oscillator period.

A - 14

Appendix C: Why We Don't Provide GMPEs for PGD

We do not provide GMPEs for PGD because PGD can be very sensitive to the low-cut filter corner. We show some examples in this appendix. We also discuss a possible bias in PGD in the NGA flatfile from accelerograms for which the NGA project only had access to records previously filtered by data providers and not to the original, unprocessed records. We also point out that some of the NGA processing may have been too conservative in the choice of low-cut filters, thus reducing the number of records available for determination of GMPEs at long periods.

C.1 SENSITIVITY TO LOW-CUT FILTER FREQUENCIES: RECORDS FROM 1999 CHI-CHI EARTHQUAKE

As shown earlier (Fig. 2.5), the number of data for which the longest useable period is greater than the oscillator period decrease rapidly for $T_{OSC} > 2$ s. For that reason, every effort should be made to choose the low-cut filter frequencies (f_{LC}) as low as possible, consistent with the noise. As is well known, this is a subjective process. Figure C.1 shows that there are many digital recordings for which T_{MAX} is less than 10 s. This seems a bit surprising, but we do not have time to look into the processing in detail for each record in the NGA flatfile. We were struck, however, with the large number of near-fault recordings from the 1999 Chi-Chi earthquake for which f_{LC} is less than 0.1 Hz (for most records, $T_{MAX} = 0.8 / f_{LC}$). Figure C.2 shows where these stations are located with respect to the fault. As Figure C.3 shows, many of these stations are close to GPS measurements of residual displacement. We have looked in detail at the horizontal

component recordings at stations TCU071 and TCU074. We computed displacement time series for a series of acausally filtered acceleration time series. These are shown for TCU074 in Figure C.4. We show the results for this station first because it is one of the rare examples where double integration of unfiltered data produces a displacement time series unaffected by long-period drifts. As the figure shows, the residual displacements are very close to those from the GPS measurements (particularly for the EW component). The filters used in the processing that gave the PGD values in the NGA flatfile are indicated in the figure. This is a very instructive figure. We first make the assumption that the noise increases with decreasing frequency; this assumption is based on extensive experience with double integration of accelerograms. Because of the lack of long-period drifts and the good correspondence of the residual displacements from the doubly-integrated accelerograms and the GPS measurements, we can then conclude that all of the filtered traces represent filtered signal and are not affected by noise. This allows us insight into the character of acausally-filtered ground motions with nonzero residual displacements; without this example, we think that many people would conclude that the character of the waveforms shown in Figure C.4 for the lower filter frequencies (e.g., 0.02 and 0.04 Hz) are controlled by noise. Instead, the "peculiar" features of the waveforms are the filter transients produced when a time series with a finite offset is filtered using an acausal filter. This being so, we think that the NGA filter corner frequencies are too high (we understand from personal communication with W. Silva that many of the recordings of the Chi-Chi earthquake have been reprocessed, but the new values are not in the NGA flatfile). Figure C.5 shows that PGD is sensitive to the filter corner frequency.
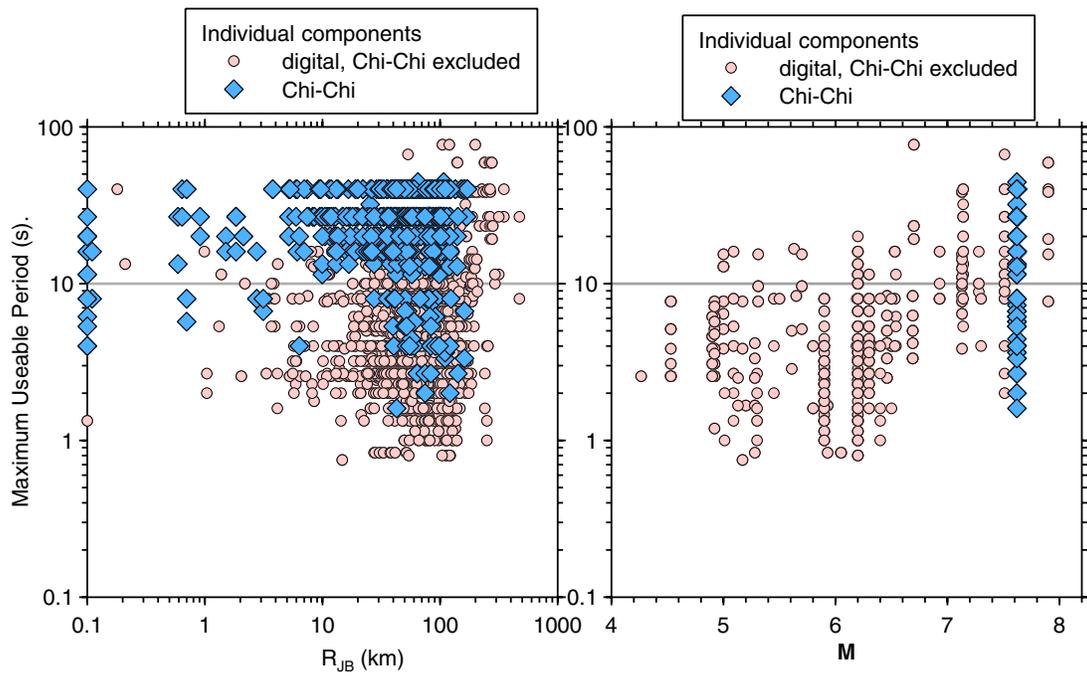
Fig. C.1 Maximum useable period (T_{MAX}) of data in NGA flatfile.
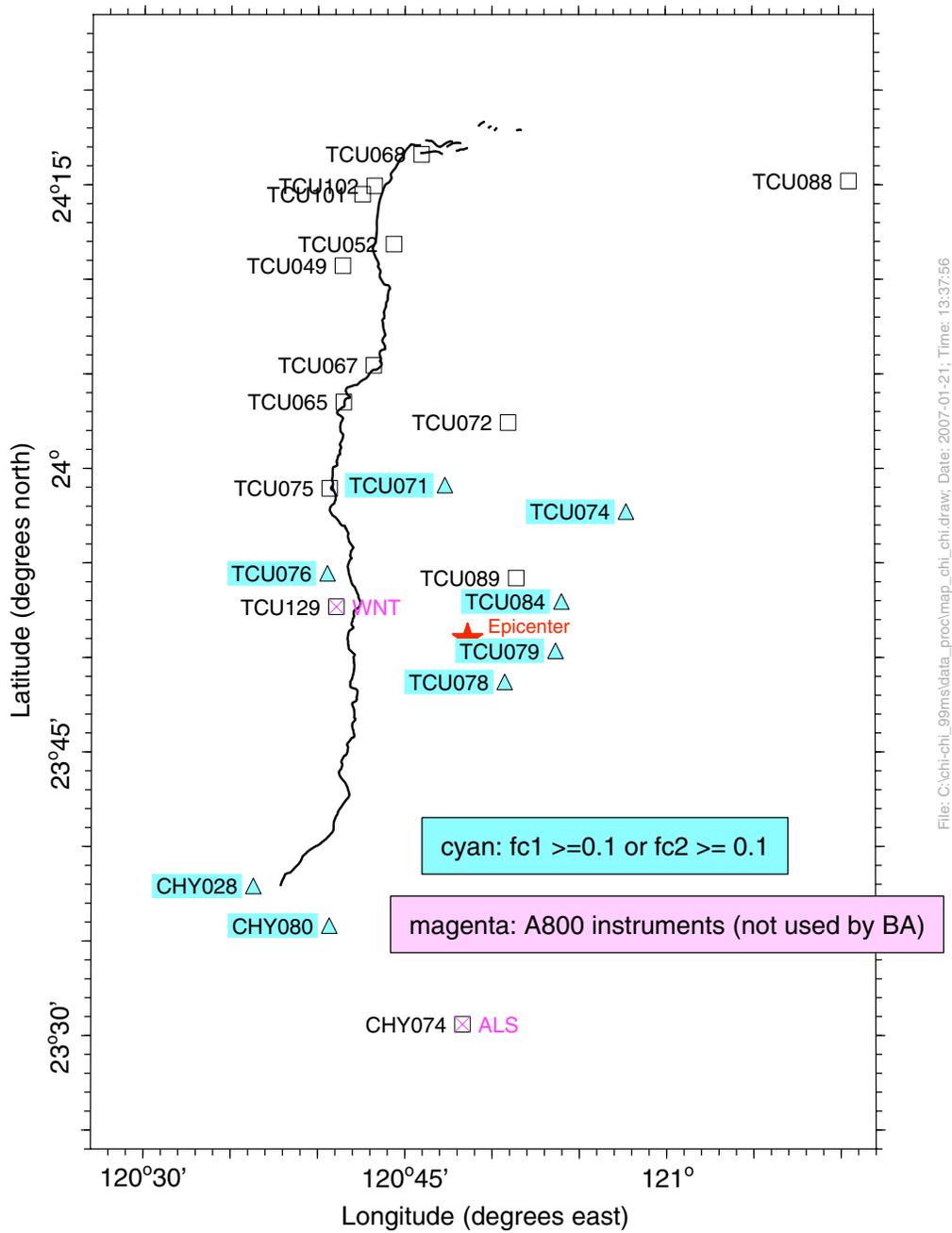
Fig. C.2 **Map of near-fault stations that recorded 1999 Chi-Chi earthquakes, highlighting stations for which one of filter corners in NGA flatfile is less than 0.1 Hz.**
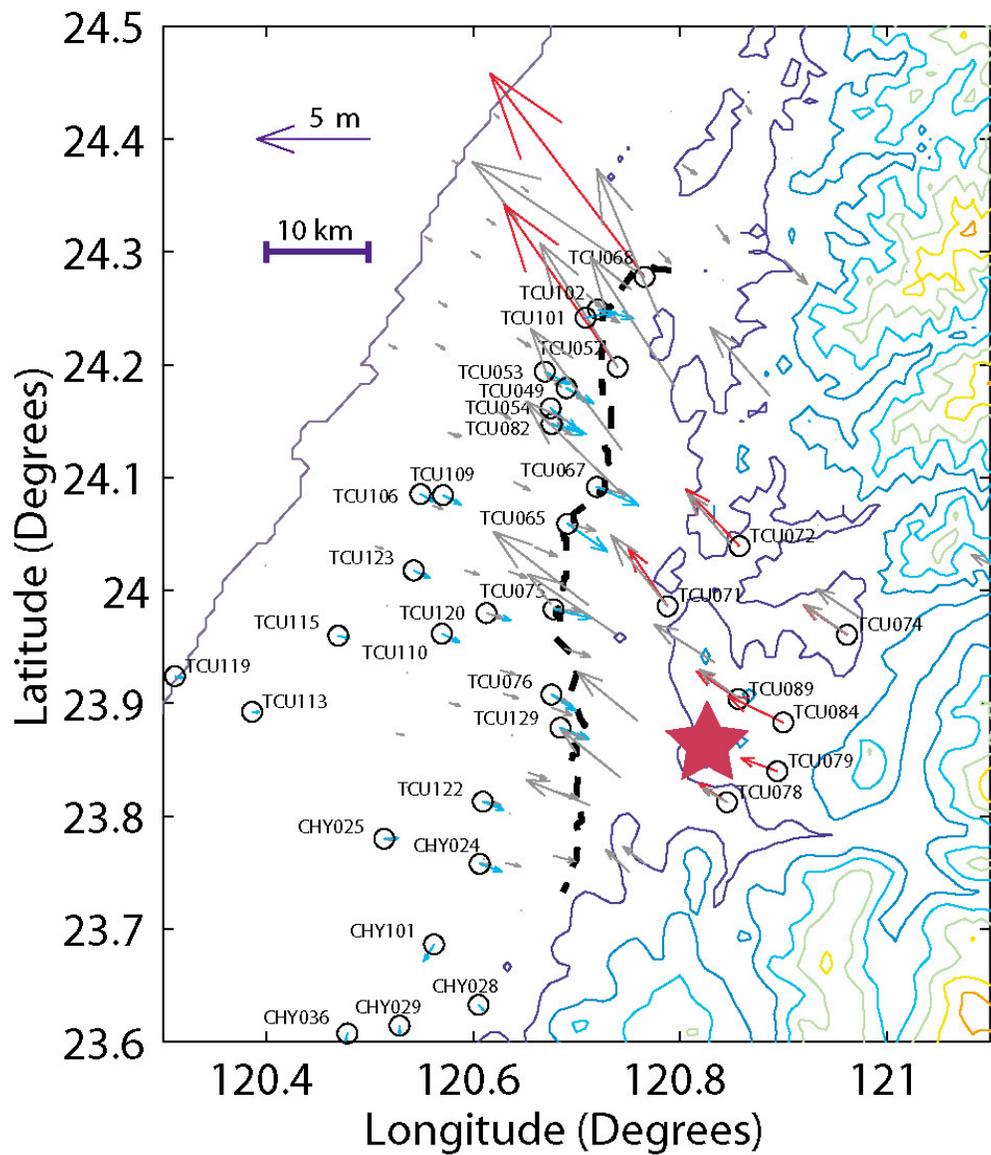
Fig. C.3 **Comparison of residual displacements obtained from accelerometer**
recordings and from GPS measurements (from Oglesby and Day 2001).

.
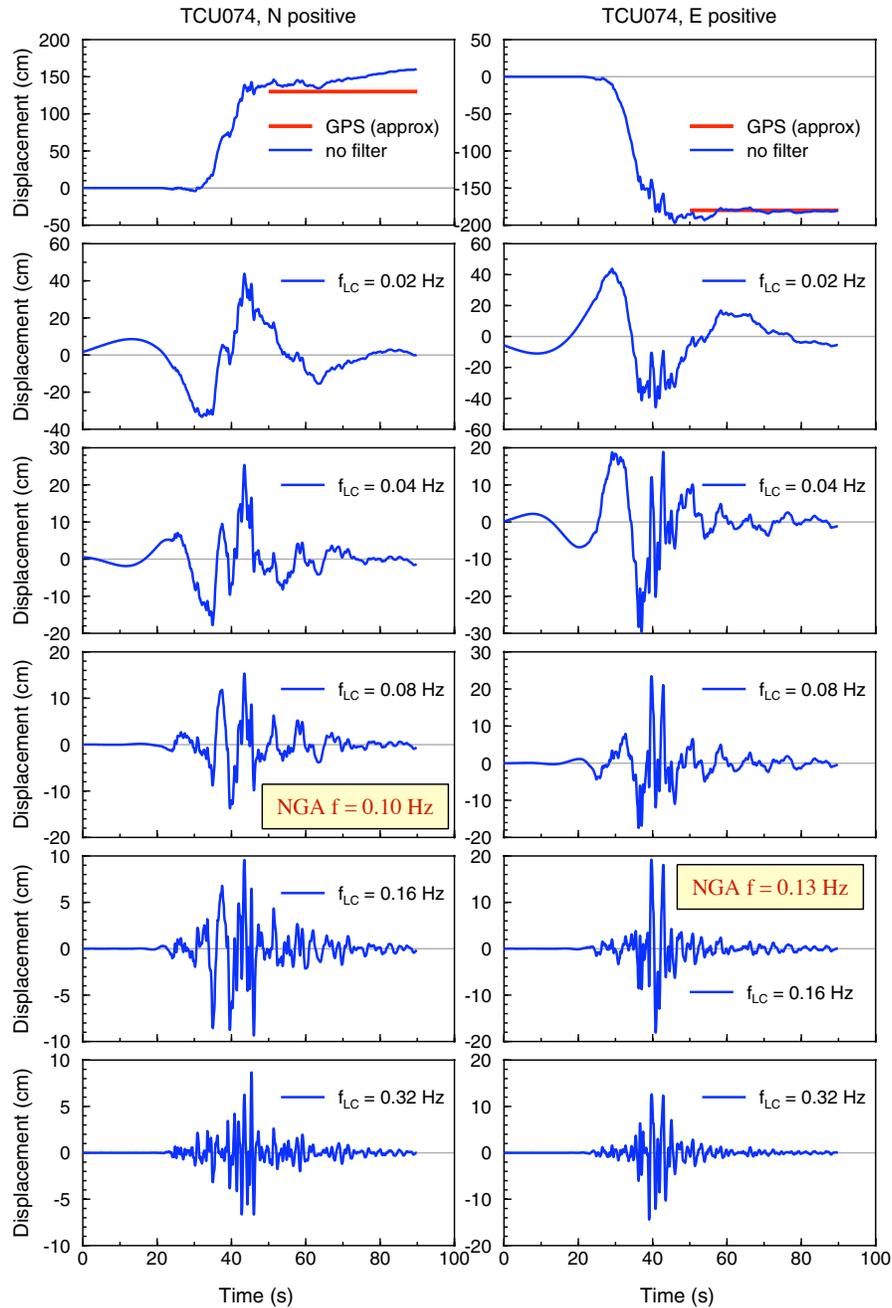
Fig. C.4 **Displacements at TCU074, obtained by double integration of filtered accelerometer recordings of 1999 Chi-Chi earthquake. Each column corresponds to different horizontal component. GPS displacements scaled from Fig. 2 of Oglesby and Day (2001). Low-cut filter frequencies used in processing data in NGA flatfile indicated by text boxes placed on time series filtered with corner frequency close to NGA frequency.**
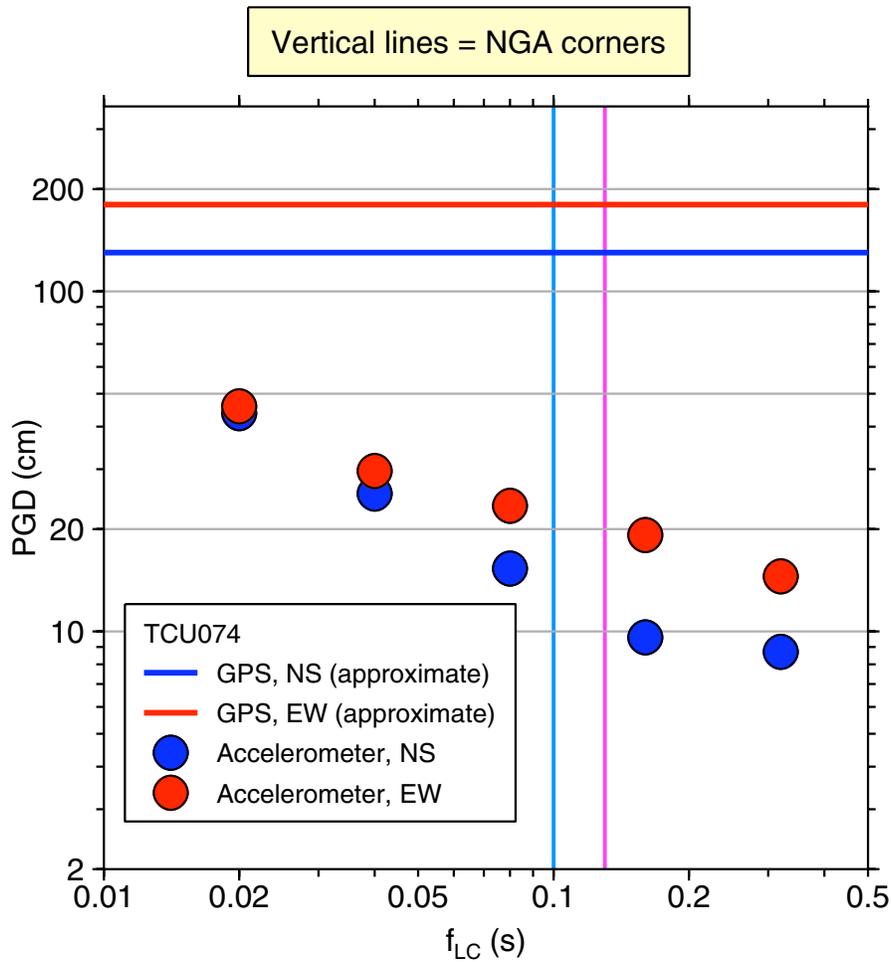
Fig. C.5 **PGD from various time series shown in previous figure. Also shown are GPS residual displacements and low-cut filter corner frequencies used in processing data in NGA flatfile.**

We did the same exercise with the horizontal component records from TCU071, as shown in Figures C.6 and C.7. For this record, it is clear that the typical long-period drifts exist, due to double integration of long-period noise in the acceleration time series. For that reason we cannot be sure that the traces filtered with low corner frequencies represent signal only. But the waveforms for $f_{LC} = 0.02$ Hz are similar to those for TCU074, so it is likely that most of the displacements in the filtered traces represent signal. One other point is that it is not clear why there is such a large difference in the NGA corner frequencies for the two components of motion. The lowest useable frequency in the NGA flatfile is determined by the maximum of the low-cut filter corners for the two horizontal components, which for TCU071 is 0.2 Hz (according to the

NGA flatfile, the lowest useable frequency for this record is 0.25 Hz). This means that with the NGA processing, the recording at this station contributes no information for the GMPEs developed for periods greater than 4 s.
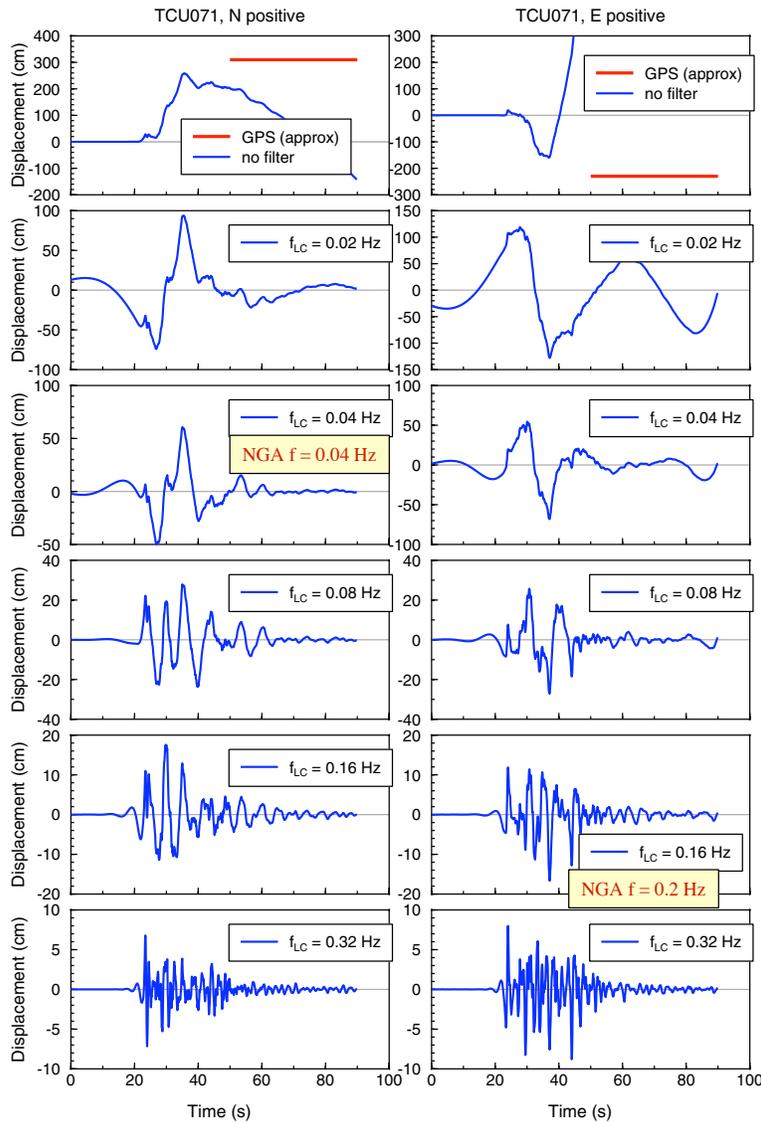
Fig. C.6 **Displacements at TCU071, obtained by double integration of filtered accelerometer recordings of 1999 Chi-Chi earthquake. Each column corresponds to different horizontal component. GPS displacements scaled from Fig. 2 of Oglesby and Day (2001). Low-cut filter frequencies used in processing data in NGA flatfile indicated by text boxes placed on time series filtered with corner frequency close to NGA frequency.**
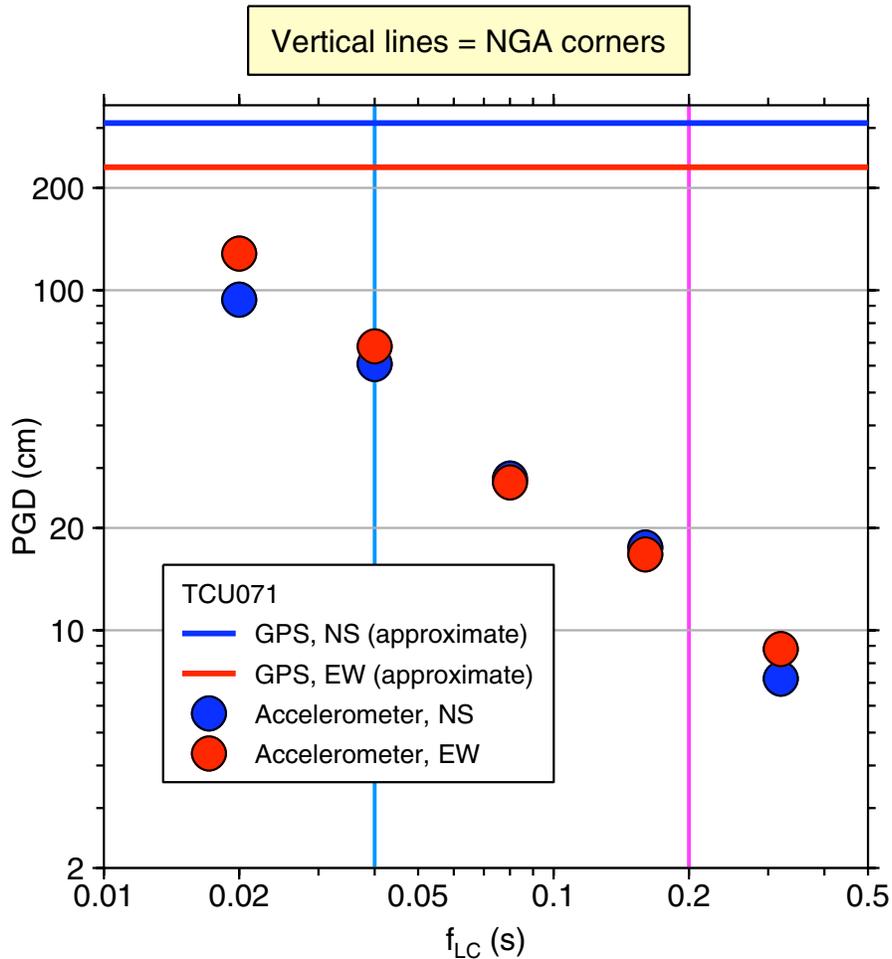
Fig. C.7 **PGD from various time series shown in previous figure. Also shown are GPS residual displacements and low-cut filter corner frequencies used in processing data in NGA flatfile.**

C.2 POSSIBLE SYSTEMATIC OVERESTIMATION OF PGD FOR "PASS-THROUGH" DATA

For several reasons, not all of the NGA data were processed starting from original, unfiltered records. Some of the acceleration time series provided by data agencies had already been filtered and/or baseline corrected to remove long-period noise. These records are referred to as "pass-through" records by W. Silva. The seismic-intensity measures other than PGA were computed from these pass-through data. Unfortunately, the pass-through data rarely, if ever, are distributed

with the zero pads that were added if acausal filtering was used to remove long-period noise. As discussed by Boore (2005), subsequent processing of pad-stripped data can lead to incompatible PSA, PGV, and PGD. This is shown in Figure C.8. The first blue and red traces are the displacement time series provided by the U.S. Geological Survey for two horizontal components recorded at the Monte Nido Fire Station during the 1994 Northridge earthquake. Note that the displacements are not zero at zero time. This is because the original processing included pre-event pads, which were stripped off the processed records made available to the public. Double integration of the pad-stripped acceleration leads to drifts in the displacements, as shown in the second traces. This was recognized in developing the NGA flatfile, but rather than use the displacement traces available from the data agencies, ad-hoc corrections were made to remove the drifts (the corrected NGA-determined displacement time series are the third time series in each set). These time series look like those from the data agency, but note the difference in PGD: 2.6 cm vs. 3.3 cm and 1.9 cm vs. 2.1 cm for the USGS-provided and PEER NGA, for the two components, respectively. We have made similar comparisons of a small set of data from the 1992 Cape Mendocino, 1992 Landers, and 1994 Northridge earthquakes. The results are summarized in Figure C.9, which shows the ratio of PGD from the NGA time series and from the reporting agency (the latter PGD were obtained from the padded and filtered acceleration time series). The results suggest a bias in the NGA values relative to the correct values. We show these results only to indicate other possible problems with PGD in the NGA flatfile. We have not done a systematic study of all pass-through data, nor have we investigated the differences in PSA and PGV. Both PSA and PGV were determined from the pad-stripped data, and therefore they may also be different than the values from the data providing agencies; we suspect, however, that the problem will be most severe for PGD.
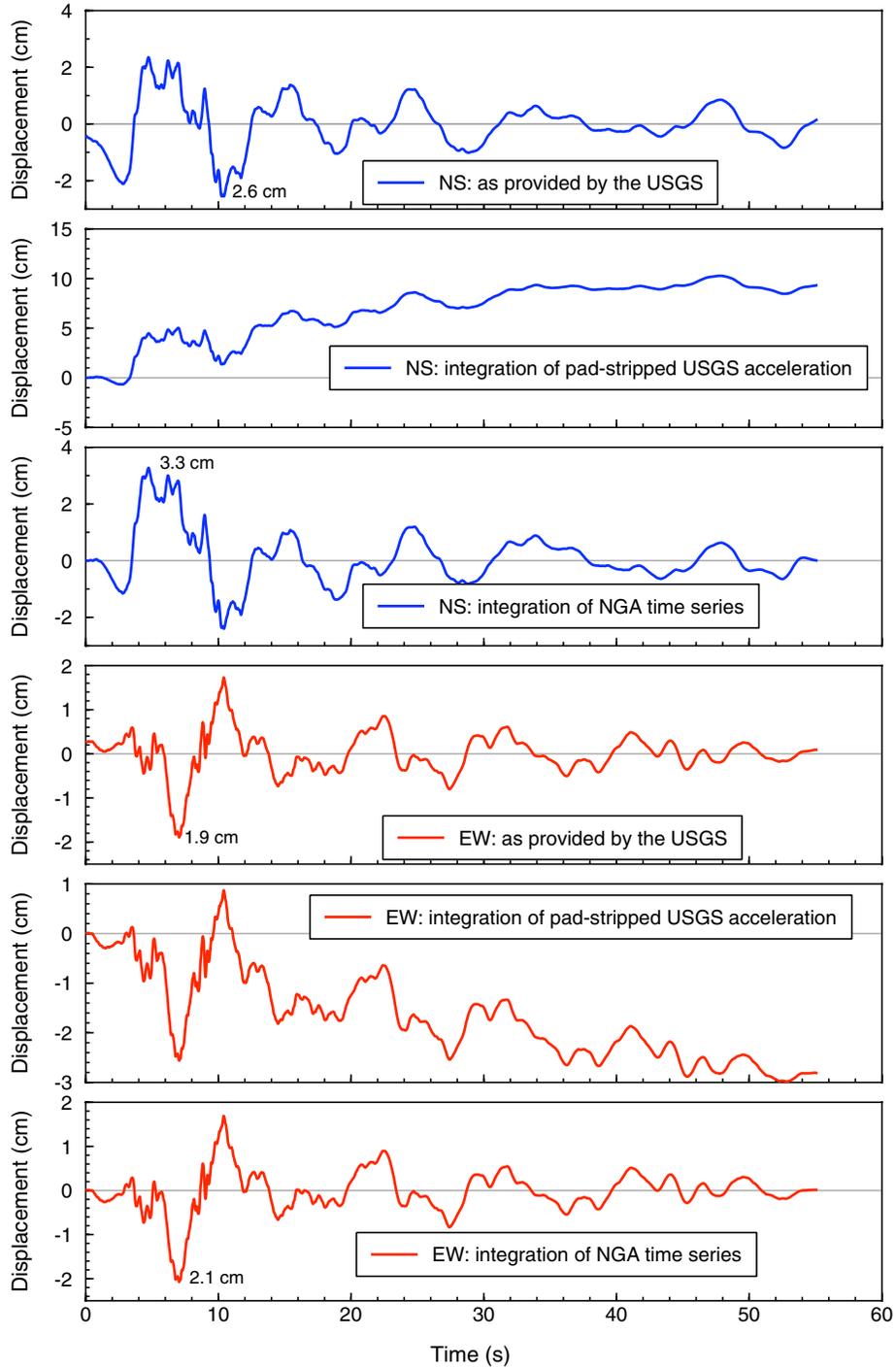
Fig. C.8 **Displacements for two components of Monte Nido recording of 1994 Northridge earthquake, processed in various ways. Values of PGD labeled for second and third time series in each set.**
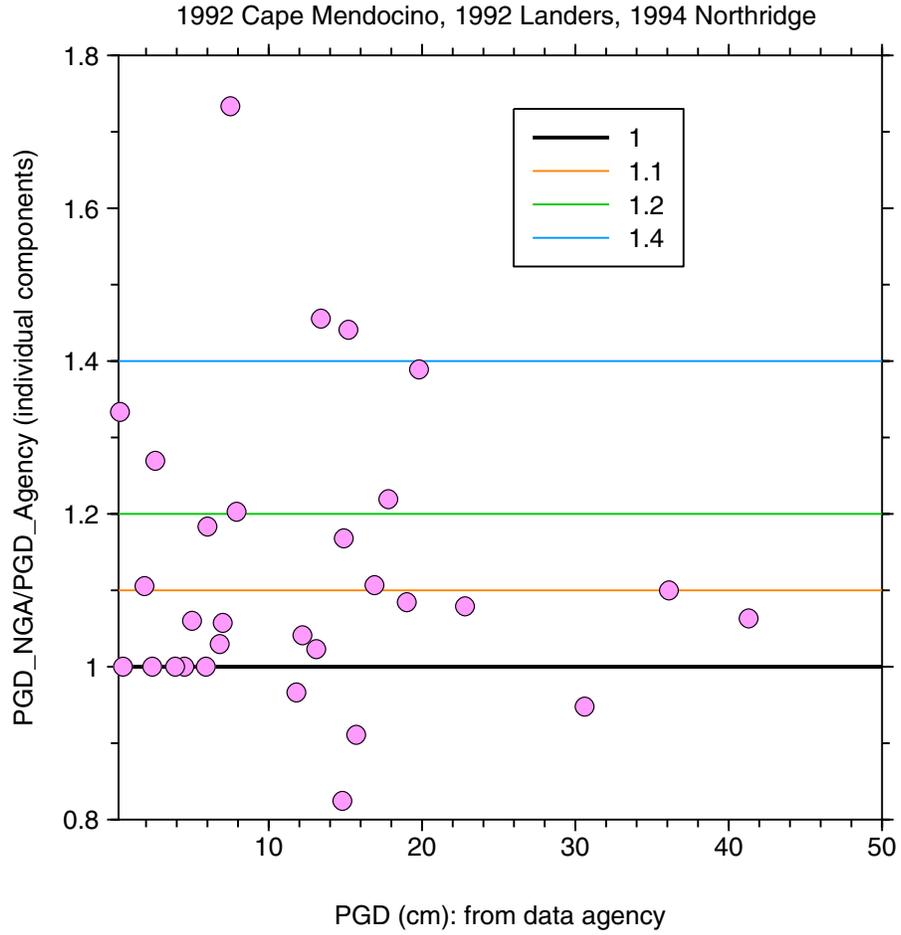
Fig. C.9 Ratio of PGD from NGA flatfile to that from agency providing data, showing bias in NGA flatfile values of PGD.

Appendix D: Classifying Fault Type Using P- and T-Axes

Rather than including a continuously varying quantity such as rake angle as the fault-type predictor variable, most, if not all, previous GMPEs group earthquakes into a few fault types (this is analogous to the use of "soil" and "rock" rather than V_{S30} as the predictor variables for site amplification). These fault types are most commonly given the names "strike-slip," "reverse," and "normal," sometimes with "oblique" appended to these names. The classification of a particular earthquake into one of these groups is usually defined in terms of rake angle, although the mapping of rake angle into a fault type can vary amongst authors (Bommer et al. 2003). For earthquakes in which one of the two possible fault planes is shallowly dipping, however, the classification into a fault type based on rake angle will be different for the two planes. A way of removing this ambiguity is to classify earthquake fault type using the plunges of the P-, T-, and B-axes. Several mappings of the plunge angles into fault types have been proposed (e.g., Frohlich and Apperson 1992 and Zoback 1992). In deciding which scheme to use, we classified the earthquakes in an early version of the NGA flatfile using Zoback (1992). Her scheme is given in the following table:

Table D.1   Definitions of fault type based on plunges of P-, T, and B-axes (after Table 3 in Zoback 1992). (pl in table is plunge angle, from horizontal.)

P-axis plunge	B-axis plunge	T-axis plunge	Fault Type
$pl \geq 52$		$pl \leq 35$	Normal
$40 \leq pl < 52$		$pl \leq 20$	Normal Oblique
$pl < 40$	$pl \geq 45$	$pl \leq 20$	Strike-slip
$pl \leq 20$	$pl \geq 45$	$pl < 40$	Strike-slip
$pl \leq 20$		$40 \leq pl < 52$	Reverse Oblique
$pl \leq 35$		$pl \geq 52$	Reverse

The classifications of the NGA data using Zoback's definitions are shown in Figure D.1. Note that only three events were not classified using the scheme, and two of these would have been classified with slight changes in the plunges. In addition, for the NGA dataset the criteria involving the plunge of the B axis is redundant (the plunge of the P- and T-axes suffices). By looking at the above figure we recommend the following simplification to Zoback's classification scheme:
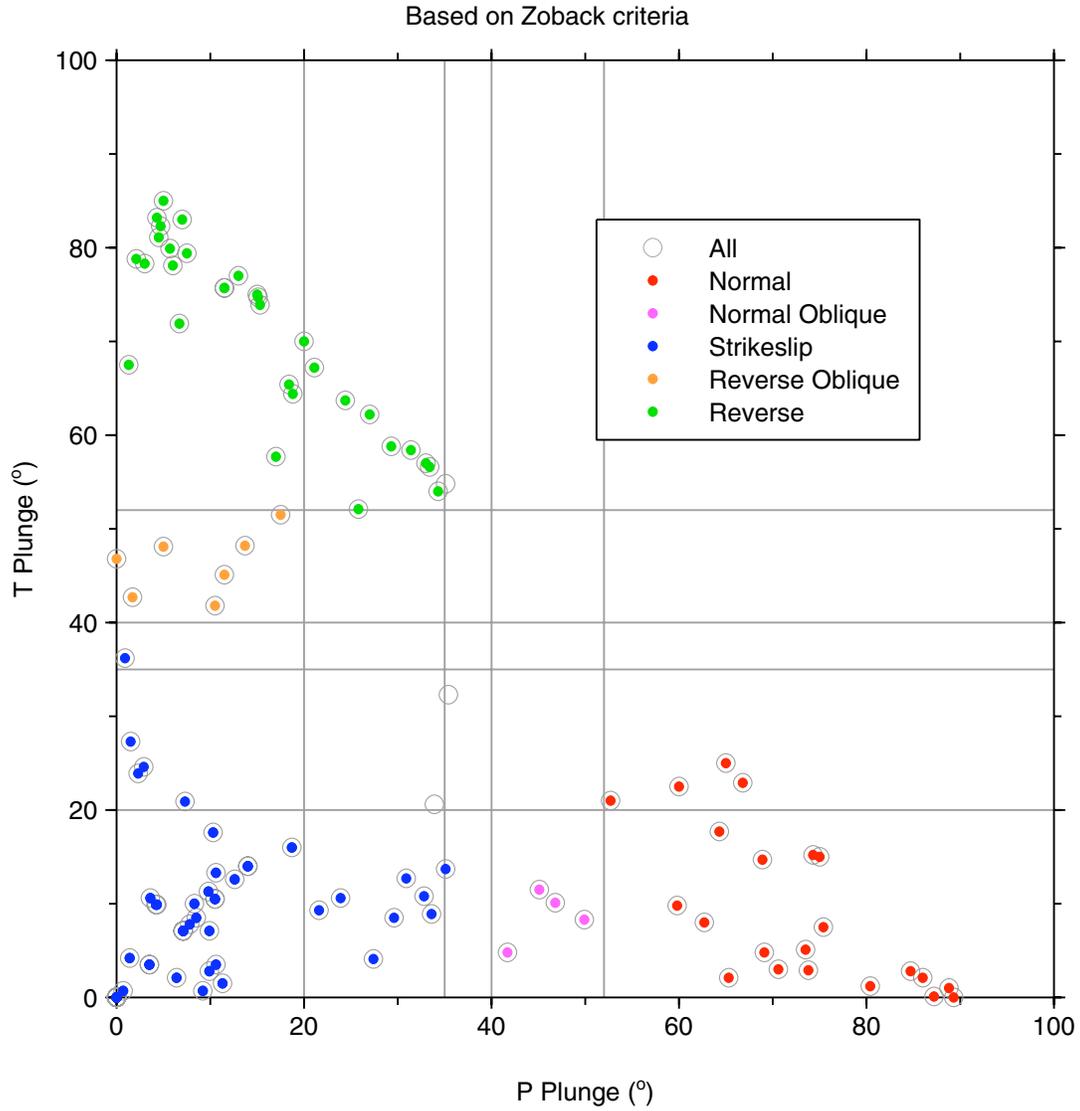
Fig. D.1 Classification using Zoback (1992).

We showed earlier (Fig. 2.6) that this simplified classification scheme agrees with that used by Boore et al. (1997); only a few singly recorded earthquakes were not classified when using Table D.2.

Table D.2 The BA07 fault-type definitions (pl is plunge angle, from horizontal).

P-axis plunge	T-axis plunge	Fault Type
$pl > 40$	$pl \leq 40$	Normal
$pl \leq 40$	$pl > 40$	Reverse
$pl \leq 40$	$pl \leq 40$	Strike-slip
$pl > 40$	$pl > 40$	undefined

To see how the classification based on the P- and T-axes compares to various classifications based on rake angles, we attach a series of figures using both the NGA flatfile definition of fault type in terms of rake angle and a definition based on 45-degree wedges of rake angle. As seen in Figures D.2–D.11, there is considerable overlap in the ways of classifying the fault types. We have not attempted to look into those events that have different classifications using the various schemes.
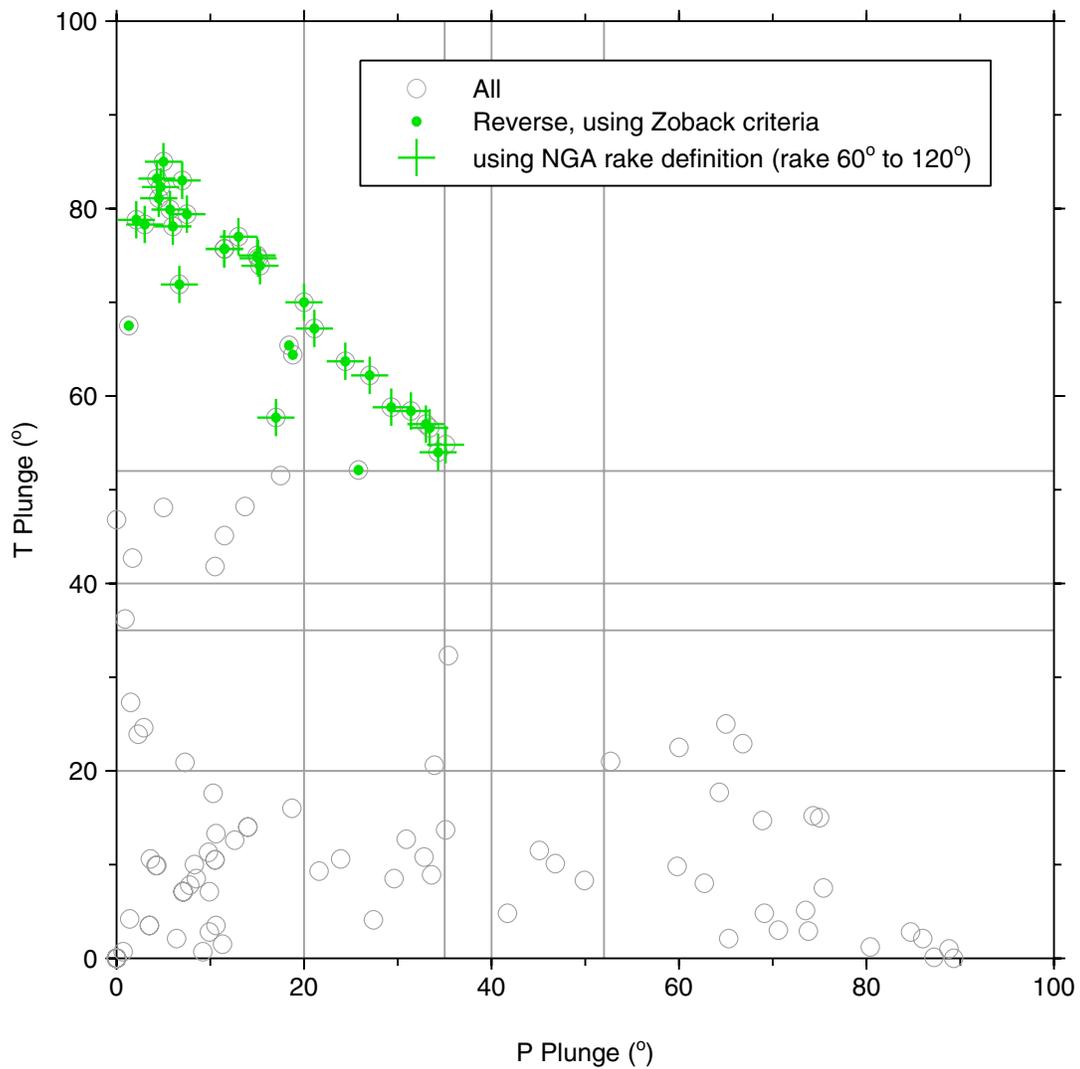
Fig. D.2 Classifications based on Zoback (1992) and rake angles (using NGA definition, shown in legend): reverse-slip earthquakes.
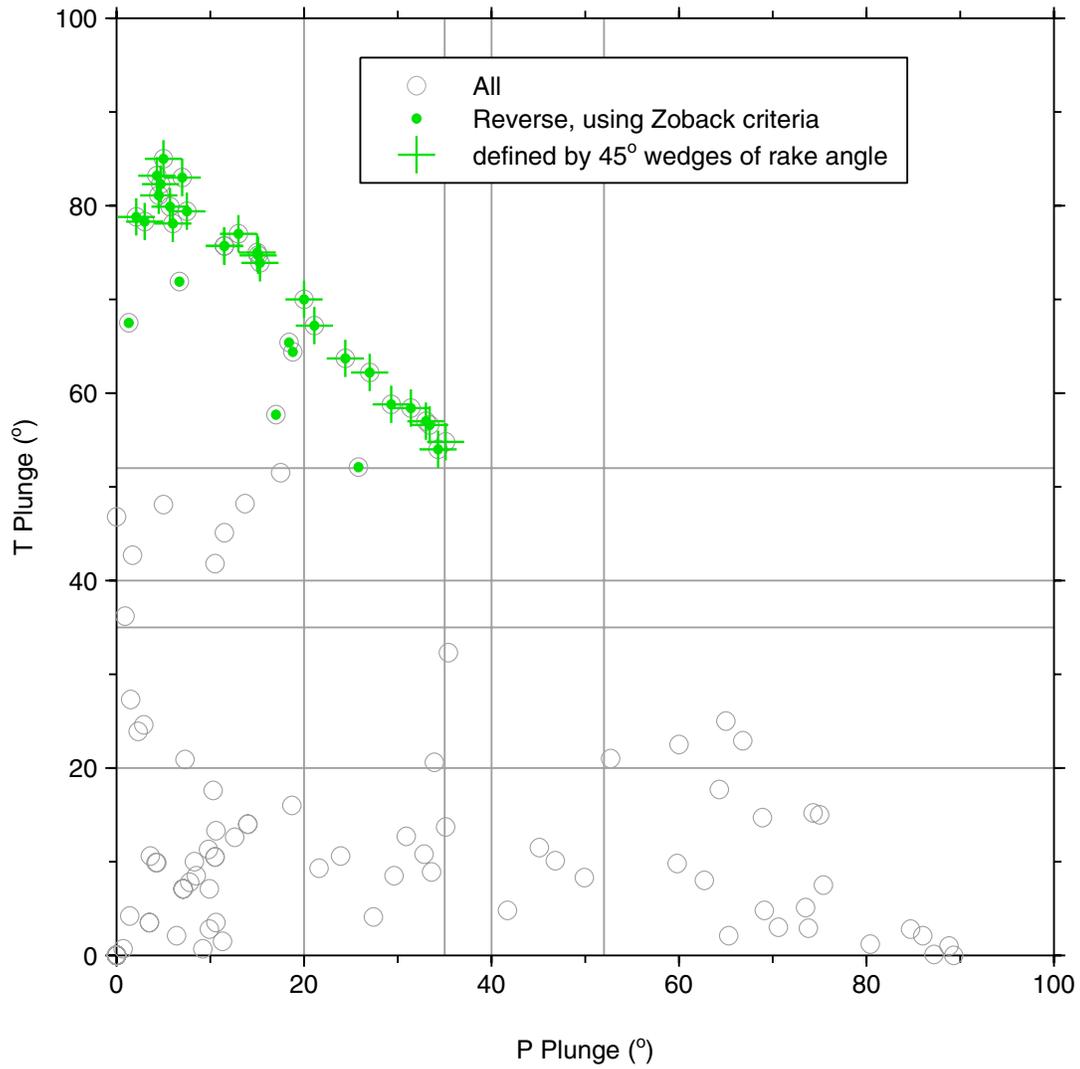
Fig. D.3   Classifications based on Zoback (1992) and using 45-degree wedges of rake angle: reverse-slip earthquakes.
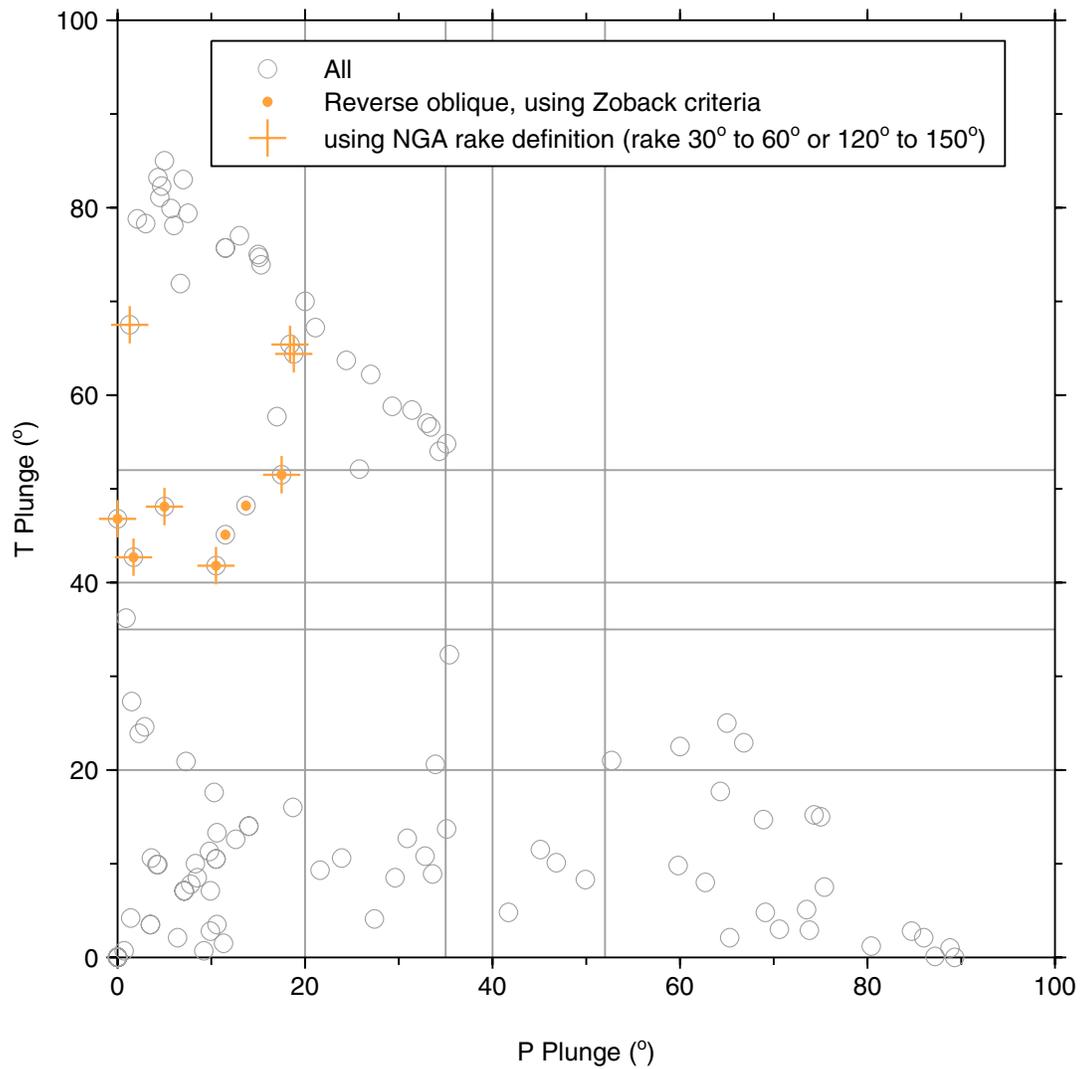
Fig. D.4   Classifications based on Zoback (1992) and rake angles (using NGA definition, shown in the legend): reverse-oblique-slip earthquakes.
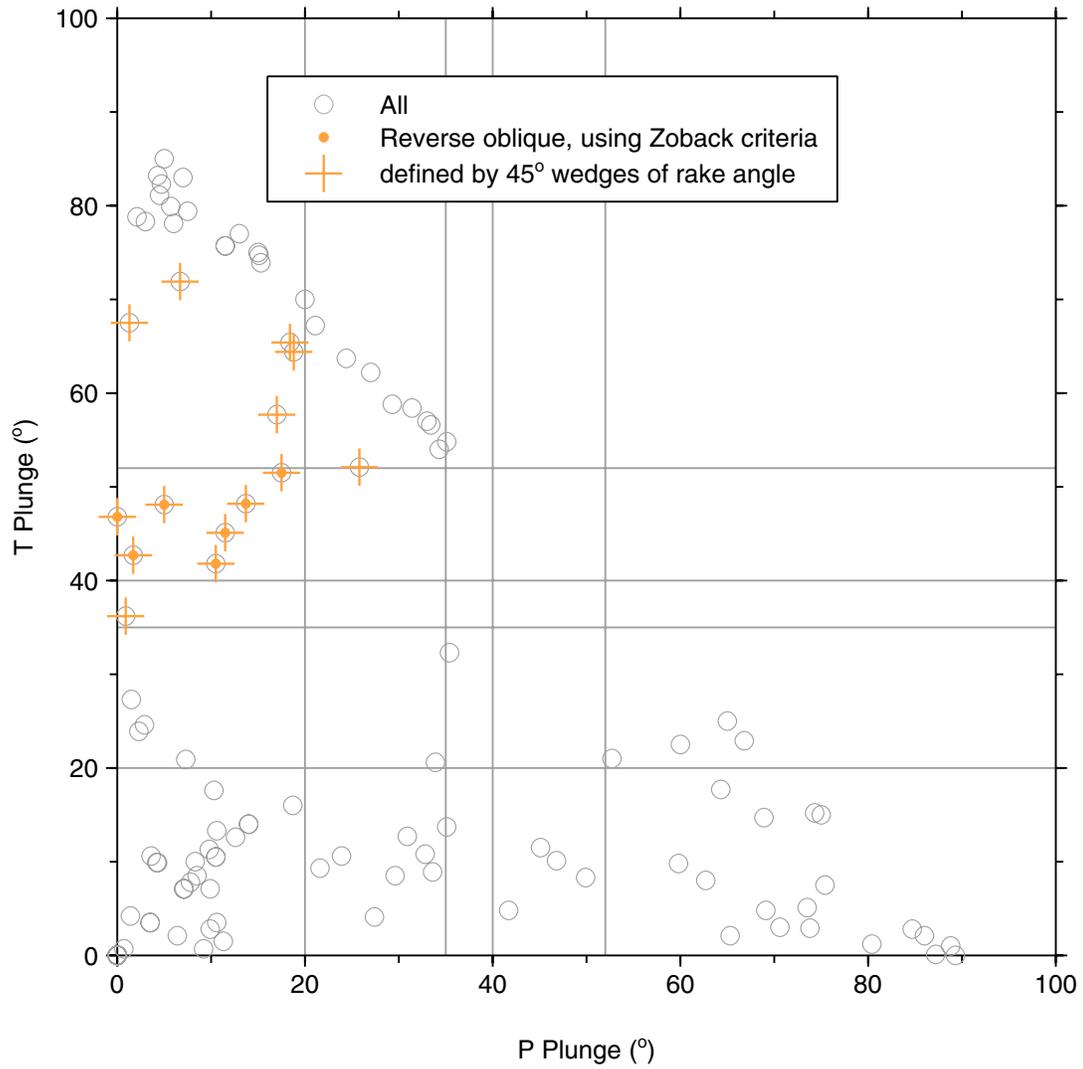
Fig. D.5 Classifications based on Zoback (1992) and using 45-degree wedges of rake angle: reverse-oblique-slip earthquakes.
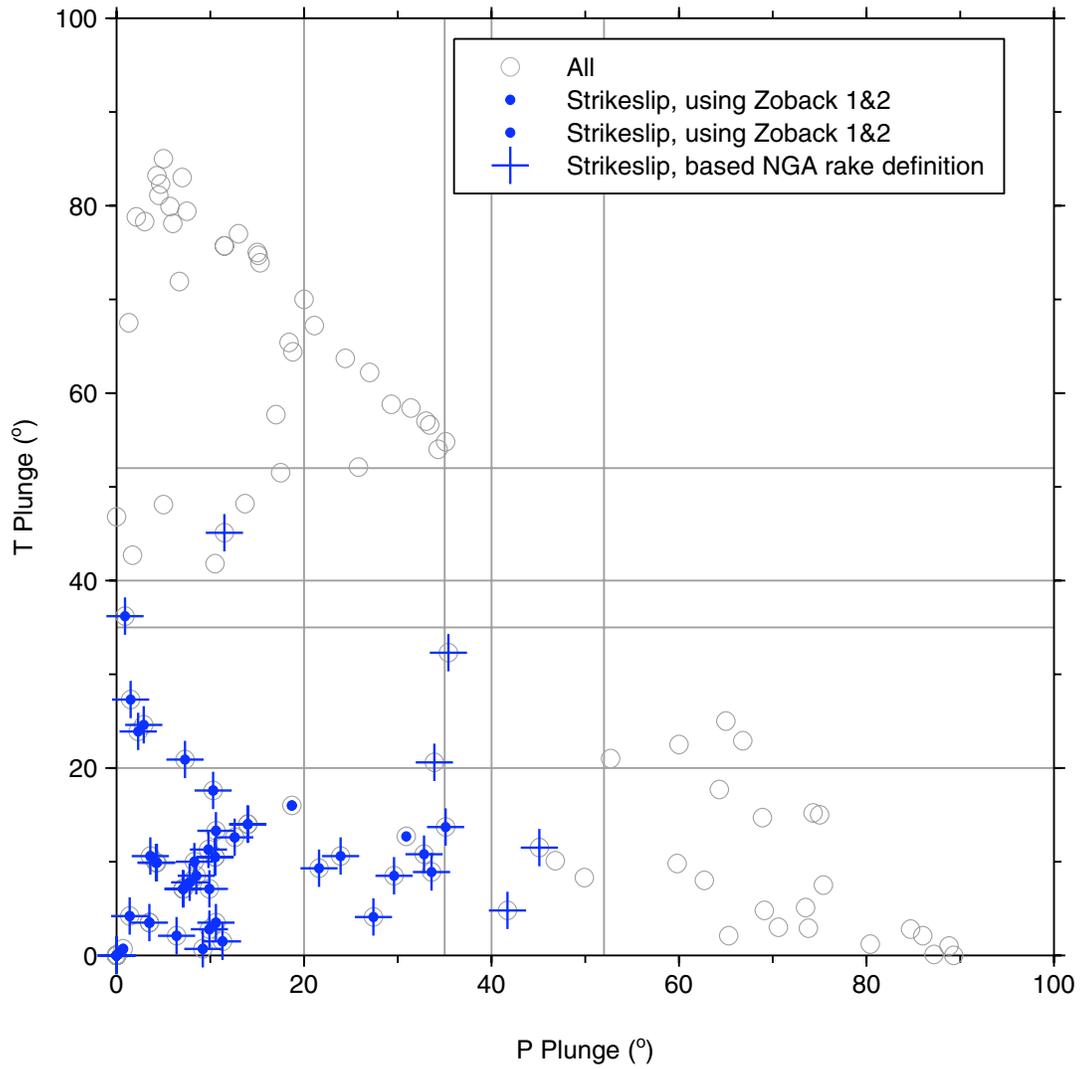
Fig. D.6   Classifications based on Zoback (1992) and rake angles (using NGA definition, shown in legend): strike-slip earthquakes.
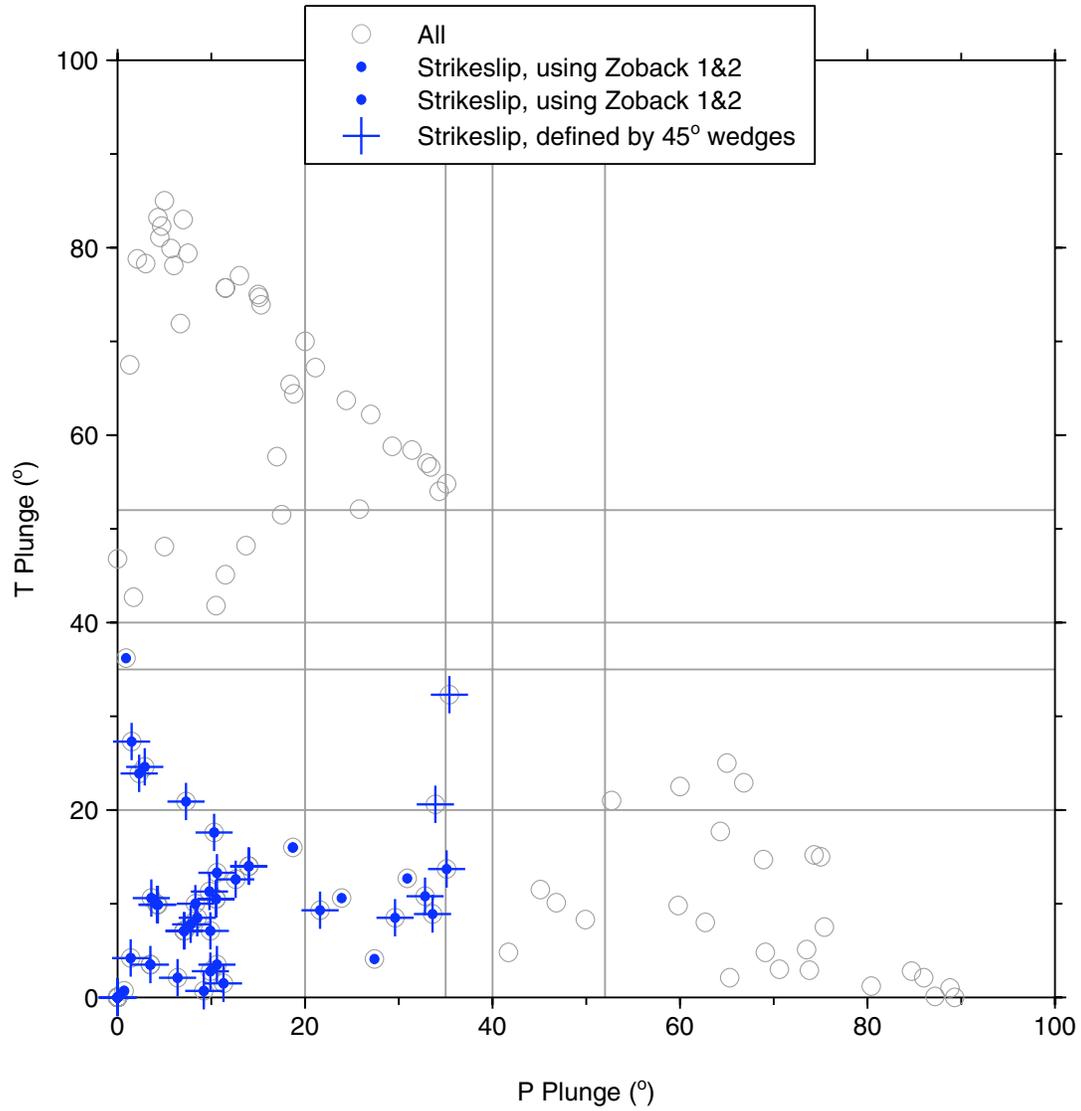
Fig. D.7 Classifications based on Zoback (1992) and using 45-degree wedges of rake angle: strike-slip earthquakes.
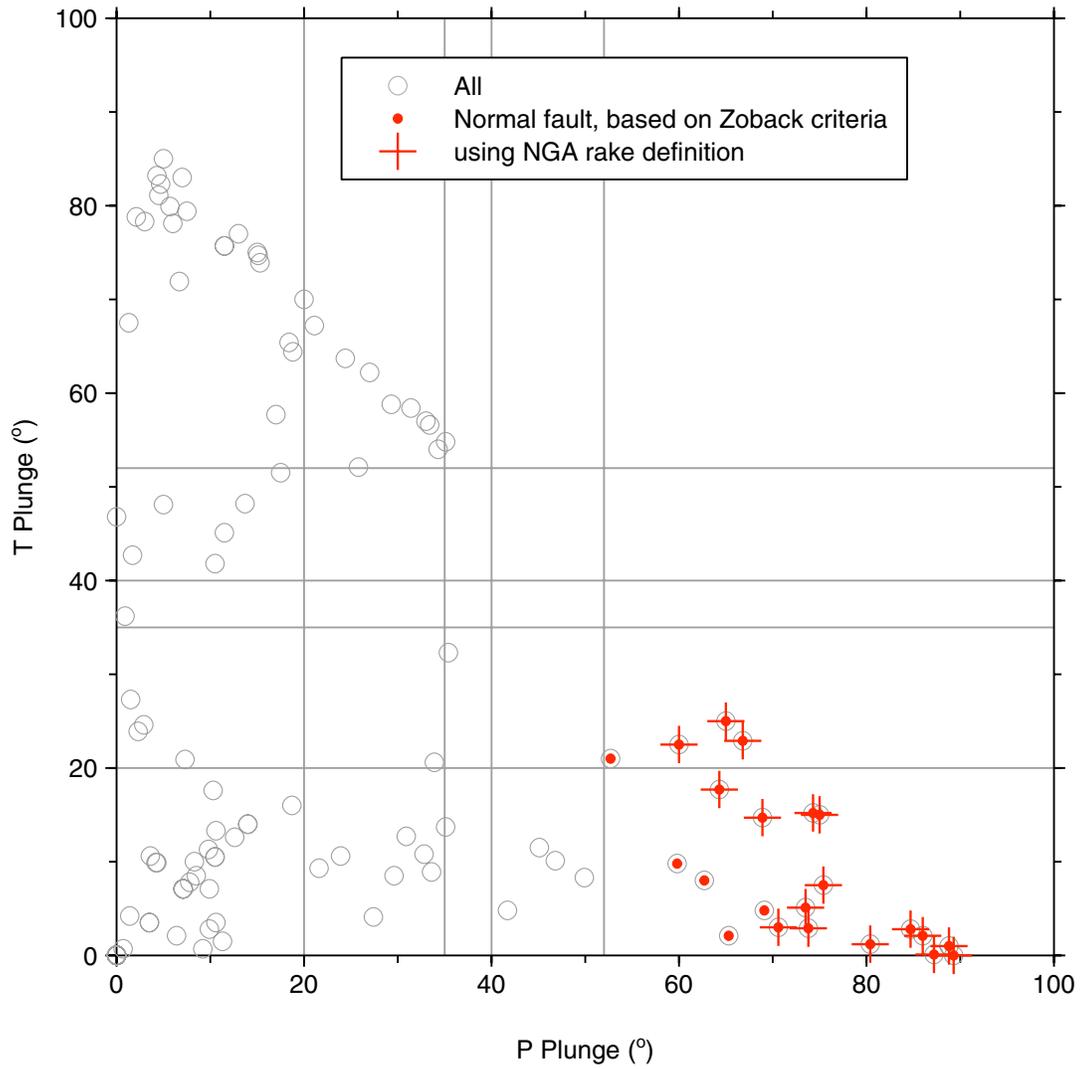
Fig. D.8 Classifications based on Zoback (1992) and rake angles (using NGA definition, shown in legend): normal-oblique-slip earthquakes.
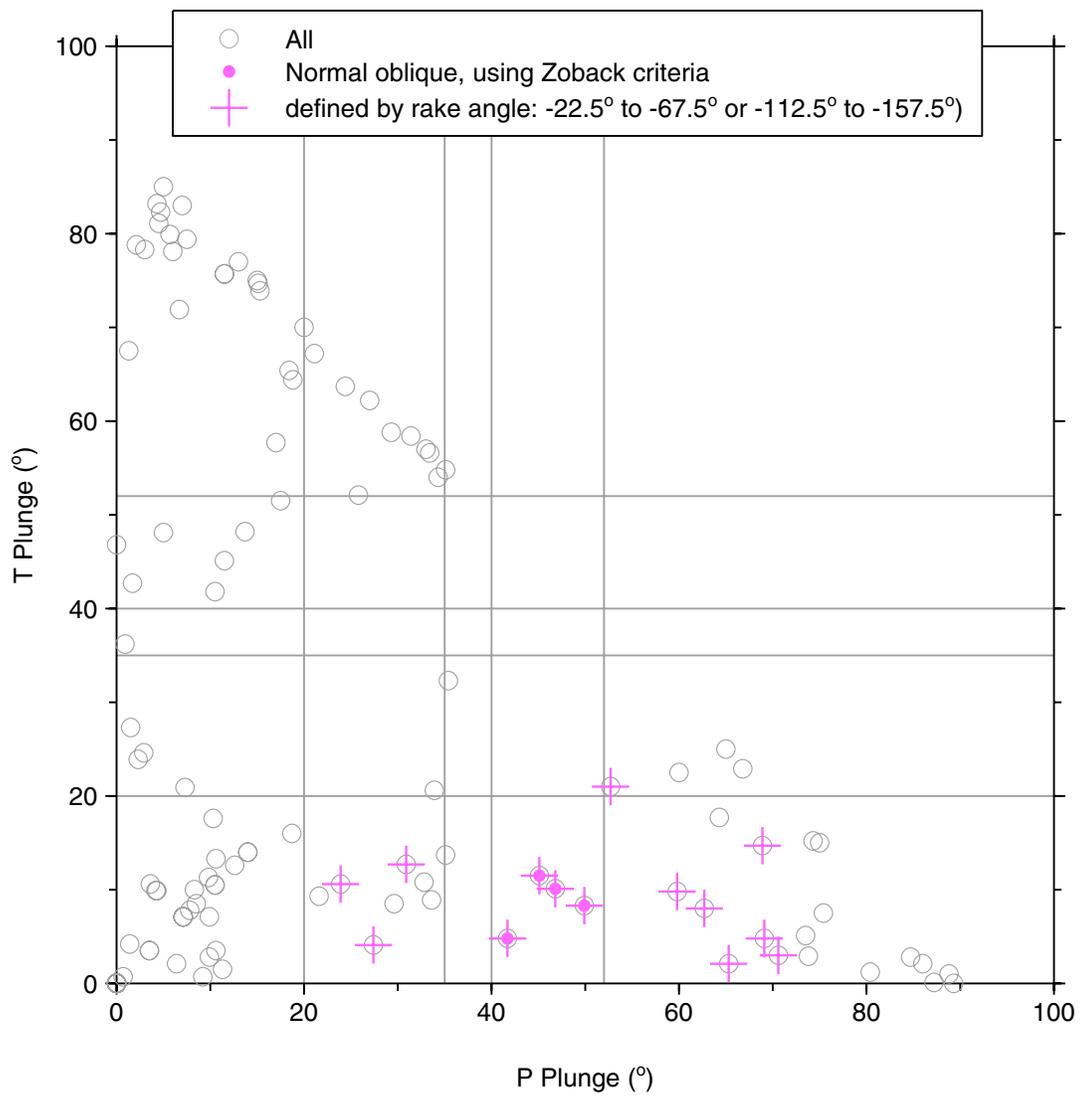
Fig. D.9   Classifications based on Zoback (1992) and using 45-degree wedges of rake angle: normal-oblique-slip earthquakes.
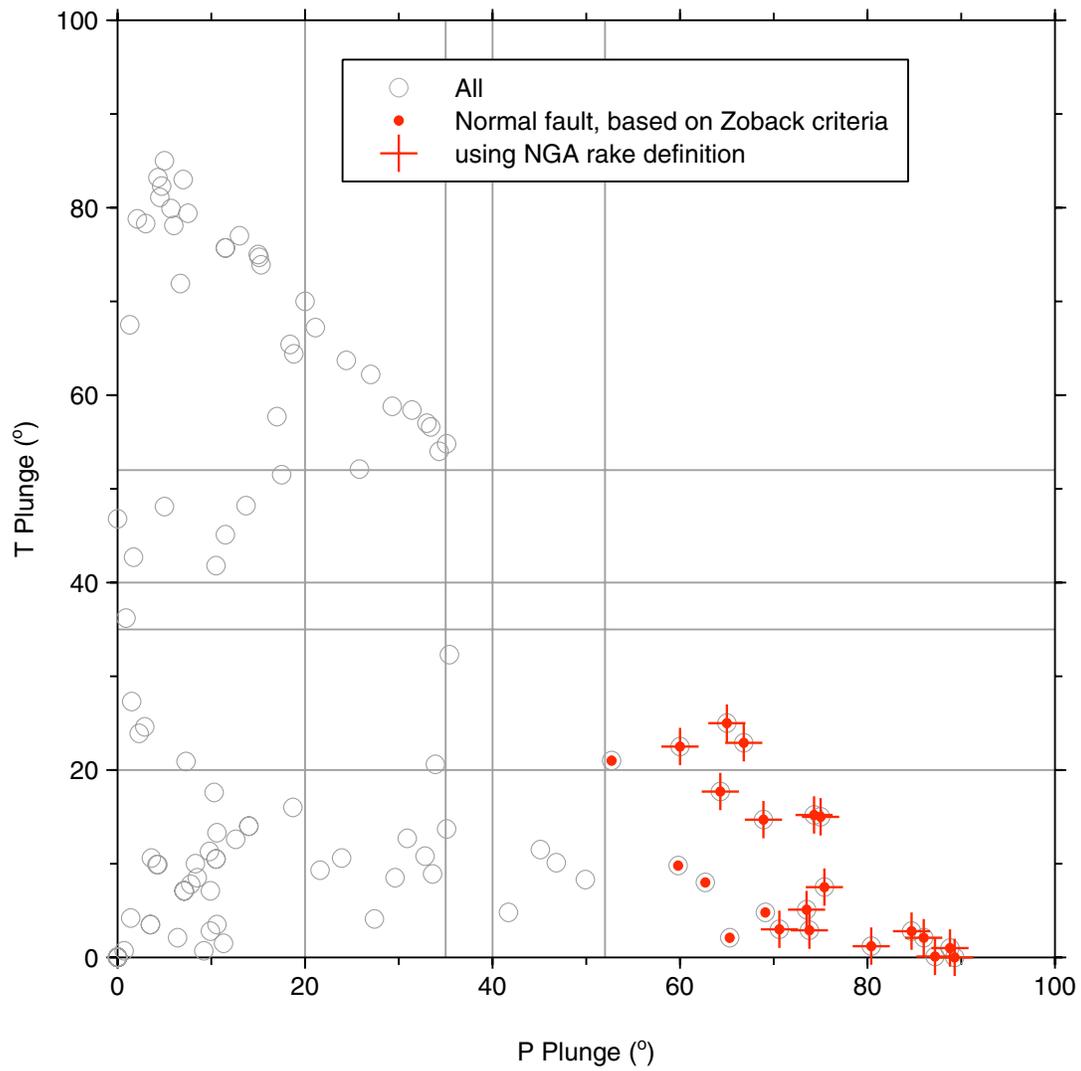
Fig. D.10 Classifications based on Zoback (1992) and rake angles (using NGA definition, shown in legend): normal-slip earthquakes.
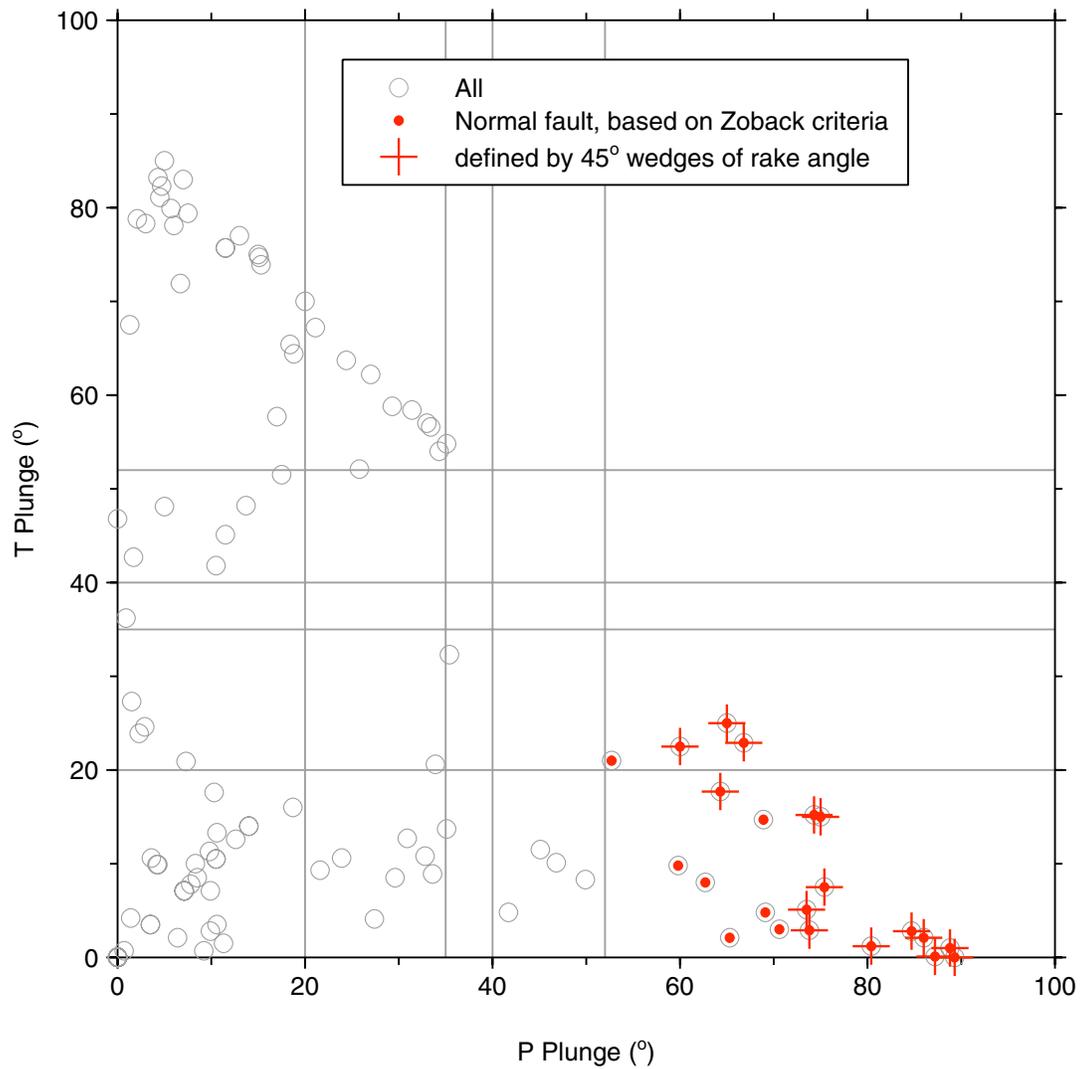
Fig. D.11 Classifications based on Zoback (1992) and using 45-degree wedges of rake angle: normal-slip earthquakes.

Appendix E: Choice of V30 for NEHRP Class

The need sometimes arises to evaluate GMPEs for a particular NEHRP site class. Because the PEER NGA GMPEs use the continuous variable V_{S30} as the predictor variable for site amplification, the question naturally arises as to what value of V_{S30} to use for a specific NEHRP class. To explore that question, I used the distribution of V_{S30} values from the borehole compilation given in Boore (2003) and from the NGA flatfile, and computed the geometric means of the average of the V_{S30} values in each NEHRP class.

I used the geometric mean of V_{S30} in each NEHRP class, as these will give the same value of $\ln Y$ as the average of the $\ln Y$'s obtained using the actual V_{S30} values in the dataset. Here is the analysis:

Because

$$\ln Y \approx b \ln V_{30}$$

the average of $\ln Y$ for a number of V_{S30}'s in a site class is:

$$\overline{\ln Y} \approx b \frac{1}{N} \sum_{i=1}^{N} \ln(V_{30})_i$$

and the same value of $\ln Y$ is obtained using the value of V_{S30} given by:

$$\ln \overline{V_{30}} = \frac{1}{N} \sum_{i=1}^{N} \ln(V_{30})_i$$

But does that mean that the values of V_{S30} in the NGA database should be used to determine the average value of V_{S30} that will be substituted into the GMPEs for a given NEHRP site class? Yes, under the assumption that the distribution of V_{S30} in the NGA database is similar to the one that would be obtained if a random site were selected. I discuss this in more detail at the end of this appendix.

To determine the geometric means of V_{S30} from the NGA flatfile, I used the Excel function *vlookup* to select only one entry per station. Figure E.1 shows the histograms. For the Boore (2003) dataset, I used values of V_{S30} for which the borehole velocities had to be extrapolated less than 2.5 m to reach 30 m. The top graph shows histograms for the Boore (2003) velocities; the middle graph shows histograms for NGA velocities for which the values of V_{S30} are based on measurements (source = 0 and 5); and the bottom graph is for NGA values from measurements and estimations (source = 0, 1, 2, and 5). In choosing the most representative value of V_{S30} for each NEHRP class, I gave most weight to the middle graph in Figure E.1. Those histograms used more data than in Boore (2003), but they are not subject to the possible bias in using an estimated value of V_{S30}, in which the value might be based on the assignment of a NEHRP class to a site, with someone else's correlation between NEHRP class and V_{S30} (correlations that may or may not have used the geometric mean of V_{S30}). I am trying to find the appropriate value independently.

The gray vertical lines in Figure E.1 are the geometric means in each NEHRP class for the data used for each graph; the black vertical lines in Figure E.1 are the V_{S30} values I recommend be used for each NEHRP class; they are controlled largely by the analysis of the source = 0 and 5 NGA data. Table E.1 contains the values of V_{S30} determined for the different histograms. Based on these values, the second-to-last column in the table contains the observation-based representative values that could substituted into the NGA GMPEs for specific NEHRP classes. The last column contains another possible set of values for evaluating the GMPEs for a specific NEHRP class; these values are the geometric means of the velocities defining each NEHRP class, rounded to the nearest 5 m/s (e.g., for NEHRP class D the value from the class definition is $\sqrt{180 \times 360} = 255$ m/s).

As mentioned before, the values in the second-to-last column of Table E.1 are valid representations of the different NEHRP classes if the distribution of velocities in the geographic region of interest is the same as that for the data used in the analysis above. Most of the measured values in the NGA database, however, come from the Los Angeles and San Francisco areas of California, so there is the potential for a bias if the V_{S30} values for those regions are not representative of a generic site. An alternative set of representative V_{S30} values for each NEHRP site class is given by the geometric mean of the velocities defining the site-class boundaries. These are given in the last column of Table E.1. The values in the last two columns of Table E.1 are similar, but to assess the impact of the two sets of representative values, I evaluated the ratios of ground motions for the two values for each NEHRP class, for a wide range of periods and distances. The differences in ground motions using the two possible sets of V_{S30} values are less than 8%, 5%, and 3% for NEHRP classes B, C, and D, respectively. The differences are largest at long periods for classes B and C and for short periods for class D. The differences in ground motions for each site class obtained using the alternative sets of representative V_{S30} values are so small that either set of could be used. The choice of one set or the other as the standard should be a group decision; I have provided information that might be used by such a group in making a choice.
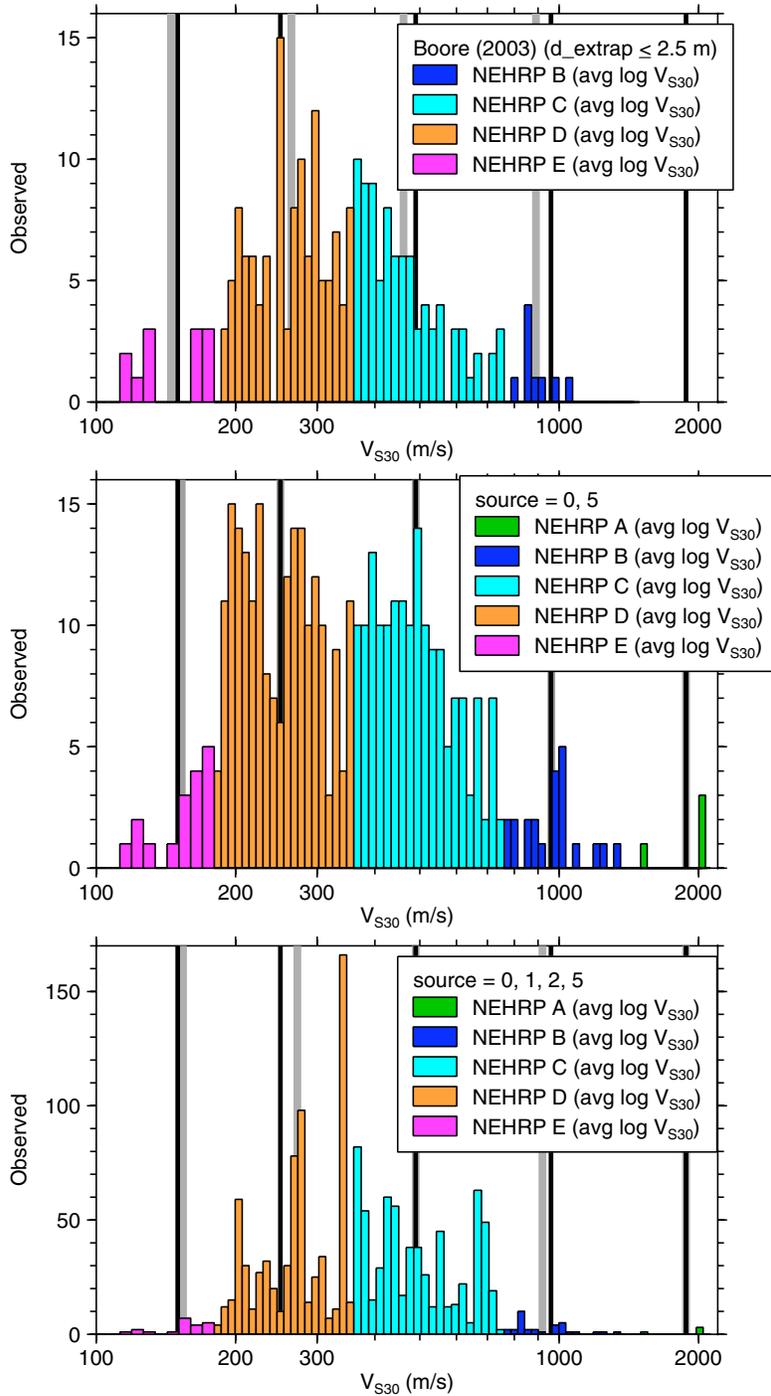
Fig. E.1 Histograms of V_{S30} used to determine value of V_{S30} to use in evaluating NGA GMPEs for particular NEHRP class (see text for details).

Table E.1 Correspondence between NEHRP class and geometric mean V_{S30} (see text).

NEHRP	nga,src0,5	nga,src0,1,2,5	Boore (2003)	Based on measured velocities	From class definitions
A	1880.5	1880.5		1880	
B	962.3	919.6	891.2	960	1070
C	489.8	489.9	461.4	490	525
D	249.8	271.5	263.7	250	255
E	153.3	153.7	145.0	150	

Appendix F: Questioning NGA Filter Values for Pacoima Dam Recording of 1971 San Fernando Earthquake

There is a large difference in the GMRotI values at long periods in the v 7.2 Excel file and those of the more recent *727brian.xls* file for the Pacoima Dam recording of the 1971 San Fernando earthquake. The reason for this is that one of the filter corners was 0.5 Hz for the 254-degree component, which trumps the filter corner of 0.1 Hz used for the 164-degree component. This results in a lowest useable frequency of 0.625 Hz. In my processing of the Pacoima data I was satisfied with a filter corner near 0.1 Hz, so I wanted to look into the reason for the large difference in filter corners for the two components. I show in Figure F.1 the displacements from the NGA processing and from my processing. For my processing I used filter corners of 0.1, 0.2, and 0.5 Hz. The first thing to note is that my results for $f_{LC} = 0.1$ Hz are close to those in the NGA flatfile for the 164-degree component, which confirms that my processing and the NGA processing return similar results for the same filter corner, at least in this case. But the next thing to note is that the dependence on filter corner is much more extreme for the 164-degree component than it is for the 254-degree component. What this tells me is that there is not much low-frequency content in the unfiltered 254-degree component record. So why was a value of 0.5 Hz used for the filter for that component?. I think it is easier to justify, from the appearance of the waveforms, a filter value of 0.1 Hz for the 254-degree component than for the 164-degree component! But I think that 0.1 Hz can be used as the filter corner for both components—doing this will add to the dataset at longer periods and close distances.
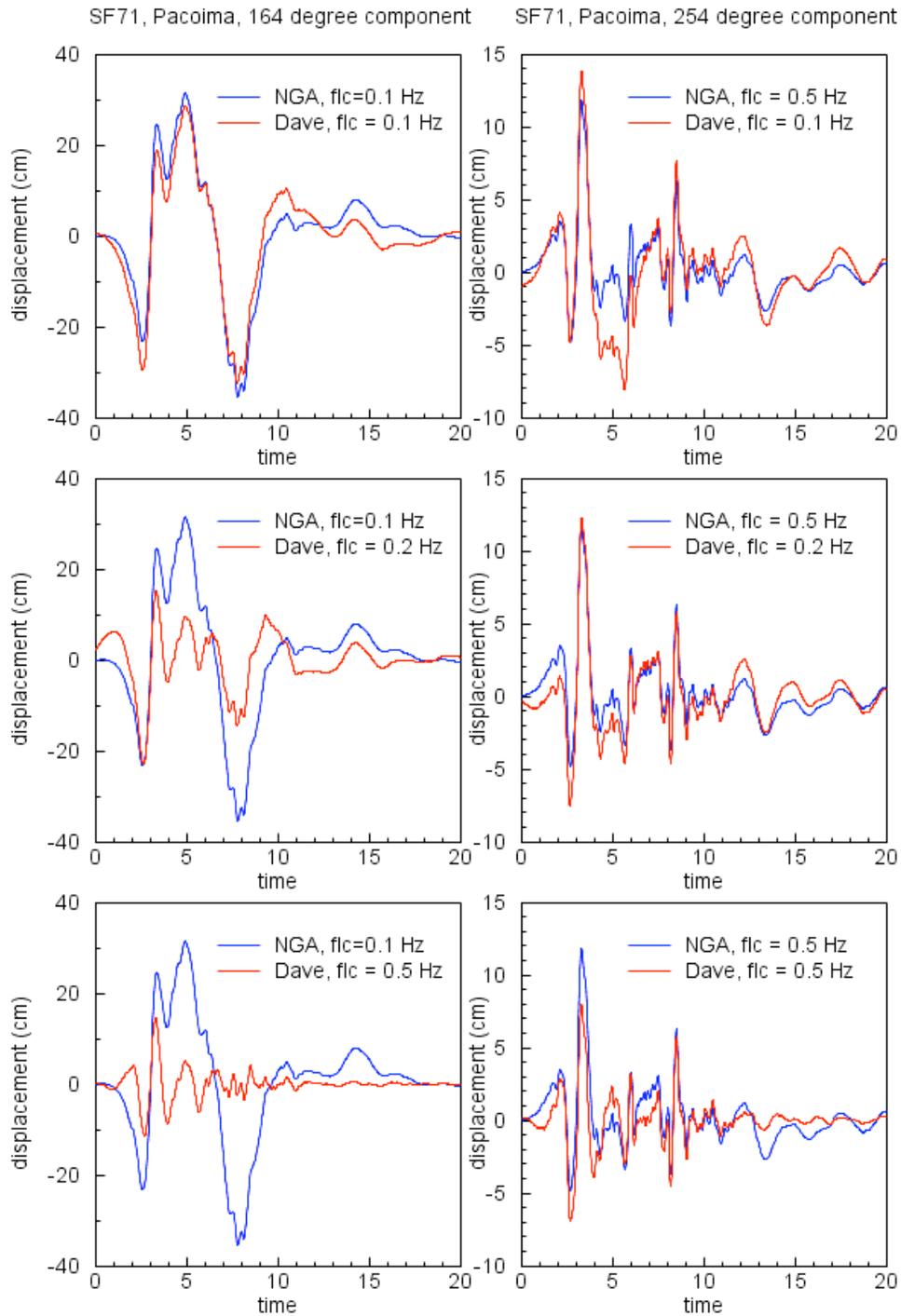
Fig. F.1 Displacements for two horizontal components at Pacoima Dam site, recorded during 1971 San Fernando earthquake, processed using different values of low-cut filter corner frequencies.

Appendix G: Notes Concerning Recordings of 1978 Tabas Earthquake

On May 7, 2004, I sent an email to all developers and a few other interested parties pointing out that the low-cut (high-pass) filter corners in the PEER NGA spreadsheet for some of the analog recordings for the 1978 Tabas, Iran, earthquake are suspiciously low (see Fig. G.1). I hypothesized that the records had had long-period noise removed via polynomial corrections, and thus the filter corners should not be used as a guide to the useable bandwidth of the response spectrum. The only reply I received was from Vladimir Graizer. As the version of the PEER NGA spreadsheet at the time that I sent the email (*Flatfile V2 (June-09-04).xls*) still contained the low-filter corners for the Tabas records, I thought I should process the data myself to get a better understanding of what is going on.

Figure G.1 contains a modified version of the plot I sent in May, 2004. In this appendix I look in detail at horizontal-component records from two stations: Tabas and Bajestan (the latter having the lowest corner of all of the Tabas recordings, although it is 120 km from the fault). I obtained the unprocessed data from the European Strong-Motion Database website. The Bajestan recording has obvious problems:. an offset at 8.3 s on the x component and spikes on the y component (Fig. G.2). Correcting for the spikes was easy—I just replaced them with the average of the two adjacent values. Dealing with the offset was more difficult. I show in Figures G.3 and G.4 the results of filtering at the PEER NGA value of 0.02 Hz, as well as at 0.1 and 0.2 Hz. Figure G.2 contains the results of filtering with no corrections for the offset on the x component. But it is clear that without removing the offset, the waveforms and peak motions are not believable for the 0.02 Hz filter. The waveforms and peaks motions are more reasonable for the higher-frequency filters, but the offset in acceleration leads to erroneous motions in the velocity and displacements with amplitudes that are close to the peak motions. I tried removing the offsets by fitting simultaneously two quadratics to the motions on each side of the offset,

constraining the linear and quadratic terms to be the same for both functions. The difference in constant terms was used as a correction. The results were not that much better. After some trial and error, I finally subtracted from the acceleration second- and fourth-order polynomials fit to the motions before and after the offset. Filtering these baseline-corrected records gave the results shown in Figure G.4. The results look better than before, but the records filtered using the 0.02 Hz filter corner are still dominated by unrealistically long-period motions. The filtered y-component record is shown in Figure G.5, after despiking. Again the motions obtained using a 0.02 Hz filter corner are not realistic. The results in Figures G.3–G.5 convince me that the filter corner given in the PEER NGA spreadsheet is not correct, at least for Bajestan (and probably not for most other records from the Tabas earthquake, the exception being the large-motion recording at Tabas).
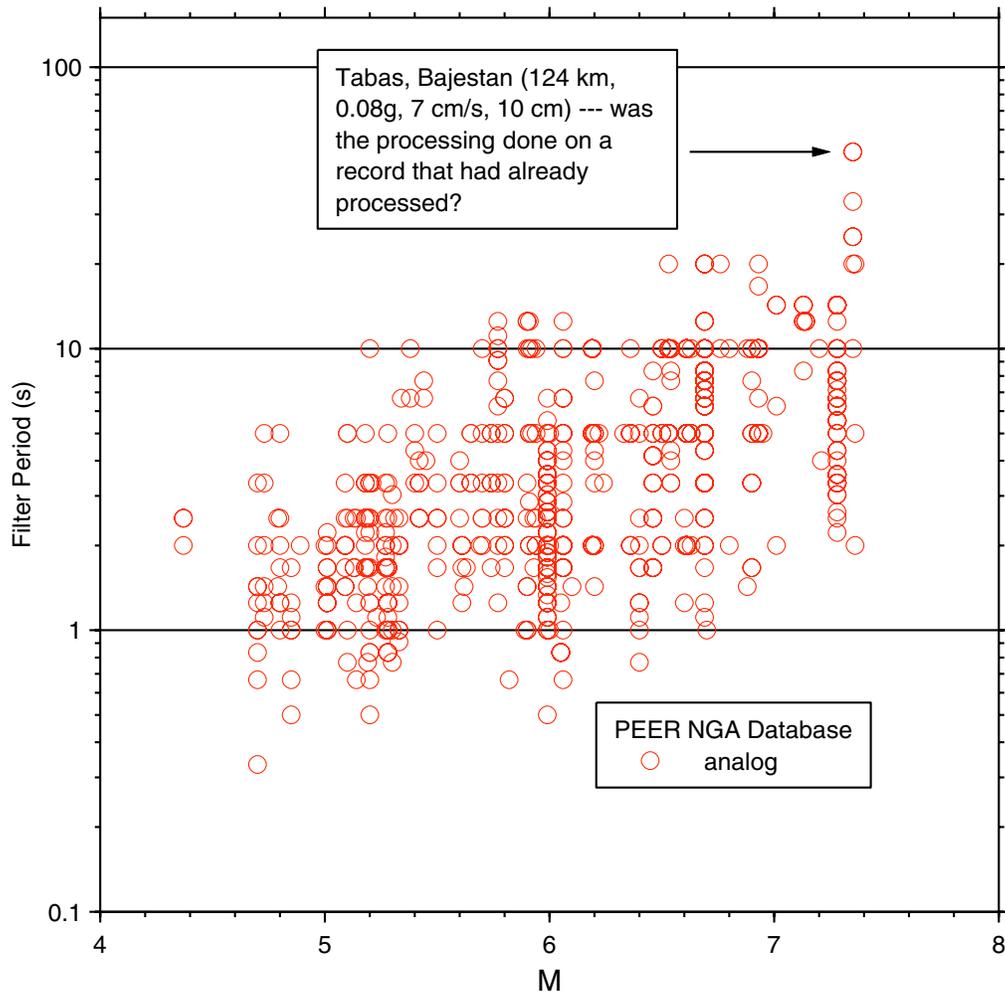
Fig. G.1 Filter period vs. M for analog records in 2004 version of NGA flatfile. Many values for Tabas earthquake seem too large.
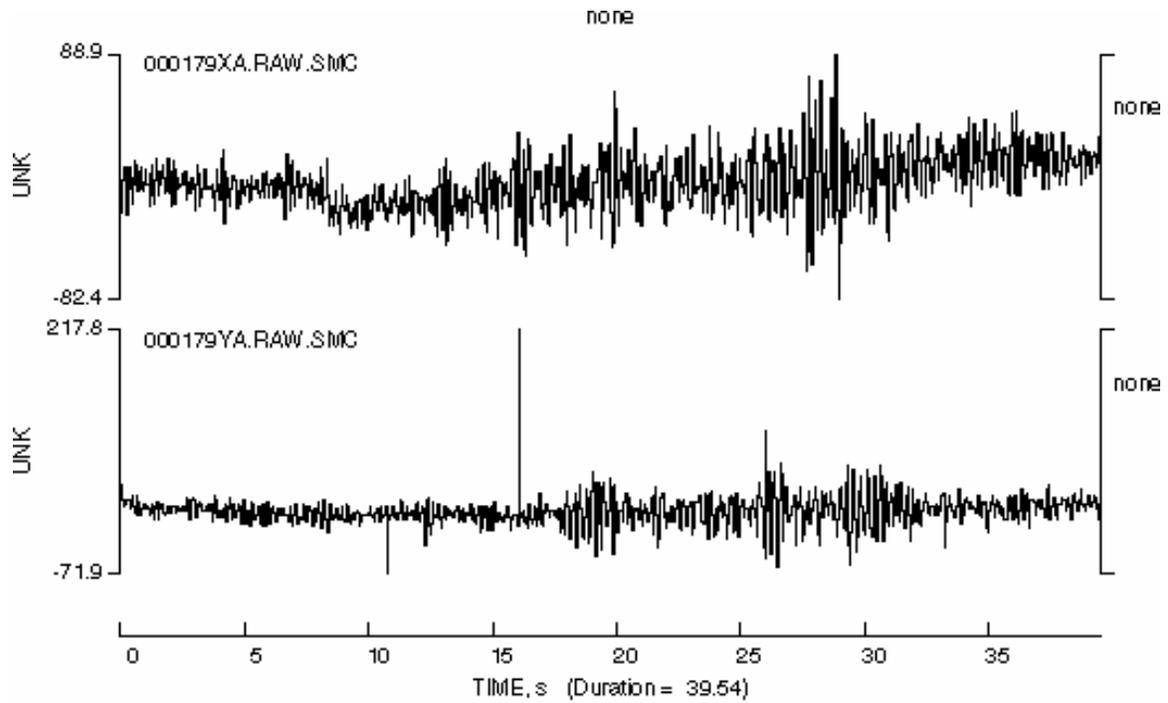
Fig. G.2 Uncorrected traces from Bajestan recording of 1978 Tabas earthquake, obtained from European Strong-Motion database website. Note step offset on x component at about 8.3 s, and large spikes on y component.
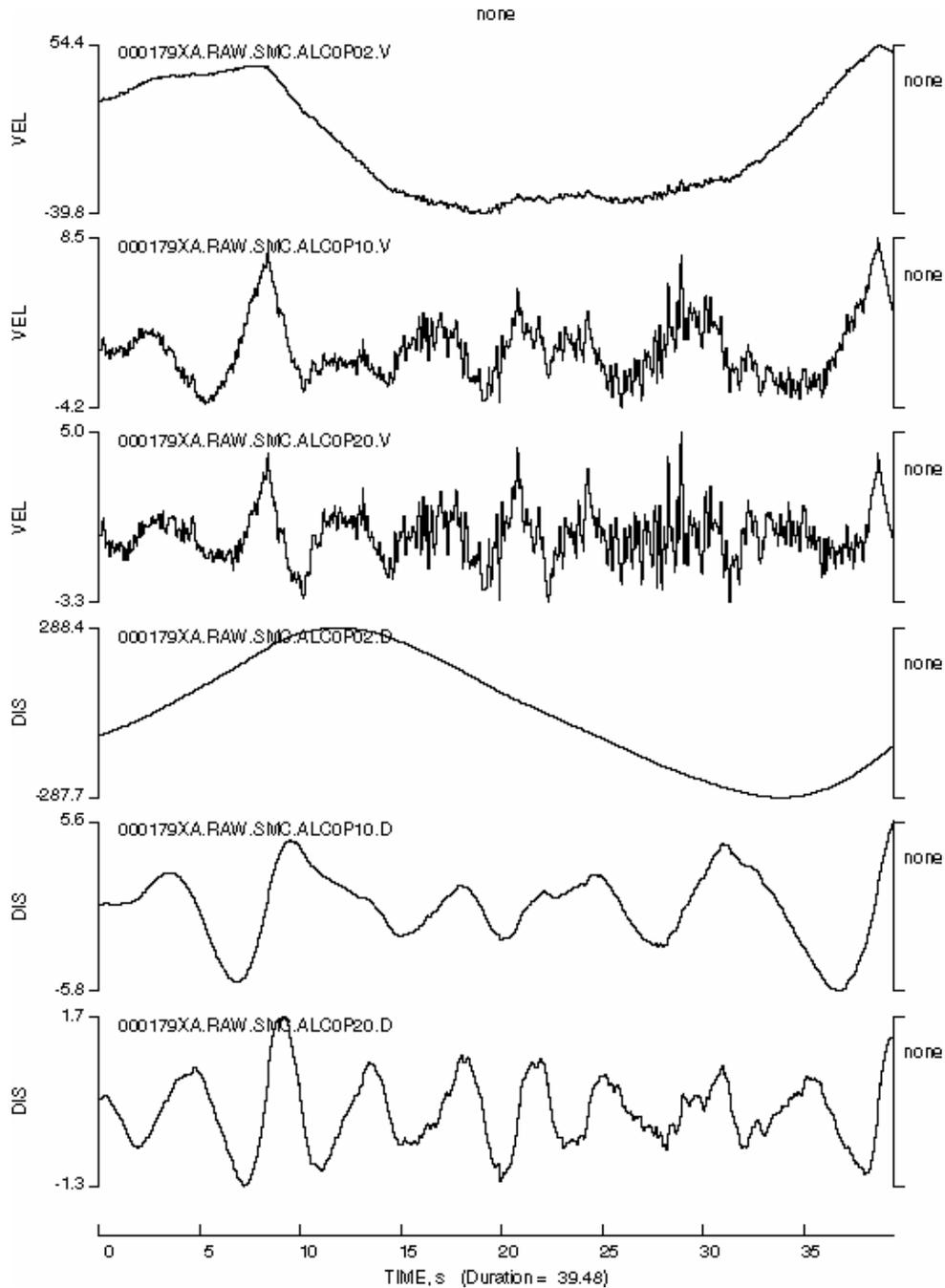
Fig. G.3 **x-component velocity and displacement traces for Bajestan recording of 1978 Tabas earthquake, obtained by filtering unprocessed acceleration with acausal Butterworth filters with corner frequencies of 0.02, 0.10, and 0.20 Hz. At low-frequencies filter decays as $1/f^8$. No correction made for step offset on x component at about 8.3 s. Only original portion of processed time series shown (pre- and post-filter transients not shown).**
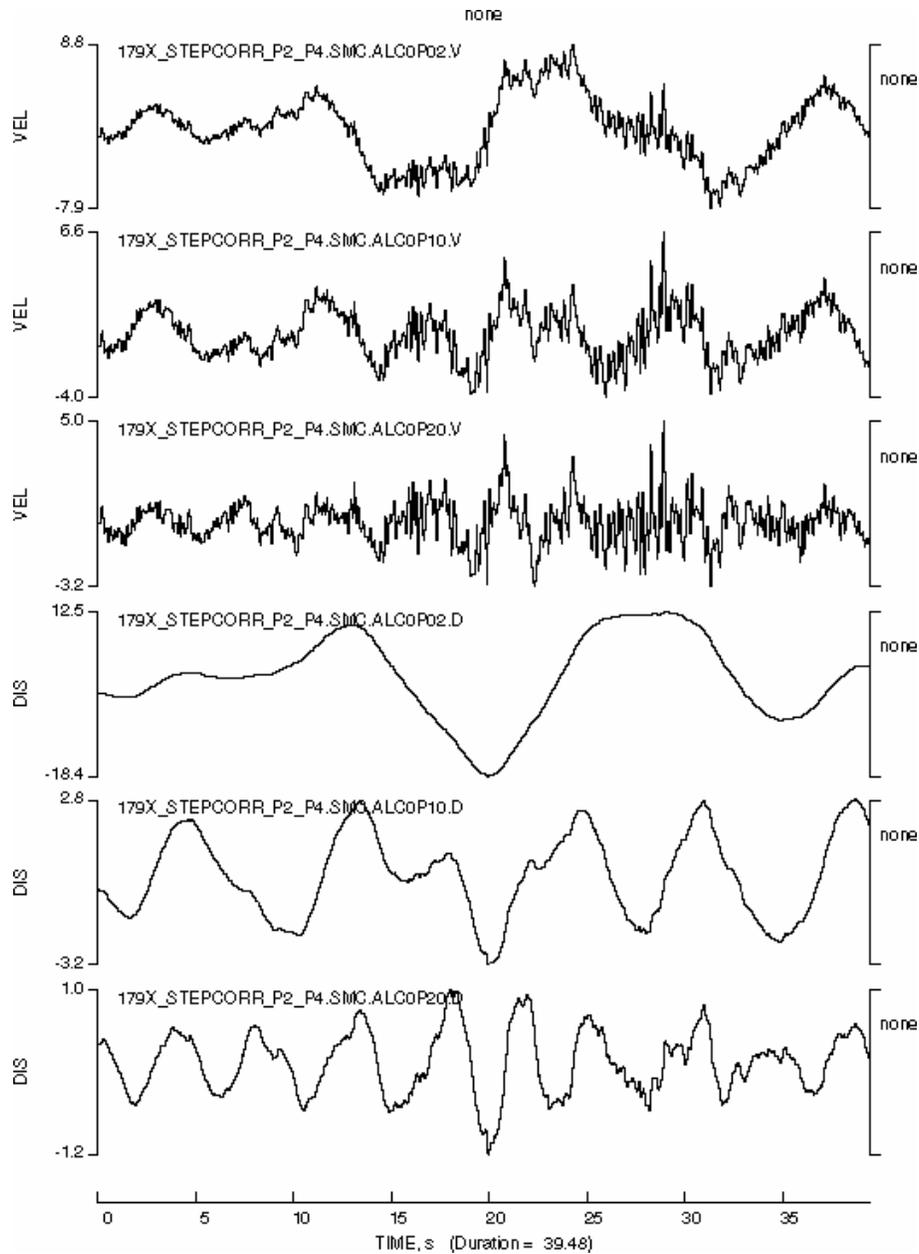
Fig. G.4 **x-component velocity and displacement traces for Bajestan recording of 1978 Tabas earthquake, obtained by filtering unprocessed, step-corrected acceleration with acausal Butterworth filters with corner frequencies of 0.02, 0.10, and 0.20 Hz. At low-frequencies filter decays as $1/f^8$. Correction for step offset on x component at about 8.3 s made by subtracting from unprocessed record second- and fourth-order polynomials fit to unprocessed accelerations on each side of offset. Only original portion of processed time series shown (pre- and post-filter transients not shown).**
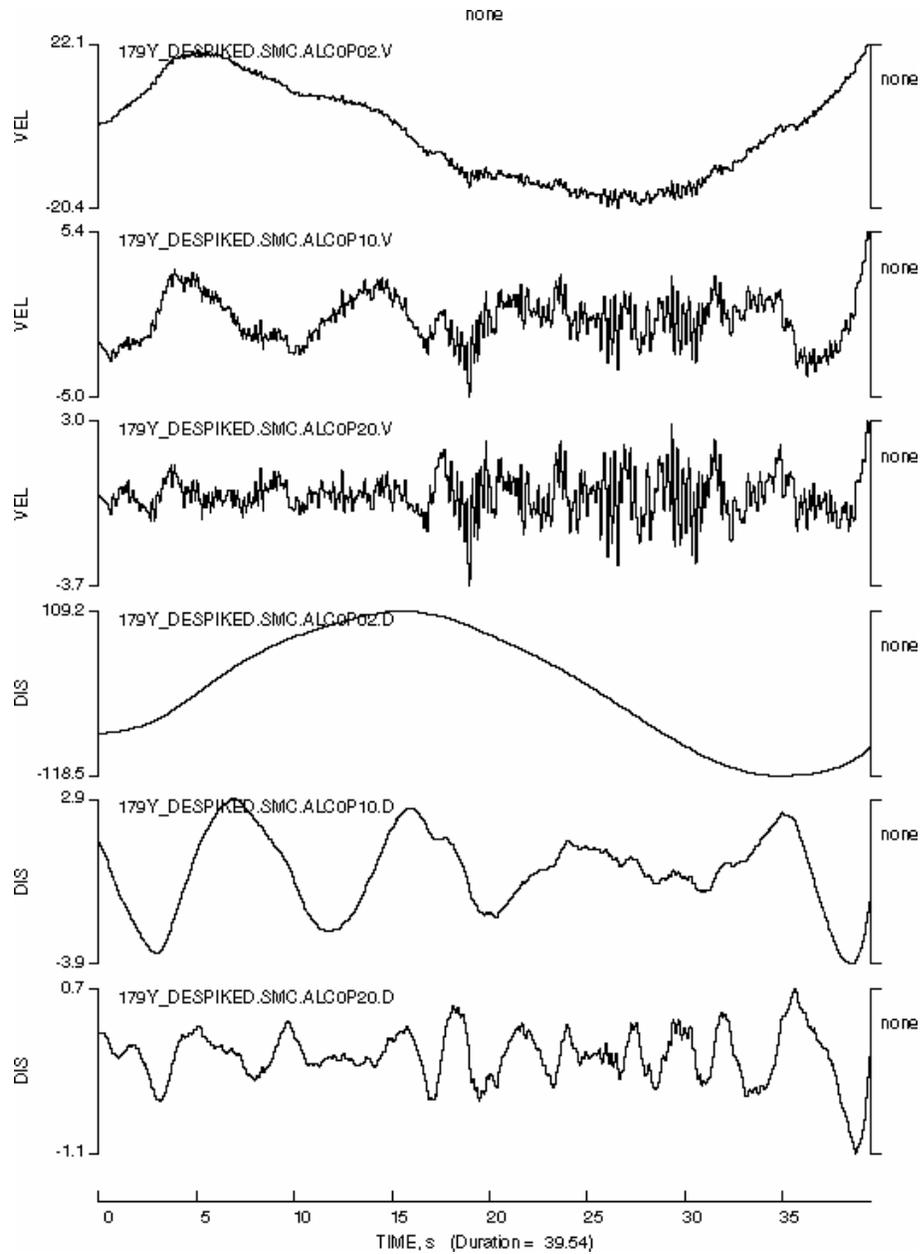
Fig. G.5 **y-component velocity and displacement traces for Bajestan recording of 1978 Tabas earthquake, obtained by filtering unprocessed, step-corrected acceleration with acausal Butterworth filters with corner frequencies of 0.02, 0.10, and 0.20 Hz, after replacing spikes at 10.74, 12.26, 16.04, 25.98, and 33.2 s with averages of values on each side of spike. At low-frequencies filter decays as** $1/f^8$ **. Only original portion of processed time series shown (pre- and post-filter transients not shown).**

The processed records for the recording at Tabas are shown in Figures G.6–G.7 for the two horizontal components. The PEER NGA value of 0.05 Hz for the low-cut filter corner seems reasonable.
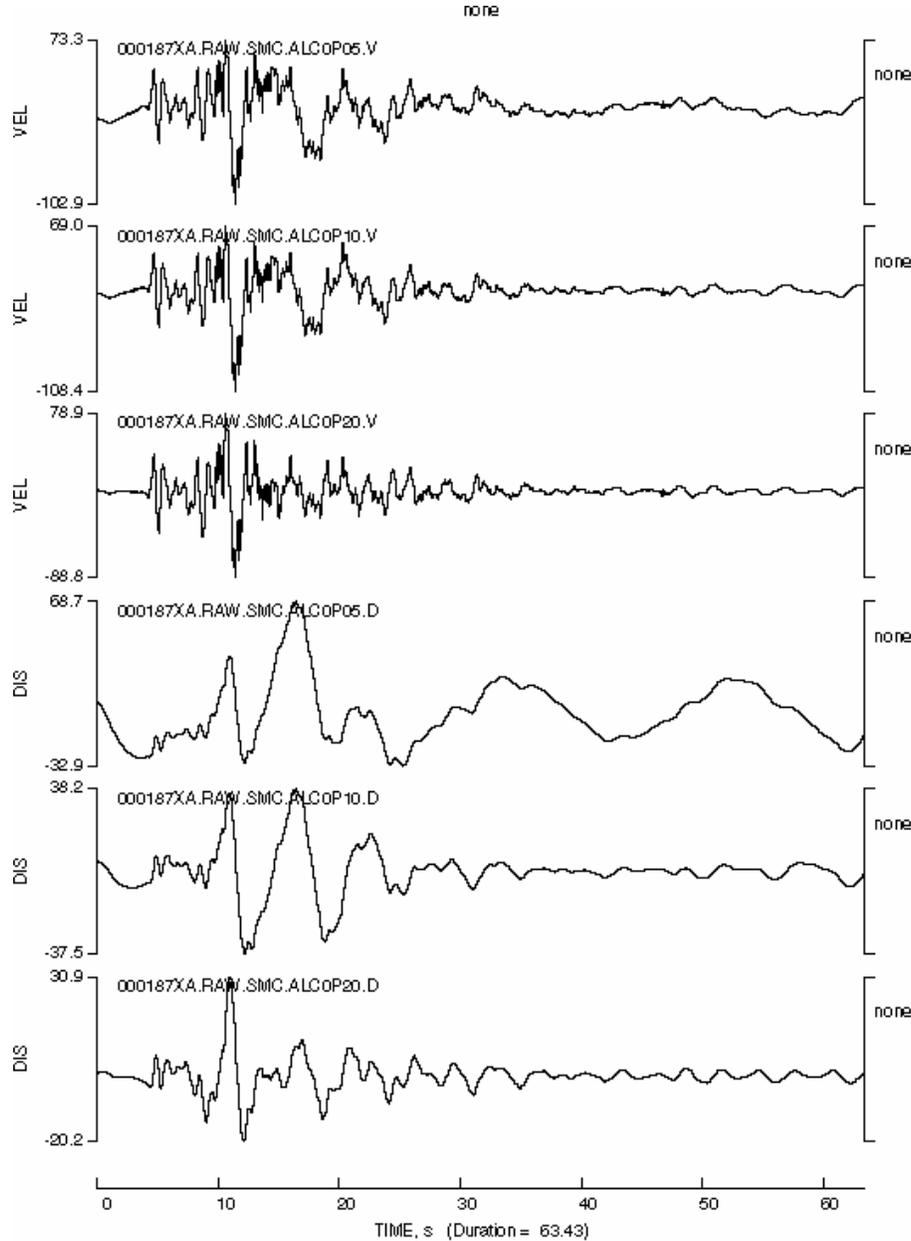
Fig. G.6   x-component velocity and displacement traces for Tabas recording of 1978 Tabas earthquake, obtained by filtering unprocessed acceleration with acausal Butterworth filters with corner frequencies of 0.05, 0.10, and 0.20 Hz.
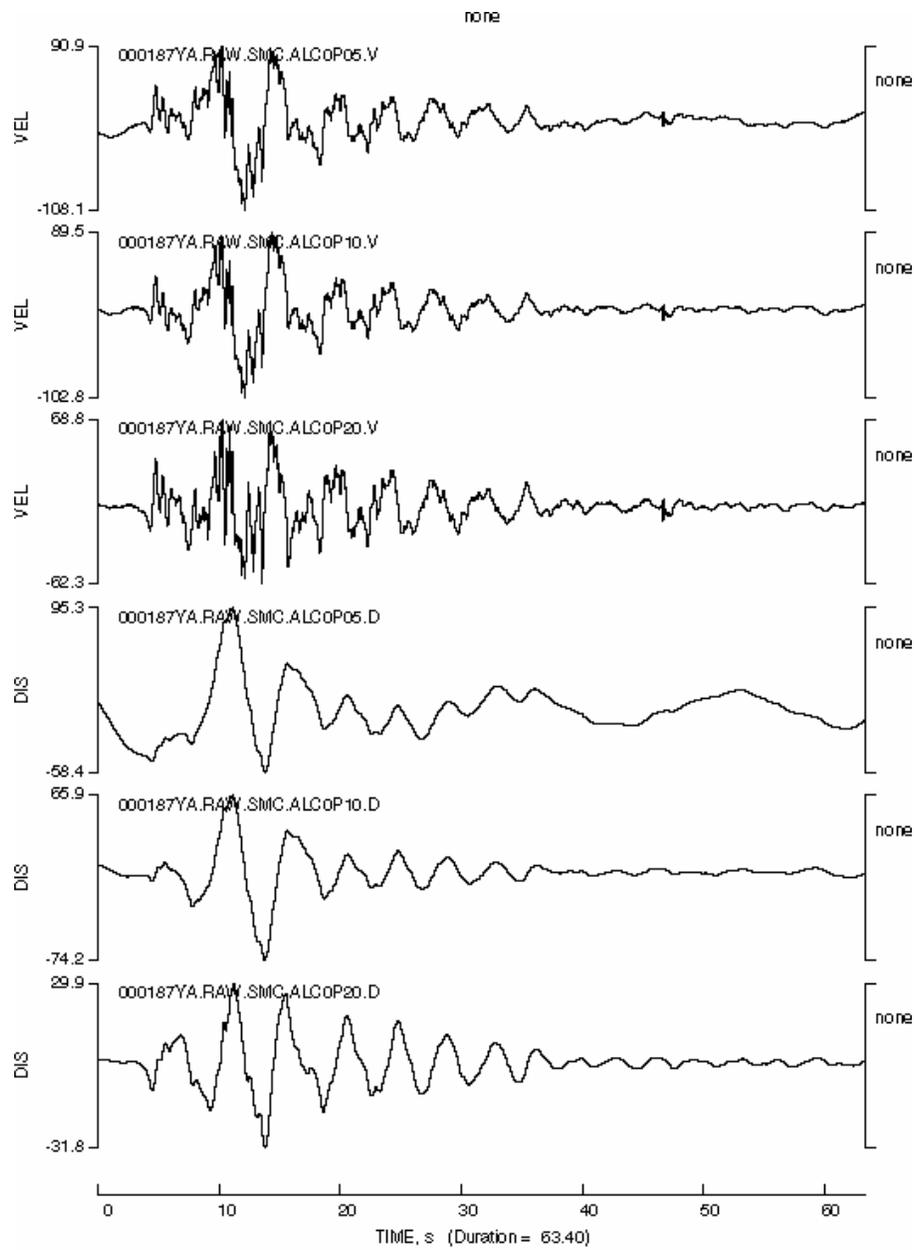
Fig. G.7 y-component velocity and displacement traces for Tabas recording of 1978 Tabas earthquake, obtained by filtering unprocessed. acceleration with acausal Butterworth filters with corner frequencies of 0.05, 0.10, and 0.20 Hz.

Table G.1 compares the geometric mean of the motions at Bajestan and Tabas obtained by my processing and contained in the PEER NGA spreadsheet (previous version). The PEER PGV value for Bajestan is similar to that obtained for a filter around 0.1 Hz, whereas the PGD value implies a lower-frequency corner (but not as low as 0.02 Hz). The Tabas values indicate that the filter corner of 0.05 Hz (the PEER NGA value) may be OK. There is relative stability in the PGV, although as often happens, the value of PGD is sensitive to the low-cut filter corner (and this is the prime reason that I will not be providing ground-motion prediction equations for PGD).

Table G.1 Geometric-mean peak ground motions for Bajestan and Tabas recordings of 1978 Tabas earthquake from records processed by PEER NGA and by D. Boore, showing influence of filter corner.

Station

Bajestan

data source	f_{LC} (Hz)	PGA(cm/s/s)	PGV(cm/s)	PGD(cm)
PEER NGA:	0.02	77.89	6.60	10.39
Filter only	0.02	74.64	34.52	183.46
Filter only	0.1	76.02	6.84	5.02
Filter only	0.2	76.48	4.30	1.37
Constant step correction	0.02	74.77	37.76	194.87
Constant step correction	0.1	75.98	7.42	5.29
Constant step correction	0.2	76.48	4.30	1.28
Polynomial step correction	0.02	76.27	13.88	46.34
Polynomial step correction	0.1	76.15	6.02	3.58
Polynomial step correction	0.2	76.48	4.30	1.15

Tabas

data source	f_{LC} (Hz)	PGA(cm/s/s)	PGV(cm/s)	PGD(cm)
PEER NGA:	0.05	827.96	109.00	59.09
Filter only	0.05	949.84	105.47	80.91
Filter only	0.1	952.11	105.56	53.24
Filter only	0.2	980.82	78.16	31.35
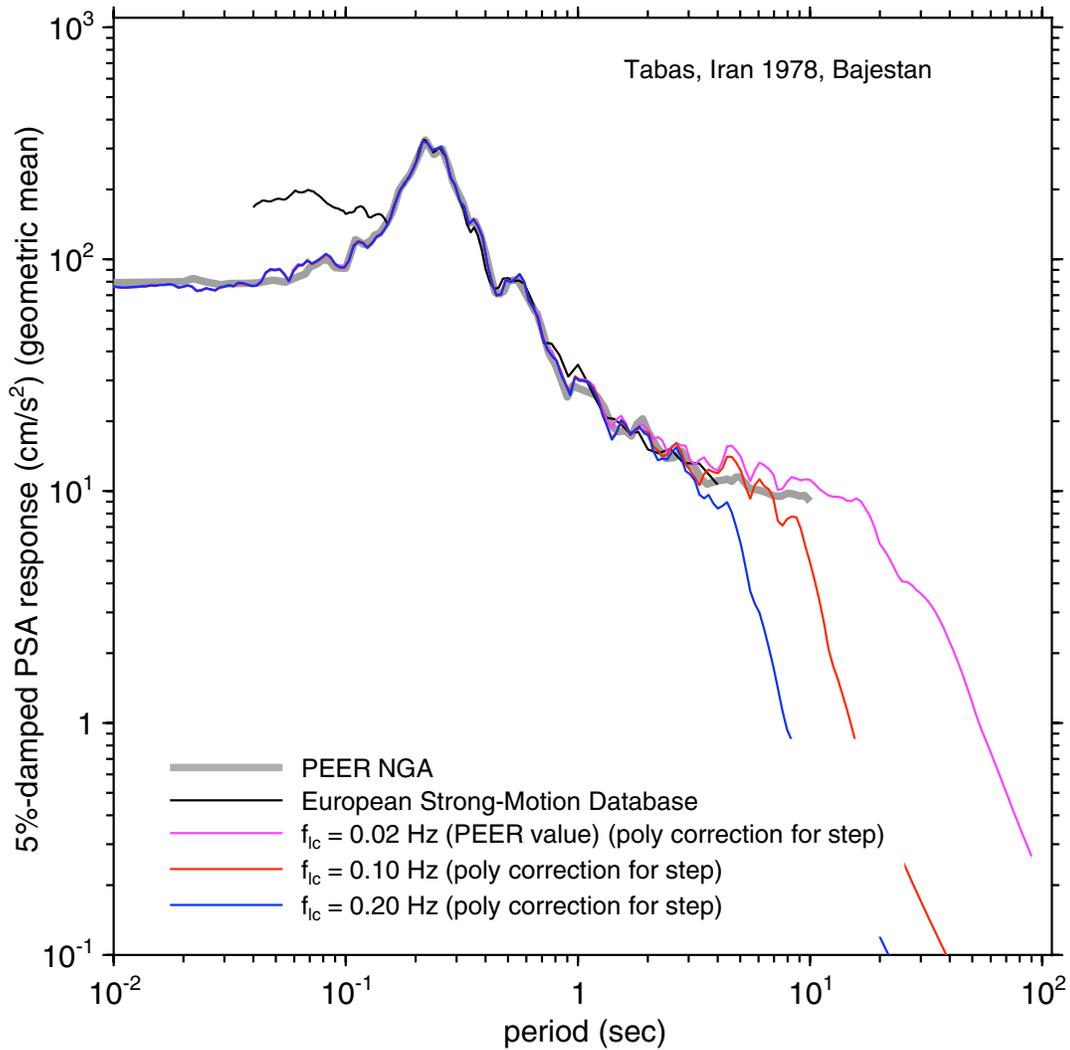
Fig. G.8 **Geometric-mean SA for Bajestan record of Tabas earthquake, processed by different groups and using different filter corners. Note that D. Boore's processing included a polynomial step correction for one component and despiking of other component (not done for processing of records available from European Strong-Motion Database website, which explains divergence at short periods).**
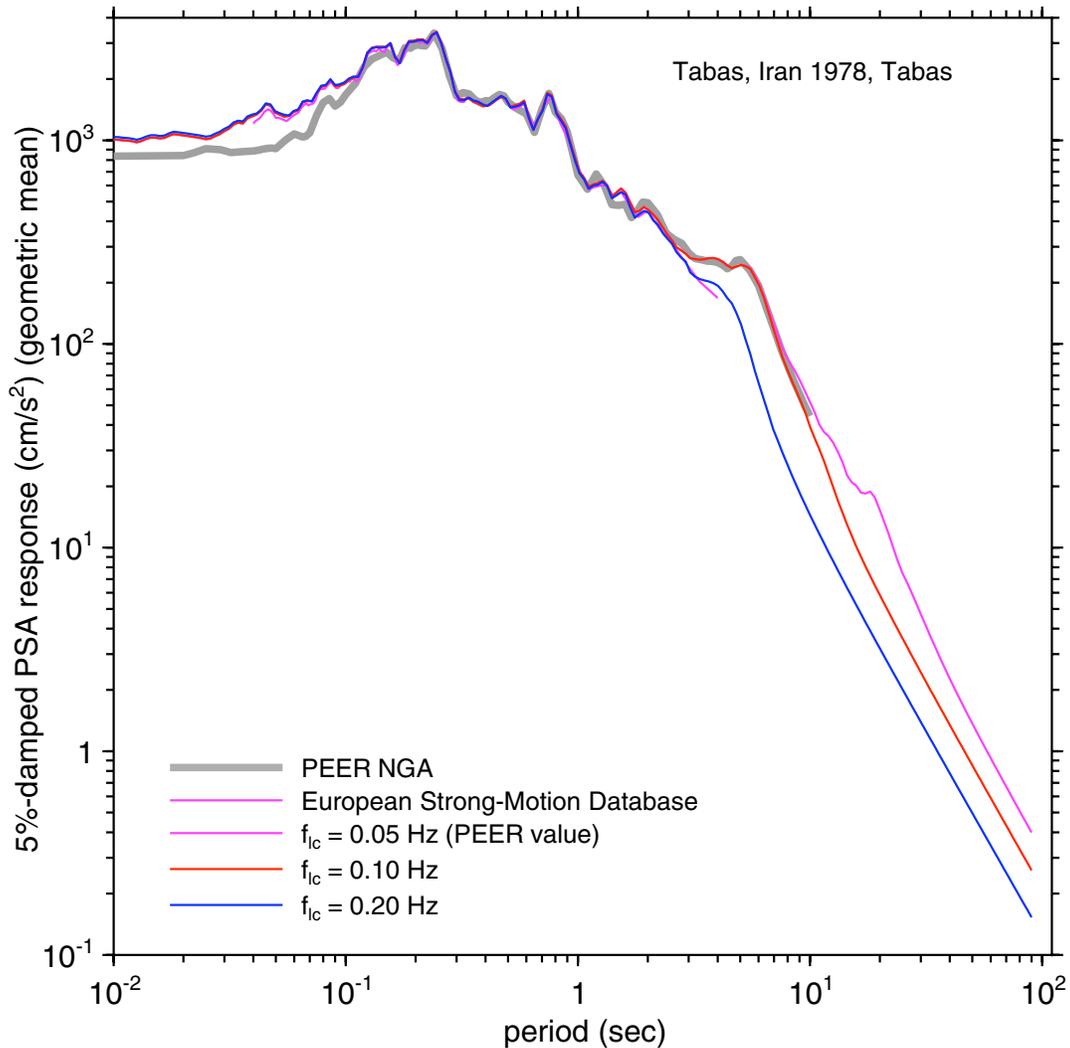
Fig. G.9 Geometric-mean SA for Tabas record of Tabas earthquake, processed by different groups and using different filter corners. Note difference between PEER–NGA and other values at short periods.

The pseudo-acceleration spectra for the Bajestan and Tabas recordings are shown in Figures G.8–G.9. The high value at short periods for the European Strong-Motion Database results are due to the presence of a large-amplitude spike on the Bajestan y-component (Fig. G.2) that was not removed during data processing. Otherwise the agreement is good over the period range 0.2–2 s. Note that the PEER NGA PGA value, and thus the short-period response spectrum, at Tabas is lower than the others (but recall that I used the European uncorrected data, so agreement should be expected between the non–PEER values at short periods, which are not as sensitive to filtering). (The processed data available from the European Strong-Motion

A -58

Database website, as opposed to the recently released CD, use a low-frequency filter of 0.25 Hz for all records.)

Another potential problem: Kashmar is an S-triggered record (Fig. G.10).
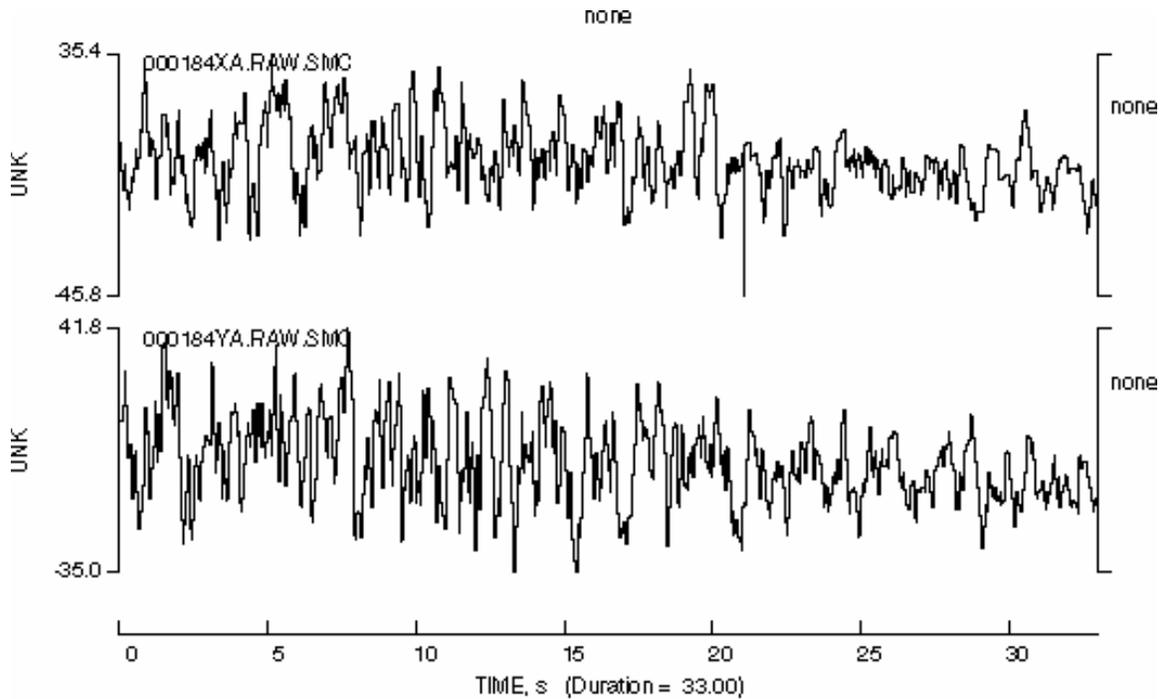
Fig. G.10 Unprocessed x- and y-component accelerations for Kashmar recording of 1978 Tabas earthquake, showing it is an S-triggered record.

Conclusions: (1) the low-cut filter corners of all but the Tabas recording of the 1978 Tabas earthquake are probably too small; (2) the PGD is sensitive to the filter corner; (3) the PEER NGA PGA for Tabas is about 15 percent lower than the value from the European Strong-Motion Database website; (4) Kashmar is an S-triggered record.

Appendix H: Notes on UCSC Recording of 1989 Loma Prieta Earthquake at Los Gatos Presentation Center

The response spectra computed by me and available in an early version of the NGA flatfile showed some disagreements for records obtained at the University of California Santa Cruz (UCSC) stations. In response to my email of July 6, 2004, Walt Silva et al. recently sent newly processed data from UC Santa Cruz for the 1989 Loma Prieta earthquake. The new spectra now seem to be in better agreement with those I computed. Figure H.1 shows a direct comparison at the UCSC station. Also shown in that figure are spectra at the Lick station on the UCSC campus.

The main topic of these notes is the Los Gatos Presentation Center (LGPC) data. I think that the data are so full of erroneous spikes (even after despiking and high-cut filtering by Silva et al.) and are so different from the relatively nearby Lexington Dam (LEXD, my code for this station) record that the motions from LGPC should not be used. As a side note, I also discovered that the coordinates of LEXD in the CGS data files and website are incorrect. Using the Topo! Program, I find that the proper coordinates for the strong-motion recorder are 37.20080 and -121.99032 (NAD27) (the other coordinates are for the center of the dam). This appendix is mainly a series of figures.
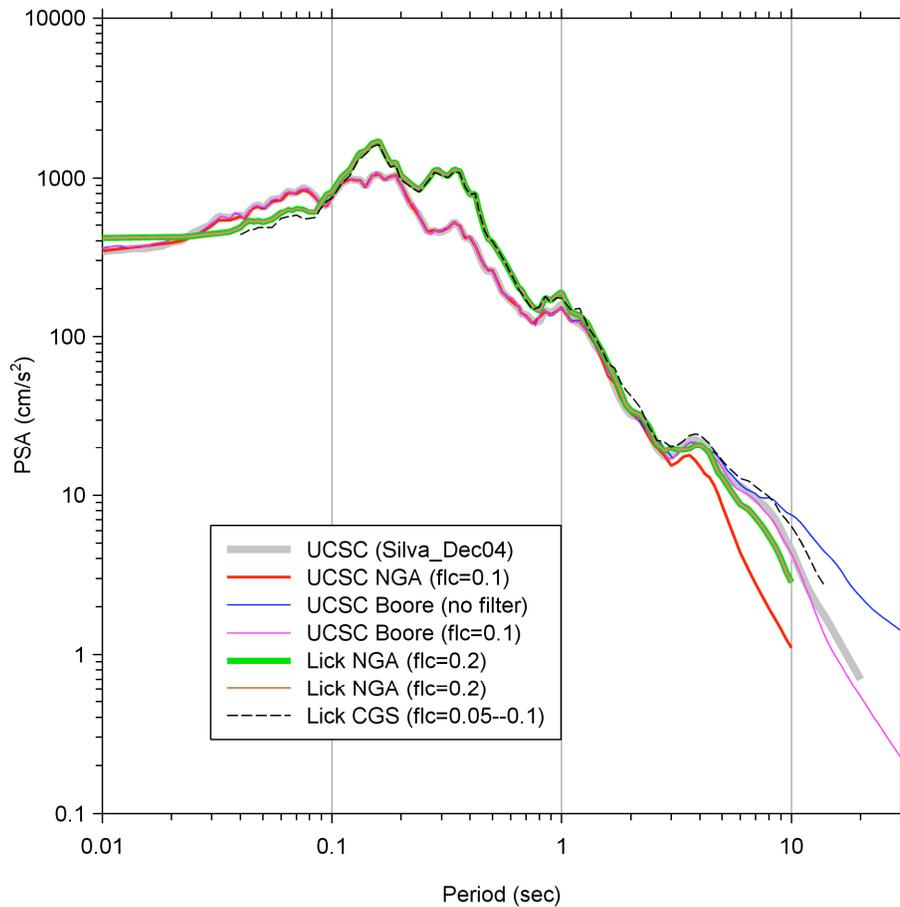
Fig. H.1 Spectra of data recorded on UCSC campus. New spectrum at UCSC (gray) is in good agreement with my spectrum of filtered motion (magenta). Note difference between Lick and UCSC spectra is probably real.

Figure H.2 is a map of the locations of LGPC and LEXD, as well as the surface projection of the Loma Prieta mainshock that Bill Joyner and I used for distance calculations in our 1993 regression work (note that with our surface projections that the JB distance is not zero for the stations, as it is for LGPC in the NGA flatfile; this is an example of differences that can occur due to the subjective choice of the dimensions and location of rupture surfaces in earthquakes. A more detailed map is given in Figure H.3.
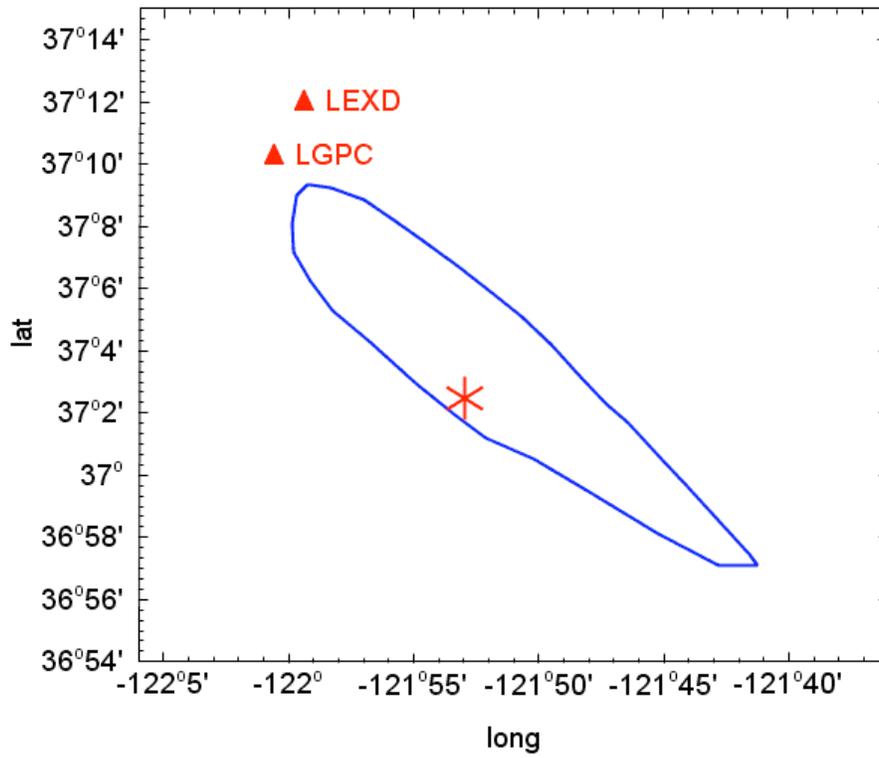
Fig. H.2 Map of surface projection of fault, epicenter (asterisk), and stations.

Fig. H.3 Map showing locations of LGPC and Lexington Dam stations (stations 3.6 km apart).

The accelerations at LGPC before despiking are shown in Figure H.4, and the first derivative of the original accelerations are given in Figure H.5 (these time series are useful for identifying spikes). Recalling that spikes in acceleration show up as double-sided pulses in jerk, the plot above suggests that there are many more spikes on the records than identified by Silva et al. To see the effect of the Silva et al. despiking (and 80 Hz high-cut filtering), I show the same two figures as before, but using the data recently sent by Silva et al. The results are shown in Figures H.6–H.7. It seems to me that much of the high-frequency chatter remains. Notice that some of the spikes in the jerk trace are single sided, implying steps in the acceleration. It is not clear to me that the despiked record (Figs. H.6–H.7) is that much better than the original record (Figs. H.4–H.5).
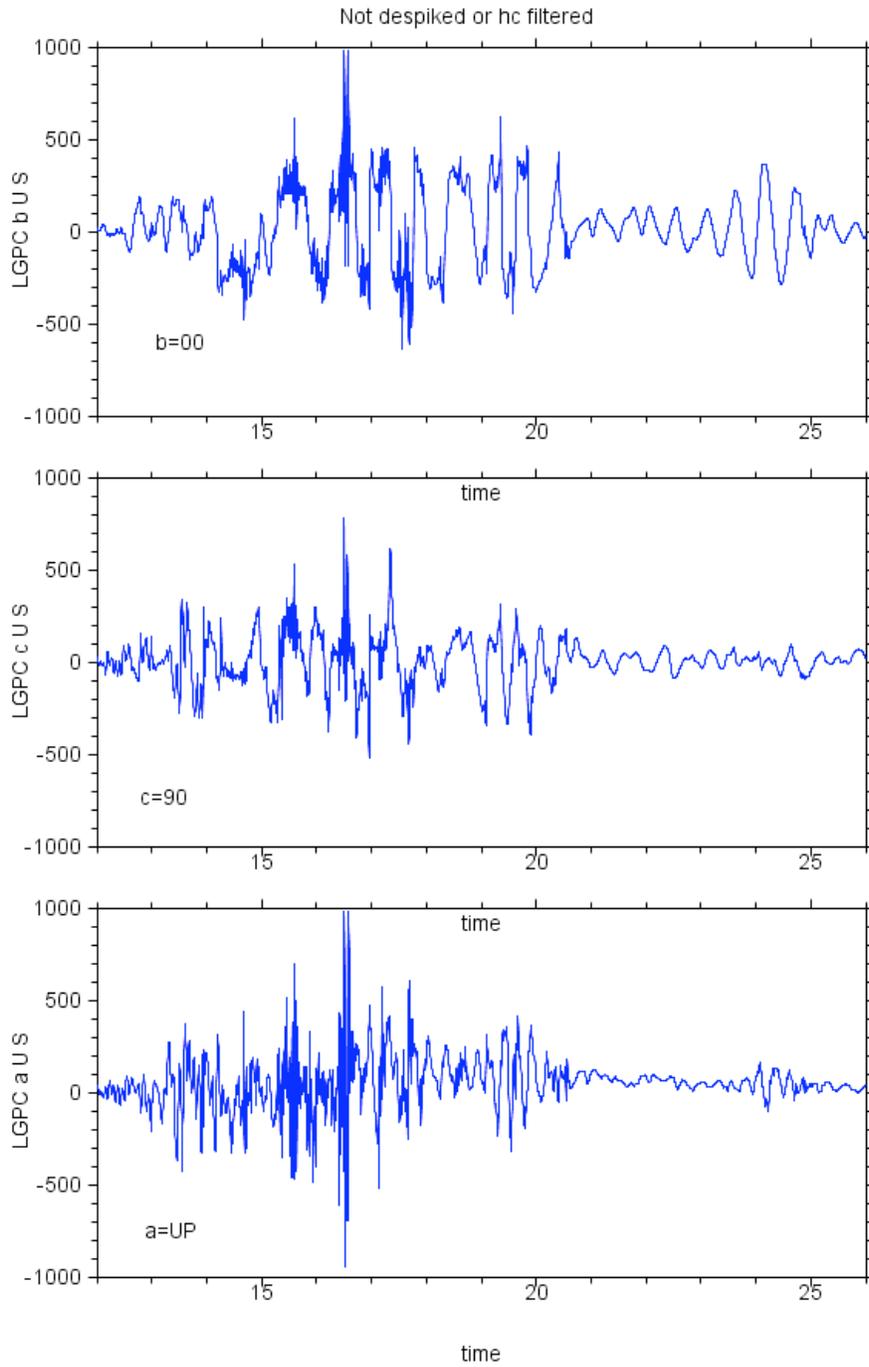
Fig. H.4 Accelerations at LGPC, before despiking.
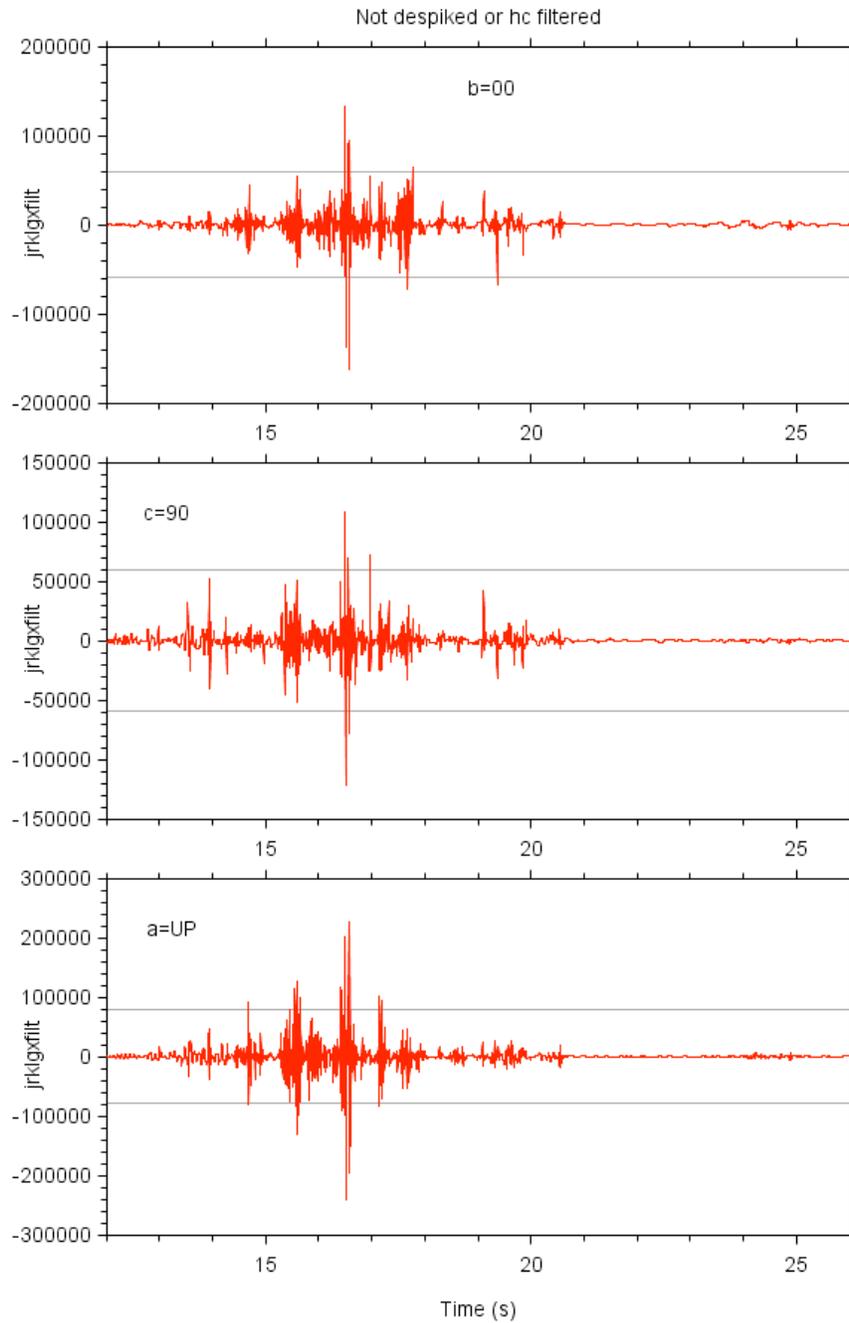
Fig. H.5 "Jerk" (first difference of acceleration) at LGPC, using original record (not despiked). Horizontal gray lines correspond to jerk level used by Silva et al. in despiking record (first difference would be 981*0.3/0.005 = 58,860 for horizontal components and 981*0.4/0.005 = 78,480 for vertical component).
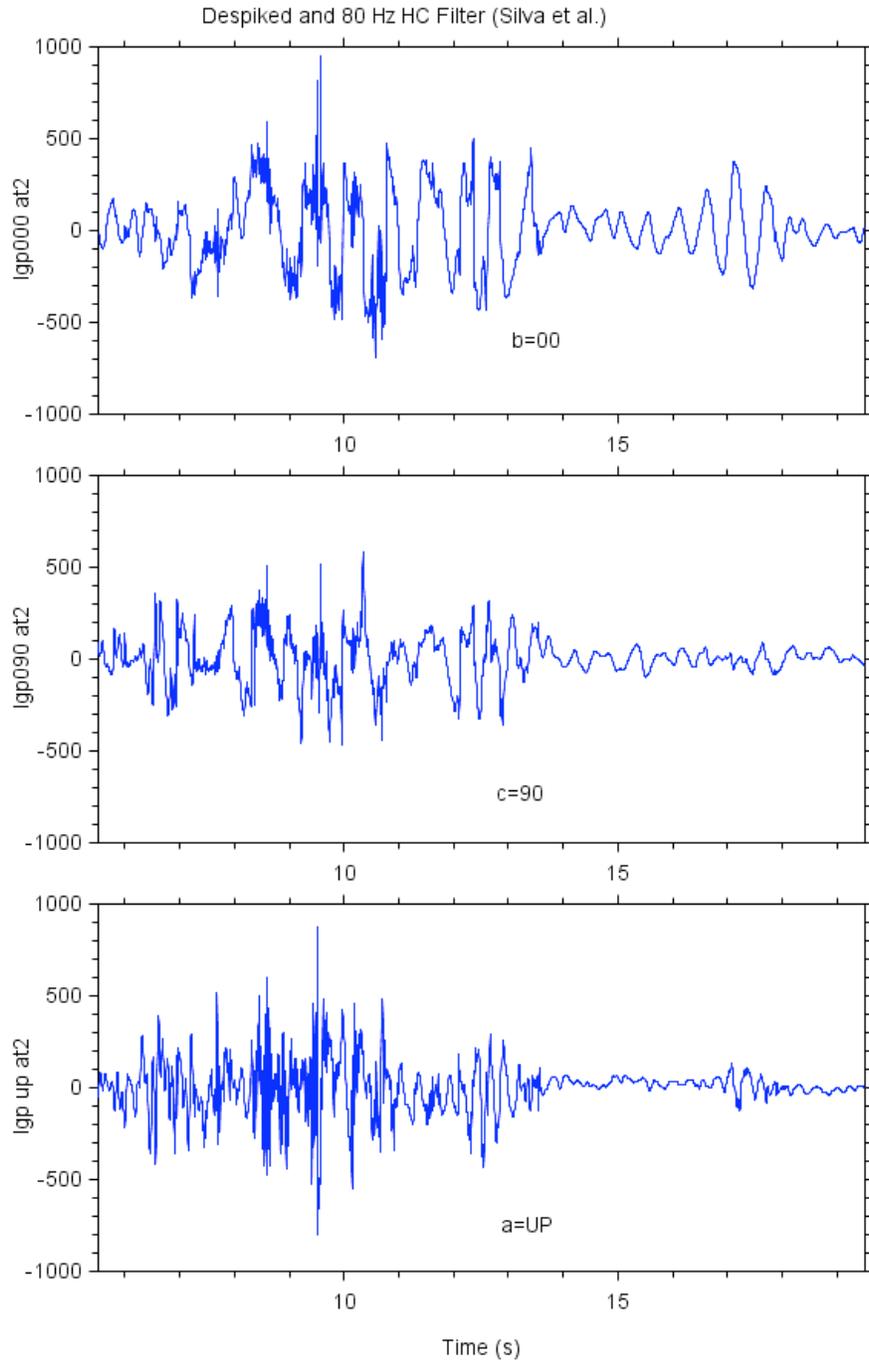
Fig. H.6 Despiked and high-cut filtered by Silva et al.

A - 67
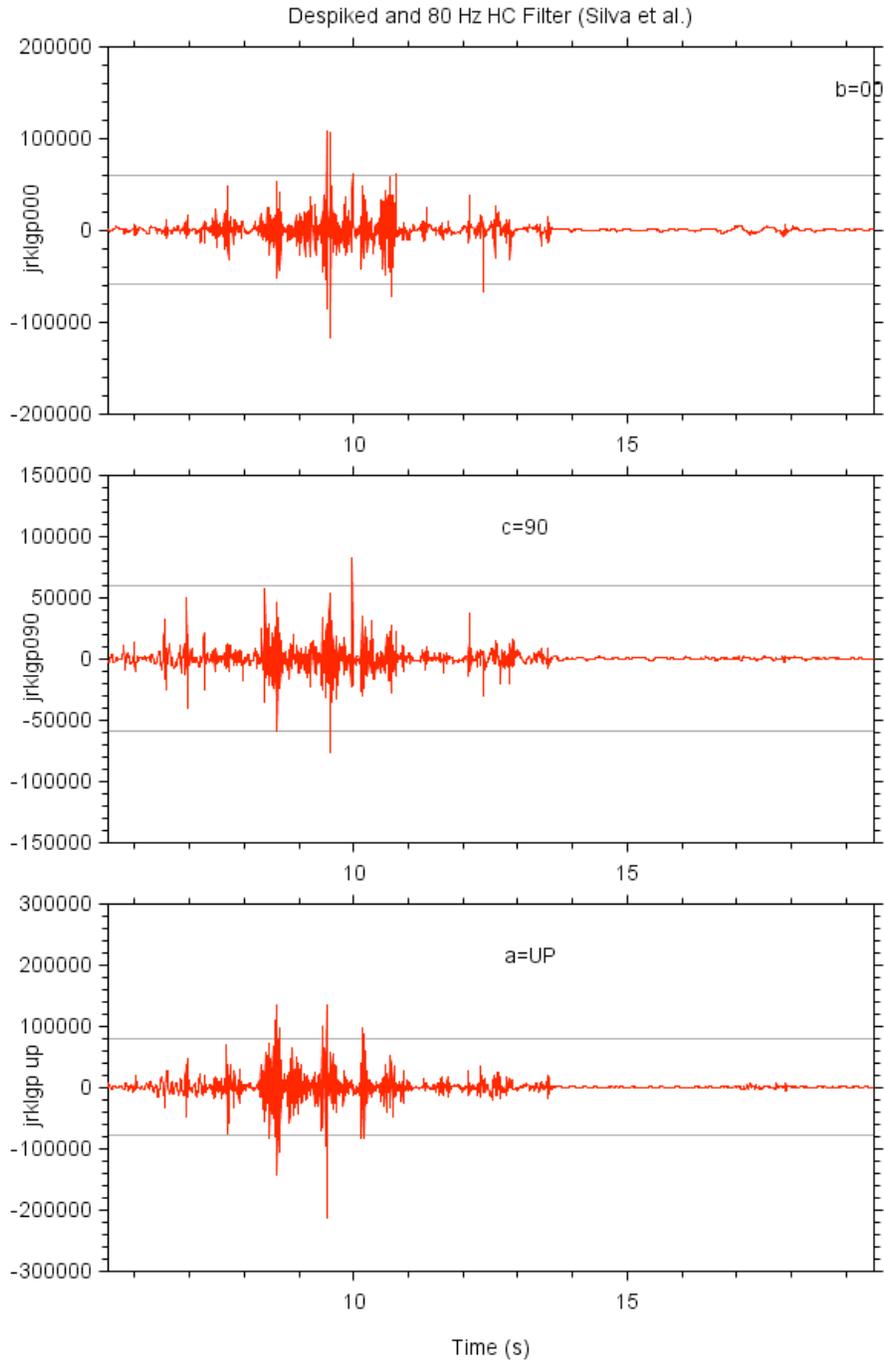
Fig. H.7 Jerk time series for despiked records.

The waveforms at LEXD and LGPC are quite different, even though the stations are only 3.6 km from one another. This is shown in the Figure H.8. The spectra of all but the EW component for $T > 1\,\mathrm{s}$ are also very different in general, as shown in the Figure H.9.
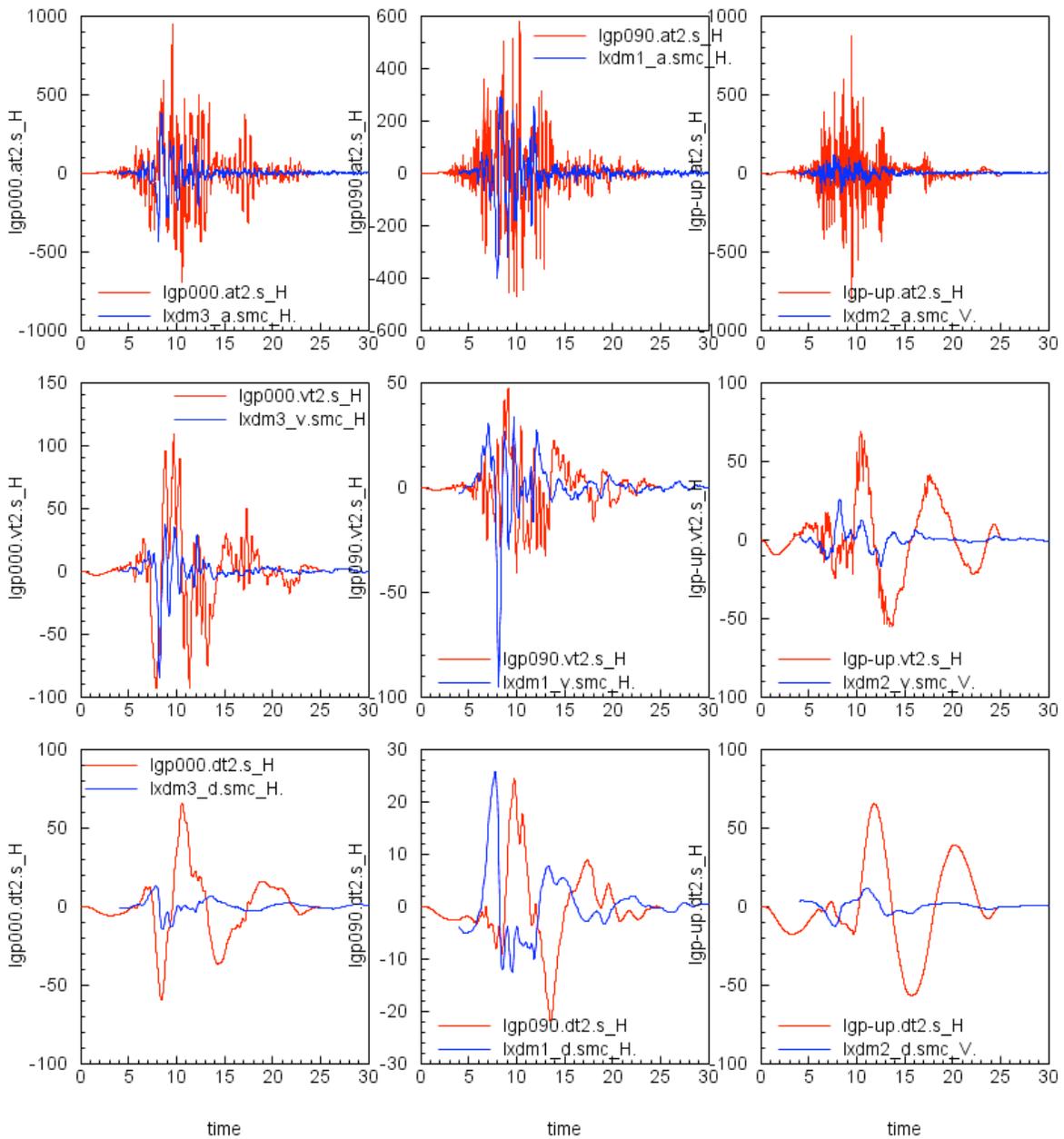
Fig. H.8 **Comparison of acceleration, velocity, and displacement traces at Lexington Dam and LGPC. Lexington Dam record low-cut filtered between 0.05 and 0.10 Hz. LGPC record low-cut filtered with causal 0.1 Hz filter. Time alignment is arbitrary; all Lexington Dam components shifted by same amount to produce general coincidence of acceleration traces.**
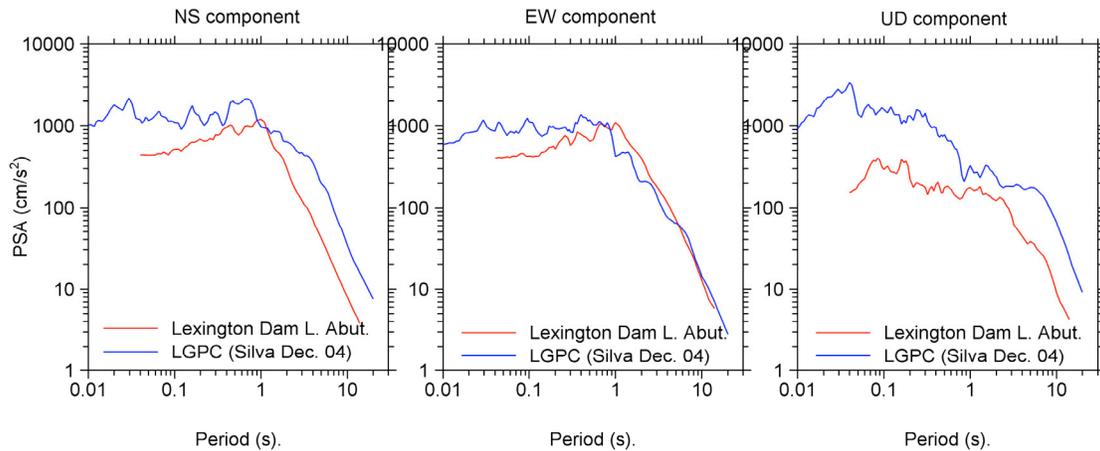
Fig. H.9 Spectra at LEXD and LGPC

Unless someone can convince me otherwise, I think that the recordings at LGPC should not be used for any analyses. The acceleration record at LGPC is very strange looking, with numerous spikes that have not been removed by despiking and high-cut filtering. In contrast, the LEXD record does not seem at all strange. If I knew what produced the spikes on the LGPC record and could be assured that the spikes only affect high frequencies, I could see using a high-cut filtered version of the record. But the comparisons of velocity and displacement waveforms at LEXD and LGPC does not give me much confidence that the problems on the LGPC record are restricted to high frequencies (with the possible exception of the EW component record).

Appendix I: USGS Data for 1992 Cape Mendocino Not Included in NGA Flatfile

I noticed in early January 2005 that there are no USGS data in the NGA database for the 1992 Cape Mendocino mainshock. This appendix, originally written on 8 January 2005, was an unsuccessful appeal that the USGS data be included.

Unprocessed data have been available for at least four years from *http://nsmp.wr.usgs.gov/data_sets/petrolia.html*. For use in the subduction ground-motion paper that Gail Atkinson and I published (Atkinson and Boore 2003), I did some quick processing of the data (using a low-cut filter of 0.2 Hz for all records), and summaries of the results of the accelerations and velocities for those records are included in Table I.1. For comparison, Table I.2 contains information for the CGS recordings. Note that the USGS data are at relevant distances and amplitudes, with a number of peak accelerations between about 0.2 and 0.4g, and PGV as large as 75 cm/s. It is quite likely that the data would permit filtering at lower frequencies (see below for one example)—the choice of 0.2 Hz was conservative, and no effort was made to explore lower-frequency filters.

One possible reason that the USGS data were not included is that the file headers indicate that there were stalls on a number of recordings. This is probably not a good reason to exclude the data: there are indications of definite stalls on 3 of the 8 recordings, possible stalls on 2 recordings, and no stalls on 3 recordings. In addition, the times of the stalls for several of the records identified as having stalls do not coincide with the portion of strong shaking. Finally, Chris Stephens looked at what seems to be the worst case (Ferndale), and thinks that the record has had a first-order correction applied to account for the stalls (he also points out that there are stretches as well as stall). It is possible to do a correction because time code traces are available on the recordings (unlike the Rinaldi Receiving Station record of the 1994 Northridge

mainshock, which also had stalls (Trifunac et al., 1998)). I also studied the displacements from two closely located stations in Fortuna (see Fig. I.1 for locations). The CGS recordings used a low-cut filter tapering from 0.07 to 0.05 Hz; in order to use a similar filter for the USGS data, I applied an acausal Butterworth filter with a 0.06 corner frequency. The comparisons are in Figure I.2. Although the file header indicates possible stalls at 50+0.5 and 50+6 s ("50" is the length of the zero pad applied before filtering), they do not seem to have had much effect on the motions (judging from the relatively good match with the CGS displacements).

In addition to the data, there are shear-wave velocity profiles at Ferndale (from Shannon and Wilson) and Loleta, College of the Redwoods, Fortuna Fire Station, Redwood Village Mall (Fortuna), and the Rio Dell overcrossing free field (the latter two are CDMG strong-motion stations for which data are in the NGA database). The velocities are in USGS OFR 02-203 and are available from the compilation I put together (see my website: *http://quake.usgs.gov/~boore*).

For the reasons above, I recommended that the USGS data be included in the NGA database. It is unfortunate that these date were not included in the flatfile.

Table I.1 USGS recordings (with 0.2 Hz low-cut filter).

Station Name	R_{EP}	ivrt	ihrz	fltr1	fltr2	PGA(cm/s/s)	PGV(cm/s)
Butler Valley Sta. 2	**60**	****	**60**	**0.2**	**-2**	**152.1**	**14.1**
Butler Valley Sta. 2	**60**	**0**	****	**0.2**	**-2**	**72.7**	**10.7**
Butler Valley Sta. 2	**60**	****	**330**	**0.2**	**-2**	**136.7**	**20.4**
Ferndale FS	**24**	****	**360**	**0.2**	**-2**	**266.5**	**39.3**
Ferndale FS	**24**	**0**	****	**0.2**	**-2**	**61.9**	**7.4**
Ferndale FS	**24**	****	**270**	**0.2**	**-2**	**452.3**	**74.8**
Loleta FS	**32**	****	**360**	**0.2**	**-2**	**251.5**	**24.5**
Loleta FS	**32**	**0**	****	**0.2**	**-2**	**132.4**	**5.7**
Loleta FS	**32**	****	**270**	**0.2**	**-2**	**246.8**	**29.4**
Centerville Beach	**22**	****	**360**	**0.2**	**-2**	**451.3**	**59.4**
Centerville Beach	**22**	**0**	****	**0.2**	**-2**	**137.2**	**11.5**
Centerville Beach	**22**	****	**270**	**0.2**	**-2**	**302.7**	**48.4**
College of the Redwoods	**38**	****	**360**	**0.2**	**-2**	**170.5**	**29.3**
College of the Redwoods	**38**	**0**	****	**0.2**	**-2**	**73.5**	**7.1**
College of the Redwoods	**38**	****	**270**	**0.2**	**-2**	**168.7**	**25.1**
South Bay Union School	**42**	****	**360**	**0.2**	**-2**	**189.6**	**23.2**
South Bay Union School	**42**	**0**	****	**0.2**	**-2**	**64.9**	**6.6**
South Bay Union School	**42**	****	**270**	**0.2**	**-2**	**149.3**	**23.5**
Fortuna FS	**29**	****	**360**	**0.2**	**-2**	**281**	**27.4**
Fortuna FS	**29**	**0**	****	**0.2**	**-2**	**80.5**	**6.3**
Fortuna FS	**29**	****	**270**	**0.2**	**-2**	**348.5**	**33.7**
Bunker Hill	**15**	****	**360**	**0.2**	**-2**	**225.5**	**29.1**
Bunker Hill	**15**	**0**	****	**0.2**	**-2**	**76.6**	**12.4**
Bunker Hill	**15**	****	**270**	**0.2**	**-2**	**185**	**46.6**

Table I.2 CGS data.

Station Name	R_{EP}	ivrt	ihrz	fltr1	fltr2	PGA(cm/s/s)	PGV(cm/s)
CAPE MENDOCINO	10	90	90	0.05	0.07	1019.4	40.5
CAPE MENDOCINO	10	0	0	0.05	0.07	738.9	60.3
CAPE MENDOCINO	10	90	0	0.05	0.07	1468.3	126.1
EUREKA - 5TH & H FEDERAL BLDG.	52	90	80	0.12	0.24	152.7	28.6
EUREKA - 5TH & H FEDERAL BLDG.	52	0	0	0.12	0.24	35.4	6.2
EUREKA - 5TH & H FEDERAL BLDG.	52	90	350	0.12	0.24	86.4	17
EUREKA - MYRTLE & WEST AVENUE	52	90	90	0.08	0.16	174.7	28.6
EUREKA - MYRTLE & WEST AVENUE	52	0	0	0.08	0.16	41.6	7.3
EUREKA - MYRTLE & WEST AVENUE	52	90	0	0.08	0.16	151	20
FORTUNA - 701 S. FORTUNA BLVD.	28	90	90	0.05	0.07	111.9	20.9
FORTUNA - 701 S. FORTUNA BLVD.	28	0	0	0.05	0.07	47.9	5.8
FORTUNA - 701 S. FORTUNA BLVD.	28	90	0	0.05	0.07	113.6	28.8
PETROLIA	5	90	90	0.05	0.07	649.4	89.5
PETROLIA	5	0	0	0.05	0.07	159.7	20.9
PETROLIA	5	90	0	0.05	0.07	578.1	48.3
RIO DELL - 101/PAINTER ST. OVE	21	90	272	0.05	0.07	378.3	44.7
RIO DELL - 101/PAINTER ST. OVE	21	0	0	0.05	0.07	191.5	10.2
RIO DELL - 101/PAINTER ST. OVE	21	90	2	0.05	0.07	538.5	42.6
SHELTER COVE - AIRPORT	36	90	90	0.25	0.5	173	6.9
SHELTER COVE - AIRPORT	36	0	0	0.25	0.5	49.5	1.8
SHELTER COVE - AIRPORT	36	90	0	0.25	0.5	222	7
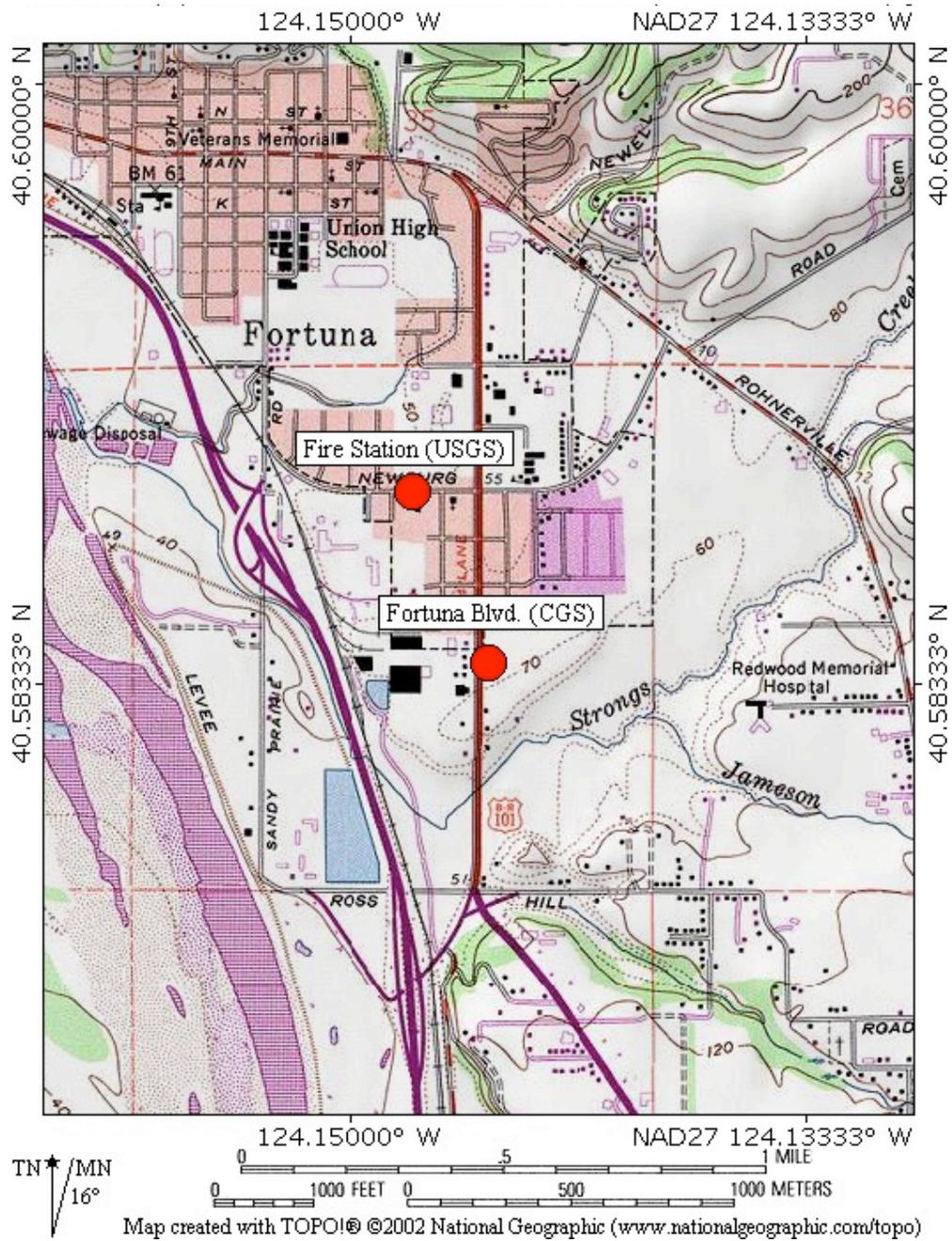
Fig. I.1 Map of two nearby stations that recorded 1992 Cape Mendocino earthquake.
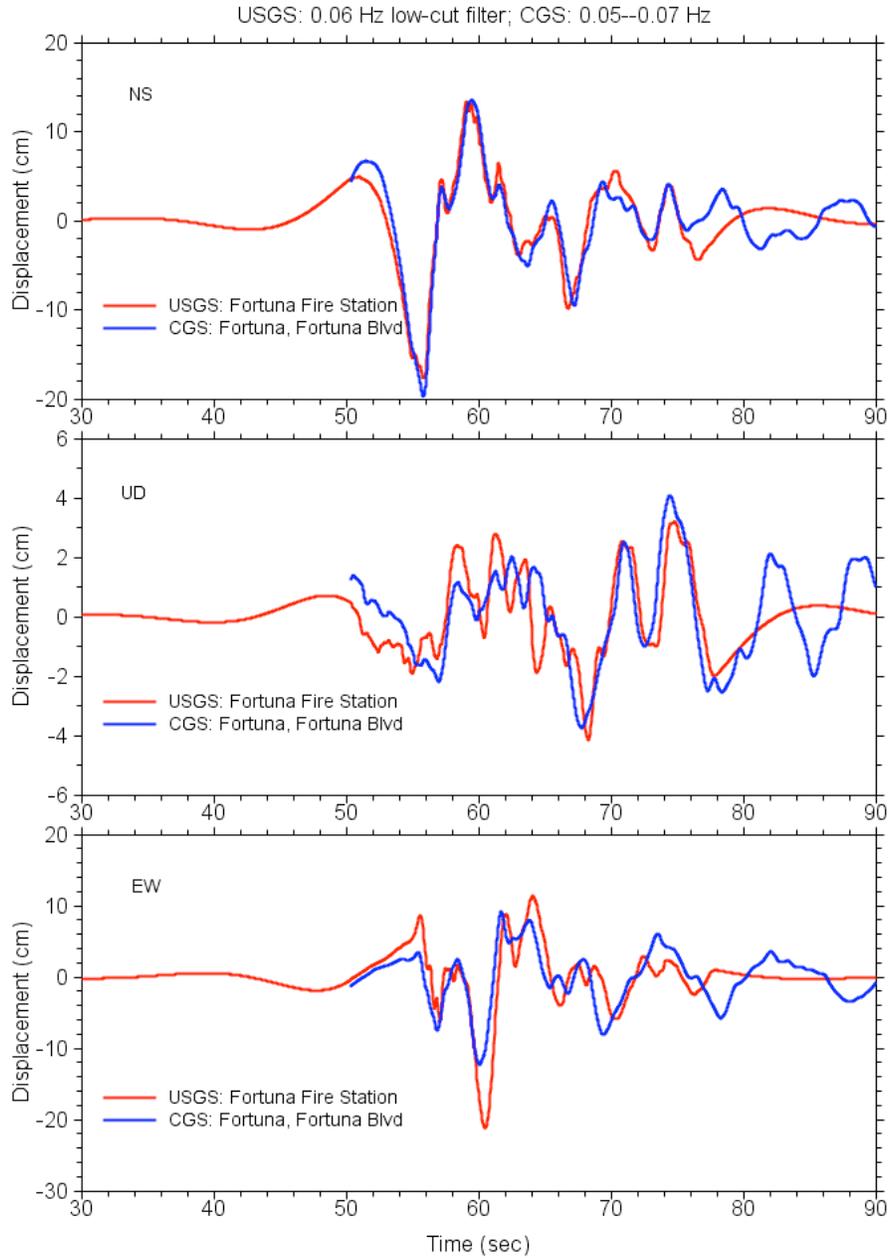
Fig. I.2 **USGS records include padded portions before (less than 50 s) and after (greater than 78 s) recorded motions.**

Appendix J: Notes on Rinaldi Receiving Station Recording of 1994 Northridge Earthquake Used in NGA Flatfile

For the Rinaldi Receiving Station recording of the 1994 Northridge mainshock, I happened to notice in early 2005 that the low-cut filter corner in the PEER NGA flatfile is 0.3 Hz, which struck me as being too high. I confirmed this with Walt Silva via telephone conversations in the first week of 2005. He is not sure where he obtained the data or what processing was done on the record. On looking into the issue, I discovered that the data in the flatfile correspond to the "old" data (with a duration of about 16 s). Trifunac et al. (1998) redigitized the data. Their version of the data differs in several ways from the old version: they included more of the record, they captured peaks not properly digitized in the old version, and they corrected for more stalls on the record. As a matter of interest, it should be noted that no internal time code marks are available for this record, and thus the peak velocities and peak displacements, as well as the spectral amplitudes, are dependent on the assumption that 1 cm = 1 s.

To see how the "new" data might differ from that used in the NGA flatfile, I include here a series of plots comparing waveforms and response spectra (Figs. J.1–J.8). I processed the new data using both causal and acausal filters, each with different rolloffs. The processed data available from USC has filtered the 228-degree trace with a transition from 0.09 to 0.11 Hz and the 318-degree component with a transition between 0.15–0.20 Hz. In Trifunac et al. (1998) the transition from 0.07 to 0.09 Hz is used for both components. In this note I used Butterworth filters with corners of 0.01, 0.02, 0.10, and 0.20 Hz. I did no baseline corrections before filtering. I show plots of the waveforms only for the recorded section of time. Because I have not included the padded portions in the plots, the displacements sometimes do not return to around zero at the end of the recorded time, although plots of the complete time series that was filtered do show

that the displacements return to zero (in other words, the filtering was done correctly and no "wrap-around" pollution exists—see Boore 2005, for a discussion).

Please note that waveforms plots were made using a quick plotting program and as a result, the traces appear to have dropouts. But they should be adequate for purposes of comparisons, and the peak motions along the ordinate axes are accurate.

Here are some observations:

1. At short periods, there are systematic differences between NGA and new for the 318-degree component, although the short-period response is essentially identical for all acausal filters. The NGA spectra are given at 0.01 and 0.02 s, but the similar values at both periods are not consistent with the new results, and, furthermore, the abrupt leveling off of the NGA spectrum for periods shorter than about 0.02 s looks strange (the spectrum for the 228-degree component also levels off at about 0.02 s, but more gradually). The spectra for the 228-degree component are similar for NGA and new (as long as acausal filtering is used).

2. At long periods, there are differences between NGA and new for periods longer than about 2 to 3 s (depending on component), but here the new results vary with the filter corner (as expected). For the 228-degree component, the NGA results are greater than the new results for periods between about 2 to 5 s and tend to lower values for greater periods. For the 318-degree component, the NGA values are lower than the new values for periods greater than about 6 s (except for the new results using a filter corner of 0.2 Hz).

Bottom line: I recommend replacing the NGA values for the Rinaldi Receiving Station recording of the 1994 Northridge mainshock with the USC digitized data, corrected for stalls. The processing of the corrected data should use acausal, not causal filters (note the sensitivity of the short-period response on the 228-degree component to long-period cutoffs for the causal filter, as well as the greater sensitivity of the peak velocity to filter corner for causal filters).
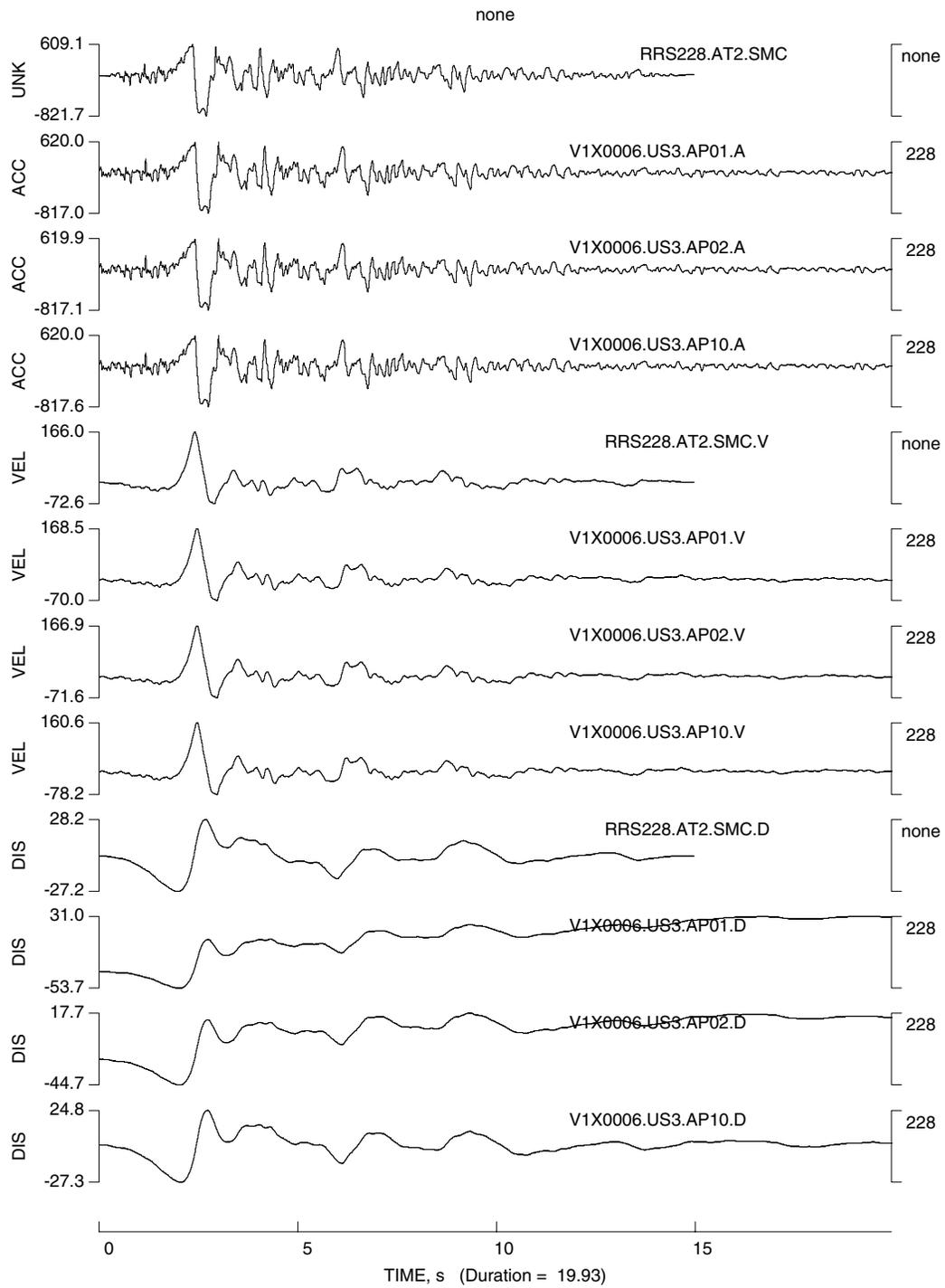
Fig. J.1 NGA time series ("RRS" file name), and acausally filtered, 228-degree
component using filter corners of 0.01, 0.02, 0.1, and 0.2 Hz.
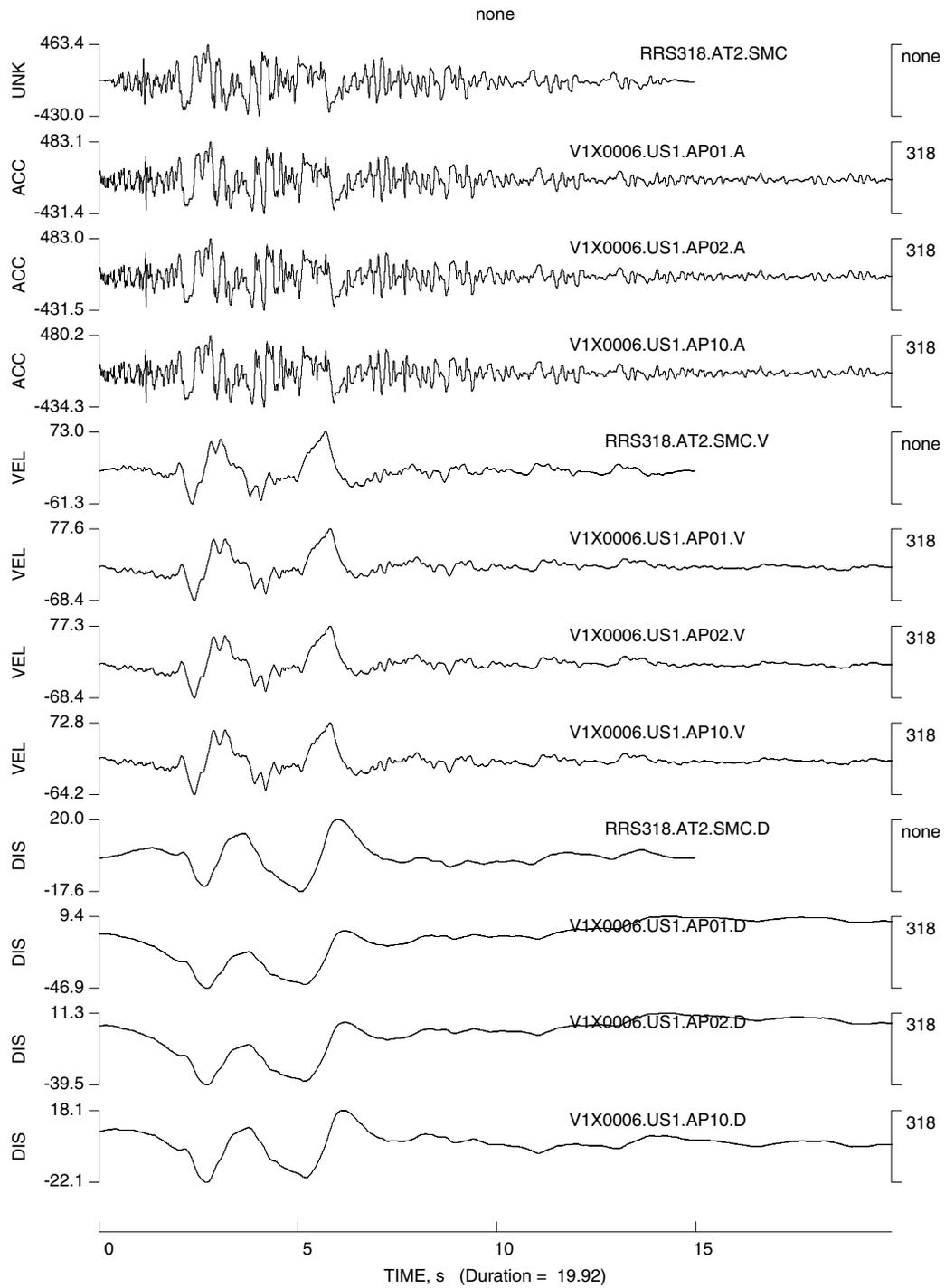
Fig. J.2   NGA time series ("RRS" file name), and acausally filtered, 318-degree component using filter corners of 0.01, 0.02, 0.1, and 0.2 Hz.
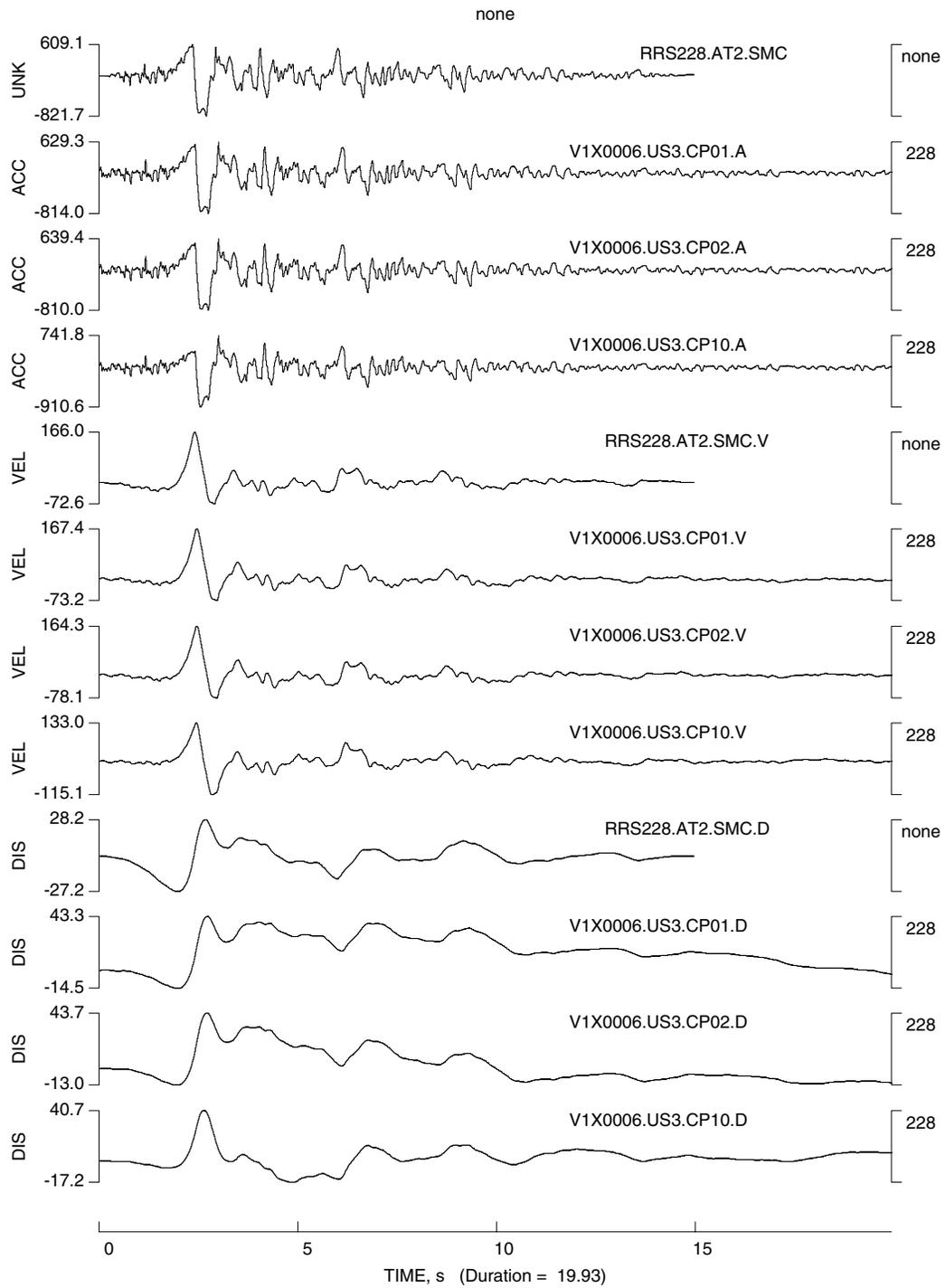
Fig. J.3 NGA time series ("RRS" file name), and causally filtered, 228-degree component using filter corners of 0.01, 0.02, 0.1, and 0.2 Hz.

A -81
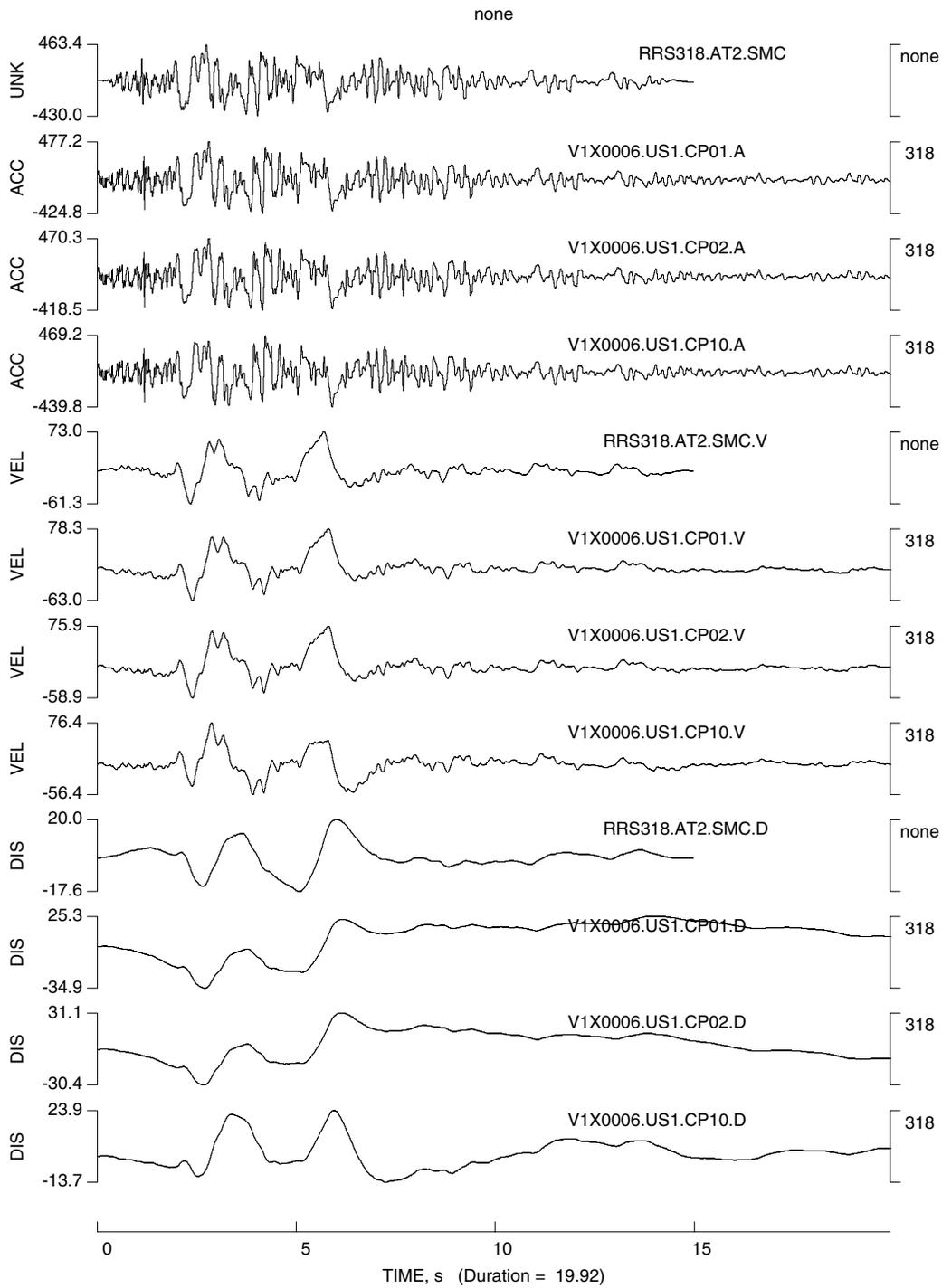
Fig. J.4   NGA time series ("RRS" file name), and causally filtered, 318-degree component using filter corners of 0.01, 0.02, 0.1, and 0.2 Hz.
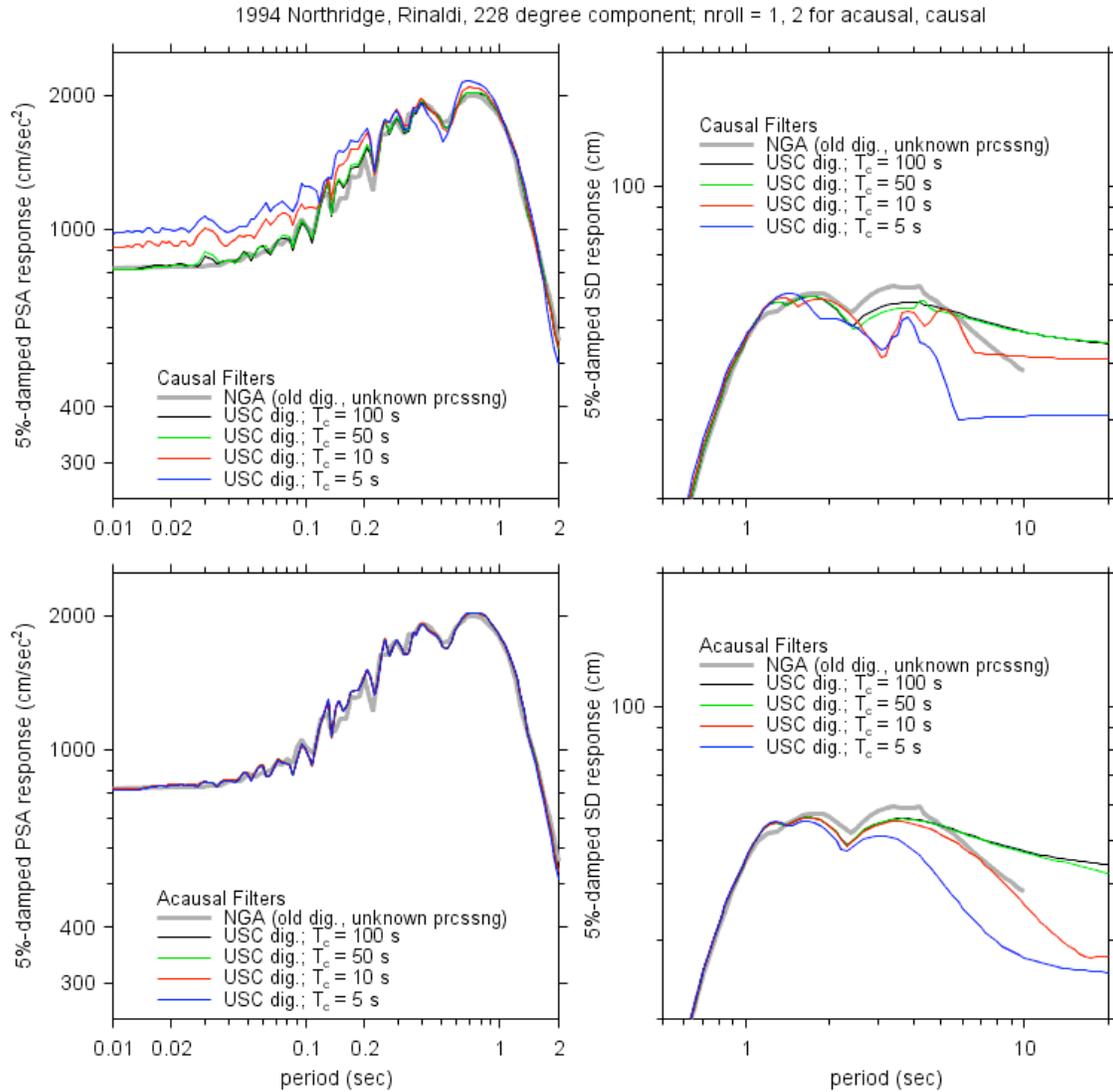
Fig. J.5 **PSA and SD response, acausal and causal filters, as well as NGA spectra, for 228-degree component. Lowest order time-domain filters used.**
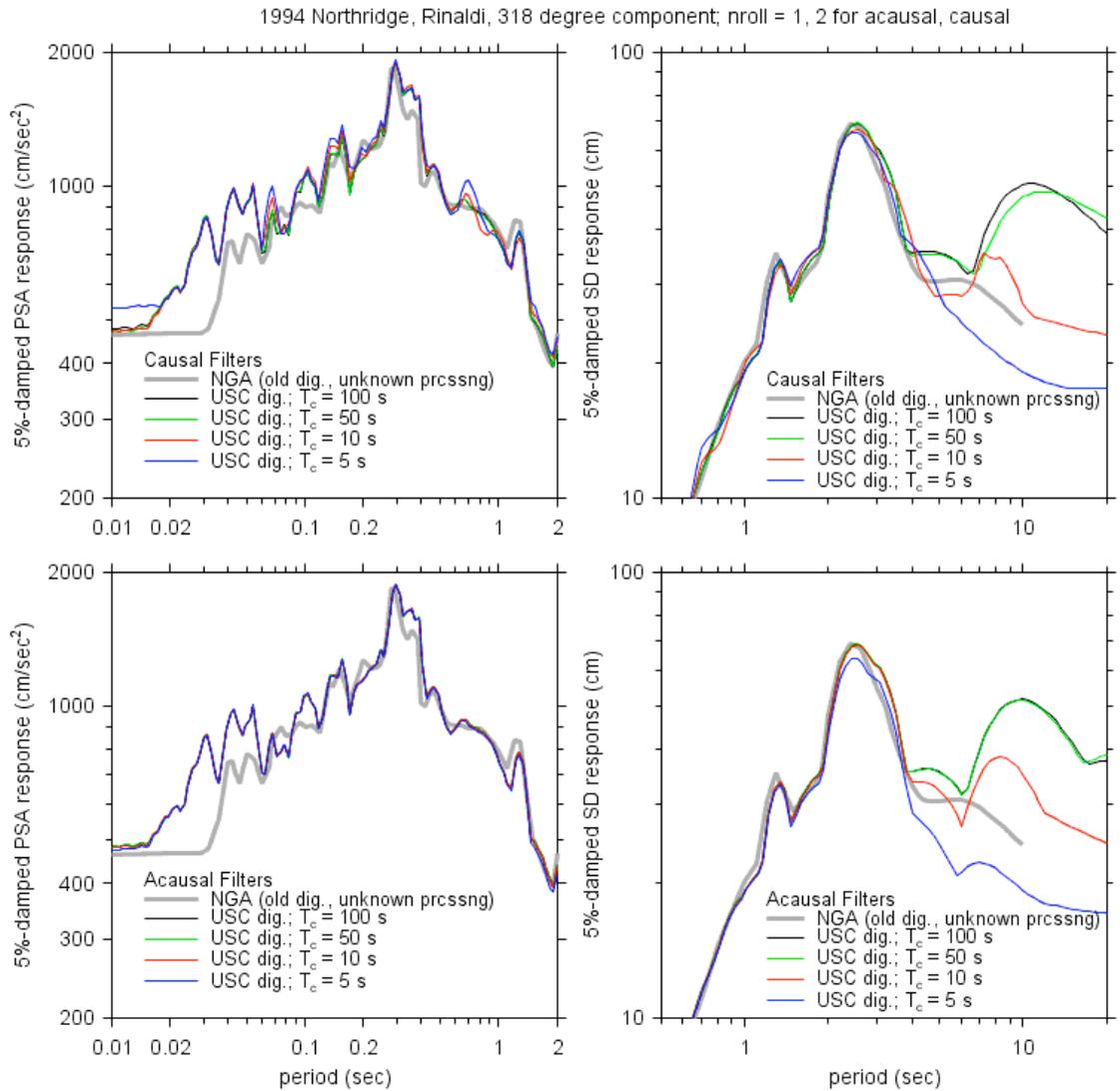
Fig. J.6 **PSA and SD response, acausal and causal filters, as well as NGA spectra, for 318-degree component. Lowest order time-domain filters used.**
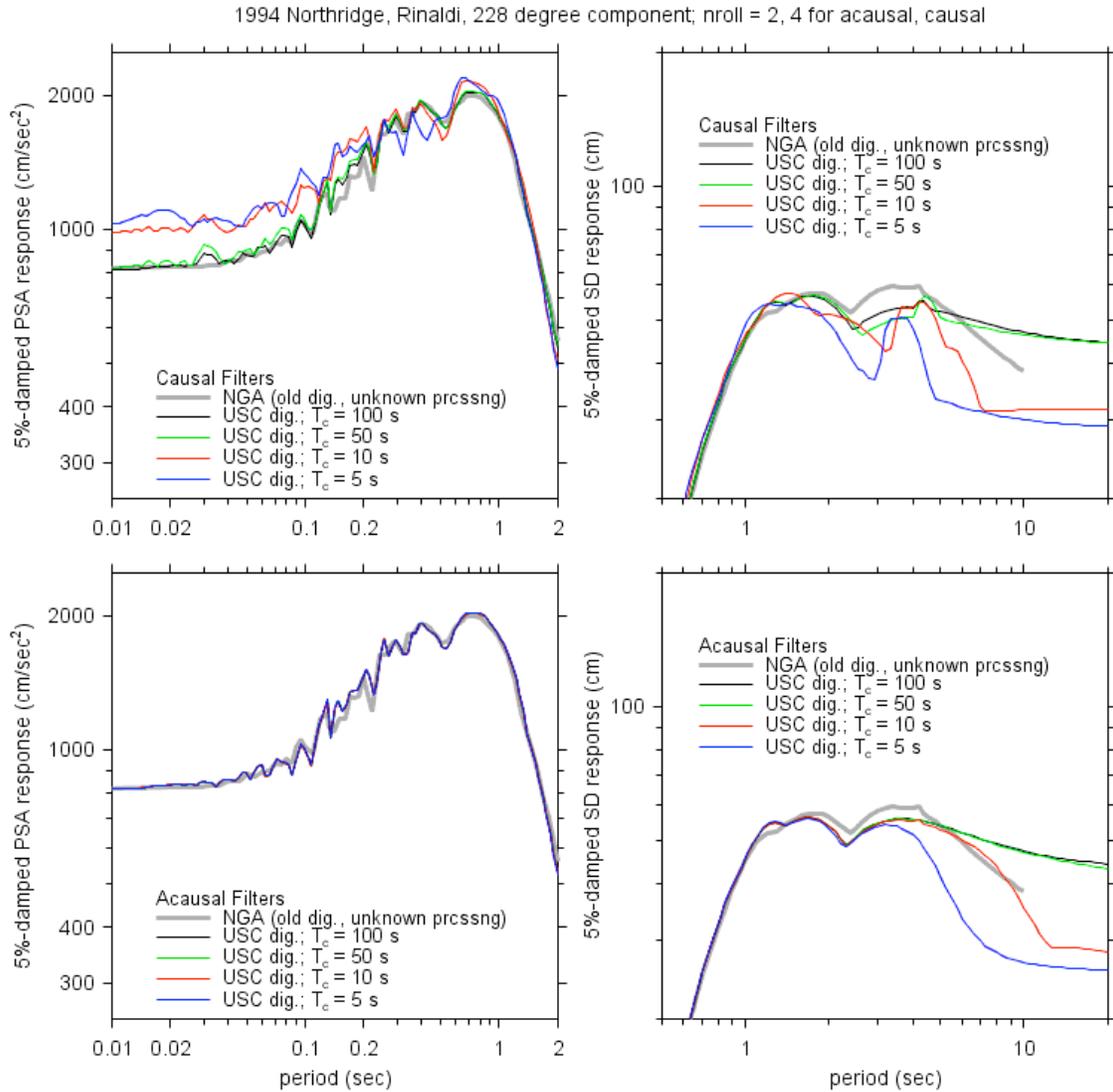
Fig. J.7 PSA and SD response, acausal and causal filters, as well as NGA spectra, for 228-degree component. Order of filters twice that used in previous two figures.
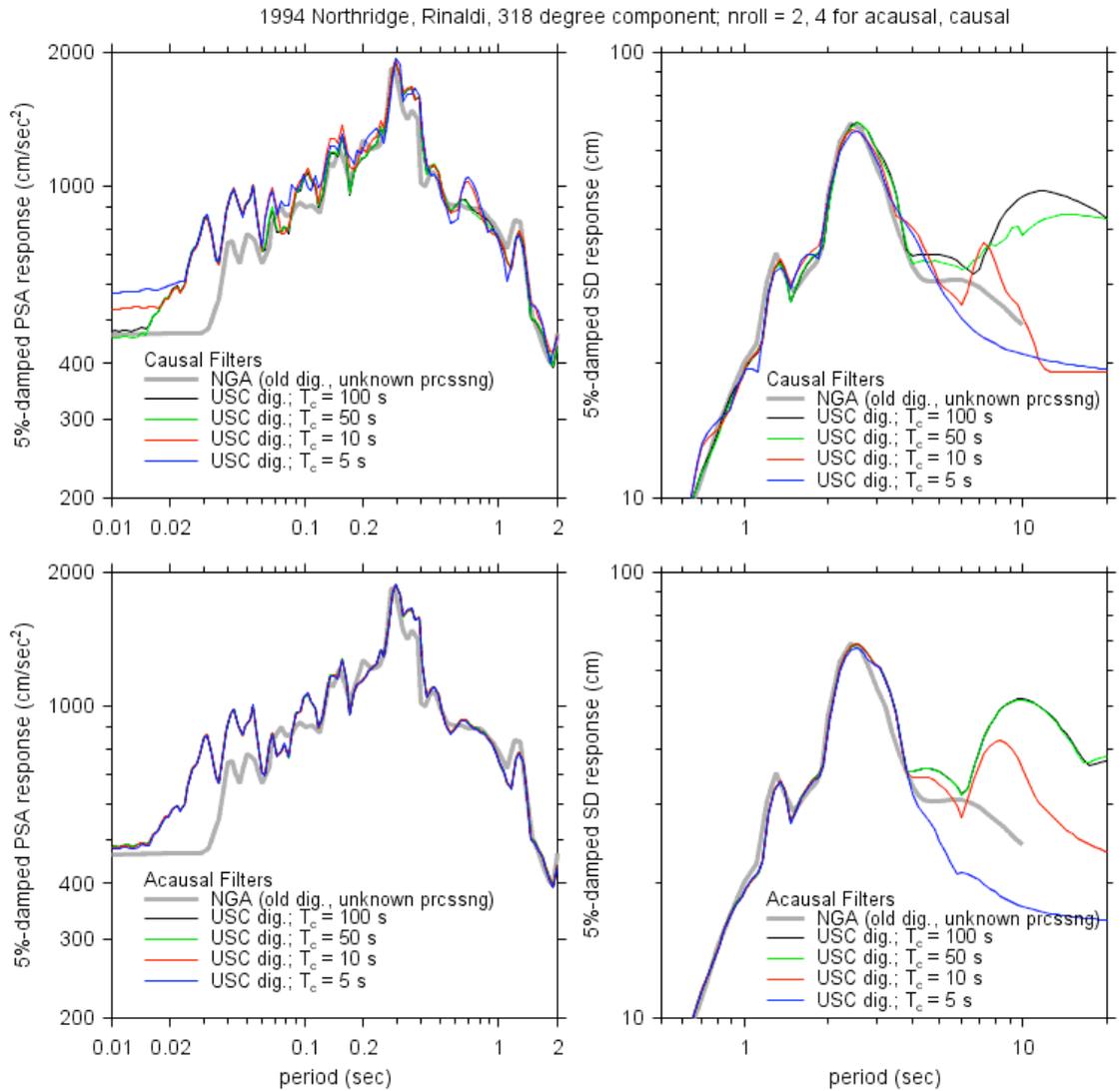
Fig. J.8   PSA and SD response, acausal and causal filters, as well as NGA spectra, for 318-degree component. Order of filters twice that used in Figs. 2.4–2.5.

Appendix K: Notes on 1999 Düzce Recordings

I noticed in the plots of events terms (Figs. K.1–K.3, updated from the figures that accompanied the original version of this note, 30 July 2005) that the Düzce event is low relative to the other strike-slip earthquakes for periods less than 5 s. This was also found by Ambraseys et al. (2005).

Figures K.4–K.9 show plots for three earthquakes with similar magnitude (corrected for site response to $V_{S30} = 760 \text{ m/s}$, using the BJF97 site amplification factors—these plots were made before we settled on the site amplifications to be used in the BA07 NGA equations). It turns out that most of the Düzce $V_{S30} > 360 \text{ m/s}$ records are from the Lamont stations, and it was recognized earlier in the NGA project that the records from these stations seemed to be peculiar—but I cannot remember details. I've indicated the Lamont stations in the plots. Although there is little distance overlap in the Lamont versus other stations, the motions from the more distant stations for the Düzce earthquake seem low with respect to those from the other events, so perhaps there is nothing peculiar about the Lamont stations. For more information on shear-wave velocities at some stations that recorded the 1999 Düzce earthquake, see Rathje et al. (2003, 2004).
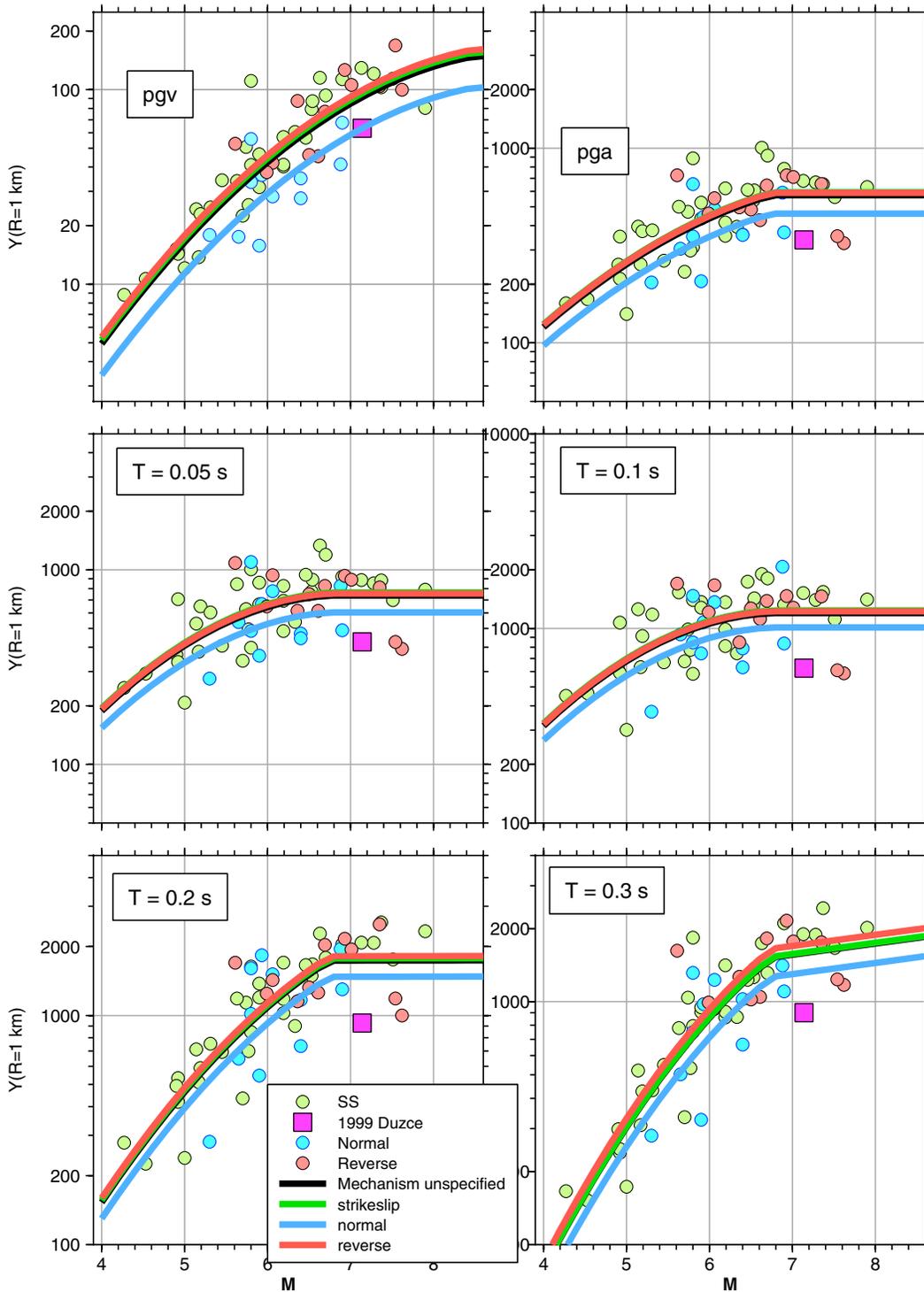
Fig. K.1　Event terms plotted against M. Same as Fig. 4.15(a), but with event term for 1999 Düzce earthquake identified.
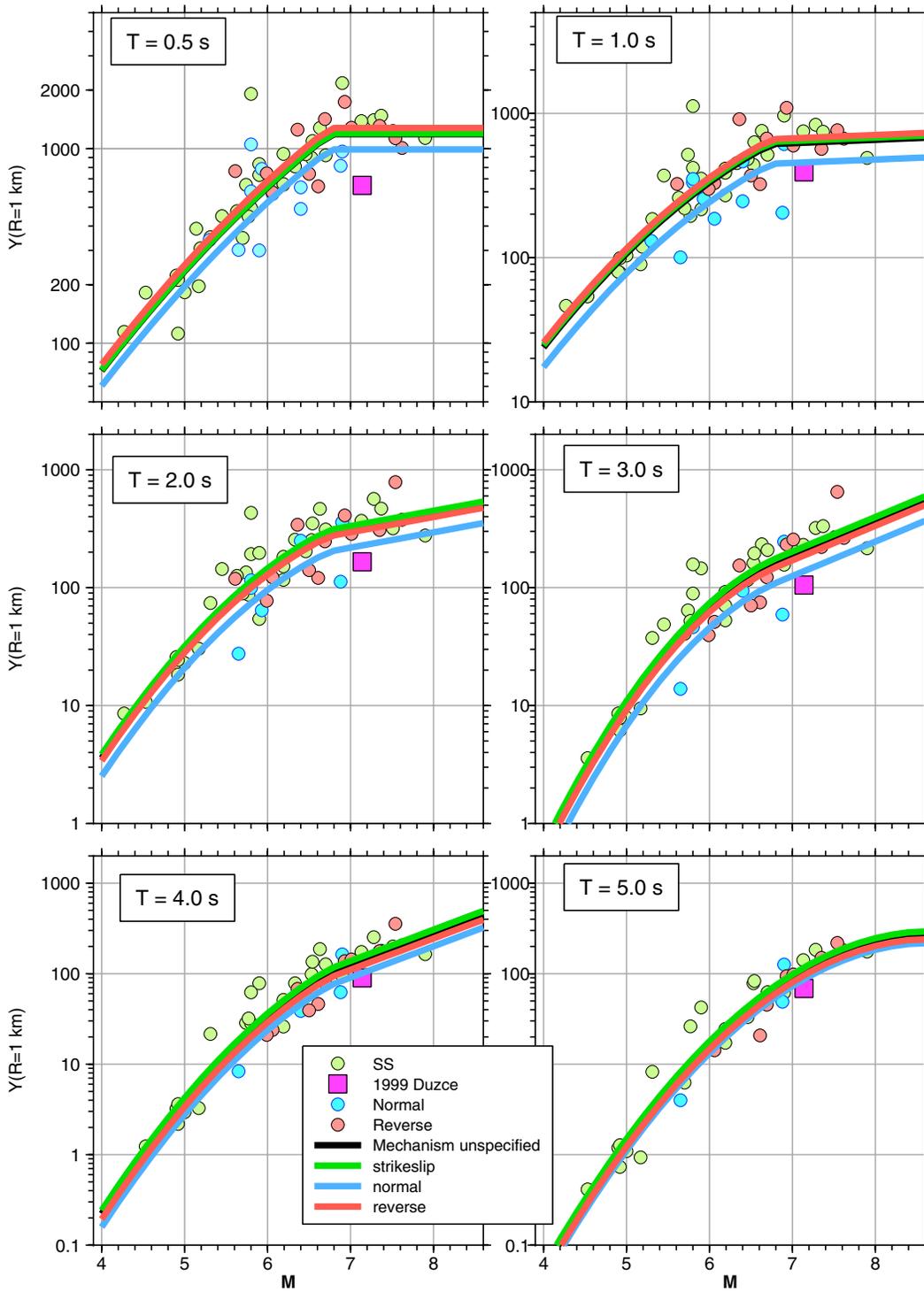
Fig. K.2 Event terms plotted against M. Same as Fig. 4.15(b) but with event term for 1999 Düzce earthquake identified.
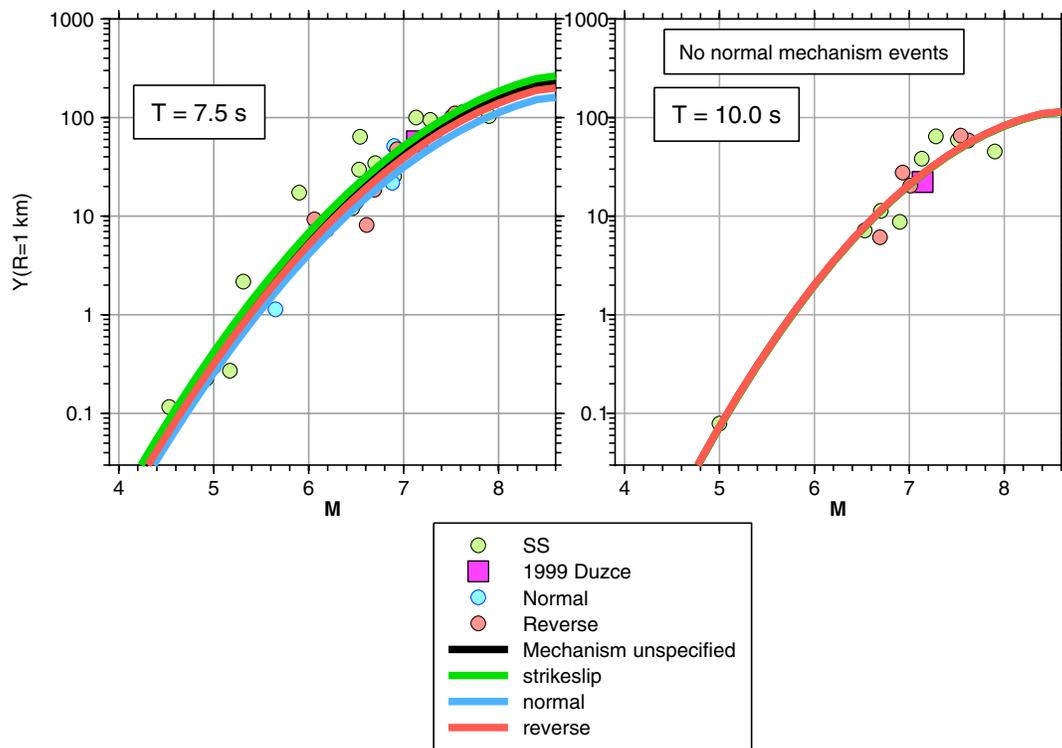
Fig. K.3 Event terms plotted against M. Same as Fig. 4.15(c), but with event term for 1999 Düzce earthquake identified.
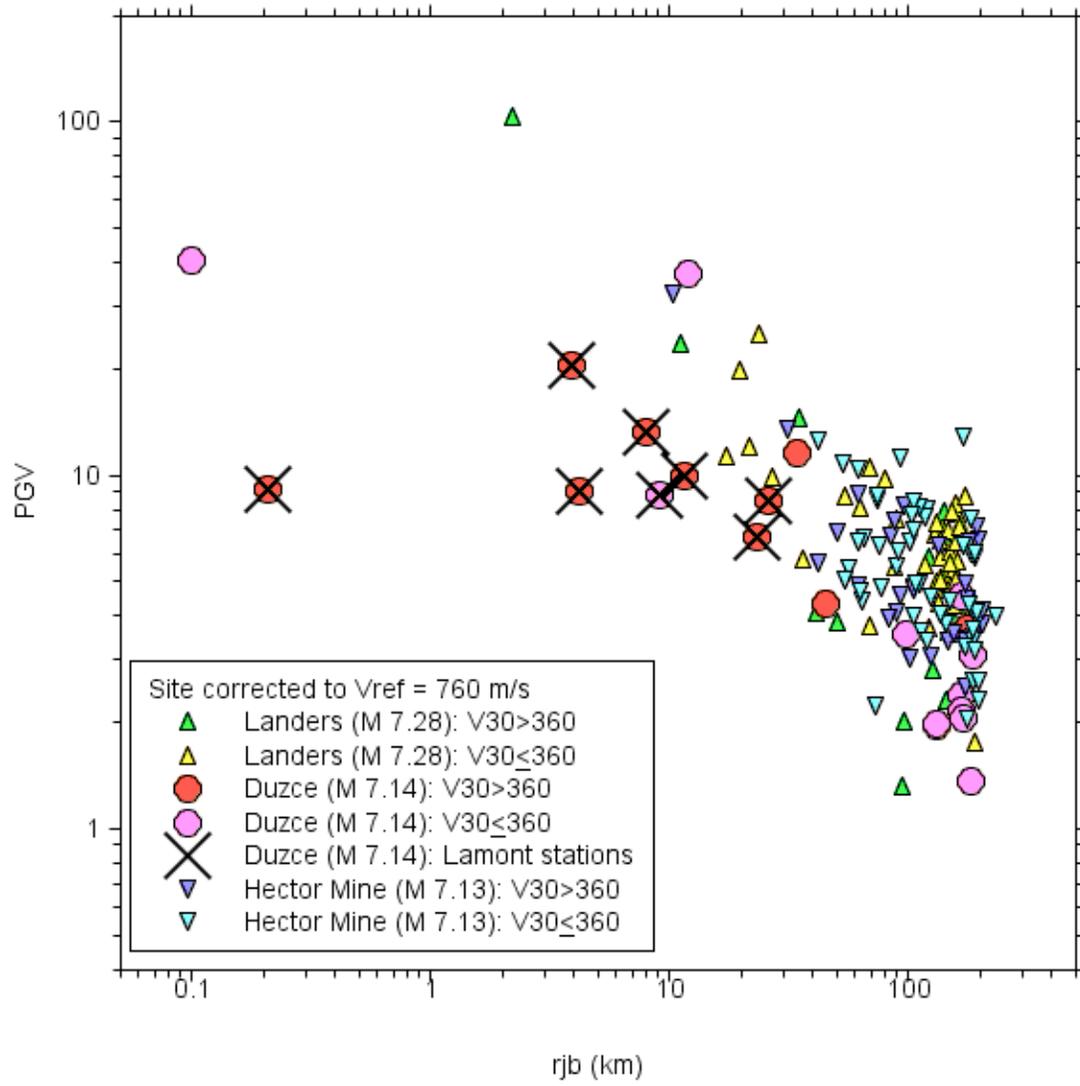
Fig. K.4 **PGV (cm/s) vs.** R_{JB} **for several earthquakes of comparable magnitude. For Düzce earthquake, values from temporary Lamont stations shown by large crosses. Values from Düzce earthquake from all stations, not just Lamont stations, seem low compared to motions from other earthquakes.**
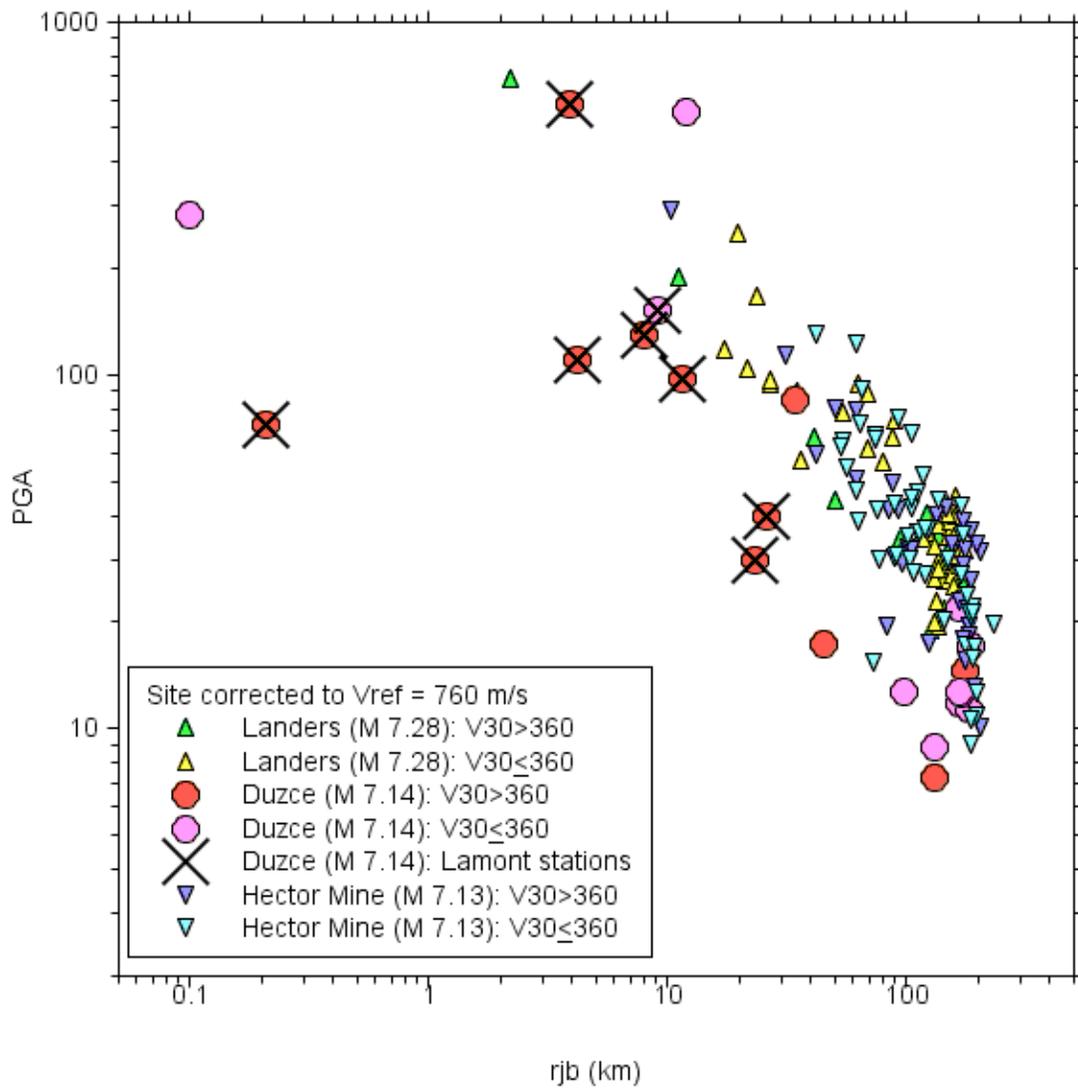
Fig. K.5   PGA (cm/s/s) vs. R_{JB} for several earthquakes of comparable magnitude. For Düzce earthquake, values from temporary Lamont stations shown by large crosses. Values from Düzce earthquake from all stations, not just Lamont stations, seem low compared to motions from other earthquakes.
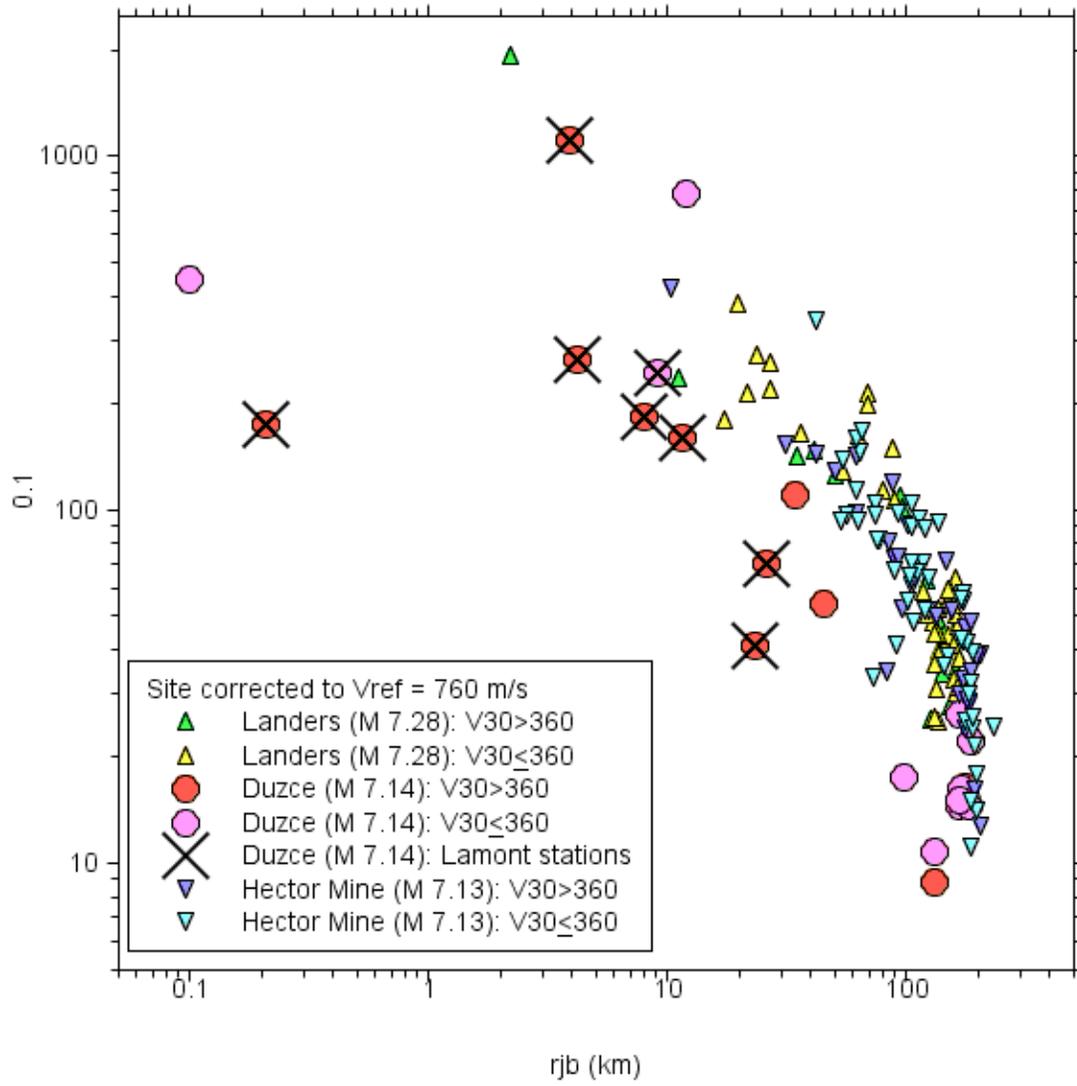
Fig. K.6 0.1 s PSA (cm/s/s) vs. R_{JB} for several earthquakes of comparable magnitude. For Düzce earthquake, values from temporary Lamont stations shown by large crosses. Values from Düzce earthquake from all stations, not just Lamont stations, seem low compared to motions from other earthquakes.
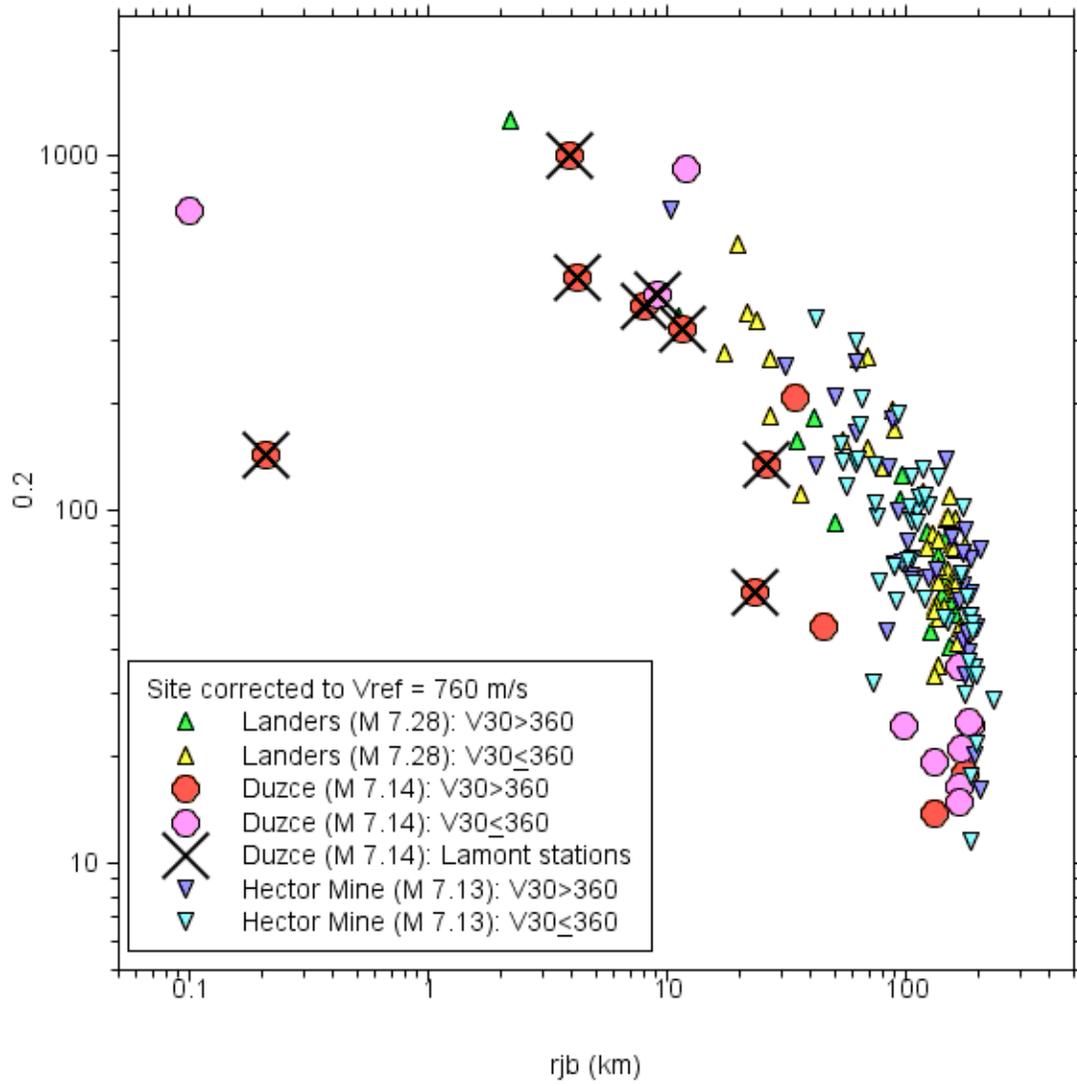
Fig. K.7   0.2 s PSA (cm/s/s) vs. R_{JB} **for several earthquakes of comparable magnitude. For Düzce earthquake, values from temporary Lamont stations shown by large crosses. Values from Düzce earthquake from all stations, not just Lamont stations, seem low compared to motions from other earthquakes.**
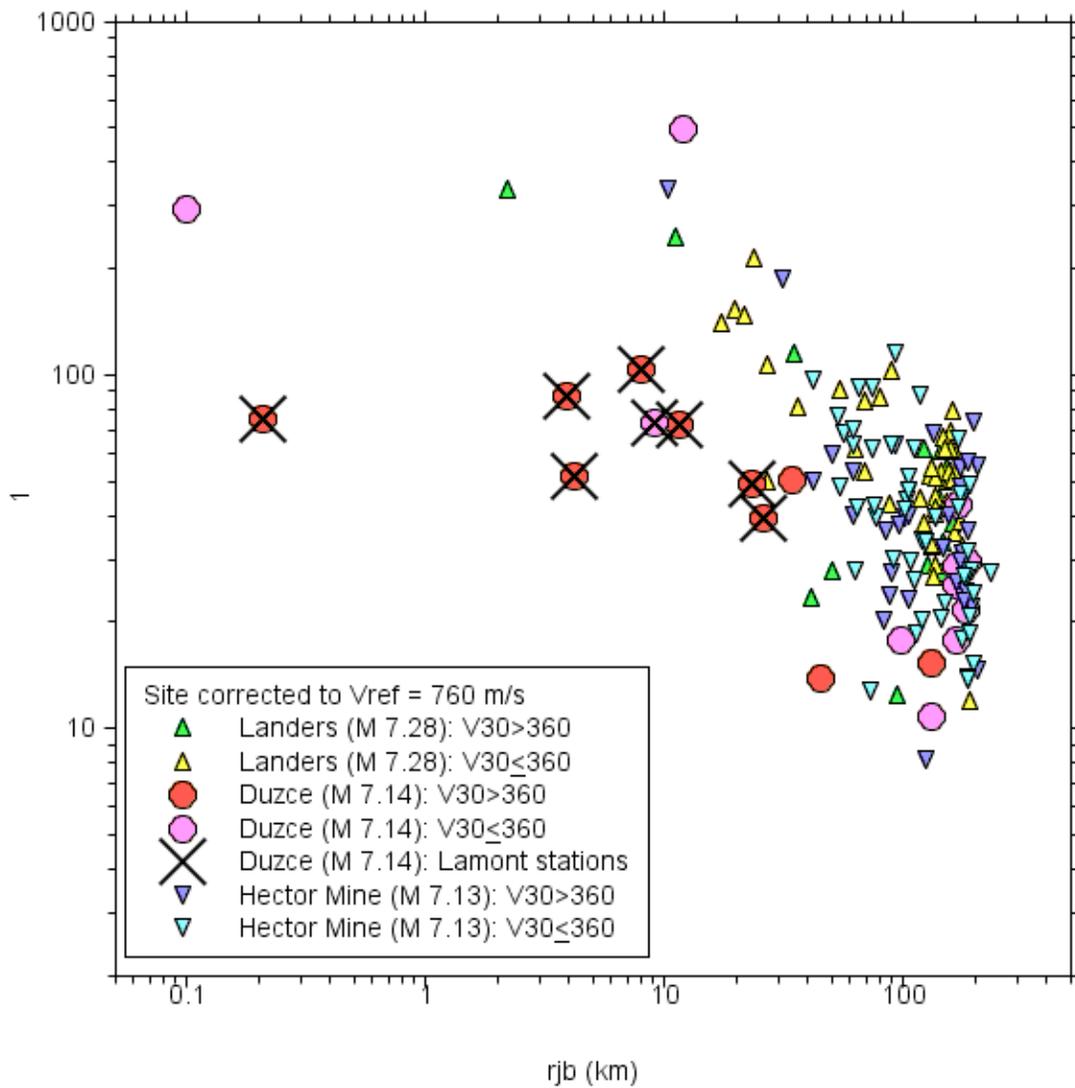
Fig. K.8 **1.0 s PSA (cm/s/s) vs.** R_{JB} **for several earthquakes of comparable magnitude. For Düzce earthquake, values from temporary Lamont stations shown by large crosses. Values from Düzce earthquake from all stations, not just Lamont stations, seem low compared to motions from other earthquakes.**
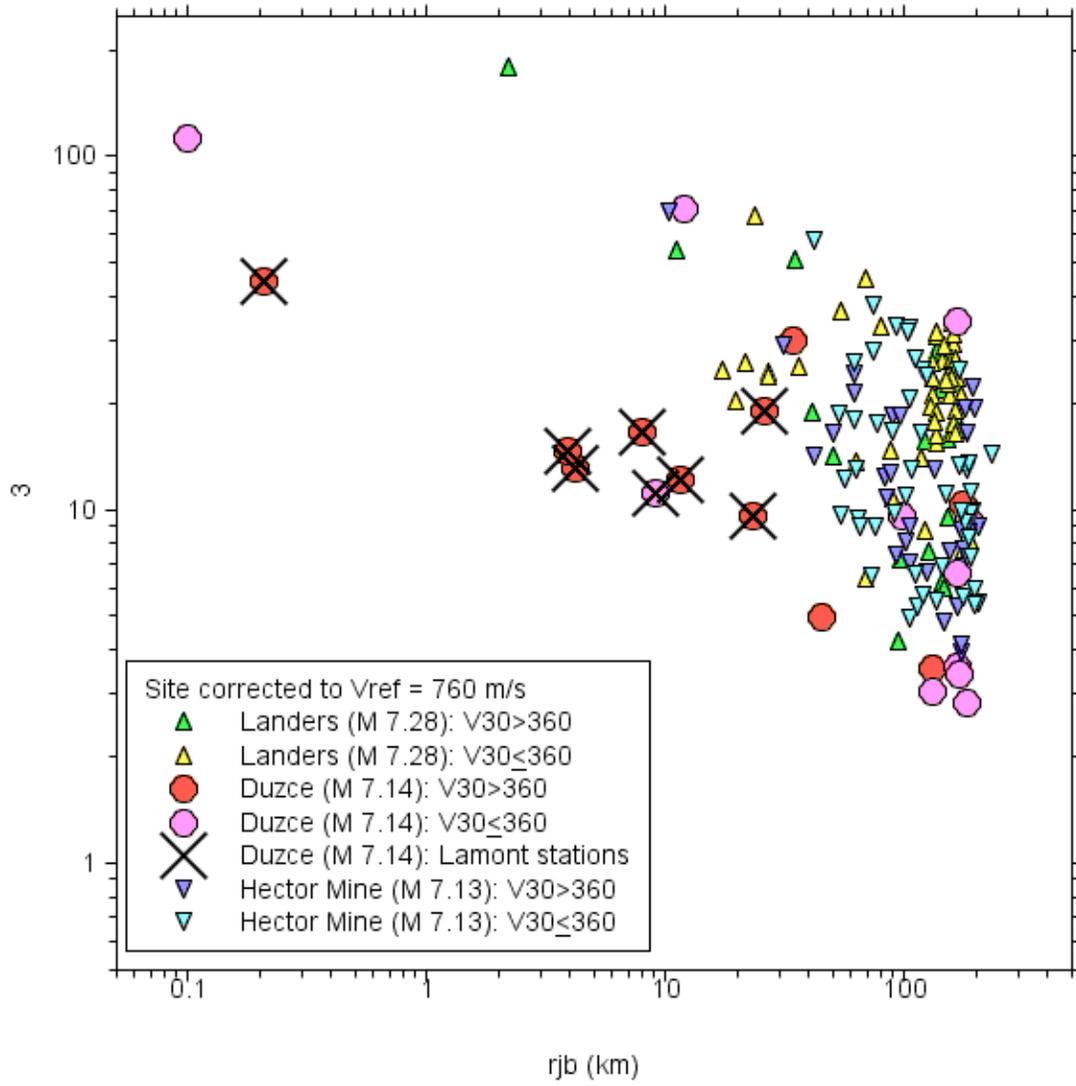
Fig. K.9 **3.0 s PSA (cm/s/s) vs. R_{JB} for several earthquakes of comparable magnitude.**
For Düzce earthquake, values from temporary Lamont stations shown by large
crosses. Values from Düzce earthquake from all stations, not just Lamont
stations, seem low compared to motions from other earthquakes.

Appendix L: Notes Regarding Record Obtained at Pump Station 10 from 2002 Denali Fault Earthquake

At Workshop 7 Walt Silva asked me about the Pump Station 10 record of the 2002 Denali fault earthquake. There was some confusion about what version of the record was used in the NGA database. Here is a short history of the record, as I know it. When first put on the USGS NSMP website (http://nsmp.wr.usgs.gov/), there was a statement that the hardware low-cut filter was at a very low frequency, on the order of 0.01 Hz. But then it was discovered that the hardware filter was actually about 0.1 Hz. The statement on the website, as shown below, has been changed. The changes are indicated by italics.

> Revised information about the nominal filter characteristics, as determined from an analysis of a circuit diagram for the filter. *Note in particular that the highpass corner is at 0.1 Hz, not 0.01 Hz* as was indicated in the files originally provided by Alyeska, *and that the highpass and lowpass filters each have 2 poles rather than 1.* Details of the nominal filter characteristics are provided in the headers.
> Due to uncertainties in the instrument response, *only uncorrected acceleration time series data are currently being served.* Results from bench tests using components similar to those deployed in the field show deviations from nominal characteristics that could produce variations of up to 20% in displacements determined by double integration of the acceleration time series. The USGS is working with Alyeska to determine more accurate calibrations, and any new information will be released as soon as it is available.

Bill Ellsworth applied a correction for the instrument filter and used this in his recent *Earthquake Spectra* paper (Ellsworth et al., 2004). His corrected data can be obtained from ftp://clover.wr.usgs.gov/pub/ehz/PS10/. I reformatted his corrected version of the data into the standard USGS NSMP SMC format. When integrating to velocity and displacement. I discovered some drifts that were easy to remove by applying a simple "v0" baseline correction (details are in the headers of the smc files, available from me). Figure L.1 is a plot of the acceleration, velocity, and displacement for the three components of motion. Figure L.2 is a plot of the geometric mean PSA and SD compared to the spectrum from the NGA flatfile. As can be seen most readily from the SD plot, there are significant differences between the NGA spectrum

(as contained in the flatfile available on 07 December 2004) and that from the instrument-filter, baseline-corrected data, the latter being higher at short and long periods. Note that the difference at long periods starts at about 6 s, so it is probably important to replace the spectrum in the flatfile with the new spectrum. The difference is in the direction expected if the NGA values are based on the uncorrected data (email from W. Silva subsequent to this confirmed my suspicions). The difference at short periods might be due to the use of a causal high-pass filter by NGA—Boore and Akkar (2003) show the surprising result that causal filters can affect short-period motions, at periods much shorter than the filter corner period. This has been confirmed in studies of a number of other records. The geometric means of the PGA are as follows: NGA: 0.316g; Dave: 0.346g. And for PGV: NGA: 85 cm/s; Dave: 128 cm/s. The difference in PGV might be explained by the use of a 0.1 high-pass filter in the data (or are the filter characteristics in the flatfile simply reporting the hardwired instrument filter? Was an additional filter applied by Walt?)

An issue not discussed by the group is that the geometric means of the two horizontal components is not invariant under rotation. This may become important when the developers are studying fault-parallel and fault-normal motions. At the time that the material in this appendix was originally prepared, I had not seen a systematic study of the dependence of geometric mean on rotation, For that reason, I was the lead author in developing a measure of strong ground motion that is independent of instrument orientation (Boore at al., 2006). For the interest of the reader, I show in Figure L.3 the acceleration, velocity, and displacement traces for the motions after rotating into fault-normal and fault-parallel directions. Figure L.4 shows the PSA and SD response spectra for the fault-normal and fault-parallel direction; note that the fault-normal spectrum exceeds the fault-parallel spectrum for the period range from about 2 s to 20 s, after which the large residual displacement in the fault-parallel direction produces a much larger response spectrum. Both the time series and the response spectra show that the character of the waveforms can depend strongly on instrument orientation, particularly at longer periods. For that reason, there can be significant differences in the geometric-mean spectra for different orientations, as shown in Figure L.5.

In summary, the NGA flatfile entries for Pump Station 10 are based on data uncorrected for the hardware instrument filter. Using corrected data leads to differences in the PGA, PGV, and PGD values, as well as short- and long-period response spectra. In addition, as a side issue I show that there can be substantial differences in the geometric mean computed from unrotated

and rotated horizontal components. This might be important in studies of fault-normal and fault-parallel motions.
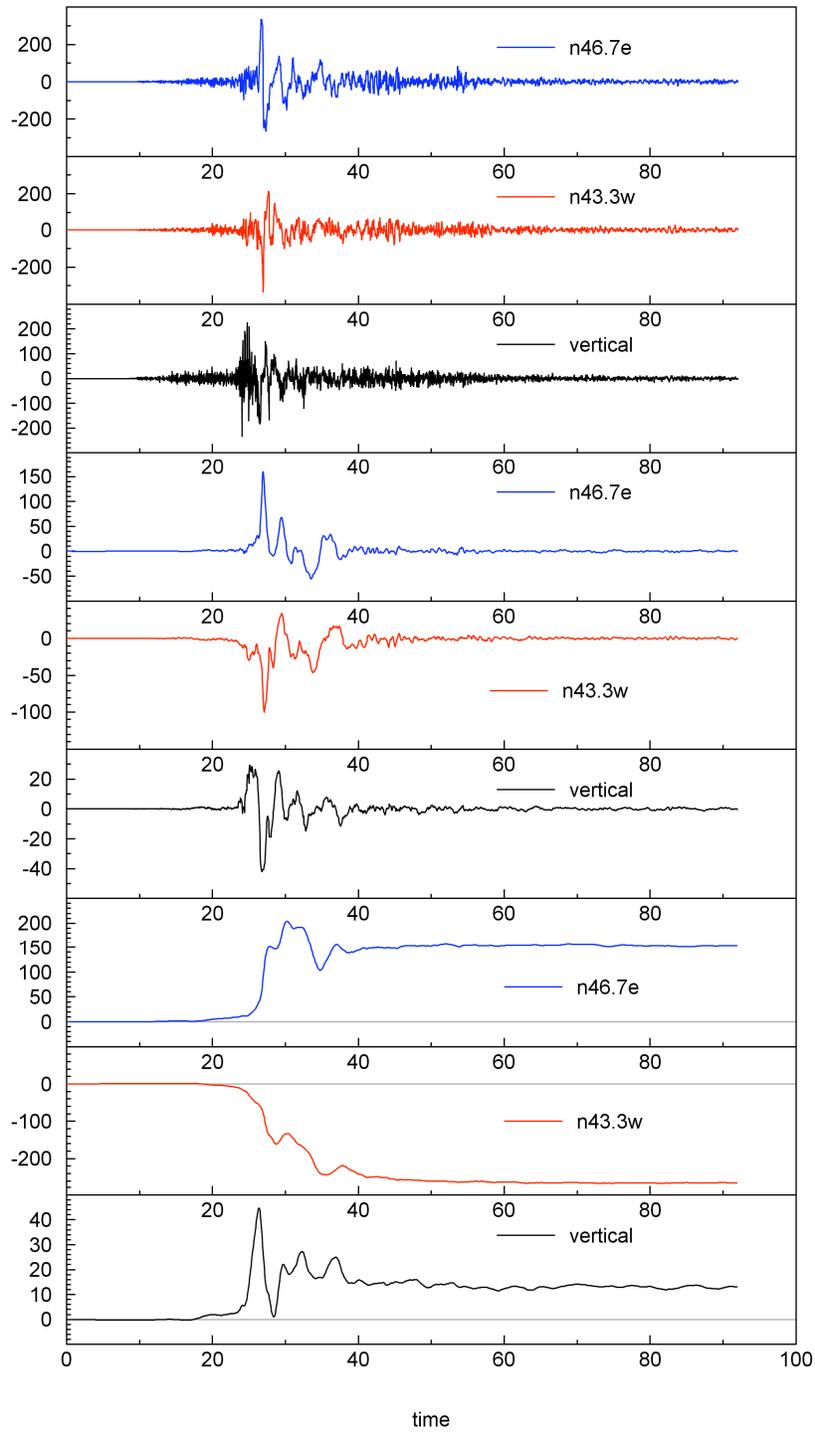
Fig. L.1 Pump Station 10 data from 2002 Denali fault earthquake (from Ellsworth), reprocessed using "V0" baseline correction.

A - 99
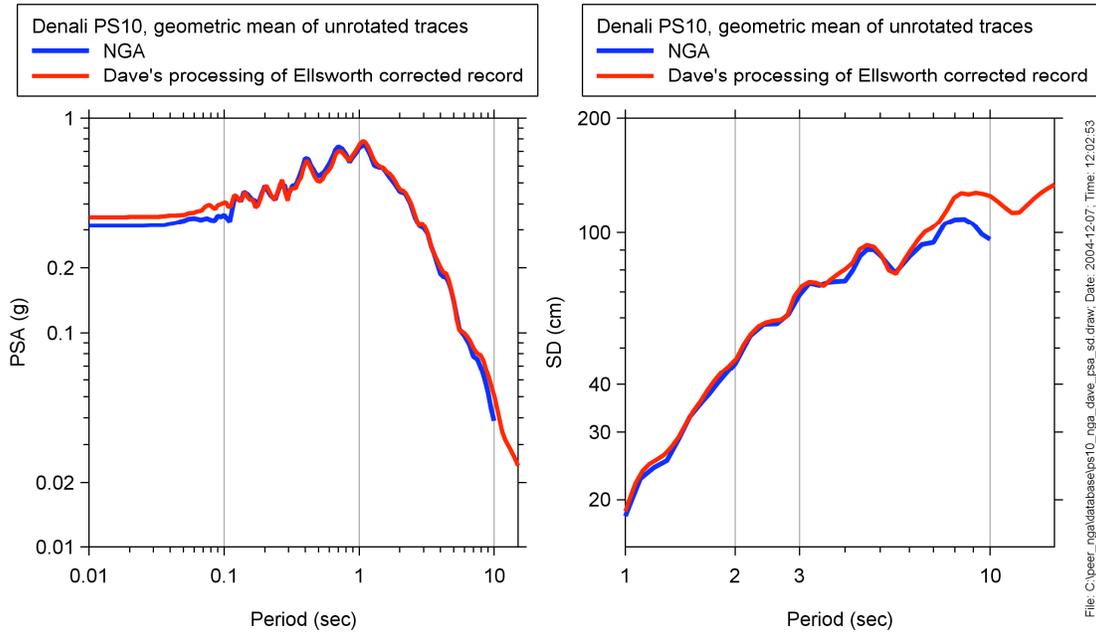
Fig. L.2 Comparison of NGA and D. Boore's PSA for Pump Station 10 data from 2002 Denali fault earthquake (from Ellsworth), reprocessed using "V0" baseline correction.
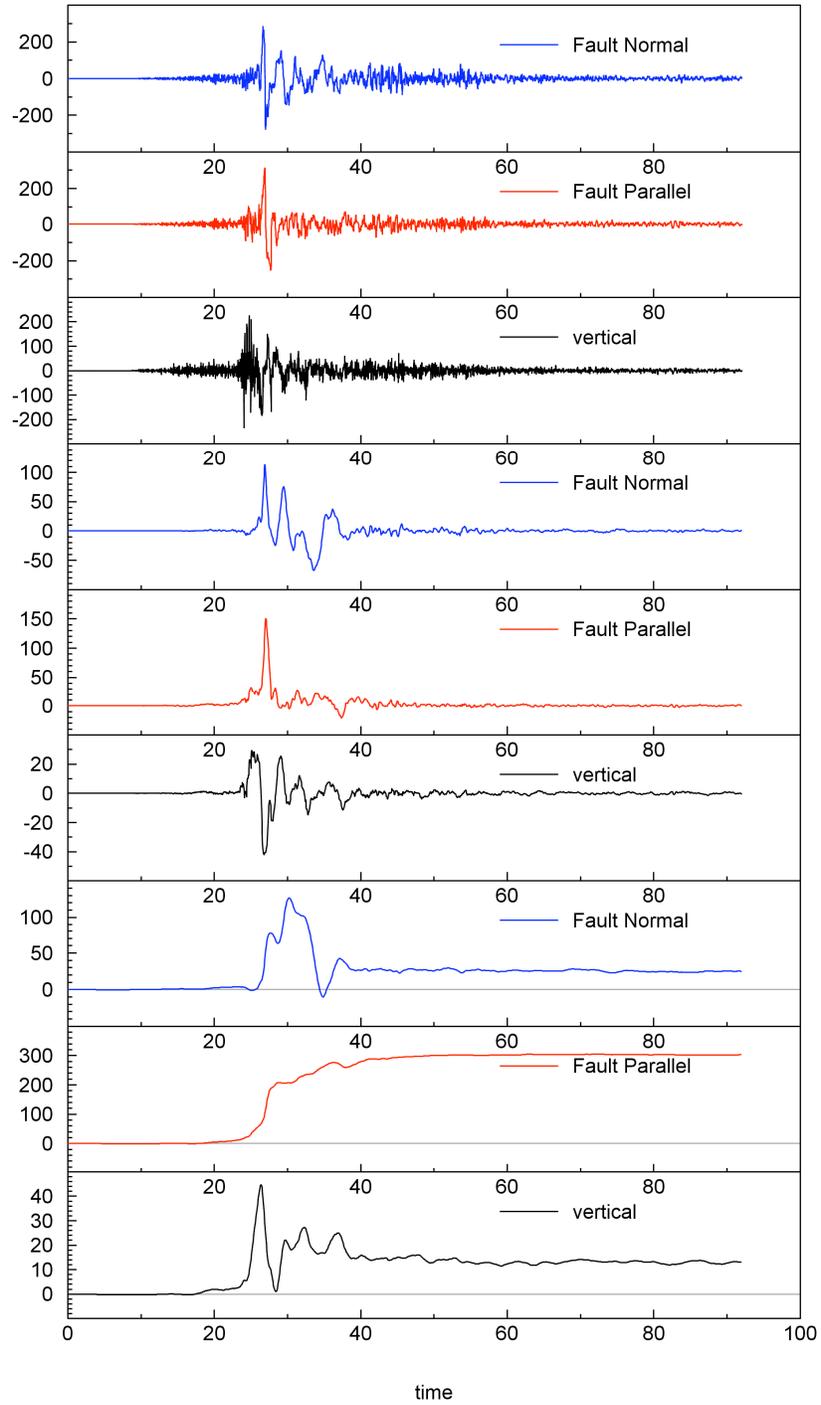
Fig. L.3 Pump Station 10 data from 2002 Denali fault earthquake (from Ellsworth), reprocessed using "V0" baseline correction and rotated into fault-normal and fault-parallel directions.
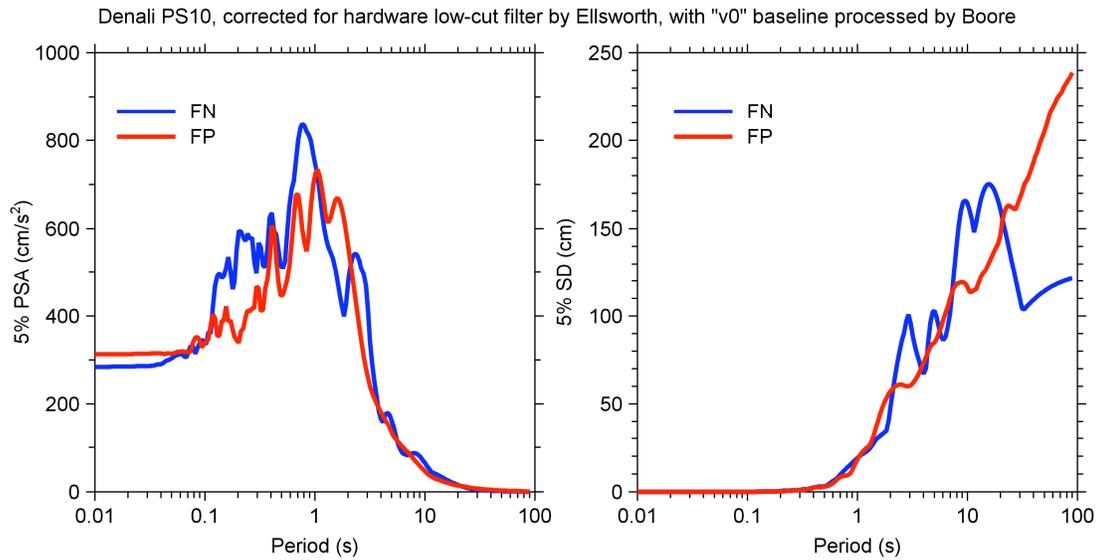
Fig. L.4 PSA and SD for Pump Station 10 data from 2002 Denali fault earthquake (from Ellsworth), reprocessed using "V0" baseline correction and rotated into fault-normal and fault-parallel directions.
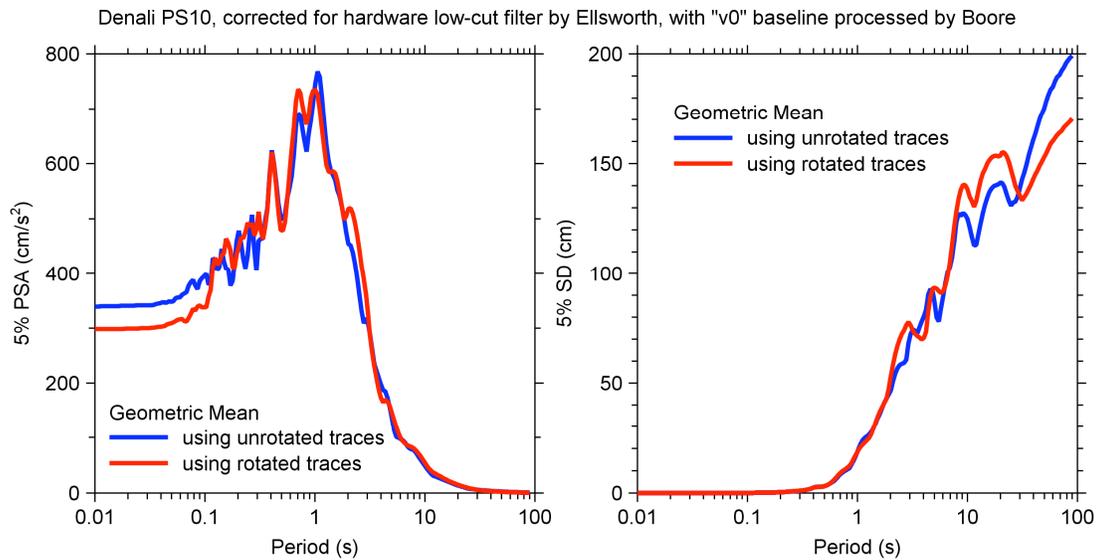
Fig. L.5 PSA and SD from geometric means of unrotated and rotated traces for Pump Station 10 data from 2002 Denali fault earthquake (from Ellsworth), reprocessed using "V0" baseline correction.

Appendix M: Magnitudes for Big Bear City and Yorba Linda Earthquakes

In a presentation given at an NGA developers workshop on 12 April 2005, I showed that the data from the 2002 Yorba Linda earthquake were systematically smaller than for other earthquakes with magnitudes near the M 4.8 given for the event in the then-current NGA flatfile. Ken Campbell's event terms from his regression confirmed this. Soon after the workshop, I came across the paper by Komatitisch et al. (2004), in which they model long-period (greater than 6 s) displacements for the event, using $\mathbf{M}$ = 4.2 rather than 4.8. They do not state how they obtained $\mathbf{M}$ for the event, but I imagine it is based on their modeling (and the method of Liu et al. 2004). As shown previously (Fig. 4.34), the ground motions from the Yorba Linda earthquake are lower than for the Anza and Big Bear City earthquakes (whose magnitudes in the flatfile are 4.92 and 5.0, respectively). Clearly, the Yorba Linda event is smaller than the other two. In addition, the attenuation with distance seems to be different for Yorba Linda than for the other two at shorter periods. In the original notes on this subject, I showed a comparison with an earlier version of the BA equations determined assuming that the magnitude of the Yorba Linda earthquakes was 4.8. I pointed out that the magnitude scaling from these earlier GMPEs gave an offset between the Yorba Linda and the other two events similar to the offset of the observations in Figure 4.34 if Komatitisch et al.'s (2004) magnitude was correct. On this basis I suggested that the magnitude for the Yorba Linda earthquake be lowered. I also pointed out that the Liu et al. (2004) paper gives $\mathbf{M}$ = 4.92 and depth = 6.3 km for the 22 February 2003 Big Bear City earthquake. The NGA flatfile gives $\mathbf{M}$ = 5.0 and 1.2 km for that event. I suggested that the flatfile values should be changed, and this was done. Some indication that the magnitudes are correct is given in Figures M.1–M.3, in which I compare the observations from the three earthquakes with simulations using the Joyner (1984) source model and the Raoof et al. (1999)

path function. The comparison is quite good considering that no effort was made to adjust the parameters of the simulation to fit the observations.
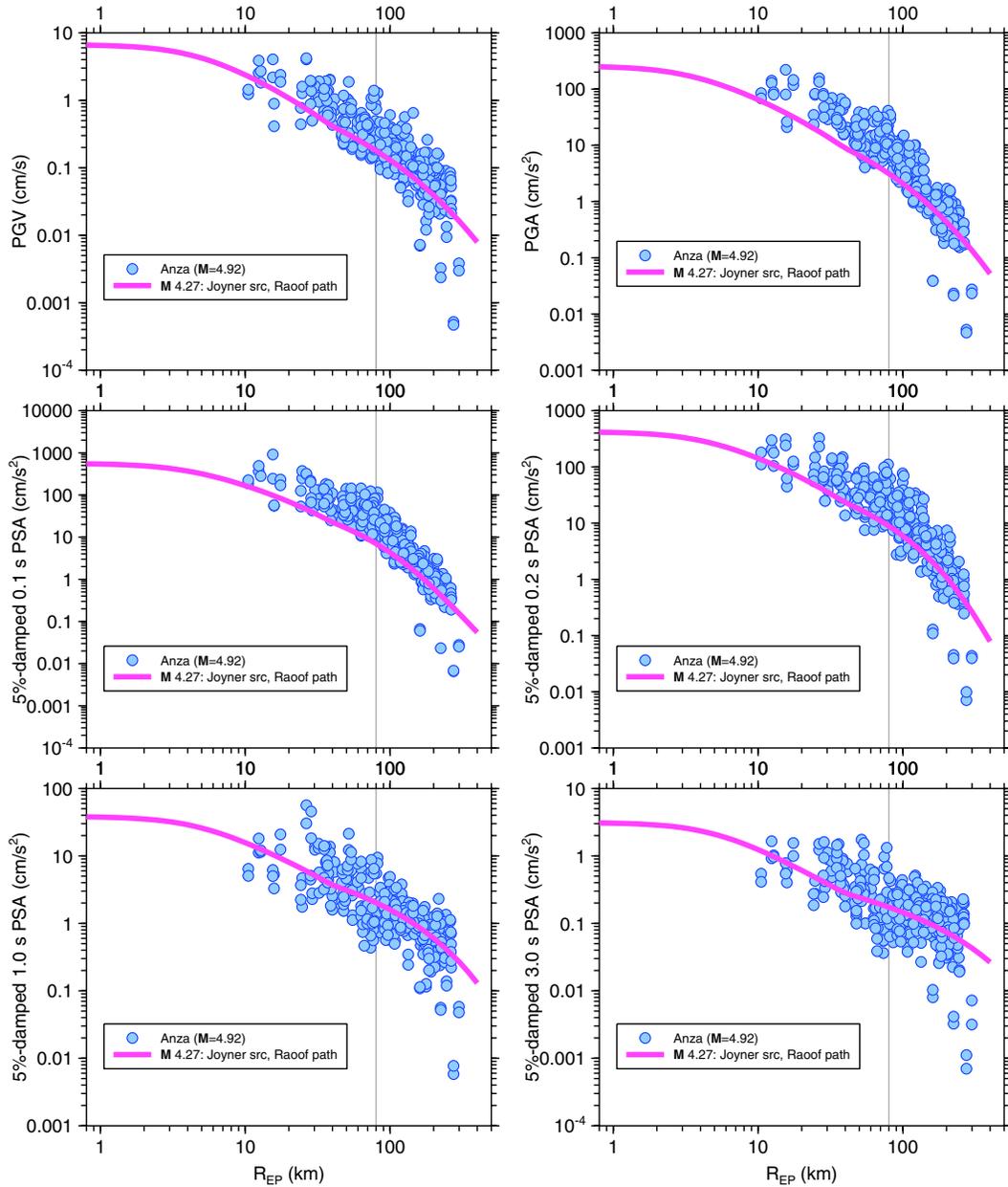
Fig. M.1 Ground motions from Anza earthquake, with simulated motions (using Joyner (1984) source model and path model from Raoof et al. (1999)).
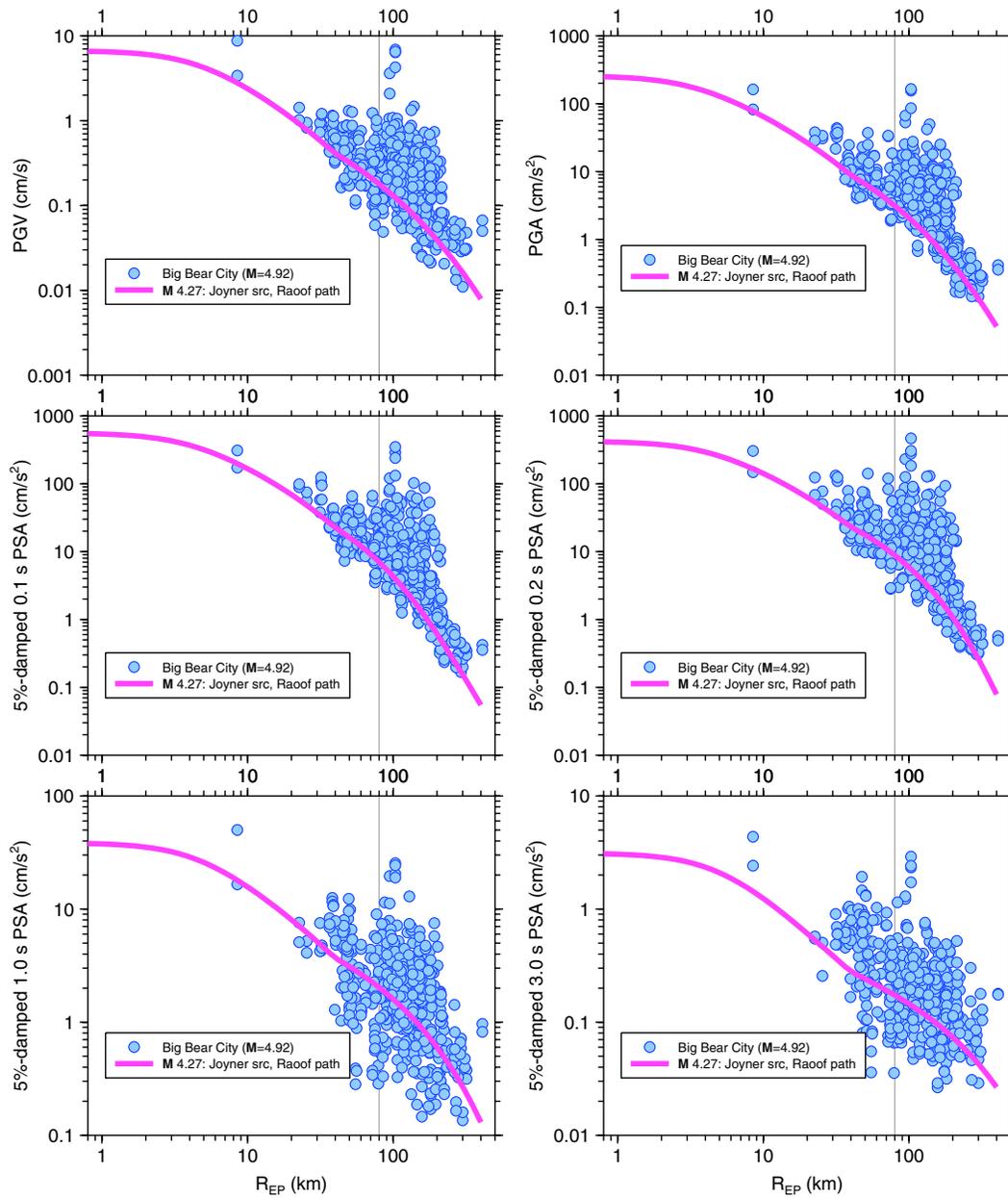
Fig. M.2 Ground motions from Big Bear City earthquake, with simulated motions (using Joyner (1984) source model and path model from Raoof et al. (1999)).
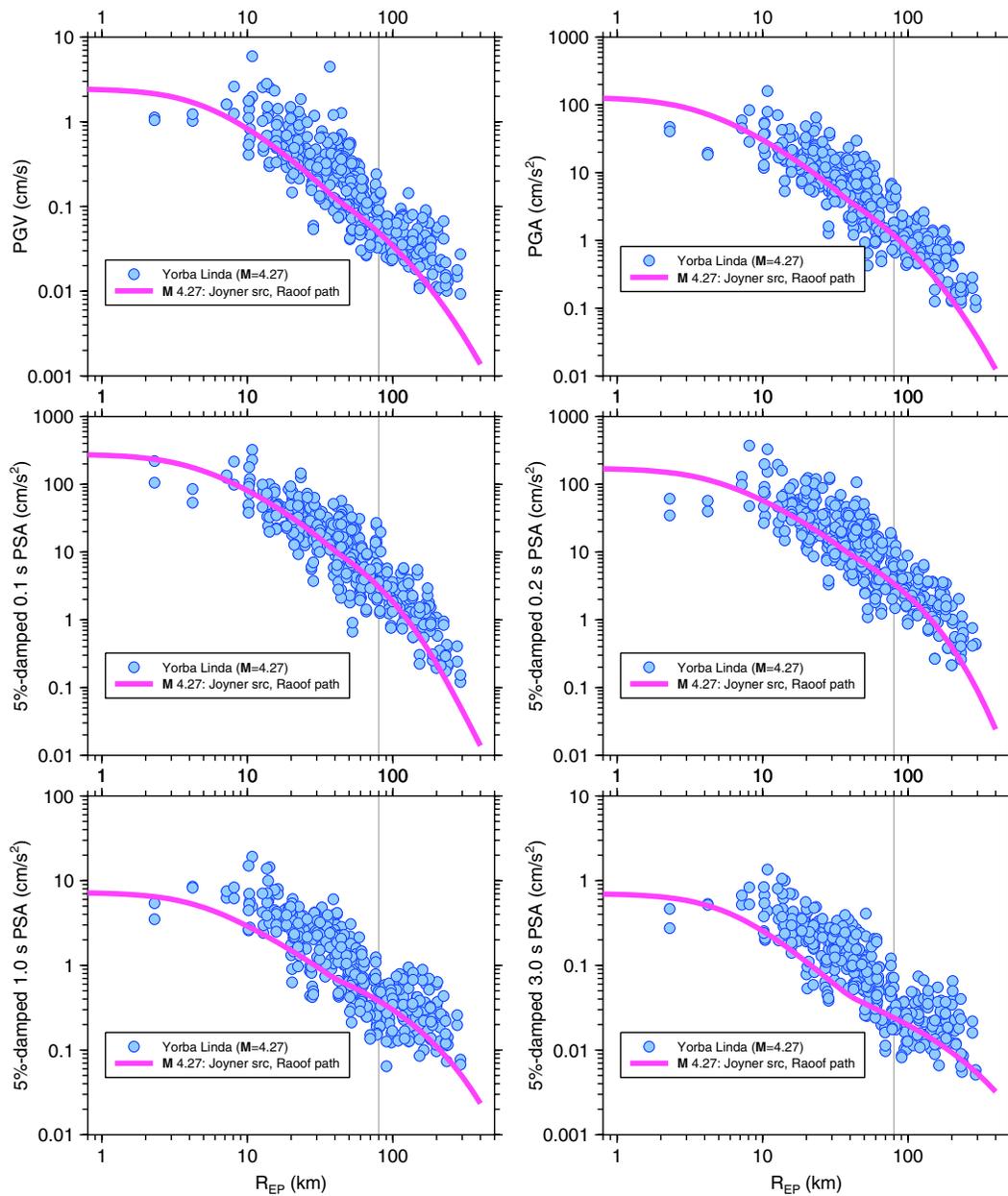
Fig. M.3   Ground motions from Yorba Linda earthquake, with simulated motions (using Joyner (1984) source model and path model from Raoof et al. (1999)).

Appendix N: Comparison of Ground Motions from 2001 Anza, 2002 Yorba Linda, and 2003 Big Bear City Earthquakes with 2004 Parkfield Earthquake

In the course of the NGA project, there was some discussion regarding the validity of the non-strong-motion source data for the three small earthquakes. The data for the three small events were gathered by Linda Seekins for Jack Boatwright. According to an email from her to me on 15 September 2005, *"All of the data from the Anza earthquake that I generated for Jack from the SCEC database was from the HLE and HLN recorders. They are low gain. accelerographs."* I understand from conversations with Linda that this is also true for the other two small events; thus no velocity sensor data from these three earthquakes were used in the analyses in this report. It is unfortunate that the extended data sets for the three small earthquakes were not included in the NGA flatfile; just because the data don't come from the USGS or CGS strong-motion groups does not make the data any different. According to the SCSN website (http://www.trinet.org/instr.html#analogvsdig), the accelerograph data come from K2 accelerographs.

One way of judging whether there is anything peculiar about the motions is to compare plots of the motions against distance with motions from the 2004 Parkfield earthquake from traditional (with one exception) strong-motion stations (many more data from non-traditional sources are available for the Parkfield earthquake, but I have not obtained those data). These comparisons are shown in Figures N.1–N.3 for PGV, PGA, and 5%-damped PSA for 0.1, 0.2, 1.0, and 3.0 s. The distance for the Parkfield earthquake is R_{JB} and for the others is R_{EP}. No site correction has been applied to the Parkfield data, but the data for the other quakes have been corrected to $V_{S30} = 760$ m/s using BJF97 amp factors (no nonlinear correction). The ground-

motion intensity measures from the two horizontal components have *not* been merged—the plots show both the intensity measures for both components for each station.

I see nothing strange in the distance decay of the three smaller events compared to the Parkfield data, although it is interesting to note that the level of motions at high frequency for the Anza and Big Bear City earthquakes is comparable to that from the larger Parkfield earthquake, although the magnitudes are quite different.
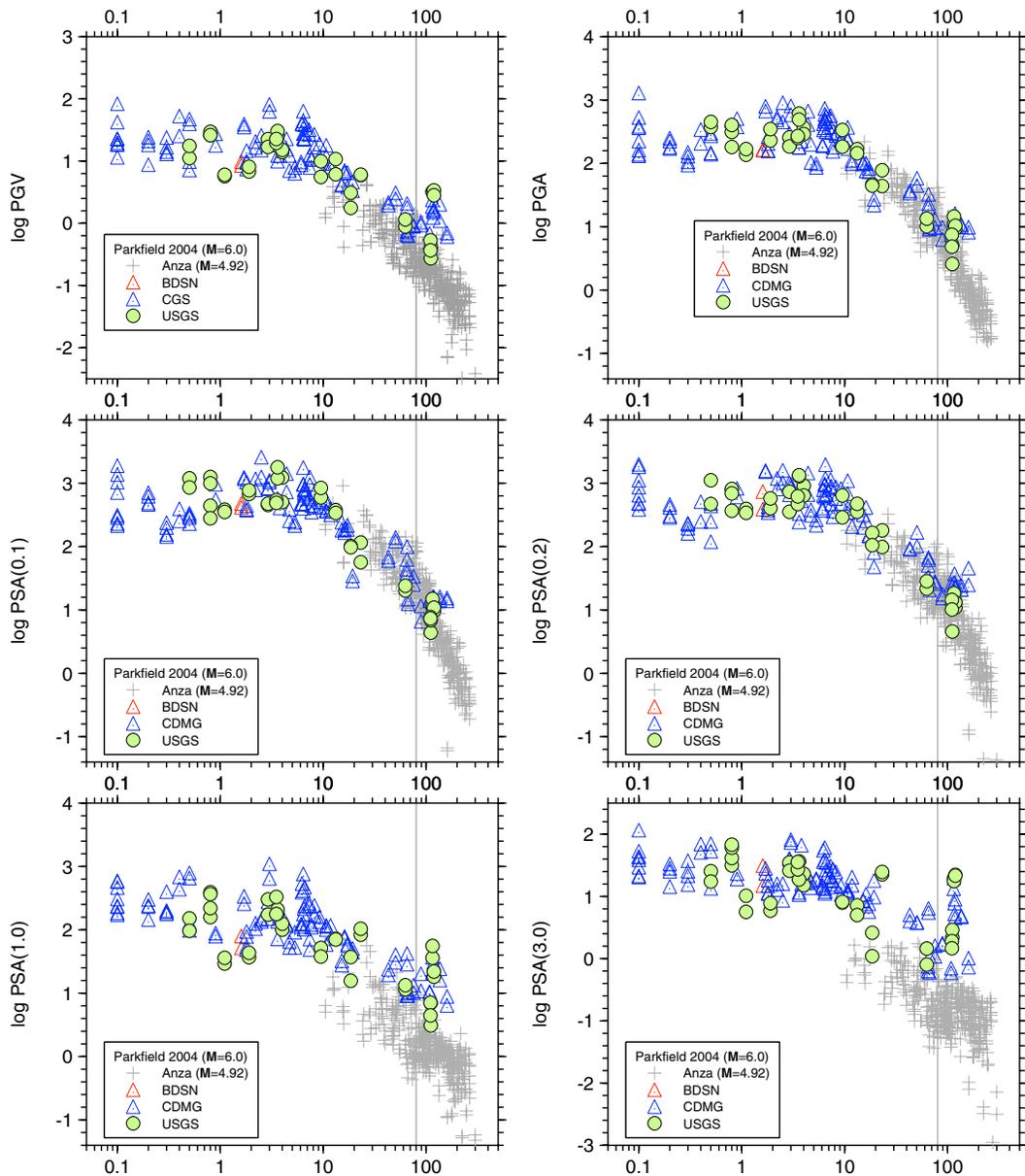
Fig. N.1   Ground motions from 2004 Parkfield earthquake compared to ground motions from smaller Anza earthquake.
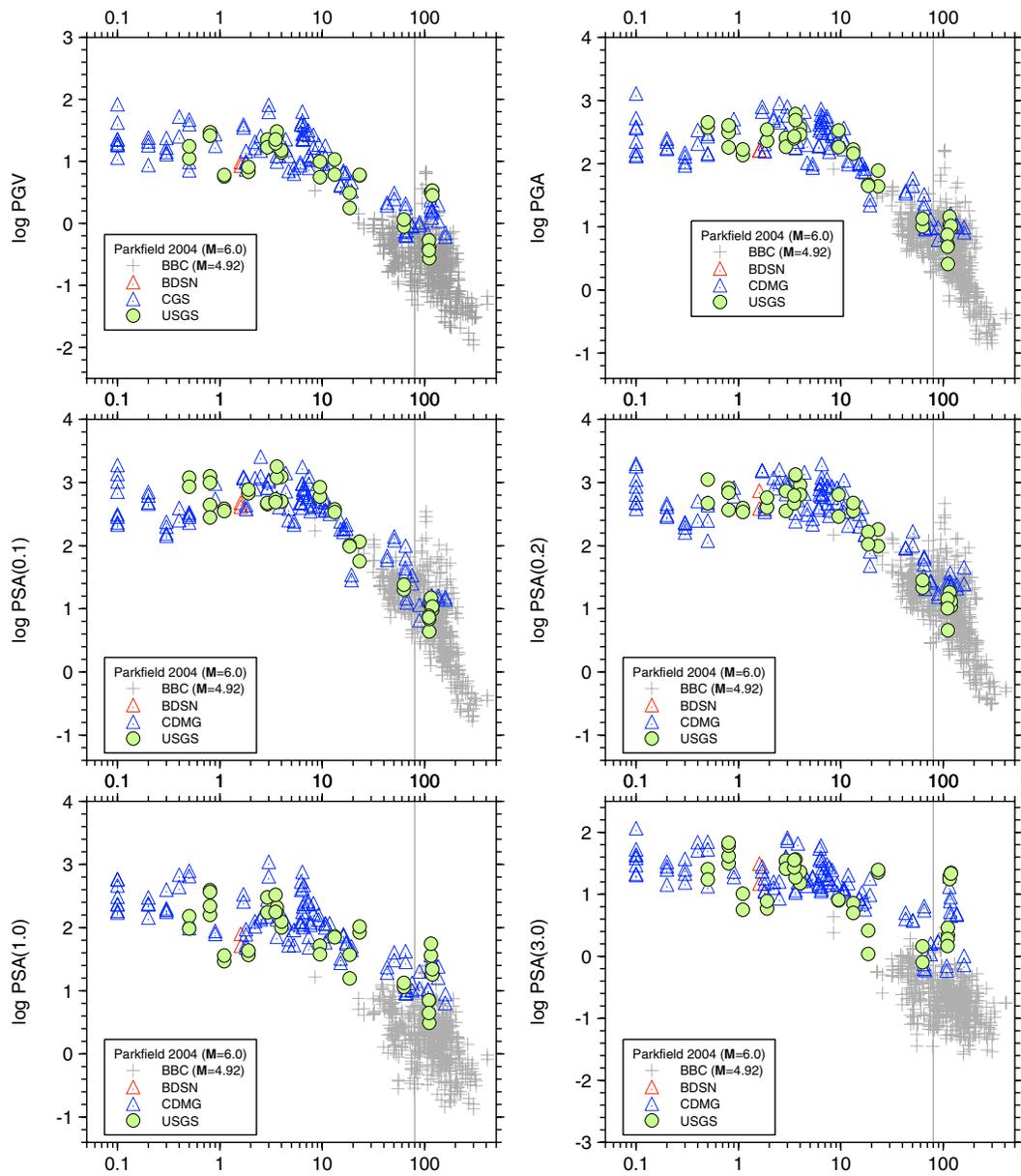
Fig. N.2 Ground motions from 2004 Parkfield earthquake compared to ground motions from smaller Big Bear City earthquake.
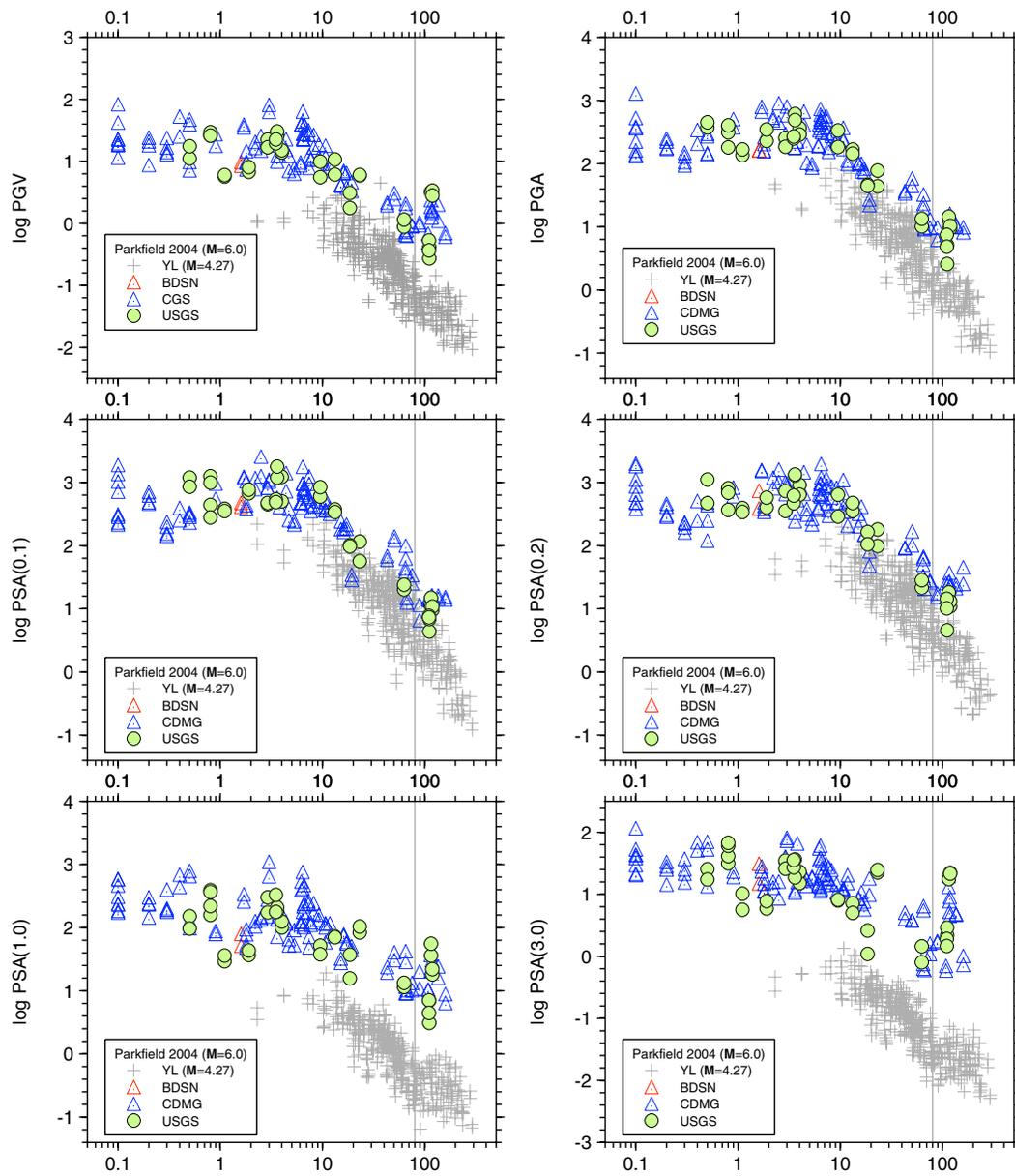
Fig. N.3 Ground motions from 2004 Parkfield earthquake compared to ground motions from smaller Yorba Linda earthquake.

PEER REPORTS

PEER reports are available from the National Information Service for Earthquake Engineering (NISEE). To order PEER reports, please contact the Pacific Earthquake Engineering Research Center, 1301 South 46th Street, Richmond, California 94804-4698. Tel.: (510) 665-3405; Fax: (510) 665-3420.

PEER 2007/01   *Boore-Atkinson NGA Ground Motion Relations for the Geometric Mean Horizontal Component of Peak and Spectral Ground Motion Parameters.* David M. Boore and Gail M. Atkinson. May. May 2007.

PEER 2006/12   *Societal Implications of Performance-Based Earthquake Engineering.* Peter J. May. May 2007.

PEER 2006/11   *Probabilistic Seismic Demand Analysis Using Advanced Ground Motion Intensity Measures, Attenuation Relationships, and Near-Fault Effects.* Polsak Tothong and C. Allin Cornell. March 2007.

PEER 2006/10   *Application of the PEER PBEE Methodology to the I-880 Viaduct.* Sashi Kunnath. February 2007.

PEER 2006/09   *Quantifying Economic Losses from Travel Forgone Following a Large Metropolitan Earthquake.* James Moore, Sungbin Cho, Yue Yue Fan, and Stuart Werner. November 2006.

PEER 2006/08   *Vector-Valued Ground Motion Intensity Measures for Probabilistic Seismic Demand Analysis*. Jack W. Baker and C. Allin Cornell. October 2006.

PEER 2006/07   *Analytical Modeling of Reinforced Concrete Walls for Predicting Flexural and Coupled–Shear-Flexural Responses.* Kutay Orakcal, Loenardo M. Massone, and John W. Wallace. October 2006.

PEER 2006/06   *Nonlinear Analysis of a Soil-Drilled Pier System under Static and Dynamic Axial Loading.* Gang Wang and Nicholas Sitar. November 2006.

PEER 2006/05   *Advanced Seismic Assessment Guidelines.* Paolo Bazzurro, C. Allin Cornell, Charles Menun, Maziar Motahari, and Nicolas Luco. September 2006.

PEER 2006/04   *Probabilistic Seismic Evaluation of Reinforced Concrete Structural Components and Systems.* Tae Hyung Lee and Khalid M. Mosalam. August 2006.

PEER 2006/03   *Performance of Lifelines Subjected to Lateral Spreading.* Scott A. Ashford and Teerawut Juirnarongrit. July 2006.

PEER 2006/02   *Pacific Earthquake Engineering Research Center Highway Demonstration Project.* Anne Kiremidjian, James Moore, Yue Yue Fan, Nesrin Basoz, Ozgur Yazali, and Meredith Williams. April 2006.

PEER 2006/01   *Bracing Berkeley. A Guide to Seismic Safety on the UC Berkeley Campus.* Mary C. Comerio, Stephen Tobriner, and Ariane Fehrenkamp. January 2006.

PEER 2005/16   *Seismic Response and Reliability of Electrical Substation Equipment and Systems.* Junho Song, Armen Der Kiureghian, and Jerome L. Sackman. April 2006.

PEER 2005/15   *CPT-Based Probabilistic Assessment of Seismic Soil Liquefaction Initiation.* R. E. S. Moss, R. B. Seed, R. E. Kayen, J. P. Stewart, and A. Der Kiureghian. April 2006.

PEER 2005/14   *Workshop on Modeling of Nonlinear Cyclic Load-Deformation Behavior of Shallow Foundations.* Bruce L. Kutter, Geoffrey Martin, Tara Hutchinson, Chad Harden, Sivapalan Gajan, and Justin Phalen. March 2006.

PEER 2005/13   *Stochastic Characterization and Decision Bases under Time-Dependent Aftershock Risk in Performance-Based Earthquake Engineering.* Gee Liek Yeo and C. Allin Cornell. July 2005.

PEER 2005/12   *PEER Testbed Study on a Laboratory Building: Exercising Seismic Performance Assessment.* Mary C. Comerio, editor. November 2005.

PEER 2005/11   *Van Nuys Hotel Building Testbed Report: Exercising Seismic Performance Assessment.* Helmut Krawinkler, editor. October 2005.

PEER 2005/10   *First NEES/E-Defense Workshop on Collapse Simulation of Reinforced Concrete Building Structures.* September 2005.

PEER 2005/09   *Test Applications of Advanced Seismic Assessment Guidelines.* Joe Maffei, Karl Telleen, Danya Mohr, William Holmes, and Yuki Nakayama. August 2006.

PEER 2005/08   *Damage Accumulation in Lightly Confined Reinforced Concrete Bridge Columns.* R. Tyler Ranf, Jared M. Nelson, Zach Price, Marc O. Eberhard, and John F. Stanton. April 2006.

PEER 2005/07   *Experimental and Analytical Studies on the Seismic Response of Freestanding and Anchored Laboratory Equipment.* Dimitrios Konstantinidis and Nicos Makris. January 2005.

PEER 2005/06   *Global Collapse of Frame Structures under Seismic Excitations.* Luis F. Ibarra and Helmut Krawinkler. September 2005.

PEER 2005//05   *Performance Characterization of Bench- and Shelf-Mounted Equipment.* Samit Ray Chaudhuri and Tara C. Hutchinson. May 2006.

PEER 2005/04   *Numerical Modeling of the Nonlinear Cyclic Response of Shallow Foundations.* Chad Harden, Tara Hutchinson, Geoffrey R. Martin, and Bruce L. Kutter. August 2005.

PEER 2005/03   *A Taxonomy of Building Components for Performance-Based Earthquake Engineering.*   Keith A. Porter. September 2005.

PEER 2005/02   *Fragility Basis for California Highway Overpass Bridge Seismic Decision Making.* Kevin R. Mackie and Bozidar Stojadinovic. June 2005.

PEER 2005/01   *Empirical Characterization of Site Conditions on Strong Ground Motion.*   Jonathan P. Stewart, Yoojoong Choi, and Robert W. Graves. June 2005.

PEER 2004/09   *Electrical Substation Equipment Interaction: Experimental Rigid Conductor Studies.*   Christopher Stearns and André Filiatrault. February 2005.

PEER 2004/08   *Seismic Qualification and Fragility Testing of Line Break 550-kV Disconnect Switches.* Shakhzod M. Takhirov, Gregory L. Fenves, and Eric Fujisaki. January 2005.

PEER 2004/07   *Ground Motions for Earthquake Simulator Qualification of Electrical Substation Equipment.* Shakhzod M. Takhirov, Gregory L. Fenves, Eric Fujisaki, and Don Clyde. January 2005.

PEER 2004/06   *Performance-Based Regulation and Regulatory Regimes.* Peter J. May and Chris Koski. September 2004.

PEER 2004/05   *Performance-Based Seismic Design Concepts and Implementation: Proceedings of an International Workshop.* Peter Fajfar and Helmut Krawinkler, editors. September 2004.

PEER 2004/04   *Seismic Performance of an Instrumented Tilt-up Wall Building.* James C. Anderson and Vitelmo V. Bertero. July 2004.

PEER 2004/03   *Evaluation and Application of Concrete Tilt-up Assessment Methodologies.* Timothy Graf and James O. Malley. October 2004.

PEER 2004/02   *Analytical Investigations of New Methods for Reducing Residual Displacements of Reinforced Concrete Bridge Columns.* Junichi Sakai and Stephen A. Mahin. August 2004.

PEER 2004/01   *Seismic Performance of Masonry Buildings and Design Implications.* Kerri Anne Taeko Tokoro, James C. Anderson, and Vitelmo V. Bertero. February 2004.

PEER 2003/18   *Performance Models for Flexural Damage in Reinforced Concrete Columns.* Michael Berry and Marc Eberhard. August 2003.

PEER 2003/17   *Predicting Earthquake Damage in Older Reinforced Concrete Beam-Column Joints.* Catherine Pagni and Laura Lowes. October 2004.

PEER 2003/16   *Seismic Demands for Performance-Based Design of Bridges.* Kevin Mackie and Božidar Stojadinovic. August 2003.

PEER 2003/15   *Seismic Demands for Nondeteriorating Frame Structures and Their Dependence on Ground Motions.* Ricardo Antonio Medina and Helmut Krawinkler. May 2004.

PEER 2003/14   *Finite Element Reliability and Sensitivity Methods for Performance-Based Earthquake Engineering.* Terje Haukaas and Armen Der Kiureghian. April 2004.

PEER 2003/13   *Effects of Connection Hysteretic Degradation on the Seismic Behavior of Steel Moment-Resisting Frames.* Janise E. Rodgers and Stephen A. Mahin. March 2004.

PEER 2003/12   *Implementation Manual for the Seismic Protection of Laboratory Contents: Format and Case Studies.* William T. Holmes and Mary C. Comerio. October 2003.

PEER 2003/11   *Fifth U.S.-Japan Workshop on Performance-Based Earthquake Engineering Methodology for Reinforced Concrete Building Structures.* February 2004.

PEER 2003/10   *A Beam-Column Joint Model for Simulating the Earthquake Response of Reinforced Concrete Frames.* Laura N. Lowes, Nilanjan Mitra, and Arash Altoontash. February 2004.

PEER 2003/09   *Sequencing Repairs after an Earthquake: An Economic Approach.* Marco Casari and Simon J. Wilkie. April 2004.

PEER 2003/08   *A Technical Framework for Probability-Based Demand and Capacity Factor Design (DCFD) Seismic Formats.* Fatemeh Jalayer and C. Allin Cornell. November 2003.

PEER 2003/07 *Uncertainty Specification and Propagation for Loss Estimation Using FOSM Methods.* Jack W. Baker and C. Allin Cornell. September 2003.

PEER 2003/06 *Performance of Circular Reinforced Concrete Bridge Columns under Bidirectional Earthquake Loading.* Mahmoud M. Hachem, Stephen A. Mahin, and Jack P. Moehle. February 2003.

PEER 2003/05 *Response Assessment for Building-Specific Loss Estimation.* Eduardo Miranda and Shahram Taghavi. September 2003.

PEER 2003/04 *Experimental Assessment of Columns with Short Lap Splices Subjected to Cyclic Loads.* Murat Melek, John W. Wallace, and Joel Conte. April 2003.

PEER 2003/03 *Probabilistic Response Assessment for Building-Specific Loss Estimation.* Eduardo Miranda and Hesameddin Aslani. September 2003.

PEER 2003/02 *Software Framework for Collaborative Development of Nonlinear Dynamic Analysis Program.* Jun Peng and Kincho H. Law. September 2003.

PEER 2003/01 *Shake Table Tests and Analytical Studies on the Gravity Load Collapse of Reinforced Concrete Frames.* Kenneth John Elwood and Jack P. Moehle. November 2003.

PEER 2002/24 *Performance of Beam to Column Bridge Joints Subjected to a Large Velocity Pulse.* Natalie Gibson, André Filiatrault, and Scott A. Ashford. April 2002.

PEER 2002/23 *Effects of Large Velocity Pulses on Reinforced Concrete Bridge Columns.* Greg L. Orozco and Scott A. Ashford. April 2002.

PEER 2002/22 *Characterization of Large Velocity Pulses for Laboratory Testing.* Kenneth E. Cox and Scott A. Ashford. April 2002.

PEER 2002/21 *Fourth U.S.-Japan Workshop on Performance-Based Earthquake Engineering Methodology for Reinforced Concrete Building Structures.* December 2002.

PEER 2002/20 *Barriers to Adoption and Implementation of PBEE Innovations.* Peter J. May. August 2002.

PEER 2002/19 *Economic-Engineered Integrated Models for Earthquakes: Socioeconomic Impacts.* Peter Gordon, James E. Moore II, and Harry W. Richardson. July 2002.

PEER 2002/18 *Assessment of Reinforced Concrete Building Exterior Joints with Substandard Details.* Chris P. Pantelides, Jon Hansen, Justin Nadauld, and Lawrence D. Reaveley. May 2002.

PEER 2002/17 *Structural Characterization and Seismic Response Analysis of a Highway Overcrossing Equipped with Elastomeric Bearings and Fluid Dampers: A Case Study.* Nicos Makris and Jian Zhang. November 2002.

PEER 2002/16 *Estimation of Uncertainty in Geotechnical Properties for Performance-Based Earthquake Engineering.* Allen L. Jones, Steven L. Kramer, and Pedro Arduino. December 2002.

PEER 2002/15 *Seismic Behavior of Bridge Columns Subjected to Various Loading Patterns.* Asadollah Esmaeily-Gh. and Yan Xiao. December 2002.

PEER 2002/14 *Inelastic Seismic Response of Extended Pile Shaft Supported Bridge Structures.* T.C. Hutchinson, R.W. Boulanger, Y.H. Chai, and I.M. Idriss. December 2002.

PEER 2002/13 *Probabilistic Models and Fragility Estimates for Bridge Components and Systems.* Paolo Gardoni, Armen Der Kiureghian, and Khalid M. Mosalam. June 2002.

PEER 2002/12 *Effects of Fault Dip and Slip Rake on Near-Source Ground Motions: Why Chi-Chi Was a Relatively Mild M7.6 Earthquake.* Brad T. Aagaard, John F. Hall, and Thomas H. Heaton. December 2002.

PEER 2002/11 *Analytical and Experimental Study of Fiber-Reinforced Strip Isolators.* James M. Kelly and Shakhzod M. Takhirov. September 2002.

PEER 2002/10 *Centrifuge Modeling of Settlement and Lateral Spreading with Comparisons to Numerical Analyses.* Sivapalan Gajan and Bruce L. Kutter. January 2003.

PEER 2002/09 *Documentation and Analysis of Field Case Histories of Seismic Compression during the 1994 Northridge, California, Earthquake.* Jonathan P. Stewart, Patrick M. Smith, Daniel H. Whang, and Jonathan D. Bray. October 2002.

PEER 2002/08 *Component Testing, Stability Analysis and Characterization of Buckling-Restrained Unbonded Braces^{TM}.* Cameron Black, Nicos Makris, and Ian Aiken. September 2002.

PEER 2002/07 *Seismic Performance of Pile-Wharf Connections.* Charles W. Roeder, Robert Graff, Jennifer Soderstrom, and Jun Han Yoo. December 2001.

PEER 2002/06 *The Use of Benefit-Cost Analysis for Evaluation of Performance-Based Earthquake Engineering Decisions.* Richard O. Zerbe and Anthony Falit-Baiamonte. September 2001.

PEER 2002/05 *Guidelines, Specifications, and Seismic Performance Characterization of Nonstructural Building Components and Equipment.* André Filiatrault, Constantin Christopoulos, and Christopher Stearns. September 2001.

PEER 2002/04 *Consortium of Organizations for Strong-Motion Observation Systems and the Pacific Earthquake Engineering Research Center Lifelines Program: Invited Workshop on Archiving and Web Dissemination of Geotechnical Data, 4–5 October 2001.* September 2002.

PEER 2002/03 *Investigation of Sensitivity of Building Loss Estimates to Major Uncertain Variables for the Van Nuys Testbed.* Keith A. Porter, James L. Beck, and Rustem V. Shaikhutdinov. August 2002.

PEER 2002/02 *The Third U.S.-Japan Workshop on Performance-Based Earthquake Engineering Methodology for Reinforced Concrete Building Structures.* July 2002.

PEER 2002/01 *Nonstructural Loss Estimation: The UC Berkeley Case Study.* Mary C. Comerio and John C. Stallmeyer. December 2001.

PEER 2001/16 *Statistics of SDF-System Estimate of Roof Displacement for Pushover Analysis of Buildings.* Anil K. Chopra, Rakesh K. Goel, and Chatpan Chintanapakdee. December 2001.

PEER 2001/15 *Damage to Bridges during the 2001 Nisqually Earthquake.* R. Tyler Ranf, Marc O. Eberhard, and Michael P. Berry. November 2001.

PEER 2001/14 *Rocking Response of Equipment Anchored to a Base Foundation.* Nicos Makris and Cameron J. Black. September 2001.

PEER 2001/13 *Modeling Soil Liquefaction Hazards for Performance-Based Earthquake Engineering.* Steven L. Kramer and Ahmed-W. Elgamal. February 2001.

PEER 2001/12 *Development of Geotechnical Capabilities in OpenSees.* Boris Jeremi . September 2001.

PEER 2001/11 *Analytical and Experimental Study of Fiber-Reinforced Elastomeric Isolators.* James M. Kelly and Shakhzod M. Takhirov. September 2001.

PEER 2001/10 *Amplification Factors for Spectral Acceleration in Active Regions.* Jonathan P. Stewart, Andrew H. Liu, Yoojoong Choi, and Mehmet B. Baturay. December 2001.

PEER 2001/09 *Ground Motion Evaluation Procedures for Performance-Based Design.* Jonathan P. Stewart, Shyh-Jeng Chiou, Jonathan D. Bray, Robert W. Graves, Paul G. Somerville, and Norman A. Abrahamson. September 2001.

PEER 2001/08 *Experimental and Computational Evaluation of Reinforced Concrete Bridge Beam-Column Connections for Seismic Performance.* Clay J. Naito, Jack P. Moehle, and Khalid M. Mosalam. November 2001.

PEER 2001/07 *The Rocking Spectrum and the Shortcomings of Design Guidelines.* Nicos Makris and Dimitrios Konstantinidis. August 2001.

PEER 2001/06 *Development of an Electrical Substation Equipment Performance Database for Evaluation of Equipment Fragilities.* Thalia Agnanos. April 1999.

PEER 2001/05 *Stiffness Analysis of Fiber-Reinforced Elastomeric Isolators.* Hsiang-Chuan Tsai and James M. Kelly. May 2001.

PEER 2001/04 *Organizational and Societal Considerations for Performance-Based Earthquake Engineering.* Peter J. May. April 2001.

PEER 2001/03 *A Modal Pushover Analysis Procedure to Estimate Seismic Demands for Buildings: Theory and Preliminary Evaluation.* Anil K. Chopra and Rakesh K. Goel. January 2001.

PEER 2001/02 *Seismic Response Analysis of Highway Overcrossings Including Soil-Structure Interaction.* Jian Zhang and Nicos Makris. March 2001.

PEER 2001/01 *Experimental Study of Large Seismic Steel Beam-to-Column Connections.* Egor P. Popov and Shakhzod M. Takhirov. November 2000.

PEER 2000/10 *The Second U.S.-Japan Workshop on Performance-Based Earthquake Engineering Methodology for Reinforced Concrete Building Structures.* March 2000.

PEER 2000/09 *Structural Engineering Reconnaissance of the August 17, 1999 Earthquake: Kocaeli (Izmit), Turkey.* Halil Sezen, Kenneth J. Elwood, Andrew S. Whittaker, Khalid Mosalam, John J. Wallace, and John F. Stanton. December 2000.

PEER 2000/08 *Behavior of Reinforced Concrete Bridge Columns Having Varying Aspect Ratios and Varying Lengths of Confinement.* Anthony J. Calderone, Dawn E. Lehman, and Jack P. Moehle. January 2001.

PEER 2000/07 *Cover-Plate and Flange-Plate Reinforced Steel Moment-Resisting Connections.* Taejin Kim, Andrew S. Whittaker, Amir S. Gilani, Vitelmo V. Bertero, and Shakhzod M. Takhirov. September 2000.

PEER 2000/06 *Seismic Evaluation and Analysis of 230-kV Disconnect Switches.* Amir S. J. Gilani, Andrew S. Whittaker, Gregory L. Fenves, Chun-Hao Chen, Henry Ho, and Eric Fujisaki. July 2000.

PEER 2000/05 *Performance-Based Evaluation of Exterior Reinforced Concrete Building Joints for Seismic Excitation.* Chandra Clyde, Chris P. Pantelides, and Lawrence D. Reaveley. July 2000.

PEER 2000/04 *An Evaluation of Seismic Energy Demand: An Attenuation Approach.* Chung-Che Chou and Chia-Ming Uang. July 1999.

PEER 2000/03 *Framing Earthquake Retrofitting Decisions: The Case of Hillside Homes in Los Angeles.* Detlof von Winterfeldt, Nels Roselund, and Alicia Kitsuse. March 2000.

PEER 2000/02 *U.S.-Japan Workshop on the Effects of Near-Field Earthquake Shaking.* Andrew Whittaker, ed. July 2000.

PEER 2000/01 *Further Studies on Seismic Interaction in Interconnected Electrical Substation Equipment.* Armen Der Kiureghian, Kee-Jeung Hong, and Jerome L. Sackman. November 1999.

PEER 1999/14 *Seismic Evaluation and Retrofit of 230-kV Porcelain Transformer Bushings.* Amir S. Gilani, Andrew S. Whittaker, Gregory L. Fenves, and Eric Fujisaki. December 1999.

PEER 1999/13 *Building Vulnerability Studies: Modeling and Evaluation of Tilt-up and Steel Reinforced Concrete Buildings.* John W. Wallace, Jonathan P. Stewart, and Andrew S. Whittaker, editors. December 1999.

PEER 1999/12 *Rehabilitation of Nonductile RC Frame Building Using Encasement Plates and Energy-Dissipating Devices.* Mehrdad Sasani, Vitelmo V. Bertero, James C. Anderson. December 1999.

PEER 1999/11 *Performance Evaluation Database for Concrete Bridge Components and Systems under Simulated Seismic Loads.* Yael D. Hose and Frieder Seible. November 1999.

PEER 1999/10 *U.S.-Japan Workshop on Performance-Based Earthquake Engineering Methodology for Reinforced Concrete Building Structures.* December 1999.

PEER 1999/09 *Performance Improvement of Long Period Building Structures Subjected to Severe Pulse-Type Ground Motions.* James C. Anderson, Vitelmo V. Bertero, and Raul Bertero. October 1999.

PEER 1999/08 *Envelopes for Seismic Response Vectors.* Charles Menun and Armen Der Kiureghian. July 1999.

PEER 1999/07 *Documentation of Strengths and Weaknesses of Current Computer Analysis Methods for Seismic Performance of Reinforced Concrete Members.* William F. Cofer. November 1999.

PEER 1999/06 *Rocking Response and Overturning of Anchored Equipment under Seismic Excitations.* Nicos Makris and Jian Zhang. November 1999.

PEER 1999/05 *Seismic Evaluation of 550 kV Porcelain Transformer Bushings.* Amir S. Gilani, Andrew S. Whittaker, Gregory L. Fenves, and Eric Fujisaki. October 1999.

PEER 1999/04 *Adoption and Enforcement of Earthquake Risk-Reduction Measures.* Peter J. May, Raymond J. Burby, T. Jens Feeley, and Robert Wood.

PEER 1999/03 *Task 3 Characterization of Site Response General Site Categories.* Adrian Rodriguez-Marek, Jonathan D. Bray, and Norman Abrahamson. February 1999.

PEER 1999/02 *Capacity-Demand-Diagram Methods for Estimating Seismic Deformation of Inelastic Structures: SDF Systems.* Anil K. Chopra and Rakesh Goel. April 1999.

PEER 1999/01 *Interaction in Interconnected Electrical Substation Equipment Subjected to Earthquake Ground Motions.* Armen Der Kiureghian, Jerome L. Sackman, and Kee-Jeung Hong. February 1999.

PEER 1998/08 *Behavior and Failure Analysis of a Multiple-Frame Highway Bridge in the 1994 Northridge Earthquake.* Gregory L. Fenves and Michael Ellery. December 1998.

PEER 1998/07 *Empirical Evaluation of Inertial Soil-Structure Interaction Effects.* Jonathan P. Stewart, Raymond B. Seed, and Gregory L. Fenves. November 1998.

PEER 1998/06 *Effect of Damping Mechanisms on the Response of Seismic Isolated Structures.* Nicos Makris and Shih-Po Chang. November 1998.

PEER 1998/05 *Rocking Response and Overturning of Equipment under Horizontal Pulse-Type Motions.* Nicos Makris and Yiannis Roussos. October 1998.

PEER 1998/04 *Pacific Earthquake Engineering Research Invitational Workshop Proceedings, May 14–15, 1998: Defining the Links between Planning, Policy Analysis, Economics and Earthquake Engineering.* Mary Comerio and Peter Gordon. September 1998.

PEER 1998/03   *Repair/Upgrade Procedures for Welded Beam to Column Connections.* James C. Anderson and Xiaojing Duan. May 1998.

PEER 1998/02   *Seismic Evaluation of 196 kV Porcelain Transformer Bushings.* Amir S. Gilani, Juan W. Chavez, Gregory L. Fenves, and Andrew S. Whittaker. May 1998.

PEER 1998/01   *Seismic Performance of Well-Confined Concrete Bridge Columns.* Dawn E. Lehman and Jack P. Moehle. December 2000.